

Modelling Degradation of Bioresorbable Polymeric Devices

by

Ying Wang

Department of Engineering

University of Leicester

UK

Thesis submitted to the Department of Engineering, University of Leicester for the

degree of Doctor of Philosophy

August 2009

Modelling Degradation of Bioresorbable Polymeric Devices

Ying Wang

Department of Engineering

University of Leicester

Abstract

Bioresorbable polymers, especially the homo and co-polymers of poly lactic acid (PLA) and poly glycolic acid (PGA), have been used for a broad range of applications for the last three decades owing to their biodegradable, biocompatible and non-toxic natures. One of the applications for these polymers is in the orthopaedic surgery as bone fixation device. According to the Wolff's law, if the bone fixation devices are overly strong to shield the healing bone from sufficient stress stimulation, the bone will resorb to an extent. Therefore the optimised design of such devices relies on the prediction of the stress redistribution between the device and the bone during the device degradation. However, the auto-catalysis nature of the polymer degradation brings extra complications to the modelling of the device degradation. Currently the time consuming trial and error approach is widely employed in the device development. In fact mathematical models and the finite element method can be a great assistance to the designing of these resorbable devices. This thesis presents a complete model for the interaction between a resorbable fixation device and a healing bone.

A phenomenological model is firstly presented that can capture the main features of the polymer degradation. An important factor in this model is the effective diffusion coefficient for the oligmers which is studied subsequently. Then an entropy theory based model is presented to relate the decay of Young's modulus to the polymer degradation. Finally the polymer degradation model and the Young's modulus decay model is integrated with a bone remodelling model and stress analysis to predict the growth or decay of a healing bone that is "protected" by a bioresorbable fixation device. The work in this thesis focuses on amorphous polymers. The work is entirely computational which is guided by existing experimental data and observations in the literature.

Acknowledgements

I would like to thank my supervisor, Professor Jingzhe Pan, for his guidance and encouragement throughout the entire course of this research. I would also like to thank the co-supervisor of my project, Dr. Csaba Sinka, for his invaluable advices. Supports from general staff in the Mathematic Modelling Centres are highly appreciated. All the numerical computations were executed with the facilities of Department of Engineering, University of Leicester.

I would also like to gratefully acknowledge a partial PhD studentship from the University of Leicester.

Finally I would like to thank all my colleagues, friends and family, especially my parents. Without the constant support from all of them, I would never be able to finish my PhD study.

Table of Contents

Chapter 1 Introduction to Bioresorbable Polymeric Medical Devices	1
1.1 Introduction to biodegradable polymers	2
1.2 Current application of biodegradable polymers.....	5
1.3 The mechanisms of biodegradation	8
1.4 Purpose and structure of the thesis	12
Chapter 2 Governing Equations for Biodegradation and Biodegradation Mechanism Maps.....	15
2.1 Introduction.....	15
2.2 A review of previous reaction-diffusion models for degradation of biodegradable polymers	16
2.3 A phenomenological diffusion-reaction model for biodegradation of biodegradable polymers	23
2.3.1 Description of the model.....	23
2.3.2 The parameter n	27
2.3.3 Nondimensionalisation of the equations.....	28
2.3.4 Heterogeneous degradation of biodegradable polymeric devices	31
2.3.5 Localisation of biodegradation	32
2.3.6 The size effect of biodegradation.....	38
2.4 Biodegradation map.....	44
2.4.1 The concept of a biodegradation map.....	44
2.4.2 A biodegradation map for plate	45
2.4.3 Biodegradation map for solid cylinder	53
2.4.4 Biodegradation map for plates using $n=2$	55
2.5 The study of half degradation time	56
2.5.1 Half degradation time for plates using $n=0.5$	57
2.5.2 Half degradation times for cylindrical pins	59
2.5.3 Half degradation times of plates using $n=2$	61
2.6 Concluding remarks	63
Chapter 3 Effective Diffusion Coefficient of Monomers in a Degrading Polymer	64

CONTENTS

3.1 Introduction.....	64
3.2 A review of the literature	65
3.3 Methods of calculating the effective diffusion coefficient for a representative unit	67
3.3.1 Direct calculation using a finite element model	67
3.3.2 Using the homogenization technique.....	69
3.4 Case studies of the effective diffusion coefficient.....	74
3.4.1 Effective diffusion coefficient in polymers containing randomly distributed pores.....	74
3.4.2 Effective diffusion coefficient of polymers containing highly localized pores.....	77
3.4.3 The tunnelling effect.....	83
3.4.4 Encapsulation case	86
3.5 Conclusion	88
Chapter 4 An Entropy Spring Model for Change in Young’s Modulus of Amorphous Biodegradable Polymers during Biodegradation	89
4.1 Introduction.....	89
4.2 Entropy theory for Young’s modulus of polymers.....	91
4.3 The degradation theory of rubber oxidation due to Tobolsky (1960).....	96
4.4 The experimental data by Tsuji (2002).....	97
4.5 An entropy based model for change in Young’s modulus.....	100
4.5.1 Description of the model.....	100
4.5.2. Comparison with the experimental data by Tsuji (2002)	105
4.5.3 Effect of the simulation parameters on the predicted Young’s modulus	108
4.5.4. A discussion on end scission versus random scission	112
4.6 Connecting biodegradation with property degradation	115
4.7 Concluding remarks	118
Chapter 5 Interaction between Device Degradation and Bone Healing in Orthopaedic Fixation – A Numerical Case Study	120

CONTENTS

5.1 Introduction.....	120
5.2 An integrated model for device degradation and bone remodelling.....	121
5.3 Numerical results	132
5.3.1 Large healing cavity.....	133
5.3.2 Crack like healing zone.....	145
5.3.3 Symmetric fixation	151
5.4 Concluding remarks	161
Chapter 6 Some Further Studies of the Degradation Model.....	162
6.1 Introduction.....	162
6.2 A phenomenological model considering end and random scissions	162
6.3 Concluding remarks	174
Chapter 7 Concluding remarks and future work.....	175
References.....	178

List of SYMBOLS

A	Rate constant for bone remodelling
\bar{A}	Normalised bone remodelling rate constant
B	Threshold value for bone remodelling
\bar{B}	Normalised bone remodelling threshold
$C_{density}$	Ratio of Young's modulus to bone density
$\bar{C}_{density}$	Normalised Young's modulus to bone density ratio
C_e	Concentration of ester bond
\bar{C}_e	Normalised concentration of ester bond
C_{e0}	Initial ester bond concentration
C_{end}	Concentration of end unit on polymer chains
\bar{C}_{end}	Normalised concentration of end unit on polymer chains
C_{end0}	Initial concentration of end unit on polymer chains
C_m	Monomer concentration
\bar{C}_m	Normalised monomer concentration
C_{middle}	Concentration of middle unit on polymer chains
\bar{C}_{middle}	Normalised concentration of middle unit on polymer chains
$C_{middle0}$	Initial concentration of middle unit on polymer chains
D	Monomer diffusion coefficient
\bar{D}	Normalised monomer diffusion coefficient
D_0	Initial monomer diffusion coefficient
\bar{D}_0	Normalised initial monomer diffusion coefficient
D_{eff}	Effective diffusion coefficient for monomer
D_{max}	Diffusion coefficient for aqueous media
DP	Degree of polymerization

LIST OF SYMBOLS

E	Young's modulus
\bar{E}	Normalised Young's modulus
E_{bone}	Young's modulus for healthy bone
F_b	Load distributed on the remodelling bone
F_p	Load distributed on the fixation plate
J	Monomer concentration flux
k, k'	Constant of effective diffusion coefficient to porosity
k_1, k_2, k_3, k_4	Rate constants for polymer degradation
$\bar{k}_1, \bar{k}_2, \bar{k}_3, \bar{k}_4$	Normalised rate constants for polymer degradation
K_{end}	End scission parameter
K_{random}	Random scission parameter
l	Length of polymeric device
M_n	Number average molecular weight
\bar{M}_n	Normalised number average molecular weight
$M_{n0} \quad M_n^0$	Initial number average molecular weight
M_{th}	Threshold molecular weight value
M_{unit}	Molecular weight for one repeating unit on the polymer chains
N	Number of polymer chains in the system
$N_{chain}^0 \quad N_{ch}^0$	Initial number of polymer chains
N_{end}	Number of end units on polymer chains in the system
N_{mono}	Critical number of repeating units of monomers
N_{total}	Number of all the repeating units on the polymer chains
p	Porosity of a representative unit
P_{end}	Probability for end scission
P_{random}	Probability for random scission

LIST OF SYMBOLS

r_{E2}	Ratio of incident E2 to incident E1
r_{R2}	Ratio of incident R2 to incident R1
r_{R3}	Ratio of incident R3 to incident R1
R_m	Number of monomers produced
R_m^{end}	Number of monomers produced by end scission
R_m^{random}	Number of monomers produced by random scission
R_s	Number of scissions
R_s^{end}	Number of end scissions
R_s^{random}	Number of random scissions
t	Time
\bar{t}	Normalised time
T	Temperature
V	Volume/area of the domain
V_{pore}	Volume fraction of pore
x	Macroscopic coordinate
x_i	Spatial coordinate
\bar{x}_i	Normalised spatial coordinate
y	Microscopic coordinate
γ	Number of the monomers randomly produced by incident R2
ε	Ratio between macroscopic and microscopic coordinate
ε	Average strain
$\varepsilon_1, \varepsilon_2, \varepsilon_3$	First, second and third principal strains
η	Number of the monomers randomly produced by incident R3
ν	Poisson's ratio
ρ	Remodelling bone density

LIST OF SYMBOLS

$\bar{\rho}$	Normalised remodelling bone density
ρ_{bone}	Healthy bone density
σ_{max}	Maximum stress
σ_x	Normal stress
$\bar{\sigma}_x$	Normalised normal stress
χ	An equivalent field
$\partial\Omega$	Boundary of the representative unit
Ω	Domain of the representative unit

List of figures

Figure 1 (a) Scaffold for tissue engineering (Wu and Ding, 2004); (b) – (c) fixation devices for orthopaedic surgeries (Gutwald <i>et al.</i> , 2002) (PolyMax®, Inion); (d) polymeric wafers loaded with anticancer drug (Moses <i>et al.</i> , 2003) (Gliadel®).....	1
Figure 1.1.1 The chemical structure of linear aliphatic polyesters (Chu and Liu, 2008).....	3
Figure 1.1.2 Chiral molecule structure of D-Lactic acid (PDLA) and L-Lactic acid (PLLA) (Gupta <i>et al.</i> , 2007).....	4
Figure 1.1.3 Ring-opening polymerisation of lactide in the presence of a catalyst and heat (Chu and Liu, 2008; Cameron and Kamvari-Moghaddam, 2008).....	5
Figure 1.3.1 Scheme of degradation process.....	9
Figure 1.3.2 Hollow structure of a PLA37.5GA25 specimen after ten days of degradation in distilled water (Li <i>et al.</i> , 1990 ^b).....	10
Figure 1.3.3 Demonstration of end scission and random scission mechanisms.....	12
Figure 2.2.1 Scheme of the drug release model by Joshi and Himmelstein (1991).....	16
Figure 2.2.2 Scheme of Monte Carlo method to calculate the porosity of the polymer matrix by Göpferich and Langer (1995).....	18
Figure 2.2.3 Scheme of the Monte Carlo-based simulation of polymer degradation: (a) initial state (b) during drug release.....	21

Figure 2.3.1 Experimental result for PLA sample kept in acetonitrile solution under 60 °C up to 60 days (Siparsky *et al.*, 1998).....28

Figure 2.3.2 A representative case to demonstrate the model is able to capture the heterogeneous degradation.....32

Figure 2.3.3 Cross-section image of a PLLA implant after 80 weeks (Gutwald *et al.*, 2002).....33

Figure 2.3.4 Computer simulated localisation of degradation using $\bar{D}_0 = 10^{-5}, \bar{k}_1 = 10^{-4}, n = 0.5$. The colour represents the average molecular weight normalised by its initial value.....35

Figure 2.3.5 Computer simulated localisation of degradation using $\bar{D}_0 = 10^{-5}, \bar{k}_1 = 10^{-4}, n = 2$. The colour represents the average molecular weight normalised by its initial value.....37

Figure 2.3.6 Observed breaking up of amorphous PLLA plate during the in vivo degradation experiment in rat muscle by Gutwald *et al.* (2002).....38

Figure 2.3.7 Experimental data (discrete symbols) of average molecular weight as a function of time obtained using DLPLA films of 0.3mm and plate of 2mm in thickness respectively (Grizzi *et al.*, 1995); the continuous line are calculated results of the model using $\bar{k}_1 = 0.25, n = 0.5, \bar{D}_0 = 0.005$ and 0.2539

Figure 2.3.8 A representative unit for a biodegradable film.....40

LIST OF FIGURES

Figure 2.3.9 The comparison between the predicted (lines) and measured (discrete) weight loss as functions of time for DLPLA films of 0.3mm and plate of 2mm respectively. This figure corresponds to figure 2.3.7.....41

Figure 2.3.10 Fitting the model prediction to the experimental data of average molecular weight versus time (Grizzi *et al.*, 1995) by using $\bar{k}_1 = 0.05$, $n = 2$, $\bar{D}_0 = 0.02$ and 0.0004 42

Figure 2.3.11 Comparison between predicted (lines) and measured (discrete symbols), weight loss of DLPLA films of 0.3mm and plate of 2mm as a functions of time. This figure corresponds to figure 2.3.10.....43

Figure 2.4.1 Effect of normalised diffusion coefficient of the monomers on the ester bond concentration averaged over the sample volume that remains in the sample at a fixed time of degradation; the five sub-figures show the calculation for (a) $\bar{k}_1 = 0.001$, (b) $\bar{k}_1 = 0.01$, (c) $\bar{k}_1 = 0.1$, (d) $\bar{k}_1 = 1$, (e) $\bar{k}_1 = 10$, (f) $\bar{k}_1 = 50$ 48

Figure 2.4.2 The biodegradation map for plate.....49

Figure 2.4.3 Cases 1 (upper line) and 2 (lower line), $\bar{k}_1 = 0.1$ 51

Figure 2.4.4 Cases 3 (upper line) and 4 (lower line), $\bar{k}_1 = 10$ 52

Figure 2.4.5 Cases 5 and 6, $\bar{k}_1 = 55$ 52

Figure 2.4.6 The biodegradation map for pin shapes.....54

Figure 2.4.7 The biodegradation map for a plate shape; exponential parameter $n=2$55

Figure 3.1.1 The effective diffusion coefficient is a function of the porosity.....64

LIST OF FIGURES

Figure 3.1.2 Scheme of multi-scale modelling.....	65
Figure 3.3.1 A scheme of the calculation of the effective diffusion coefficient.....	68
Figure 3.3.2 The idea of homogenization technique.....	69
Figure 3.3.3 Concentration field using FE method.....	72
Figure.3.3.4 The field of χ_1 obtained by solving equation (3.3.9).....	73
Figure 3.4.1 Finite element model of randomly generated pores by Jiang and Pan (2008).....	75
Figure 3.4.2 Effective diffusion coefficient versus the porosity for randomly generated pores.....	75
Figure 3.4.3 Demonstration of the percolation theory.....	76
Figure 3.4.4 The highly localized pore structure (Cai <i>et al.</i> , 2003).....	77
Figure 3.4.5 Cross section image of 3D representative unit with a central spherical pore.....	78
Figure 3.4.6 Effective diffusion coefficient versus porosity for a cubic representative unit of the polymer containing one spherical pore.....	79
Figure 3.4.7 The scheme of the “sub-domain” of the system.....	80

LIST OF FIGURES

Figure 3.4.8 The average value of relative effective diffusion coefficient from 10 random cases compare to the effective diffusion coefficient from one central spherical pore.....	81
Figure 3.4.9 The effective diffusion coefficient of a tunnel structure can be recognized as the combination of the two structures.....	83
Figure 3.4.10 Cross section image of 3D representative unit with a tunnel and central spherical pore.....	85
Figure 3.4.11 The relative effective diffusion coefficient for the tunnel with centre spherical pore structure on 3D level.....	85
Figure 3.4.12 The explanation of encapsulation structure.....	86
Figure 3.4.13 Effective diffusion coefficient for polymer of microstructures (a) and (c).....	87
Figure 3.4.14 Effective diffusion coefficient for polymer of microstructures (a) and (b).....	87
Figure 4.2.1 A single polymer chain.....	93
Figure 4.2.2 Change in entropy of a single chain as the polymer deforms.....	93
Figure 4.3.1 The change of Young's modulus for rubber in stress-relaxation experiment with respect to time (Tobolsky, 1960).....	97
Figure 4.4.1 GPC curves for PLLA at four different times (Tsuji, 2002).....	98

Figure 4.4.2 GPC curves for PDLA at four different times (Tsuji, 2002).....99

Figure 4.4.3 The number average molecular weight loss versus time (Tsuji, 2002) for PLLA (triangles) and PDLA (squares).....99

Figure 4.4.4 Young’s Modulus versus time averaged from four samples (Tsuji, 2002) for PLLA (triangles) and PDLA (squares).....100

Figure 4.5.1 Illustration of entropy theory for elasticity.....102

Figure 4.5.2 Flowchart showing the Monte Carlo scheme to simulate polymer chain scissions and to calculate the corresponding Young’s modulus and average molecular weight.....103

Figure 4.5.3 Data structure for computer simulation of polymer chain scission.....104

Figure 4.5.4 Normalised Young’s modulus versus normalised average molecular weight for PDLA. Solid line – model prediction using $M_{th} = 1.15 \times 10^5$ g/mol initial sample size of 3000 polymer chains and the random to end scission ratio of 1:1; discrete dots – experimental data obtained from figures 4.4.3 and 4.4.4.....106

Figure 4.5.5. Normalised Young’s modulus versus normalised average molecular weight for the PLLA used by Tsuji (2002). Solid line – model prediction using $M_{th} = 1.3 \times 10^5$ g/mol, initial sample size of 3000 polymer chains and the random to end scission ratio of 1:1; discrete dots – experimental data obtained by Tsuji (2002).....107

Figure 4.5.6 Relation between mechanical property and degree of polymerisation according to Kaufman and Falcetta (1976).....108

Figure 4.5.7 The normalised Young’s Modulus versus normalised number average molecular weight with sample size of 3000 (red), 10000 (dotted), 30000 (solid line) for PDLA.....109

Figure 4.5.8 The normalised Young’s modulus versus normalised number average molecular weight with end scission to random scission of 10:1 (red), 1:1 (dotted), 1:10 (solid line) for PDLA.....110

Figure 4.5.9 (a) Influence of M_{th} on the model result for PDLA; $M_{th} = 1.15 \times 10^5$ (solid line) and $M_{th} = 1.3 \times 10^5$ (dashed line); (b) Influence of M_{th} on the model result for PLLA; $M_{th} = 1.3 \times 10^5$ (solid line) and $M_{th} = 1.1 \times 10^5$ (dashed line).....111

Figure 4.5.10 (a) End scission probability versus total number of chain scissions with initial input $\frac{P_{end}}{P_{random}} = 10:1$ for PDLA; (b) End scission probability versus total number of chain scissions with initial input $\frac{P_{end}}{P_{random}} = 1:1$ for PDLA; (c) End scission probability versus total number of chain scissions with initial input $\frac{P_{end}}{P_{random}} = 1:10$ for PDLA.....115

Figure 4.6.1 A biodegradable rod and its finite element model.....116

Figure 4.6.2 Distribution of normalised average molecular weight obtained by solving equations (2.3.12) and (2.3.13) using the finite element method at two normalised times of degradation.....117

Figure 4.6.3 Effective Young’s modulus of a biodegradable rod in its axial direction as a function of the normalised degradation time.....118

Figure 5.2.1 Scheme of the load transfer for biodegradable bone-supporting device applied to fractured bone during the healing process.....121

Figure 5.2.2 Schematic illustration of ideal load transfer from a fixation device to a healing bone corresponding to the bone healing stages.....123

Figure 5.2.3 Integrated model for bone healing supported by a biodegradable fixation device.....124

Figure 5.2.4 One-sided bone fixation (Reichert *et al.*, 2009).....124

Figure 5.2.5 Geometry of the case study.....125

Figure 5.2.6 FE model of large bone defect with fixation showing boundary conditions.....130

Figure 5.3.1 Bone density and polymer molecular weight averaged over the bone and polymer domains respectively as functions of time for large bone defect fixation with $\bar{A} = 5 \times 10^{-4}$ (scenario A).....134

Figure 5.3.2 Load transfer from the supporting device to the healing bone for large bone defect fixation with $\bar{A} = 5 \times 10^{-4}$ (scenario A).....134

Figure 5.3.3 The spatial distribution of the average molecular weight in the fixation device at $\bar{t} = 5 \times 10^{-4}$, $\bar{t} = 6 \times 10^{-4}$, $\bar{t} = 7 \times 10^{-4}$, $\bar{t} = 8 \times 10^{-4}$, respectively. The colour represents the normalised average molecular weight.....135

Figure 5.3.4 The spatial distribution of bone density at $\bar{t} = 0.5$, $\bar{t} = 1$, $\bar{t} = 1.5$, $\bar{t} = 2$, respectively. The colour represents the bone density normalised by 20GPa.....136

LIST OF FIGURES

Figure 5.3.5 Bone density averaged over the bone domain as a function of time for large bone defect fixation with $\bar{A} \rightarrow \infty$ (scenario B).....137

Figure 5.3.6 Load transfer from the fixation device to the healing bone for large bone defect with $\bar{A} \rightarrow \infty$ (scenario B).....137

Figure 5.3.7 The spatial distribution of bone density at $\bar{t}=0.4$, $\bar{t}=0.8$, $\bar{t}=1.2$, $\bar{t}=1.6$, respectively. The colour represents the bone density normalised by 20GPa.....138

Figure 5.3.8 Distribution of direct strain in the horizontal direction along the side a-b of the healing bone.....139

Figure 5.3.9 Bone density and polymer molecular weight averaged over the bone and polymer domains respectively as functions of time for large bone defect with $\bar{A}=0.5$ (scenario C).....140

Figure 5.3.10 Load transfer from the supporting device to the healing bone for large bone defect with $\bar{A}=0.5$ (scenario C).....141

Figure 5.3.11 The spatial distribution of the average molecular weight at $\bar{t}=0.5$, $\bar{t}=0.6$, $\bar{t}=0.7$, $\bar{t}=0.8$, respectively. The colour represents the distribution of polymer concentration.....142

Figure 5.3.12 The spatial distribution of bone density at $\bar{t}=1$, $\bar{t}=2$, $\bar{t}=4$, $\bar{t}=8$, respectively. The colour represents the bone density normalised by 20GPa.....143

Figure 5.3.13 Bone density and polymer molecular weight averaged over the bone and polymer domains respectively as functions of time for large bone defect for $\bar{A}=2$ 144

Figure 5.3.14 Load transfer from the supporting device to the healing bone for large bone defect fixation with critical value $\bar{A} = 2$ 145

Figure 5.3.15 A schematic illustration of bone fracture and fixation.....146

Figure 5.3.16 FE mesh and boundary conditions for a bone with crack like defect and fixation.....146

Figure 5.3.17 Bone density and polymer molecular weight averaged over the bone and polymer domains respectively as functions of time for crack like defect with $\bar{A} = 5 \times 10^{-4}$ (scenario A).....147

Figure 5.3.18 Load transfer from the supporting device to the healing bone for crack like bone defect using $\bar{A} = 5 \times 10^{-4}$ (scenario A).....147

Figure 5.3.19 Bone density averaged over the bone domain as function of time for crack like small bone defect with $\bar{A} \rightarrow \infty$ (scenario B).....148

Figure 5.3.20 Load transfer from the supporting device to the healing bone with a crack like defect for $\bar{A} \rightarrow \infty$ (scenario B).....149

Figure 5.3.21 Bone density and polymer molecular weight averaged over the bone and polymer domains respectively as functions of time for small crack like bone defect with $\bar{A} = 0.5$ (scenario C).....150

Figure 5.3.22 Load transfer from the supporting device to the healing bone with a crack like defect for $\bar{A} = 0.5$ (scenario C).....150

Figure 5.3.23 FE mesh of symmetric fixation with boundary condition.....151

Figure 5.3.24 The deformation of one-side bone fixation, colour represents average strain.....152

Figure 5.3.25 The deformation of symmetric bone fixation, colour represents average strain.....153

Figure 5.3.26 Bone density and polymer molecular weight averaged over the bone and polymer domains respectively as functions of time for symmetric fixation with $\bar{A} = 5 \times 10^{-4}$ (scenario A).....154

Figure 5.3.27 Load transfer from the supporting device to the healing bone with symmetric fixation for $\bar{A} = 5 \times 10^{-4}$ (scenario A).....154

Figure 5.3.28 The spatial distribution of bone density at $\bar{t} = 0.5, \bar{t} = 1, \bar{t} = 1.5, \bar{t} = 2$, respectively. The colour represents the distribution of bone density normalised by 20GPa.....155

Figure 5.3.29 Bone density averaged over the bone domain as function of time for symmetric fixation with $\bar{A} \rightarrow \infty$ (scenario B).....156

Figure 5.3.30 Load transfer from the supporting device to the healing bone with symmetric fixation for $\bar{A} \rightarrow \infty$ (scenario B).....156

Figure 5.3.31 The spatial distribution of bone density at $\bar{t} = 0.4, \bar{t} = 0.8, \bar{t} = 1.2, \bar{t} = 1.6$, respectively. The colour represents the distribution of bone density normalised by 20GPa.....157

Figure 5.3.32 The normal strain distribution on the right boundary of the bone remodelling domain.....158

Figure 5.3.33 Bone density and polymer molecular weight averaged over the bone and polymer domains respectively as functions of time for symmetric fixation with $\bar{A} = 0.5$ (scenario C).....159

Figure 5.3.34 Load transfer from the supporting device to the healing bone with symmetric fixation for $\bar{A} = 0.5$ (scenario C).....159

Figure 5.3.35 The spatial distribution of bone density at $\bar{t} = 1, \bar{t} = 2, \bar{t} = 4, \bar{t} = 8$, respectively. The colour represents the distribution of bone density normalised by 20GPa.....160

Figure 6.2.1 The scheme for incident E1.....164

Figure 6.2.2 The scheme for incident E2.....164

Figure 6.2.3 The scheme for incident R1.....165

Figure 6.2.4 The scheme for incident R2.....165

Figure 6.2.5 The scheme for incident R3.....166

Figure 6.2.6 A numerical fitting to the experimental data of two thicknesses in the amended phenomenological model (Grizzi *et al.*, 1995).....173

List of tables

Table 1.2.1 Medical applications of biodegradable polymeric devices.....7

Table 1.2.2 Major applications of the three linear aliphatic polymers.....8

Table 2.5.1 The normalized half degradation time of various \bar{k}_1 \bar{D}_0 values for plate shape using $n=0.5$58

Table 2.5.2 The normalized half degradation time of various \bar{k}_1 \bar{D}_0 values for pin shape using $n=0.5$60

Table 2.5.3 The normalized half degradation time of various \bar{k}_1 \bar{D}_0 values for plate shape using $n=2$62

Table 3.4.1 The 10 group of random distributed spherical pore structure and their effective diffusion coefficient's plot against the porosity.....82

Table 5.2.1 The initial conditions for the case study.....131

Table 5.2.2 Material parameters used in the analysis.....131

Table 6.2.1 The changing rate for C_m C_{middle} and C_{end} caused by incidents E1, E2, R1, R2, R3.....168

Published Papers from this PhD Project

- Wang, Y.**, Pan, J., Han, X., Sinka, C., Ding, L., 2008. A phenomenal model for degradation of biodegradable polymers. *Biomaterials* 29, 3393-3401.
- Wang, Y.**, Han, X., Pan, J., Sinka, C., 2009. An entropy spring model for the Young's modulus change of biodegradable polymers during biodegradation. *Journal of the Mechanical Behaviour of Biomedical Materials*, Accepted, Available online.
- Wang, Y.**, Pan, J., 2009. Interaction between device degradation and bone healing in orthopaedic fixation, 1st draft, to be submitted to *Biomechanics*.

Chapter 1

Introduction to Bioresorbable Polymeric Medical Devices

Sutures made of bioresorbable polymers have been successfully used in surgery since the 1970s (Ratner *et al.*, 2004). Screws and plates made of similar polymers are being increasingly used to fix broken bones (Athanasίου *et al.*, 1996; Barber *et al.*, 2000; Rokkanen *et al.*, 2000). Bioresorbable wafers loaded with anticancer drugs are placed into resection cavity after cancer surgery to slowly release the drugs, preventing the cancer from coming back (Moses *et al.*, 2003). Intensive research is being carried out worldwide to use porous foams made of bioresorbable polymers as scaffolds for tissue regeneration (Sanz-Herrera *et al.*, 2009). In all these applications, the bioresorbable devices firstly provide some temporary functions, then degrade to let biology take over and are eventually metabolised into carbon dioxide and water. Figure 1 shows some typical examples of the biodegradable devices including scaffolds for tissue engineering, fixation screws for broken bones and drug-loaded matrices for controlled release.

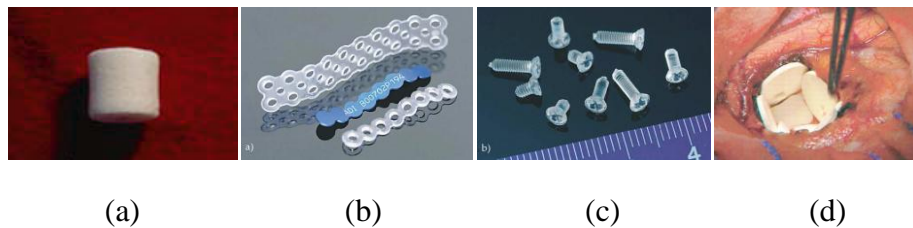


Figure 1 (a) Scaffold for tissue engineering (Wu and Ding, 2004); (b) – (c) fixation devices for orthopaedic surgeries (Gutwald *et al.*, 2002) (PolyMax®, Inion); (d) polymeric wafers loaded with anticancer drug (Moses *et al.*, 2003) (Gliadel®).

The development is, however, entirely based on trial and error. The degradation rate strongly depends on the shape and size of the devices (Grizzi *et al.*, 1995), making it difficult to transfer experience from one device to another. The degradation time for biodegradable polymers ranges from weeks to years (Cameron and

Kamvari-Moghaddam, 2008); animal and ultimately human trials have to be carried out, making the trial and error approach time-consuming and expensive. The research and development of bioresorbable devices would benefit enormously from mathematical models capable of predicting the degradation rate and the corresponding change in elastic properties of the devices as well as the interaction between polymer degradation and the healing bone. This thesis sets out to develop such models.

1.1 Introduction to biodegradable polymers

Biodegradable polymers are the kind of polymers that will eventually disappear once introduced into a living organism. The term biodegradable can also be found in literature together with the term bioabsorbable, with no clear distinction made between the definitions. Like all other polymers, biodegradable polymers are also comprised of large numbers of repeating units and the number of these units on one single polymer chain is defined as the degree of polymerisation and a small molecule of these repeating units is called a monomer. This type of polymer, either naturally generated or synthetically manufactured, has attracted great attention from researchers and commercial markets within the last three decades. These innovative materials enjoy such increasing popularity mainly because they can be degraded by the hydrolysis process and the products can be eliminated by natural pathways. Of the two kinds of biodegradable polymers, it is the synthetic materials which have much wider application in daily life as these materials can be designed and controlled to meet certain practical requirements – physical, mechanical, etc. Among all the biodegradable polymers that are currently used, three linear aliphatic polyesters have found the broadest range of application owing to their great bio-compatibility and non-toxicity (Gupta *et al.*, 2007; Chu and Liu, 2008; Athanasiou *et al.*, 1996). These linear polymers are: poly (lactic) acid, poly (glycolic) acid and poly (ϵ -caprolactone) (Cameron and Kamvari-Moghaddam, 2008; Gupta *et al.*, 2007). Their chemical structures are listed in figure 1.1.1 (Chu and Liu, 2008).

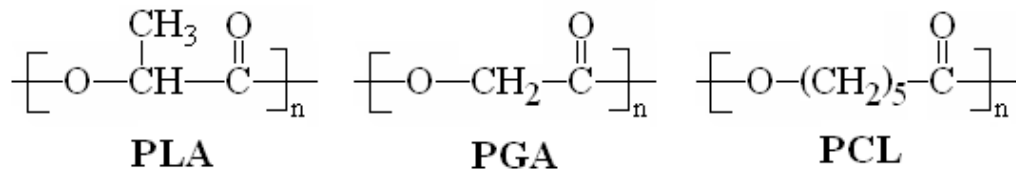


Figure 1.1.1 The chemical structure of linear aliphatic polyesters (Chu and Liu, 2008).

Owing to the variety of their chemical structures (figure 1.1.1), polymers behave differently from each other in terms of their degradation rate and mechanical properties, especially as regarding to the impact of those factors, such as crystallinity, co-polymerization, fabrication techniques, composite formation, and so on. The degradation time of the above polymers can be tailored from weeks to years to suit different applications by changing the average molecular weight and the initial degree of crystallinity, and by co-polymerising or blending in different proportions (Li *et al.*, 1990^a; Li *et al.*, 1990^b; Li *et al.*, 1990^c; Saha and Tsuji, 2006; Renouf-Glauser *et al.*, 2005).

PGA is the simplest linear polyester with a faster degradation rate and higher crystallinity. The first totally synthetic, absorbable suture to be commercially manufactured was sold under the trade name ‘Dexon’ in 1970 and made from poly (glycolic acid) (PGA). The disadvantage of PGA was that its mechanical property was lost rapidly within two to four weeks (Ratner *et al.*, 2004). To ensure a wider range of application, poly (lactic acid) (PLA) was later introduced, as it is more hydrophobic than PGA and therefore degrades at a much slower rate (Cameron and Kamvari-Moghaddam, 2008). Meanwhile their co-polymers rapidly lost their crystallinity and degraded much faster than both of the polymers (Ratner *et al.*, 2004).

PLA is of several kinds, since the lactic acid is a chiral molecule, as figure 1.1.2 suggests (Gupta *et al.*, 2007).

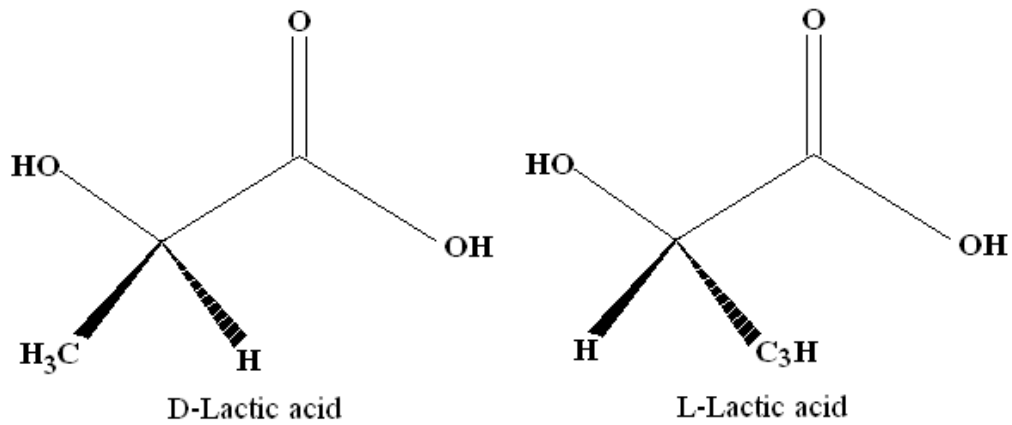


Figure 1.1.2 Chiral molecule structure of D-Lactic acid (PDLA) and L-Lactic acid (PLLA) (Gupta *et al.*, 2007).

The structure in figure 1.1.2 gives two morphologies of the polymers: D-PLA, L-PLA; these two optical isomers can generate their racemic form D, L-PLA, from which the rarely used meso-PLA can be obtained. L-PLA is more frequently used than D-PLA because the hydrolysis product yields L(+)-lactic acid, a naturally occurring stereoisomer of lactic acid. The D, L-PLA is always amorphous and therefore it has a degradation rate faster than that of L-PLA whereas the latter has higher mechanical strength. The co-polymers of PLA and PGA can be designed to fit requirements, i.e. by changing the crystallinity, morphology and molecular weight (Chu and Liu, 2008). It is notable that the co-polymer loses its crystallinity considerably, despite PGA itself being a highly crystallising material (Ratner *et al.*, 2004; Chu and Liu, 2008). If PDLA is the composite of the co-polymer, the material becomes amorphous in nature (Ratner *et al.*, 2004; Chu and Liu, 2008). The lower crystallinity of the co-polymer obviously reduces the degradation time of these materials. PCL is hydrophobic polyester with a much longer degradation time than PLA and therefore can be used for long-term drug delivery devices that remain active for over a year (Chu and Liu, 2008). It is mechanically much more flexible than PLA or PGA. The polymers can be made by either direct condensation, which produces a polymer of low molecular weight, or by ring-opening polymerisation to obtain high and controllable molecular weight products. Figure 1.1.3

shows PLA derived from lactic acid by ring-opening polymerisation stimulated by a catalyst and heat (Cameron and Kamvari-Moghaddam, 2008; Chu and Liu, 2008).

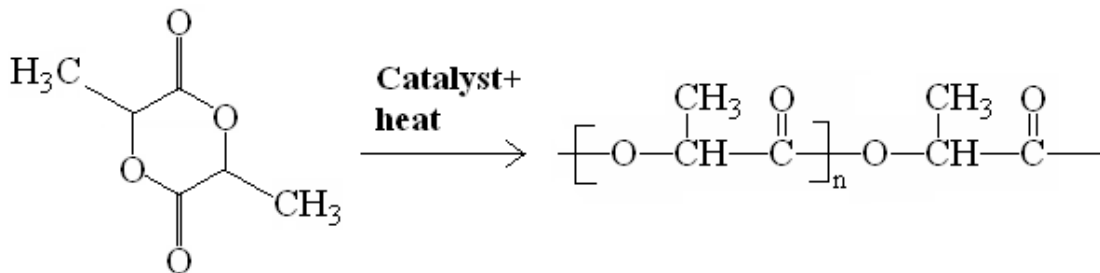


Figure 1.1.3 Ring-opening polymerisation of lactide in the presence of a catalyst and heat (Chu and Liu, 2008; Cameron and Kamvari-Moghaddam, 2008).

Molecular weight is a factor that has to be given consideration in the selection or design of the material because the molecular weight can affect both the degradation rate and the mechanical properties of the polymers (Park, 1995).

1.2 Current application of biodegradable polymers

The typical applications of biodegradable polymers can be sub-categorised into five types (Ratner *et al.*, 2004):

- (1) Temporary support device: provides an artificial mechanical support when the original tissue bed is broken or weakened by disease, injury or surgery. The device should be able to take the load instead of the tissue and gradually transfer it back as the tissue heals. The adjustment of the degradation rate to suit the healing of the environment is one of the major challenges in design.
- (2) Temporary barrier: prevents the adhesion of two nearby tissue surfaces that are not meant to bond together as the failure of separation may cause pain, functional impairment, and other problems. The normal forms of these barriers are films and membranes
- (3) Implantable drug delivery device: implanted into the patient's body as the carrier of the drug particles and vanishes after a certain period of time, preferably after the drug

is totally released or the disease fully cured. The release rate of the loaded drug is decided by the material's diffusivity, therefore its geometry and structure as well.

(4) Tissue engineering scaffold: provides space for cells to grow into and to reorganise into functional tissue. For tissue engineering scaffolds, pore interconnectivity is a key property as body cells need to grow throughout the material, similarly to the temporary support implant; one of the major challenges in design is to adjust the rate of degradation to the rate of tissue healing.

(5) Multifunctional devices: combine the several functions mentioned above within one device. For instance, a bone fixation device may also carry some bone healing substances with known effectiveness.

These bioresorbable devices are listed below in table 1.2.1 together with some comments on their status of development.

Table 1.2.1 Medical applications of biodegradable polymeric devices

<i>Applications</i>	<i>Device examples</i>	<i>Comments</i>
Wound management	Sutures; Staples; Clips; Adhesives; Surgical meshes	Currently occupy most of market share in biodegradable devices
Orthopaedic fixation	Pins; Rods; Screws; Tacks; Ligaments	In wide clinical use; over-designed, problem with bone regeneration
Dental applications	Tissue regeneration membrane; Void filler	In clinical use
Cardiovascular applications	Stents	Unsuccessful so far
Intestinal applications	Anastomosis rings	
Drug delivery systems	Excipients	Under active research, a few drugs already approved for clinical use
Tissue engineering	Scaffolds of various forms	Under intensive research and undergoing multi-clinical trials

The three aliphatic polymers have been used differently in these applications. For example, the D, L-PLA is often used in drug delivery systems owing to its faster degradation rate (Cameron and Kamvari-Moghaddam, 2008) whereas the L-PLA is more useful in applications like fixation devices because of its high mechanical strength (Cameron and Kamvari-Moghaddam, 2008). The co-polymers of PLA and PGA were used as sutures as long ago as 1974. The major applications of these polymers are listed in table 1.2.2:

Table 1.2.2 Major applications of the three linear aliphatic polymers

<i>Polymers</i>	<i>Major applications</i>
PCL	Long-term drug delivery, tissue engineering
PGA	Bone fixation (bone pins)
PLGA	Drug delivery, suture
PDLLA	Drug delivery where it is important to have a homogeneous dispersion within the carrier matrix.
PLLA	Sutures and orthopaedic devices, where high mechanical strength and toughness are required.

The reason why the different types of polymers can be made into several types of devices with various functions lies in the difference between the two main characteristics of the polymers: degradation rate and mechanical strength. Therefore it is vital for a mathematical model to capture these two aspects.

1.3 The Mechanisms of Biodegradation

The biodegradation of polymers in the body is a two-phase process (Chu and Liu, 2008; Ratner *et al.*, 2004; Gupta *et al.*, 2007): (a) chemical hydrolysis of the polymer backbone and (b) active metabolism. During the first phase, water penetrates the biodegradable device, preferentially attacking the ester bonds in the amorphous phase and converting the long polymer chains into shorter water-soluble fragments. In the second phase, enzymes released from white blood cells attack these fragments, causing the further degradation of the polymer to natural monomeric acids found in the body, such as lactic acid. These acids enter the citric acid cycle and are excreted as water and carbon dioxide. The cleavage of the unstable polymer backbone could be mediated by water or by biological agents such as enzymes and micro-organisms called hydrolytic

degradation and biodegradation, respectively. A scheme for the hydrolysis reaction is shown in figure 1.3.1 (Ratner *et al.*, 2004).

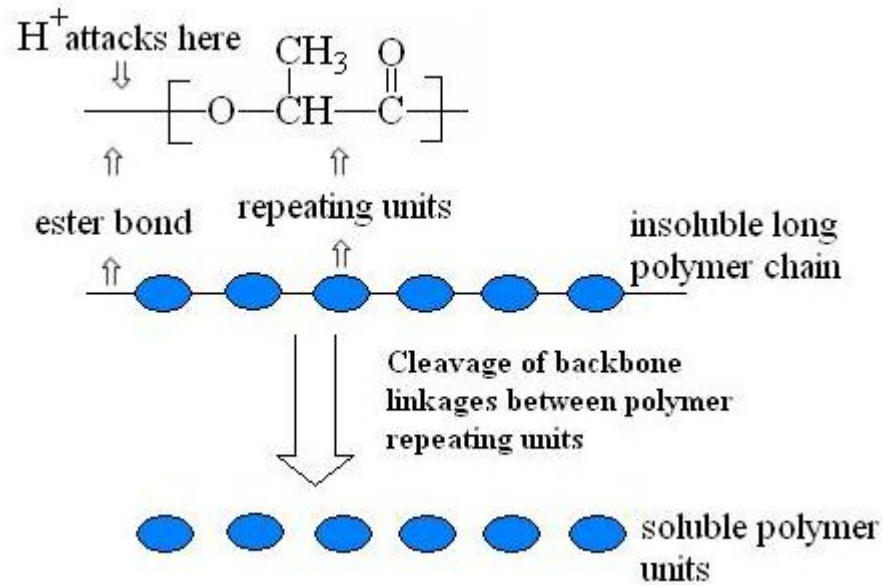


Figure 1.3.1 Scheme of degradation process.

The H^+ from water attacks the ester bond and releases those repeating units from the backbone to generate soluble fragments of low molecular weight. For the most common polyesters such as polyglycolic acid (PGA), polylactic acid (PLA) and polycaprolactone (PCL), the degradation rate depends not only on the polymer but also on the shape and size of the device (Grizzi *et al.*, 1995). It is well established that the degradation is heterogeneous in larger devices as shown in figure 1.3.2 – the inside degrades much faster than the surface (Li *et al.*, 1990^b).

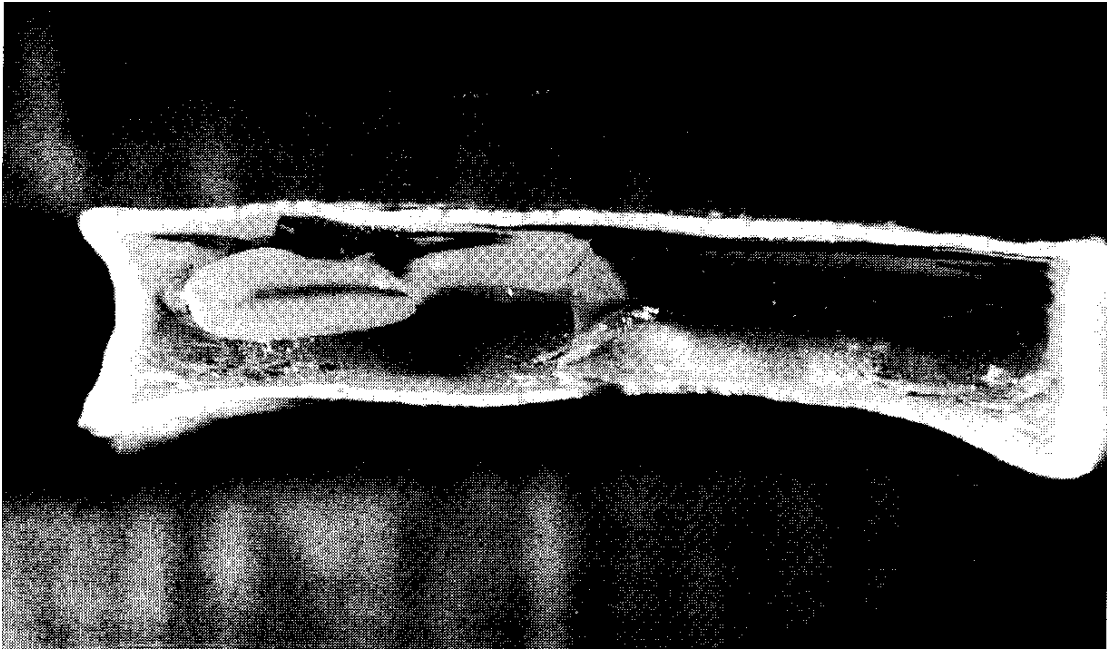


Figure 1.3.2 Hollow structure of a PLA37.5GA25 specimen after ten days of degradation in distilled water (Li *et al.*, 1990^b).

This size effect makes it difficult to transfer experience from one device to another even if they are made of the same polymer. The reason why this material degrades into hollow structures is the co-existence of hydrolytic degradation as well as an auto-catalytic mechanism. If some small and water-soluble fragment can diffuse away, then the acidity of the local environment is reduced. This explains why the surface degrades more slowly than the core of a device (Li *et al.*, 1990^b; Li *et al.*, 1990^a). Auto-catalysis is a factor that complicates the biodegradation. The chemical reaction of hydrolysis of the polymer's unstable backbone can be categorised by acid-catalysed hydrolysis and base-catalysed hydrolysis depending on the pH value within the system (Cameron and Kamvari-Moghaddam, 2008). Polymer hydrolysis rate increases as the concentration of the reaction product increases. The hydrolysis of polyester produces shorter chains with acid and alcohol end groups. For PLA, the acid end groups have a high degree of dissociation which gives rise to an acidic environment, significantly accelerating the hydrolysis rate (Siparsky *et al.*, 1998). Therefore elimination of these shorter chains within the system is important for control of the overall degradation rate. The interplay between monomer diffusion and the hydrolysis reaction is a central issue

that any model must consider. Furthermore, the monomers diffuse in a degrading polymer which has increasing porosity, crystallinity and water content as the degradation progresses. A four degradation stage mechanism is proposed to describe the degradation of PGA polymers (Hurrell and Cameron, 2001^a; Hurrell and Cameron, 2001^b; Hurrell and Cameron, 2002; Hurrell *et al.*, 2003; Milroy *et al.*, 2003; Hurrell and Cameron, 2003). In the first stage, a small amount of water quickly diffuses into the sample reaching an equilibrium concentration and forming a homogeneous water distribution. This procedure happens several hours after the polymer is exposed to the aqueous medium. During the second stage, very little water is absorbed and very little polymer mass is lost. Relatively long polymer chains undergo scissions on reaction with water that reduces polymer molecular weight in this stage. In the third stage, the polymer reaches a critical molecular weight so the inside oligomer chains are small enough to dissolve into the degradation medium and subsequently diffuse out of the polymer matrix. The diffusion of these oligomers leaves space for massive water to come into the system, the absorption of water will allow even faster diffusion for the oligomers. Therefore a reaction-erosion front is formed owing to the autocatalysis difference between centre and surface of the material. The position of this reaction-erosion front moves towards the polymer centre and hypothetically there is a fourth stage that the reaction-erosion fronts meet in the polymer centre, degradation continues in this stage until the polymer is all degraded. The variation of the effective diffusion coefficient with respect to the above factors has to be modelled, this brings extra complication to the modelling of the diffusion coefficient.

The degradation mechanism is basically the scission of the polymer chains. It can be further divided into end scission and random scission (Shih, 1995^a; Shih, 1995^b; de Rong *et al.*, 2001; Belbella *et al.*, 1996; van Nostrum *et al.*, 2004) as figure 1.3.3 demonstrates, depending on the position of the chain cleavage when attacked by acid.

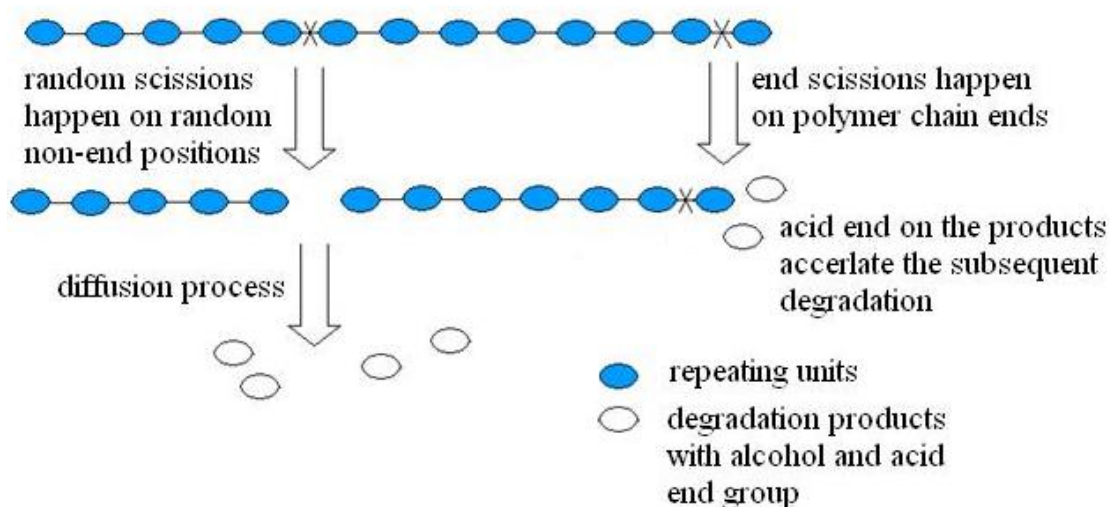


Figure 1.3.3 Demonstration of end scission and random scission mechanisms.

End scission occurs at the end position of polymer chains. Random scission, on the other hand, takes place at any random place of a polymer chain. Because the monomer product released from the polymer chain has an acid end that locally accelerates the degradation in the following steps, further end scission is very likely to take place with the presence of acid ends, or in other words, where end scissions have happened. Therefore this polymer chain will become shorter and shorter by losing its end units one by one because of auto-catalysis. This mechanism is often known as ‘unzipping’.

1.4 Purpose and structure of the thesis

Despite the intensive research taking place in polymeric biomaterials, little modelling work has been undertaken. Trial and error, as a classical research method, is practised all around the world in the development of the bioresorbable devices. “Given the benefits of modelling, there is a surprising lack of work in this area. Many published studies of degradation characterise and describe changes in properties such as molecular weight, crystallinity, strength and mass loss over time. However, there is rarely any attempt to link these aspects.” (Farrar, 2008). A more detailed literature review on the existing models of polymer degradation will be presented in Chapter 2. However it is

worth pointing out here that only a few papers can be found in the literature on modelling degradation of bioresorbable devices. Rate equations for hydrolysis reaction were proposed and compared with experimental data (Siparsky *et al.*, 1998). Reaction-diffusion equations were developed and solved for one-dimensional problems to predict drug release (Göpferich and Langer, 1995; Joshi and Himmelstein, 1991). Population balance models were developed to simulate polymer chain scissions (Staggs, 2002; Staggs, 2004). Kinetic Monte Carlo models were developed to simulate scaffold degradation (Mohammadi and Jabbari, 2006). Molecular dynamic models were used to calculate activation energies for hydrolysis reactions (Entrialgo-Castano *et al.*, 2006). An over-simplistic degradation model was combined with a bone remodelling model for scaffold design (Sanz-Herrera *et al.*, 2009). These previous models, however, do not form an integrated framework for device design.

This thesis focuses on orthopaedic fixation devices made of amorphous resorbable polymers. The aim of this thesis is to present a complete mathematical framework to predict the interplay between the degradation of fixation devices and bone healing. Governing equations for the polymer degradation are developed. A simple entropy spring theory is established to predict the change in the Young's modulus of amorphous polymers caused by polymer chain scission. The effective diffusion coefficient for monomer diffusion in a degrading polymer is calculated. Where possible, the models are validated using existing experimental data from the literature. These models are then integrated with a model for bone remodelling and stress analysis. The multi-physics problem of polymer degradation, monomer diffusion, bone remodelling and stress analysis are solved using the finite element method to study the interaction between bone healing and device degradation.

The author is fully aware of the complications on the modelling effort caused by the observed continuous crystallisation during biodegradation, the use of composites in the current development of the fixation devices and, more importantly, the effect of the biological environment on the degradation. These factors are however ignored in this

study mainly due to the time limit of this PhD project. However the work presented here forms a solid foundation for further research to take these factors into account, some of which have already been studied by a follow up PhD project (Han and Pan, 2009) at Leicester.

The structure of the thesis is organised as follow.

Chapter 2 presents a phenomenological model for the degradation of biodegradable polymers.

Chapter 3 presents a study on the effective diffusion coefficient of oligmers in a degrading polymer.

Chapter 4 presents a study on the relation between Young's modulus change and polymer molecular weight loss.

Chapter 5 integrates all the models in Chapter 2, 3, 4 with a bone growth model and stress analysis to provide a complete case study for the biodegradation of orthopaedic fixation devices and its interplay with the healing bone.

Chapter 6 provides some further studies on the degradation model by separating end scission and random scission in the phenomenological model.

Chapter 2

Governing Equations for Biodegradation and Biodegradation Mechanism Maps

2.1 Introduction

In this chapter, we focus on the degradation of the biodegradable polymers and present a phenomenological model for the hydrolysis of polymers, the diffusion of the monomers that are produced by the hydrolysis reaction and the interplay between the hydrolysis and monomer diffusion. The equations are then solved using the finite element method, predicting the spatial and temporal evolution of the average molecular weight in a biodegradable device of any sophisticated shape. A large number of detailed studies, both *in vitro* and *in vivo*, have been published on degradation mechanisms and the factors controlling the degradation rate of a range of biodegradable polymers (Li *et al.*, 1990^a; Li *et al.*, 1990^b; Li *et al.*, 1990^c; Hurrell and Cameron, 2003; Belbella *et al.*, 1996; Park, 1995; Shih, 1995^a). One characteristic phenomenon of the degradation is that a thicker plate degrades faster than a thinner one made of the same polymer (Grizzi *et al.*, 1995). This is because the structural change of PLA is heterogeneous in an implant owing to the auto-catalytic nature of the hydrolysis reaction of PLA (Li *et al.*, 1990^a; Li *et al.*, 1990^b). The choice of dimensions for a particular device is therefore not straightforward – a thicker device can take higher load compared with a thinner one but it also degrades faster. This complicated behaviour makes it difficult to optimise the design of a biodegradable device. The purpose of this chapter is to demonstrate that it is possible to extract a general phenomenological model for biodegradation from the existing experimental and modelling works, and that modern numerical techniques can be used to solve the corresponding equations for devices of both simple and complicated geometries.

2.2 A review of previous reaction-diffusion models for degradation of biodegradable polymers

This section provides detailed descriptions of three existing reaction-diffusion models for polymer degradation. It is these models that inspired the work presented in this thesis. Joshi and Himmelstein (1991) established a relatively comprehensive reaction-diffusion model for drug release from an infinitely extended slab made of biodegradable polymers. Their scheme is shown in Figure 2.2.1.

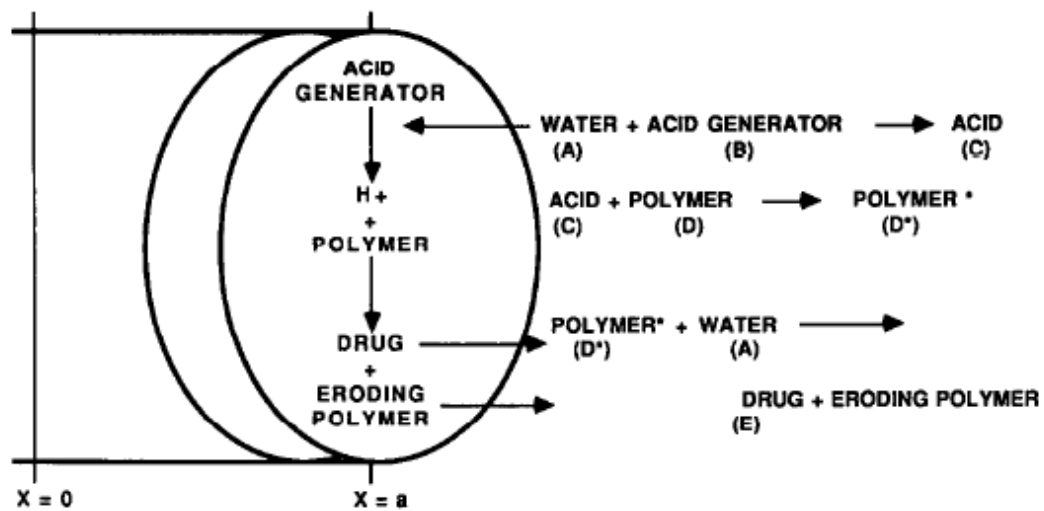


Figure 2.2.1 Scheme of the drug release model by Joshi and Himmelstein (1991).

The distribution of drug particles (denoted by E) inside the big slab is assumed to be homogeneous and so is the acid generator (denoted by B). After the system surface meets water (denoted by A), water hydrolyze B to generate acid (denoted by C). Then the acid will hydrolyze the polymer (denoted by D) therefore intermediate polymer (D^*) is produced. The degradation would be finalized once D^* react with water and small water soluble chains would be diffused out of the system. No volume change is considered during degradation and perfect sink condition is applied on the boundary; Fickian diffusion law is applied to the system:

$$\frac{\partial C_i}{\partial t} = \frac{\partial}{\partial x} \left[D_i(x,t) \frac{\partial C_i}{\partial x} \right] + v_i \quad (2.2.1)$$

**CHAPTER 2 GOVERNING EQUATIONS FOR BIODEGRADATION AND
BIODEGRADATION MECHANISM MAPS**

in which, C_i is the concentration of species i (water, acid generator, acid or drug), $D_i(x,t)$ is the corresponding diffusion coefficient of that species, x is the distance from the centre of the slab; v_i is the net sum of synthesis and degradation of species i (water, acid generator, acid or drug); t is time. The diffusion coefficient in this model is assumed to be an exponential function to the polymer concentration:

$$D_i = D_i^0 \exp\left(\frac{\mu(C_D^0 - C_D)}{C_D^0}\right) \quad (2.2.2)$$

in which D_i and D_i^0 are the diffusion coefficients of species i (water, acid generator, acid or drug) at any time and at $t=0$ respectively, C_D^0 and C_D are the concentrations of the polymer in the initial state and at time t , and μ is a constant. Polymer degradation mechanism is considered as the random hydrolysis of ester bonds in this model and molecular weight change with time of the polymer can be obtained from a statistical expression. Good but limited experimental evidence was provided by Joshi and Himmelstein (1991) to show that the model was able to capture the trend in the drug release profile and molecular weight change.

Göpferich and Langer (1995) developed a model combining the erosion mechanism of the polymer matrix with the diffusion of monomers. The model suggests that the erosion of the matrix produces two types of monomers, named SA (sebacic acid) and CPP (1,3-bis(*p*-carboxyphenoxy)propane)) respectively. These two types of monomers are produced by polymer degradation and the monomers produced are mostly suspended within the system due to the limited solubility for both types. The diffusion of these two types of monomers follows Fick's second law and the diffusion coefficient is a function of porosity. A Monte Carlo simulation is set up to obtain the effective diffusion coefficient (figure 2.2.2).

**CHAPTER 2 GOVERNING EQUATIONS FOR BIODEGRADATION AND
BIODEGRADATION MECHANISM MAPS**

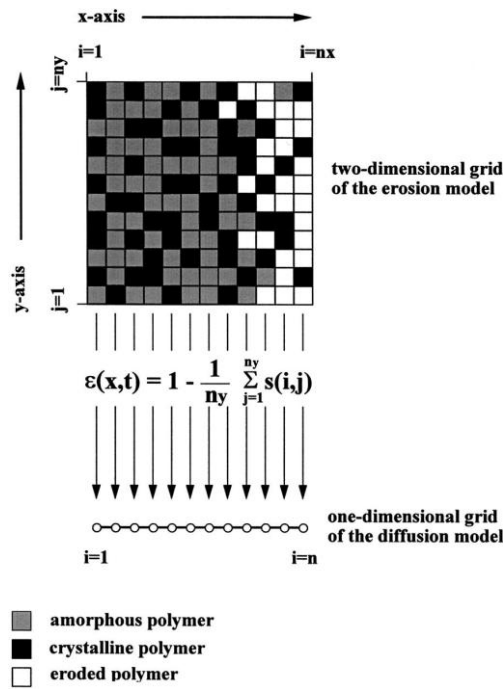


Figure 2.2.2 Scheme of Monte Carlo method to calculate the porosity of the polymer matrix by Göpferich and Langer (1995).

This model uses a two-dimensional grid to simulate the porosity and diffusion in one dimension shown at the bottom of the grid. The pixels in the matrix are randomly distinguished as crystal or amorphous. The erosion time for either amorphous or crystal pixels is randomly decided when they contact the ‘aqueous media’ (eroded pixel) and the crystal pixels need a much longer time to erode, comparing to the amorphous pixels. The column porosity $\varepsilon(x,t)$ is a function of time and column position, this value can be calculated by summing up the value $s(i,j)$ for all the pixels within the same column by:

$$s(i,j) = 1 \quad \text{if the pixel is not eroded (either crystal or amorphous).}$$

$$s(i,j) = 0 \quad \text{if the pixel is eroded.}$$

The Monte Carlo method generates randomly distributed pixels that have degraded in the polymer matrix. Fick’s second law is modified to calculate the diffusion of the monomers:

$$\frac{\partial}{\partial t} C(x,t)\varepsilon(x,t) = \frac{\partial}{\partial x} D_{eff}(C)\varepsilon(x,t) \frac{\partial C(x,t)}{\partial x} \quad (2.2.3)$$

in which $C(x,t)$ is the concentration for either SA or CPP monomers, $\varepsilon(x,t)$ is the porosity along the diffusion pathway obtained from the Monte Carlo method. Equation (2.2.3) can be rewritten as:

$$\begin{aligned} \frac{\partial C(x,t)}{\partial t} &= \frac{\partial D_{eff}(C)}{\partial x} \frac{\partial C(x,t)}{\partial x} + \frac{D_{eff}(C)}{\varepsilon(x,t)} \frac{\partial C(x,t)}{\partial x} \frac{\partial \varepsilon(x,t)}{\partial x} \\ &- \frac{\partial \varepsilon(x,t)}{\partial t} \frac{C(x,t)}{\varepsilon(x,t)} + D_{eff}(C) \frac{\partial^2 C(x,t)}{\partial x^2} \end{aligned} \quad (2.2.4)$$

Most of the SA and CPP monomers produced crystallized instantaneously owing to the very limited solubility of these two types of monomers. Therefore the dissolution of the suspended monomers and the diffusion of the monomers in the solvent are considered simultaneously. Monomer dissolution is introduced to the above equation by including a source term from the suspended crystalline:

$$\begin{aligned} \frac{\partial C(x,t)}{\partial t} &= \frac{\partial D_{eff}(C)}{\partial x} \frac{\partial C(x,t)}{\partial x} + \frac{D_{eff}(C)}{\varepsilon(x,t)} \frac{\partial C(x,t)}{\partial x} \frac{\partial \varepsilon(x,t)}{\partial x} \\ &- \frac{\partial \varepsilon(x,t)}{\partial t} \frac{C(x,t)}{\varepsilon(x,t)} + D_{eff}(C) \frac{\partial^2 C(x,t)}{\partial x^2} + \frac{\partial S}{\partial t} \end{aligned} \quad (2.2.5)$$

in which the source term is calculated according to

$$\frac{\partial S(x,t)}{\partial t} = k \cdot m(x,t) \cdot [C_s - C(x,t)] \quad (2.2.6)$$

where k is a constant, C_s is the solubility of the monomer and $m(x,t)$ is the amount of suspended monomer. The impact of pH is taken into account as well. Given that the solubility of SA is a constant that is independent of the pH value, the following expression was used:

**CHAPTER 2 GOVERNING EQUATIONS FOR BIODEGRADATION AND
BIODEGRADATION MECHANISM MAPS**

$$pH(x,t) = \frac{1}{2}[pKa_{SA} - \log_{10} C_{SA}(x,t)] \quad (2.2.7)$$

in which pKa_{SA} is the logarithm acid dissociation constant that describes the strength of acid for SA monomers. The governing equation for SA monomers is then given by

$$\begin{aligned} \frac{\partial C_{SA}(x,t)}{\partial t} = & \frac{\partial D_{eff}(C_{SA})}{\partial x} \frac{\partial C_{SA}(x,t)}{\partial x} + \frac{D_{eff}(C_{SA})}{\varepsilon(x,t)} \frac{\partial C_{SA}(x,t)}{\partial x} \frac{\partial \varepsilon(x,t)}{\partial x} \\ & - \frac{\partial \varepsilon(x,t)}{\partial t} \frac{C_{SA}(x,t)}{\varepsilon(x,t)} + D_{eff}(C_{SA}) \frac{\partial^2 C_{SA}(x,t)}{\partial x^2} + k_{SA} \cdot m_{SA}(x,t) \cdot [C_{SA} - C_{SA}(x,t)] \end{aligned} \quad (2.2.8)$$

For CPP monomer suspension, its solubility is affected by the SA solubility as the latter is a deciding factor in pH value in the surroundings:

$$C_{CPP}(x,t) = \alpha \cdot 10^{-\beta[pKa_{SA} - \log C_{SA}(x,t)]/2} \quad (2.2.9)$$

The governing equation for CPP monomers is then given by

$$\begin{aligned} \frac{\partial C_{CPP}(x,t)}{\partial t} = & \frac{\partial D_{eff}(C_{CPP})}{\partial x} \frac{\partial C_{CPP}(x,t)}{\partial x} \\ & + \frac{D_{eff}(C_{CPP})}{\varepsilon(x,t)} \frac{\partial C_{CPP}(x,t)}{\partial x} \frac{\partial \varepsilon(x,t)}{\partial x} \\ & - \frac{\partial \varepsilon(x,t)}{\partial t} \frac{C_{CPP}(x,t)}{\varepsilon(x,t)} + D_{eff}(C_{CPP}) \frac{\partial^2 C_{CPP}(x,t)}{\partial x^2} \\ & + k_{CPP} \cdot m_{CPP}(x,t) \cdot [\alpha \cdot 10^{-\beta[pKa_{SA} - \log C_{SA}(x,t)]/2} - C_{CPP}(x,t)] \end{aligned} \quad (2.2.10)$$

Equations (2.2.10) and (2.2.8) are the complete equations for the diffusion of CPP and SA monomers with pH effect and monomer dissolution, respectively.

**CHAPTER 2 GOVERNING EQUATIONS FOR BIODEGRADATION AND
BIODEGRADATION MECHANISM MAPS**

Siepmann *et al.* (2002) used a Monte Carlo model to simulate the drug release for surface eroding polymer matrices. They represent a 3D spherical micro particle using a quarter of a 2D axisymmetric circle as shown in figure 2.2.3.

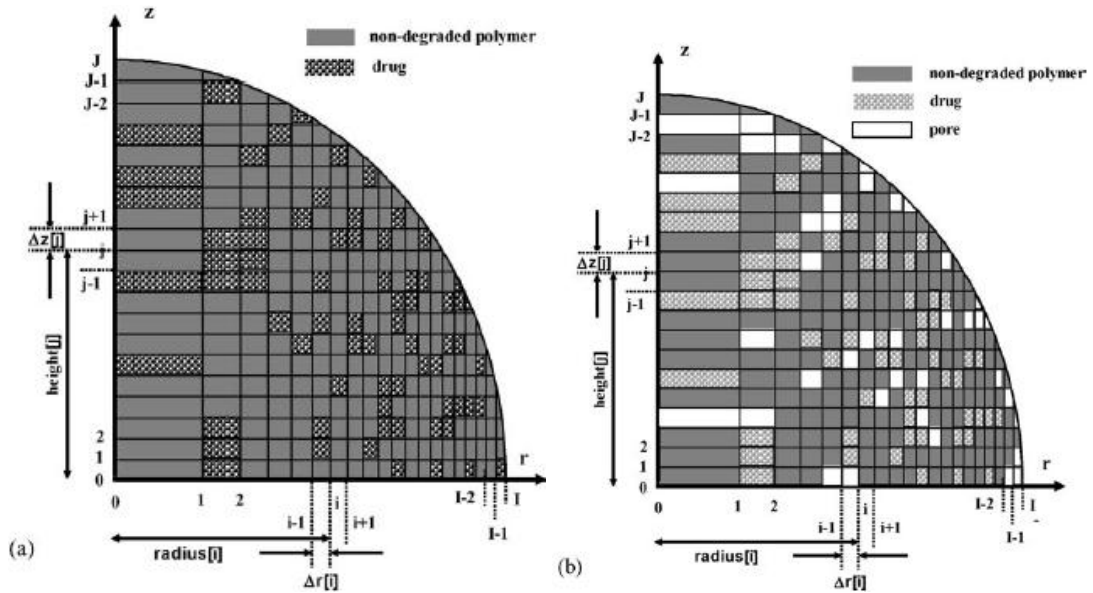


**Figure 2.2.3 Scheme of the Monte Carlo-based simulation of polymer degradation:
(a) initial state (b) during drug release.**

Each unit pixel in figure 2.2.3 represents one of the components in the system which could be drug (dotted unit), polymer (grey unit), or pore (white unit). All these pixels are marked as being either intact or eroded. An intact unit started to dissolve once coming into contact with water. A fixed life time, i.e. a ‘life expectancy’, was defined for each type of pixel. When its lifetime expired, a pixel was assumed to ‘dissolve’ instantaneously and became either a pore or a non-solvable solid. The life time of a pixel is given by

$$t_{lifetime} = t_{average} + \frac{(-1)^\varepsilon}{\lambda} \ln\left(1 - \frac{\varepsilon}{100}\right) \quad (2.2.11)$$

**CHAPTER 2 GOVERNING EQUATIONS FOR BIODEGRADATION AND
BIODEGRADATION MECHANISM MAPS**

in which ε is a random integer number between 0 and 99, λ is a constant, and $t_{average}$ is the average “lifetime” for all the pixels. With this random process, the porosity along the r and z directions can be calculated as

$$\begin{aligned}\varepsilon(r, t) &= 1 - \frac{1}{n_z} \cdot \sum_{j=1}^{j=n_z} s(i(r), j, t) \\ \varepsilon(z, t) &= 1 - \frac{1}{n_r} \cdot \sum_{j=1}^{j=n_r} s(i, j(z), t)\end{aligned}\tag{2.2.12}$$

in which n_r and n_z are the number of elements in that row or column along r or z direction and

$$\begin{aligned}s(i, j, t) &= 1 \quad \text{for non-eroded polymer} \\ s(i, j, t) &= 0 \quad \text{for pores}\end{aligned}$$

The effective diffusion coefficient is calculated as a function of time and position:

$$\begin{aligned}D(r, t) &= D_{crit} \cdot \varepsilon(r, t) \\ D(z, t) &= D_{crit} \cdot \varepsilon(z, t)\end{aligned}\tag{2.2.13}$$

in which D_{crit} represents a critical diffusion coefficient being characteristic for a specific drug-polymer combination. This diffusion coefficient is then applied to Fick’s second law describing the diffusion of the drug particles.

The problems with the Joshi and Himmelstein (1991) model are that

- (a) a rather arbitrary expression for the effective diffusion coefficient was taken
- (b) the reaction equations used do not apply to PLA/PGA co-polymers
- (c) it was only applied to one-dimensional problems, and
- (d) polymer degradation is estimated by statistical analysis of purely random scission.

**CHAPTER 2 GOVERNING EQUATIONS FOR BIODEGRADATION AND
BIODEGRADATION MECHANISM MAPS**

The problems with the models by Göpferich and Langer (1995) and that by Siepmann and co-workers (2002) are that

- (a) the matrix erosion was modelled independently from monomer diffusion. It therefore excludes the autocatalytic effect. In fact the hydrolysis reaction was over-simplified into a uniform random event in these models, and
- (b) the effective diffusion coefficient was related to the random change of polymer into monomers. This is logically incorrect since the effective diffusion coefficient is altered mostly by monomers diffusing out of the system rather than by polymer turning into monomers.

It is in fact possible to generalise and improve the work by Joshi and Himmelstein (1991) to model the degradation of fixation devices made of biodegradable polymers in general, which is the topic of this chapter. It is also possible to redevelop the work by Göpferich and Langer (1995) and that by Siepmann (2002) to build up an appropriate multi-scale model for device degradation, which is the topic of another PhD project (Xiaoxiao Han) at Leicester. Another key development presented in this thesis is that the finite element method, a well-established engineering tool, is used to solve the equations, hence moving the models beyond simple devices such as plates and spheres.

2.3 A phenomenological diffusion-reaction model for biodegradation of biodegradable polymers

2.3.1 Description of the model

To model the biodegradation process in full, a complicated mathematical model is needed, such as the one discussed in Chapter 6, to account for all the reaction steps and all the structural and morphological changes. The parameters in such a model require extensive experimentation to calibrate. In this chapter a simplified model is presented to

CHAPTER 2 GOVERNING EQUATIONS FOR BIODEGRADATION AND BIODEGRADATION MECHANISM MAPS

capture the key features of the process and give predictions consistent with existing experimental observations. A biodegradable device loses all its strength within the first phase of the biodegradation while the device remains as a complete piece, which is the focus of this chapter. In this phase, the material can be viewed as consisting of four species:

- (a) amorphous polymer chains, which can hydrolyse but cannot diffuse;
- (b) monomers and oligomers, the small fragments that consist of one or a few repeating chemical units, which are the product of the hydrolysis reaction and can diffuse; monomers and oligomers together are considered as the diffusing species in this thesis, hence we don't distinguish them when no confusion can be caused.
- (c) water molecules, which are always assumed to be abundant anywhere in the device.

The size distributions of the polymer chains and hydrolysis products are ignored for simplicity. The water penetration in the device is assumed to be much faster than the other kinetic processes, normally about several days compared with the lengthy degradation time. The diffusion front discovered by Hurrell and Cameron (2001^a) was not considered as this phenomenon may be unique to PGA. The assumption of fast water diffusion does not exclude hydrophobic polymers from the model as long as the biodegradation is not controlled by the water diffusion. If the biodegradation is indeed controlled by the slow ingress of water into the device, then surface erosion would dominate the biodegradation. Such polymer systems are often used in controlled drug release but not in fixation devices. In fact, the hydrophilicity of the polymers is reflected by the effective reaction and diffusion coefficients in the model. The state of a biodegrading polymer can therefore be described using

- (a) the mole concentration of the ester bonds of the amorphous polymer, and
- (b) the mole concentration of the ester bonds of the monomers and oligomers remaining in the device

which are referred to as C_e , and C_m respectively. In the hydrolysis reaction, the water molecules attack the ester bonds of the polymer chain which is accelerated by the acid

**CHAPTER 2 GOVERNING EQUATIONS FOR BIODEGRADATION AND
BIODEGRADATION MECHANISM MAPS**

end-groups of the monomers is present. In a general co-polymer system the rate of the chain scission of the polymers, referred to as $\frac{dR_s}{dt}$, can be written as

$$\frac{dR_s}{dt} = k_1 C_e + k_2 C_e C_m^n \quad (2.3.1)$$

The first term on the right-hand side reflects un-catalysed hydrolysis while the second term reflects the acid-catalysed hydrolysis. k_1 and k_2 are phenomenological reaction constants for the two types of hydrolysis reactions. The power n in the second term accounts for the dissociation of the acid end groups. The water concentration does not appear in the equation because the water molecules are assumed to be abundant. Equation (2.3.1) is therefore designed for hydrolysis reaction in a general co-polymer system. The chain scission may produce:

- (a) monomers; if the scissions occur at the end of a polymer chain;
- (b) oligomers; if the scissions occur a few monomers away from the end of a long chain.
- (c) neither monomers or oligomers; if the scissions occur somewhere in the middle of the long polymer chains; the molecular weight is nevertheless always reduced by the chain scission.

In general the mole concentration of the ester bonds of the monomers R_m , and oligomers produced by scission can be related to the mole concentration of the total number of chain scission, R_s , through an empirical power relation:

$$R_m = AR_s^\alpha \quad (2.3.2)$$

In most part of this thesis, it is further assumed that $A=1$ and $\alpha=1$, which are only strictly correct if the hydrolysis reaction is controlled by end scission. There is no difficulty in solving the equations without this further simplification but there is

**CHAPTER 2 GOVERNING EQUATIONS FOR BIODEGRADATION AND
BIODEGRADATION MECHANISM MAPS**

experimental evidence showing that the hydrolysis reaction in PLAs is indeed dominated by end scission within acid environment (Shih, 1995^a; Shih, 1995^b).

Equation (2.3.1) can then be written as:

$$\frac{dR_m}{dt} = \frac{dR_s}{dt} = k_1 C_e + k_2 C_e C_m^n. \quad (2.3.3)$$

The ester bond concentration in the amorphous phase reduces as a consequence of the monomer and oligomer production. We then have

$$\frac{dC_e}{dt} = -\frac{dR_m}{dt} \quad (2.3.4)$$

Assuming Fick's law for monomer/oligomer diffusion, we have the following governing equation for the ester bond concentration of the monomers and oligomers:

$$\frac{dC_m}{dt} = \frac{dR_m}{dt} + \frac{\partial}{\partial x_1} \left[D \frac{\partial C_m}{\partial x_1} \right] + \frac{\partial}{\partial x_2} \left[D \frac{\partial C_m}{\partial x_2} \right] + \frac{\partial}{\partial x_3} \left[D \frac{\partial C_m}{\partial x_3} \right]. \quad (2.3.5)$$

The phenomenological diffusion coefficient D increases as more and more monomers and oligomers diffuse out of the system, replaced by pores filled with the aqueous medium. Chapter 3 presents a detailed study on the dependence of the diffusion coefficient on the pore structures. For randomly distributed pores the effective diffusion coefficient is given by (Chapter 3):

$$D = D_0 + (1.3p^2 - 0.3p^3)(D_{\max} - D_0) \quad (2.3.6)$$

in which D_{\max} is the diffusion coefficient of monomers in the liquid filled pore, D_0 is the diffusion coefficient of monomers in the fresh polymer and p is the porosity caused by monomers leaving the system. The porosity can be estimated as

**CHAPTER 2 GOVERNING EQUATIONS FOR BIODEGRADATION AND
BIODEGRADATION MECHANISM MAPS**

$$p = 1 - (C_m + C_e) / C_{e0} \quad (2.3.7)$$

where C_{e0} represents the initial ester bond concentration of the polymer.

2.3.2 The parameter n

This section presents a discussion by Siparsky *et al.* (1998) on the second term in the reaction rate equation (2.3.1). Considering the case without diffusion, Siparsky *et al.* (1998) firstly considered the following hydrolysis reaction equation

$$\frac{dC_e}{dt} = -kC_e C_m \quad (2.3.8)$$

i.e. the case where $n=1$ which means the monomers participate in the autocatalytic reaction fully. They showed that equation (2.3.8) leads to a linear relation between $\ln(C_m^{0.5} / C_e)$ and time t with a slope of $[C_e^0 + (K_a C_m^0)^{0.5}]k$ and the intercept of $\ln((C_m^0)^{0.5} / C_e^0)$ on the y axis, in which K_a is a dissociation constant. However their experimental data on a group of PLA samples ($M_n = 55,000$ solute in acetonitrile and kept under $60^\circ C$ up to 60 days) did not support this theoretical prediction. An improvement was made whereby the acidic end groups participate in the hydrolysis reaction partially through $n=0.5$. They used the following equation:

$$\frac{dC_e}{dt} = -kC_e (K_a C_m)^{0.5} \quad (2.3.9)$$

This reaction equation leads to a linear relation between $(1/a^{0.5}) \ln\{(a - C_e)^{0.5} - a^{0.5} / (a - C_e)^{0.5} + a^{0.5}\}$ and time t with a slope of $kK_a^{0.5}$ and an intercept of $(1/a^{0.5}) \ln\{(a - C_e^0)^{0.5} - a^{0.5} / (a - C_e^0)^{0.5} + a^{0.5}\}$ to the y axis, where

**CHAPTER 2 GOVERNING EQUATIONS FOR BIODEGRADATION AND
BIODEGRADATION MECHANISM MAPS**

$a = C_e^0 + C_m^0$. This prediction was supported by their experimental data as shown in figure 2.3.1.

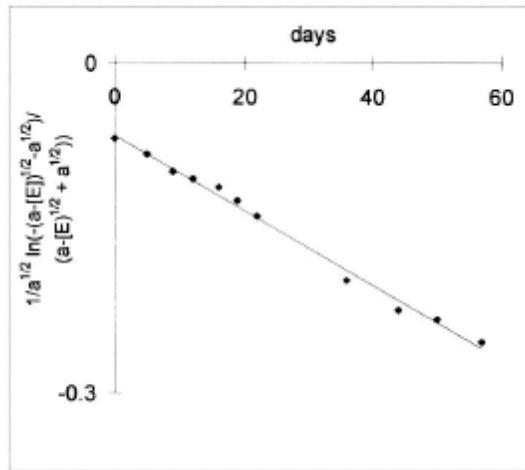
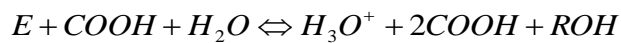


Figure 2.3.1 Experimental result for PLA sample kept in acetonitrile solution under 60°C up to 60 days (Siparsky *et al.*, 1998).

Siparsky *et al.* (1998) showed that the fact that $n=0.5$ agrees with a simple version of the hydrolysis reaction:



in which E is the ester bond, $COOH$ is the carboxyl group, ROH is the hydroxyl group.

It is important to notice that the degradation experiment was conducted in solution rather than solid state.

2.3.3 Nondimensionalisation of the equations

In a numerical analysis, it is convenient to use a non-dimensional form of the equations so that the numerical results are not specific to the dimensions and material parameters used in the analysis. Using the reaction rate of the catalysed hydrolysis as a reference, we introduce the following non-dimensional variables:

$$\bar{C}_e = \frac{C_e}{C_{e0}}; \bar{C}_m = \frac{C_m}{C_{e0}}; \bar{x}_i = \frac{x_i}{l}; \bar{t} = (k_2 C_{e0}^n) t \quad (2.3.10)$$

and material parameters:

$$\bar{k}_1 = \frac{k_1}{k_2 C_{e0}^n}; \bar{D}_0 = \frac{D_0}{C_{e0}^n k_2 l^2} \quad (2.3.11)$$

in which C_{e0} is the ester bond concentration of the amorphous phase at the beginning of the biodegradation, and l is a characteristic length of the device. The reaction-diffusion model for biodegradation can then be summarised as consisting of a hydrolysis reaction equation for the polymer:

$$\frac{d\bar{C}_e}{d\bar{t}} = -(\bar{k}_1 \bar{C}_e + \bar{C}_e \bar{C}_m^n), \quad (2.3.12)$$

and a diffusion equation for monomers and oligomers:

$$\frac{d\bar{C}_m}{d\bar{t}} = \bar{k}_1 \bar{C}_e + \bar{C}_e \bar{C}_m^n + \frac{\partial}{\partial \bar{x}_1} [\bar{D} \frac{\partial \bar{C}_m}{\partial \bar{x}_1}] + \frac{\partial}{\partial \bar{x}_2} [\bar{D} \frac{\partial \bar{C}_m}{\partial \bar{x}_2}] + \frac{\partial}{\partial \bar{x}_3} [\bar{D} \frac{\partial \bar{C}_m}{\partial \bar{x}_3}] \quad (2.3.13)$$

in which the effective diffusion coefficient is given by

$$\bar{D} = \bar{D}_0 \left\{ 1 + (1.3p^2 - 0.3p^3) \left(\frac{D_{\max}}{D_0} - 1 \right) \right\},$$

Where the porosity is calculated by

$$p = 1 - (\bar{C}_m + \bar{C}_e).$$

**CHAPTER 2 GOVERNING EQUATIONS FOR BIODEGRADATION AND
BIODEGRADATION MECHANISM MAPS**

The model is perhaps the simplest form possible that can capture the key features of the device degradation. Apart from the dissociation exponent n , only three non-dimensional parameters enter the governing equations:

- \bar{k}_1 - reflecting the relative reaction rate of the non-catalysed hydrolysis with respect to that of the catalysed one;
- \bar{D}_0 - reflecting the diffusion rate relative to the combination of catalysed hydrolysis rate and the characteristic length of the material, and
- $\frac{D_{\max}}{D_0}$ - reflecting the relative diffusion rate of the monomers in the liquid filled pores to that in the undegraded polymer.

$\frac{D_{\max}}{D_0}$ can be set as a very large value, 100 for example. As can be seen in the rest of this thesis, the degradation behaviour is controlled by the interplay between \bar{k}_1 and \bar{D}_0 .

The number average molecular weight is calculated as

$$M_n = \frac{C_e \times M_{unit}}{N_{chain}^0 + (R_s - R_m)} \quad (2.3.14)$$

in which C_e is the total number of ester bonds, M_{unit} is the molecular weight of one repeating unit, N_{chain}^0 is the initial number of polymer chains, R_s is the total number of chain cleavage and R_m is the total number of monomers.

Noticing that the initial value of M_n is given by

$$M_{n0} = \frac{C_{e0} \times M_{unit}}{N_{chain}^0}, \quad (2.3.15)$$

And that $R_m = AR_s^\alpha$, equation (2.3.14) can be written in a normalised form as

$$\bar{M}_n = \frac{\bar{C}_e}{1 + \frac{C_{e0}}{N_{chain}^0} (\bar{R}_s - AC_{e0}^{\alpha-1} \bar{R}_s^\alpha)} = \frac{\bar{C}_e}{1 + DP_0 (\bar{R}_s - AC_{e0}^{\alpha-1} \bar{R}_s^\alpha)} \quad (2.3.16)$$

where DP_0 represents the initial degree of polymerisation of the polymer. In the simple case of $A=1$ and $\alpha=1$, we have $\bar{M}_n = \bar{C}_e$.

2.3.4 Heterogeneous degradation of biodegradable polymeric devices

A characteristic phenomenon of biodegradation is that PLA/PGA polymers tend to form a hollow structure at the later stage of the degradation as shown in figure 1.3.2. Li *et al.* (1990^b) suggested that this is because the hydrolysis reaction is auto-catalysed when the acids produced and accumulated inside the system accelerate the degradation of the material in the centre rather than on the boundaries. The picture in figure 1.3.2 was obtained by Li *et al.* (1990^b) using PLA37.5GA25 (75% DL-lactide and 25% glycolide in the feed) after 10 days of degradation in distilled water. This surface-centre differentiation has been widely observed by researchers. It is therefore constructive to test if our model can capture this phenomenon. We consider a brick sample as shown in figure 1.3.2 and apply our phenomenological equations with $\bar{D}_0 = 0.001$, $\bar{k}_1 = 0.1$. Assuming the sample surface is perfect sink for the monomers (i.e. $\bar{C}_m = 0$), the equations were solved using the finite element method. The distribution of the ester bond concentration remained after a period of degradation (at $\bar{t} = 0.24$) over the mid-cross section of the sample is shown in figure 2.3.2.

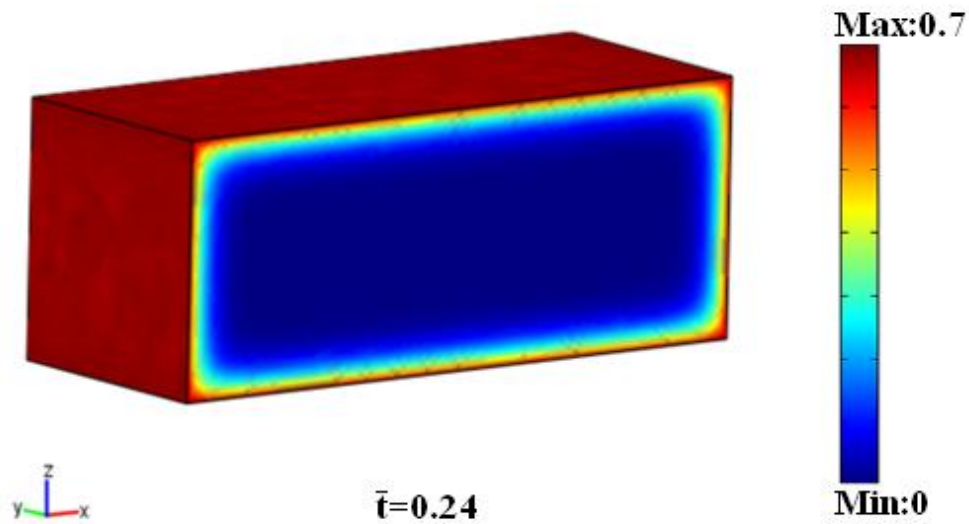


Figure 2.3.2 A representative case to demonstrate the model is able to capture the heterogeneous degradation, colour represent the ester bond concentration.

The red colour indicates a relatively high concentration while the blue colour indicates a low concentration. The value of the colour bar is normalised by the initial ester bond concentration. The surface/core differentiation of the biodegradation is clearly captured by the model.

2.3.5 Localisation of biodegradation

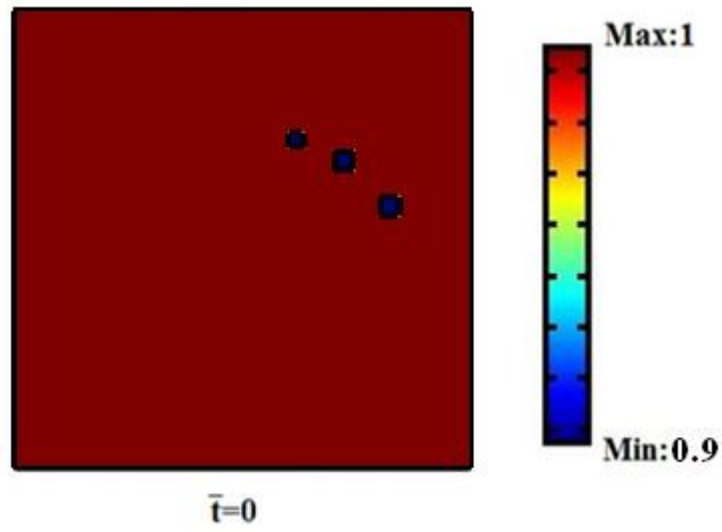
Localisation is often observed in the degradation of PLA/PGA polymers. Figure 2.3.3 shows an example (Gutwald *et al.*, 2002).



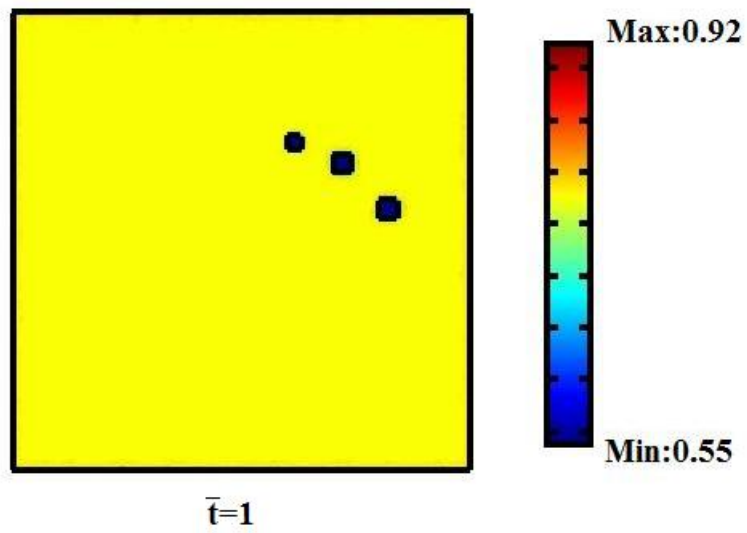
Figure 2.3.3 Cross-section image of a PLLA implant after 80 weeks (Gutwald *et al.*, 2002).

The photo shows isolated pores formed during the degradation at micron scale. Grizzi *et al.* (1995) also observed the formation of cavities in their degradation experiment using PDLA plates. The cause for the localisation may be due to heterogeneity of the initial polymer, for example, being locally rich of residual monomers. To test this idea, we introduce a small initial concentration of the monomers in some selected “defect” regions as shown in Figure 2.3.4. The initial monomer concentration in the small “defect” regions is set as $C_m = 0.1C_{e0}$ in contrast to zero in the rest of the device. Figure 2.3.4 shows the computer simulated degradation using $\bar{D}_0 = 10^{-5}$, $\bar{k}_1 = 10^{-4}$, $n = 0.5$ in equation (2.3.12) & (2.3.13). It can be observed from Figure 2.3.4 that the introduced “defects” indeed accelerate the local degradation to some extent. However the difference between the degradation rates in the defect and normal regions is not significant enough to explain the observed formation of cavities.

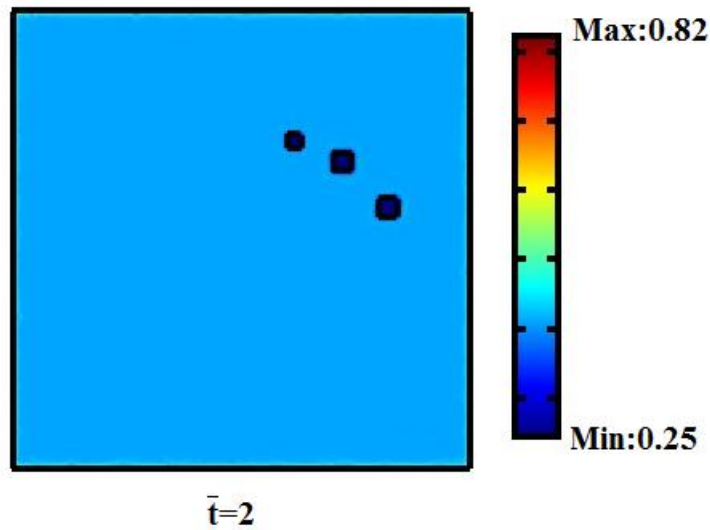
CHAPTER 2 GOVERNING EQUATIONS FOR BIODEGRADATION AND
BIODEGRADATION MECHANISM MAPS



(a) $\bar{t} = 0$



(b) $\bar{t} = 1$

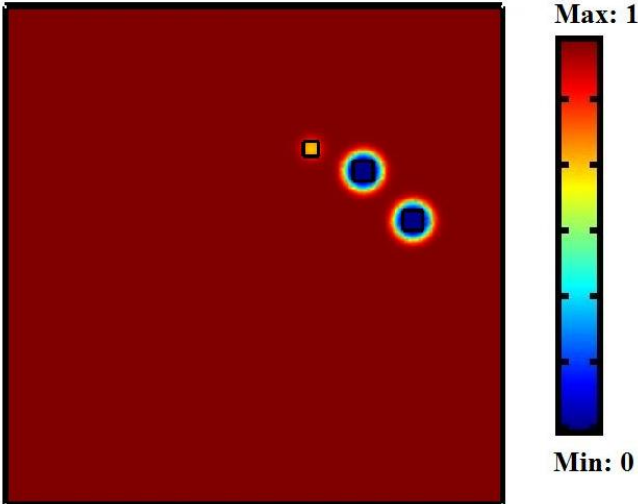


(c) $\bar{t} = 2$

Figure 2.3.4 Computer simulated localisation of degradation using $\bar{D}_0 = 10^{-5}, \bar{k}_1 = 10^{-4}, n = 0.5$. The colour represents the average molecular weight normalised by its initial value.

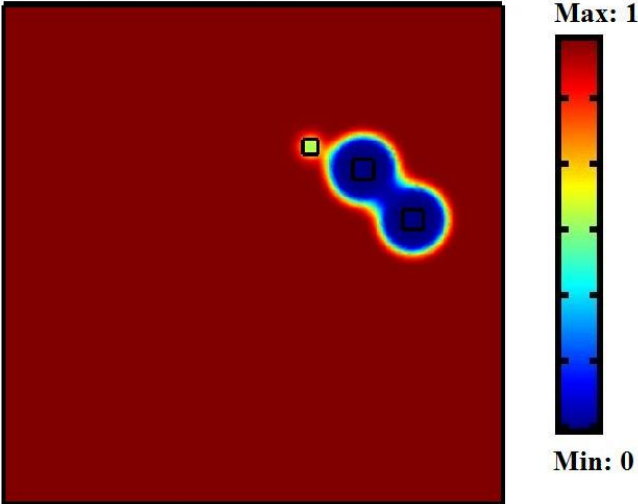
In section 2.3.2, it is shown that the parameter, n , takes the value of 0.5 according to Siparsky *et al.* (1998). However this is the only literature that we are aware of discussing the hydrolysis reaction mechanism in this detail. Their conclusion is based on a hydrolysis test in PLA solution rather than in the solid state. Here we hypothesise that parameter n may take other values. The simulation is repeated using $\bar{D}_0 = 10^{-5}, \bar{k}_1 = 10^{-4}, n = 2$ and the results are presented in figure 2.3.5 at four normalised times.

CHAPTER 2 GOVERNING EQUATIONS FOR BIODEGRADATION AND
BIODEGRADATION MECHANISM MAPS



$\bar{t}=28$

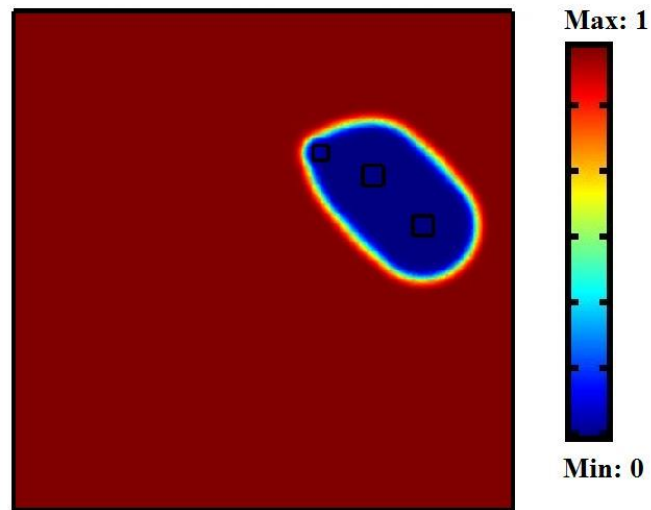
(a) $\bar{t} = 28$



$\bar{t}=38$

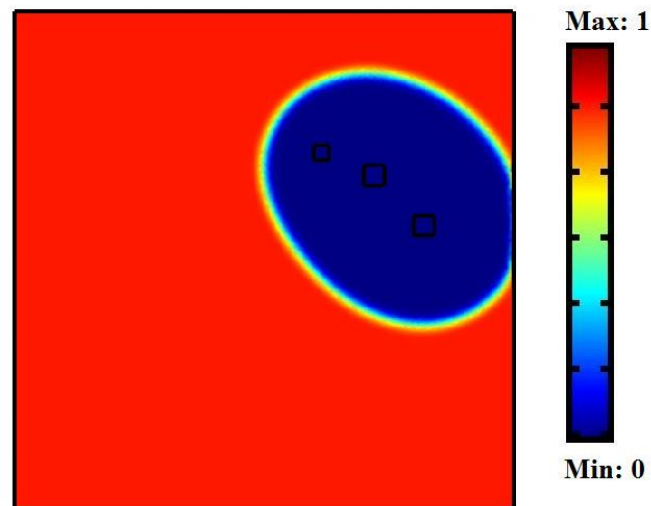
(b) $\bar{t} = 38$

**CHAPTER 2 GOVERNING EQUATIONS FOR BIODEGRADATION AND
BIODEGRADATION MECHANISM MAPS**



$\bar{t}=48$

(c) $\bar{t} = 48$



$\bar{t}=68$

(d) $\bar{t} = 68$

Figure 2.3.5 Computer simulated localisation of degradation using $\bar{D}_0 = 10^{-5}, \bar{k}_1 = 10^{-4}, n = 2$. The colour represents the average molecular weight normalised by its initial value.

A very different behaviour can be observed in Figure 2.3.5 from that in Figure 2.3.4. Firstly the defect region degrades much faster than the normal region. Figure 2.3.5 (a) shows that by $\bar{t} = 28$, the molecular weight in the defect zones has reached almost zero

**CHAPTER 2 GOVERNING EQUATIONS FOR BIODEGRADATION AND
BIODEGRADATION MECHANISM MAPS**

while the normal zone is still intact. Secondly the defects zones clearly interact and propagate as shown the Figure 2.3.5 (b) – (d) unlike for the case of $n=0.5$ shown in figure 2.3.4. In almost all the biodegradation experiments, the testing materials or devices break up well before the averaged molecular weight reaches zero. Figure 2.3.6 shows an example.

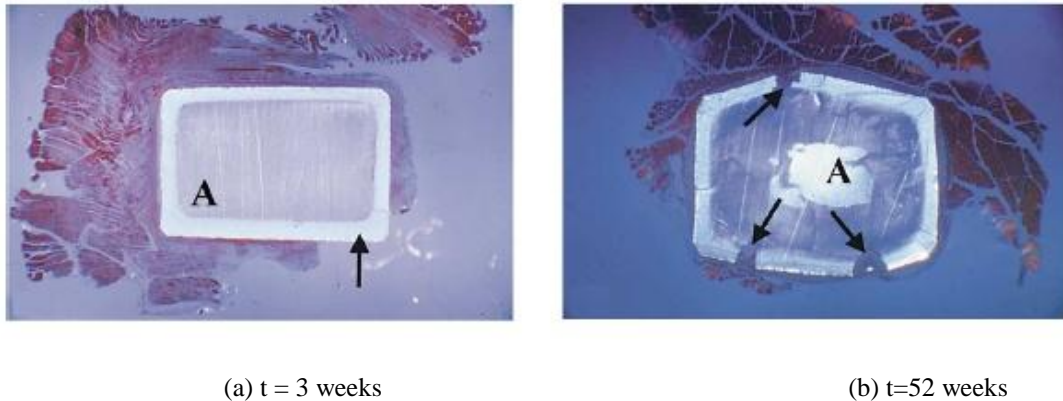


Figure 2.3.6 Observed breaking up of amorphous PLLA plate during the in vivo degradation experiment in rat muscle by Gutwald *et al.* (2002).

Therefore defect propagation may be a rule rather than an exception during the degradation of biodegradable devices.

2.3.6 The size effect of biodegradation

A related phenomenon of biodegradation of resorbable polymers is the size effect: a thicker device degrades faster than a thinner one which was discovered by Grizzi *et al.* (1995). They explained the size effect by arguing that it is more difficult for soluble oligomers to diffuse out of a thicker plate than those in a thinner plate. An acidic environment is therefore built up in a thicker plate making it degrade faster than a thinner one. This interplay between oligomers diffusion and hydrolysis can be demonstrated using our phenomenological model. Figure 2.3.7 shows the degradation data (discrete symbols) collected by Grizzi *et al.* (1995) using DLPLA plate samples of

**CHAPTER 2 GOVERNING EQUATIONS FOR BIODEGRADATION AND
BIODEGRADATION MECHANISM MAPS**

2mm thickness (diamond symbols) and DLPLA film samples of 0.3mm thickness (triangle symbols) respectively.

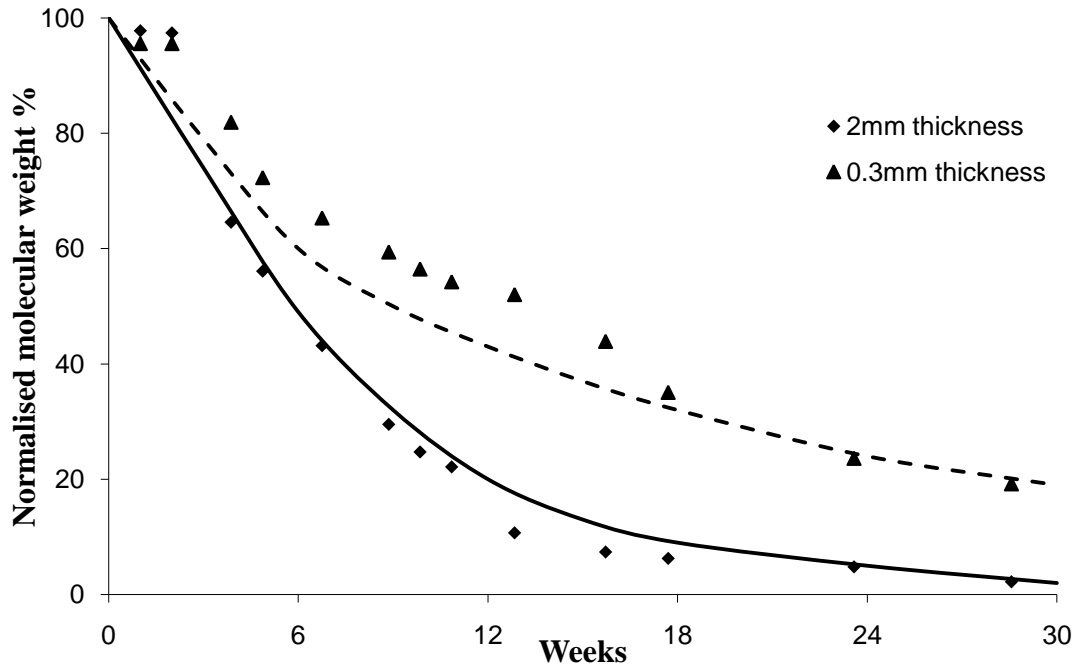


Figure 2.3.7 Experimental data (discrete symbols) of average molecular weight as a function of time obtained using DLPLA films of 0.3mm and plate of 2mm in thickness respectively (Grizzi *et al.*, 1995); the continuous line are calculated results of the model using $\bar{k}_1 = 0.25, n = 0.5, \bar{D}_0 = 0.005$ and 0.25 .

The figure shows number average molecular weights for both samples as a function of the degradation time. Figure 2.3.8 shows our computational model which considers a representative element of the plates in which both the C_m and C_e are assumed to be independent of the y and z coordinates.

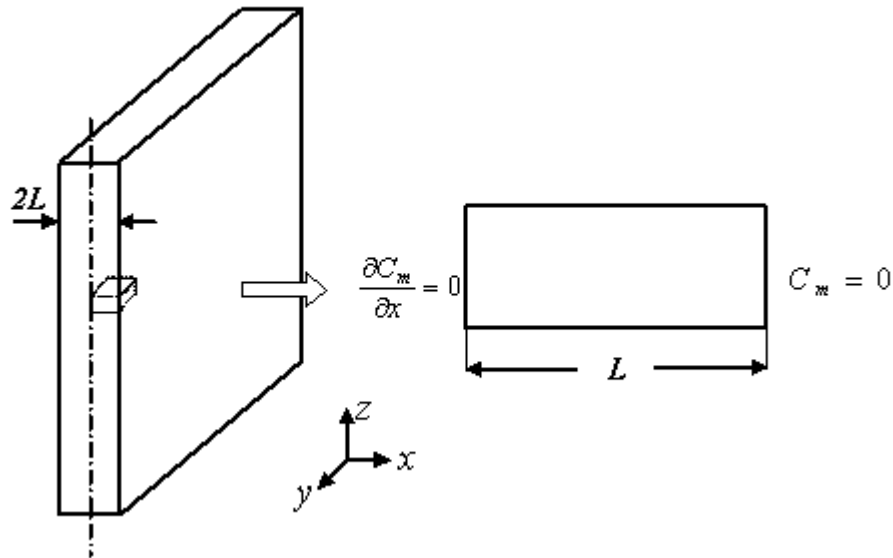


Figure 2.3.8 A representative unit for a biodegradable film

For the representative unit showed on the right hand side of the figure, the right boundary, i.e. the interface between the polymer and the aqueous medium, is assumed to be a perfect sink for the monomer diffusion (i.e. any monomer arriving at the boundary is immediately taken away by the aqueous medium, which is a simplification); the other boundary has zero diffusive flux of the monomers due to the fact that it is a symmetry line. The solid and dashed lines in figure 2.3.7 show the prediction of equations (2.3.12) and (2.3.13) using $\bar{k}_1 = 0.25$, $n = 0.5$, $\bar{D}_0 = 0.005$ and 0.25 , which correspond to $k_1 = 0.042 / week$, $k_2 = 1.27 \times 10^{-3} \sqrt{m^3 / mol} / week$, and $D_0 = 5.5 \times 10^{-15} m^2 / s$.

**CHAPTER 2 GOVERNING EQUATIONS FOR BIODEGRADATION AND
BIODEGRADATION MECHANISM MAPS**

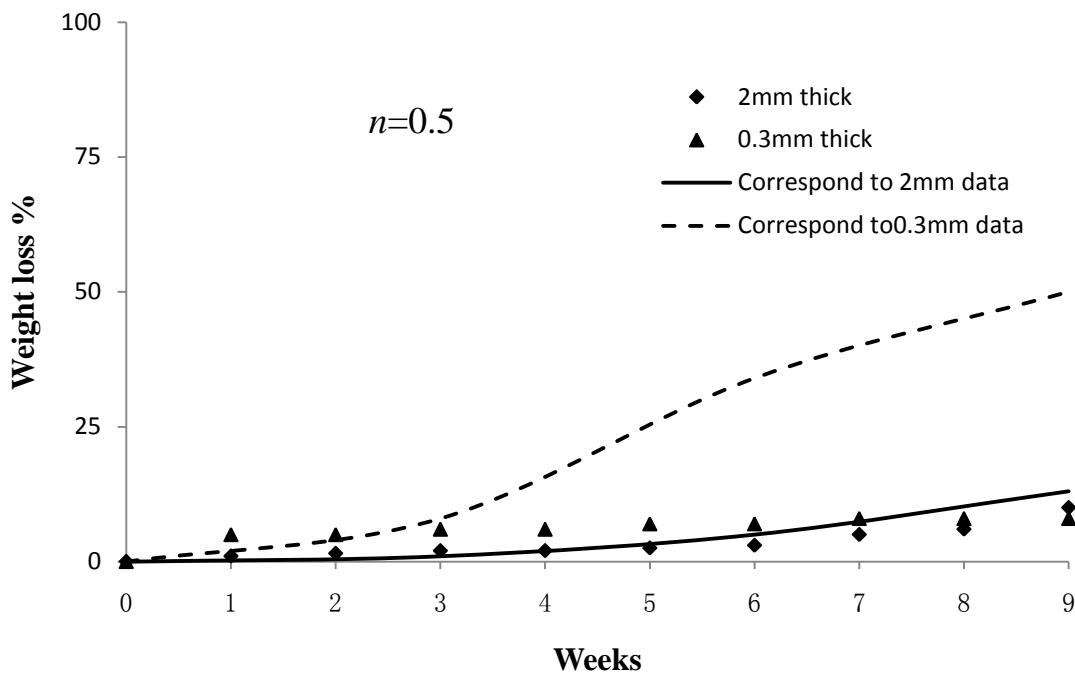


Figure 2.3.9 The comparison between the predicted (lines) and measured (discrete symbols) weight loss as functions of time for DLPLA films of 0.3mm and plate of 2mm respectively. This figure corresponds to figure 2.3.7.

Figure 2.3.9 compares the predicted and experimental data for weight loss of the samples. It is apparent that the agreement is poor. In the model, a much larger weight loss is required than that observed in the experiment, for the thin sample to achieve the degradation rate shown in figure 2.3.7. Detailed study of the model prediction also revealed that the difference in the average molecular weights of the core and surface polymers is much smaller compared to that reported by Grizzi *et al.* (1995). As discussed in section 2.3.4, we consider the possibility of $n=2$ and repeated the above analysis. Figure 2.3.10 and 2.3.12 compare the model predictions with the experimental data using $n=2$.

CHAPTER 2 GOVERNING EQUATIONS FOR BIODEGRADATION AND
BIODEGRADATION MECHANISM MAPS

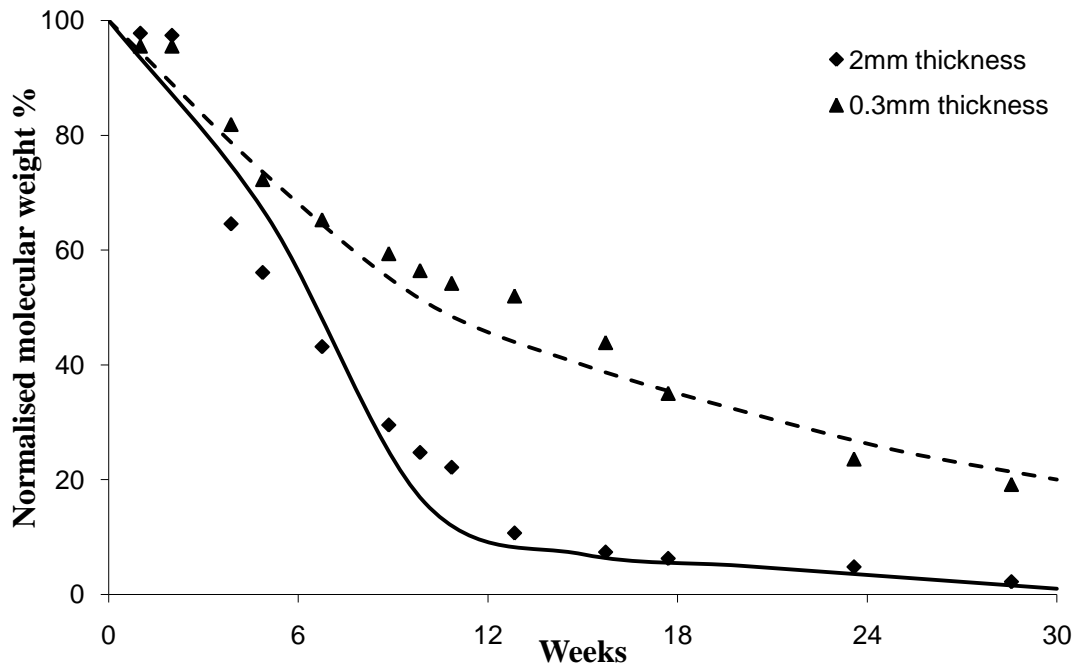


Figure 2.3.10 Fitting the model prediction to the experimental data of average molecular weight versus time (Grizzi *et al.*, 1995) by using $\bar{k}_1 = 0.05$, $n = 2$,

$$\bar{D}_0 = 0.02 \text{ and } 0.0004.$$

**CHAPTER 2 GOVERNING EQUATIONS FOR BIODEGRADATION AND
BIODEGRADATION MECHANISM MAPS**

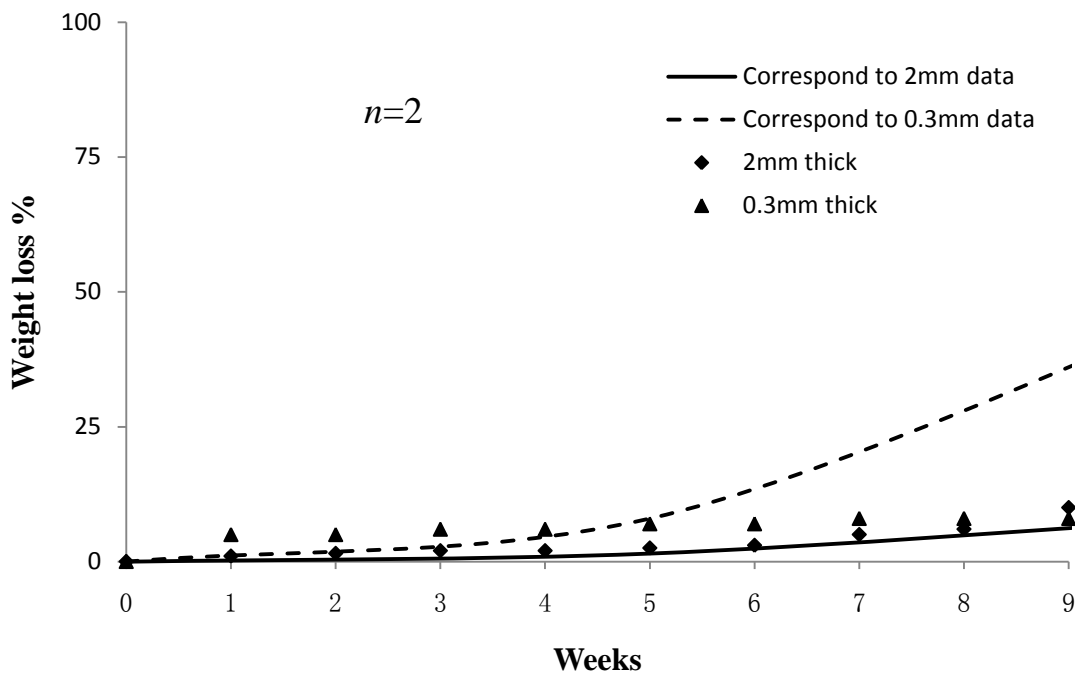


Figure 2.3.11 Comparison between predicted (lines) and measured (discrete symbols), weight loss of DLPLA films of 0.3mm and plate of 2mm as a functions of time. This figure corresponds to figure 2.3.10.

It can be observed from figure 2.3.10 and 2.3.12 that both the molecular weight and the weight loss data can be fairly well fitted using $n=2$. The numerical study presented in section 2.3.5 and in the current section show that the acid disassociation exponent n in the hydrolysis reaction equation has a key effect on the model prediction. There is however confusion on the actual value of n that should be used. Some authors used $n=1$ (Farrar, 2008) while Siparsky *et al.* (1998) showed that $n=0.5$. Siparsky and co-workers' (1998) experiment is however for PLA degradation in solutions. Our numerical studies show that a much larger value of n is necessary to capture the observed surface/core differentiation that has been observed in the experiment. The mechanism responsible for the large value of n is however unclear. There is a need for further fundamental study on the hydrolysis reactions.

Apart from the experimental evidence provided above, Han and Pan (2009) have recently extended the model to include the effect of chain cleavage induced

crystallisation and validated the model using experimental data for 3 different biodegradable polymers.

2.4 Biodegradation map

2.4.1 The concept of a biodegradation map

The size effect suggests that the difference in the material thickness decides the difference in biodegradation. Apart from that, there are still other factors controlling the degradation. Even for the one-dimensional case, the degradation behaviour is affected not only by the thickness of the plate but also the four parameters in equations (2.3.4) and (2.3.5). The non-dimensional version of the model given by equations (2.3.12) and (2.3.13) provides a much clearer picture as it reduces the parameter to two. To show how these two parameters can control the degradation mechanism, some numerical explorations are undertaken in which the auto-catalysed hydrolysis is used as the reference in the non-dimensionalisation. The two-dimensional problem shown in figure 2.3.8 is solved numerically to give the spatial distribution of \bar{C}_e at various degradation times. The ester bond concentration \bar{C}_e is then averaged over the entire area at these times. For the degradation mechanism, there are two extreme cases. The first one is the fast diffusion limit above which the product of the hydrolysis reaction is immediately taken away from the plate. At this extreme the auto-catalysed hydrolysis reaction is starved of the catalyst because the second item on the right-hand side of the equation (2.3.13) is approaching zero. Consequently, the polymer degradation rate is relatively slow and entirely controlled by the non-catalysed reaction which is the first item on the right-hand side of equation (2.3.13). For this case, the thickness of the material is no longer a factor in the degradation process. Another extreme is the slow diffusion limit under which all the reaction product remains in situ as catalyst. At this extreme the polymer degradation rate is fast and controlled by the auto-catalysed reaction rate, as the second right-hand side item is dominant over the first right-hand side item in equation (2.3.13). These limits are also affected by the rate of the non-catalysed

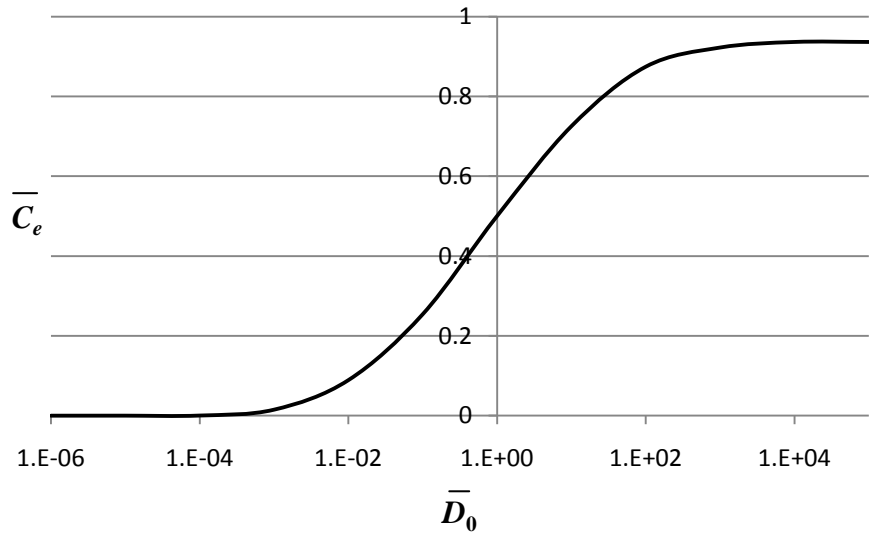
**CHAPTER 2 GOVERNING EQUATIONS FOR BIODEGRADATION AND
BIODEGRADATION MECHANISM MAPS**

hydrolysis reaction as well. For example, if the non-catalysed hydrolysis reaction is very fast, then diffusion of the reaction product becomes irrelevant to the hydrolysis reaction and the degradation is entirely controlled by the non-catalysed hydrolysis reaction. There is always a critical value of the normalised diffusion coefficient, above which the degradation time is not affected by the material thickness any longer. Similarly there is always a critical value of the normalised diffusion coefficient below which the degradation time is not affected by the material thickness either. These limits can be plotted together to form a biodegradation map showing different degradation mechanisms.

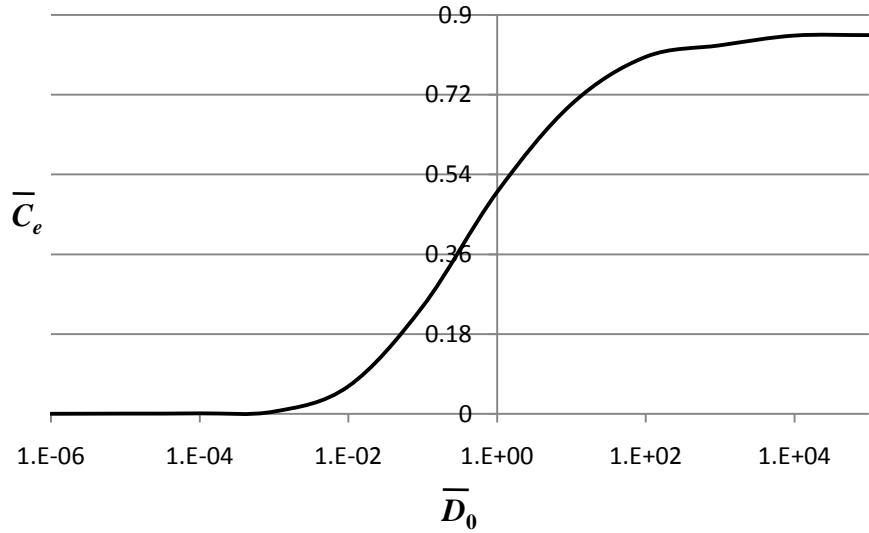
2.4.2 A biodegradation map for plate

To find out the fast and slow diffusion limits we set up numerical tests using the non-dimensional model for plate (figure 2.3.8). When constructing the degradation map, the value of n in equation (2.3.12) and (2.3.13) is taken as 0.5 following the discussion in section 2.3.2. The effect of n on the degradation map will be discussed in section 2.4.4. For any fixed value of \bar{k}_1 , at a reference non-dimensional time, the upper limit of \bar{D}_0 can be found if the spatially averaged ester bond concentration \bar{C}_e does not change any further while \bar{D}_0 is increasing. Similarly, a lower limit of \bar{D}_0 can be found if the spatially averaged ester bond concentration \bar{C}_e does not change any further while \bar{D}_0 is decreasing. These calculations of the upper and lower limits of \bar{D}_0 are repeated for different values of \bar{k}_1 . The reference non-dimensional time is selected as $\bar{C}_t = 0.5\bar{C}_{e0}$ when $\bar{D}_0 = 1$. This is because the other data under different \bar{D}_0 value can be well presented. Some examples of the calculations are given below in figure 2.4.1.

**CHAPTER 2 GOVERNING EQUATIONS FOR BIODEGRADATION AND
BIODEGRADATION MECHANISM MAPS**

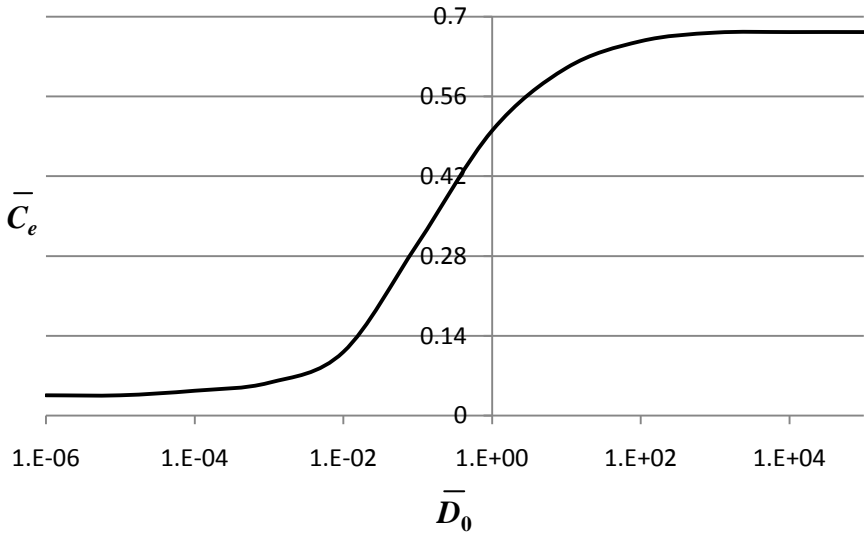


(a) $\bar{k}_1 = 0.001, \bar{t} = 25.7$.

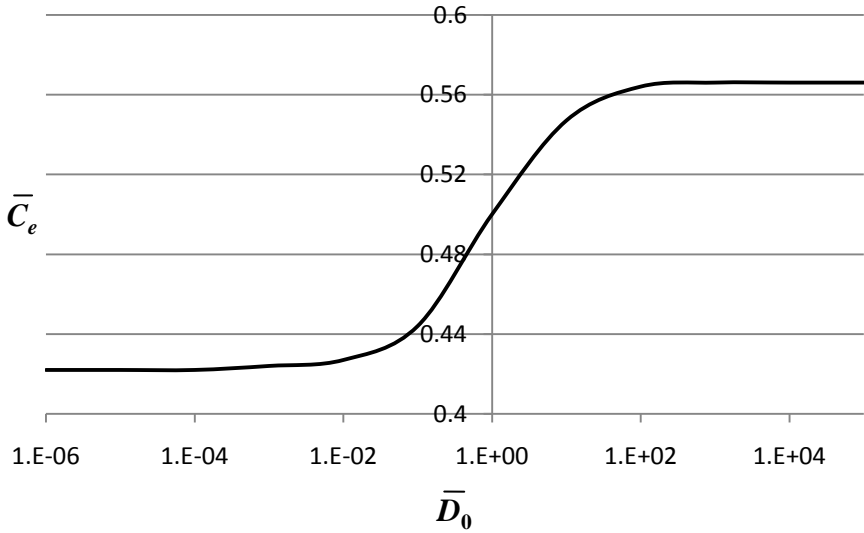


(b) $\bar{k}_1 = 0.01, \bar{t} = 15.25$.

**CHAPTER 2 GOVERNING EQUATIONS FOR BIODEGRADATION AND
BIODEGRADATION MECHANISM MAPS**

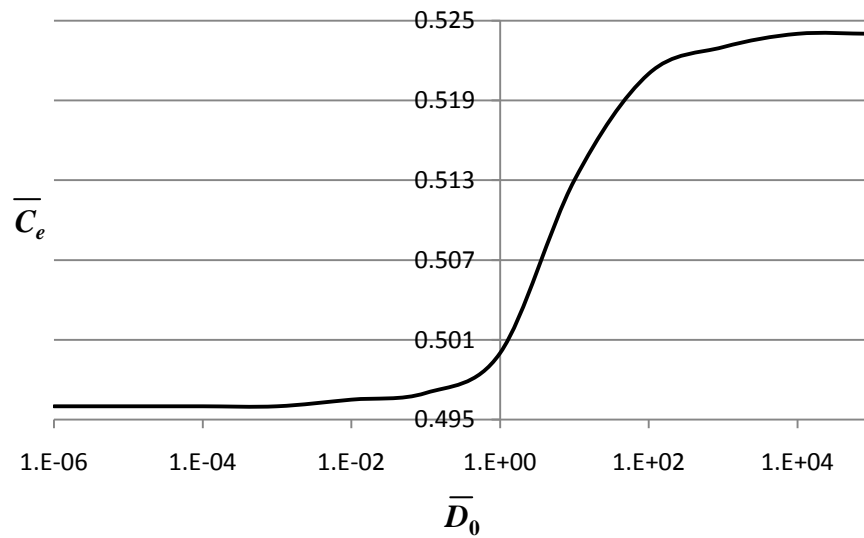


(c) $\bar{k}_1 = 0.1, \bar{t} = 3.94$.

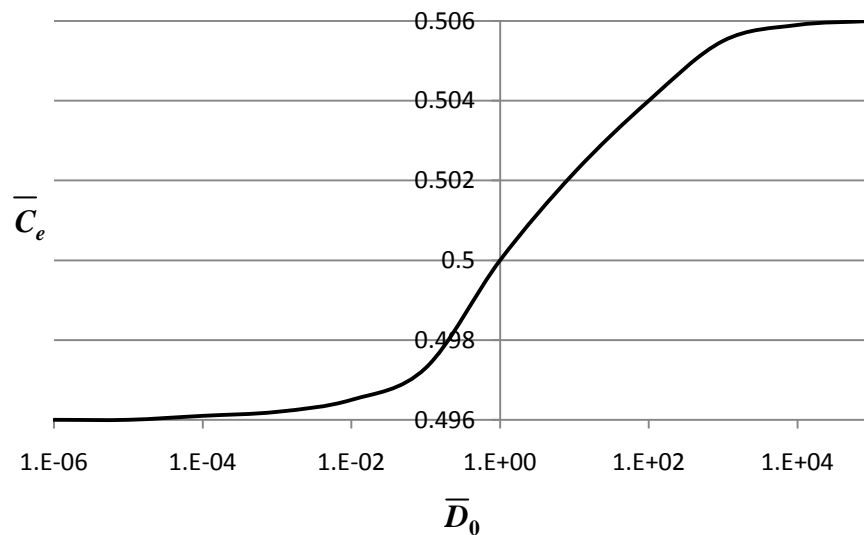


(d) $\bar{k}_1 = 1, \bar{t} = 0.58$.

**CHAPTER 2 GOVERNING EQUATIONS FOR BIODEGRADATION AND
BIODEGRADATION MECHANISM MAPS**



(e) $\bar{k}_1 = 10, \bar{t} = 0.07$.



(f) $\bar{k}_1 = 50, \bar{t} = 0.014$.

Figure 2.4.1 Effect of normalised diffusion coefficient of the monomers on the ester bond concentration averaged over the sample volume that remains in the sample at a fixed time of degradation; the five sub-figures show the calculation for (a) $\bar{k}_1 = 0.001$, (b) $\bar{k}_1 = 0.01$, (c) $\bar{k}_1 = 0.1$, (d) $\bar{k}_1 = 1$, (e) $\bar{k}_1 = 10$, (f) $\bar{k}_1 = 50$.

The series of figures above (figure 2.4.1 (a)-(e)) shows that for every fixed \bar{k}_1 value, there always exists an upper limit and a lower limit for the normalised diffusion

**CHAPTER 2 GOVERNING EQUATIONS FOR BIODEGRADATION AND
BIODEGRADATION MECHANISM MAPS**

coefficient, beyond which the degradation is no longer controlled by \bar{D}_0 . The range of \bar{D}_0 in which \bar{C}_e is controlled by \bar{D}_0 is gradually reduced as \bar{k}_1 increases. The upper and lower limits converge to each other when \bar{k}_1 reaches a certain value as shown in figure 2.4.1 (f). Figure 2.4.1 (f) is considered as a ‘converging case’ because we take the difference of $\bar{C}_e < 1\%$ as a standard for judging convergence. All the limits in this series of cases have their correspondent values of \bar{k}_1 and \bar{D}_0 . These upper and lower diffusion limits can be plotted against \bar{k}_1 forming a biodegradation map, as shown by figure 2.4.2.

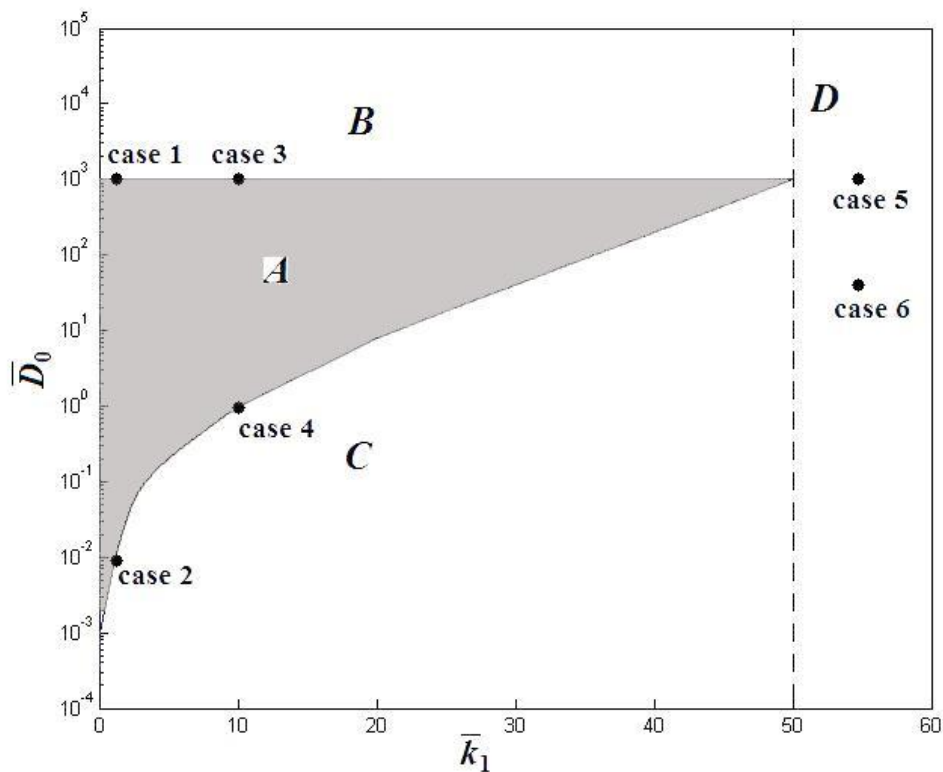


Figure 2.4.2 The biodegradation map for plate

The vertical axis is \bar{D}_0 in the log scale and the horizontal axis is \bar{k}_1 . There are four different zones on the map marked by A, B, C and D. Zone B is the fast diffusion zone where the polymer degradation is entirely controlled by the non-catalysed hydrolysis

($\bar{C}_m = 0$). Zone *C* is the slow diffusion zone where the degradation is controlled by the auto-catalysed hydrolysis ($\bar{C}_m = R$). Zone *D* ($\bar{C}_m = R = 0$) is the fast non-catalysed hydrolysis zone ($k_2 = 0$). Finally, zone *A* is where all three kinetic processes affect the degradation rate. Under the assumption of fast water penetration into the device, degradation in zones *C*, *B* and *D* is spatially uniform and there is no need to solve the partial differential equation (2.3.12) and (2.3.13). For zones *B* and *D* equations (2.3.12) and (2.3.13) become:

$$\begin{aligned}\bar{C}_e &= e^{-\bar{k}_1 t} \\ \bar{C}_m &= 0\end{aligned}\tag{2.4.1}$$

For zone *C*, equations (2.3.12) and (2.3.13) become:

$$\begin{aligned}\frac{d\bar{C}_m}{d\bar{t}} &= \bar{k}_1 \bar{C}_e + \bar{C}_e \bar{C}_m^n \\ \frac{d\bar{C}_e}{d\bar{t}} &= -(\bar{k}_1 \bar{C}_e + \bar{C}_e \bar{C}_m^n)\end{aligned}\tag{2.4.2}$$

Under these conditions the device geometry and dimensions have no effect on the degradation and one can simply apply equation (2.4.1) or (2.4.2) to obtain the degradation rate. Only when parameters fall in zone *A* do the equations (2.3.12) and (2.3.13) need to be solved simultaneously.

The degradation map is immediately useful for the design of biodegradation experiments. For example, all the experimental data collected by Tsuji (2000, 2002; Tsuji and Muramatsu, 2001; Tsuji and Ikarashi, 2004; Tsuji and Ikada, 2000) despite being extremely valuable, are within zone *B* as very thin specimens were used in these experiments. Consequently these experiments alone provided no information on the auto-catalysed reaction and diffusion. Data in zone *C* have to be collected to characterise the auto-catalysed degradation and data in zone *A* are needed to determine

**CHAPTER 2 GOVERNING EQUATIONS FOR BIODEGRADATION AND
BIODEGRADATION MECHANISM MAPS**

the diffusion coefficient. It is important to recognise that \bar{D}_0 can be varied to a wide range by changing the thickness of the sample (see equation (2.3.11)) for the same material.

The case points shown on the two boundaries separating zone *A*, *B* and *C* on the degradation map in figure 2.4.2 can be illustrated using the degradation figures 2.4.3 to 2.4.5).

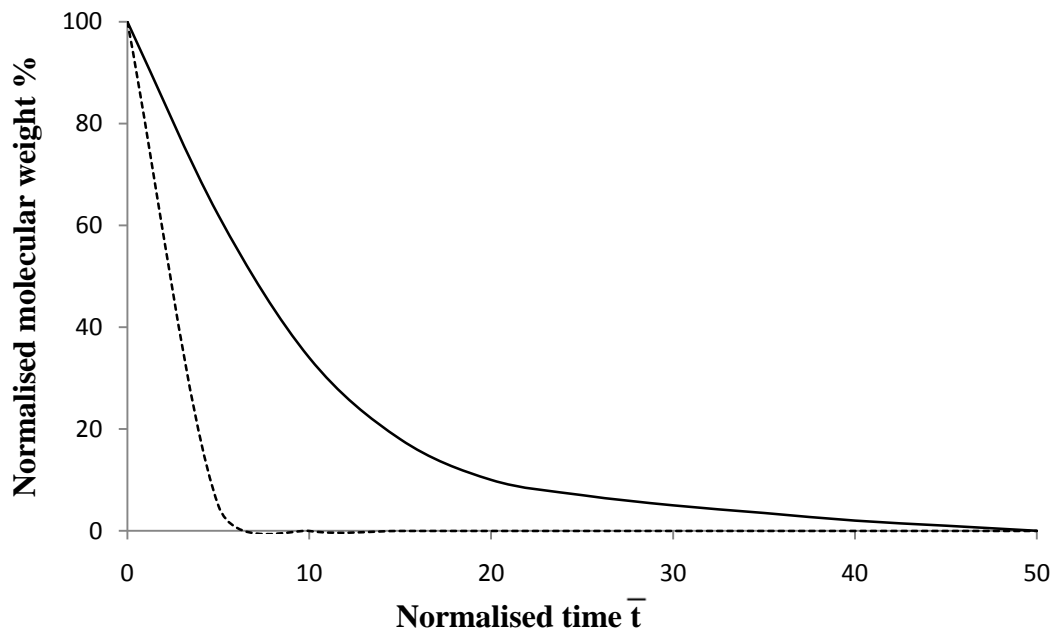


Figure 2.4.3 Cases 1 (upper line) and 2 (lower line), $\bar{k}_1 = 0.1$.

CHAPTER 2 GOVERNING EQUATIONS FOR BIODEGRADATION AND
BIODEGRADATION MECHANISM MAPS

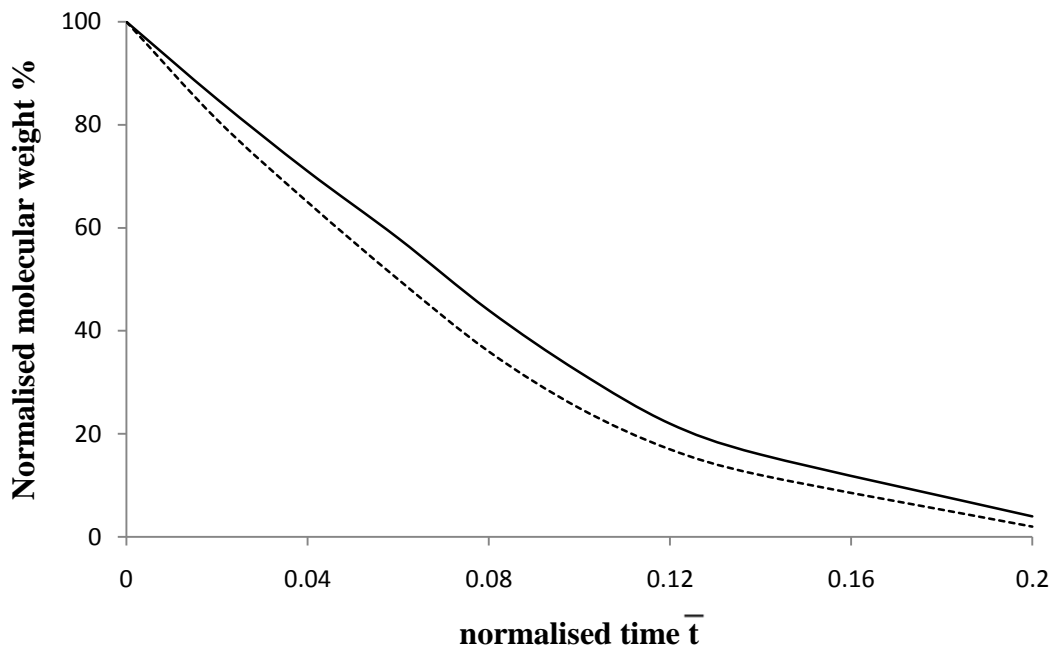


Figure 2.4.4 Cases 3 (upper line) and 4 (lower line), $\bar{k}_1 = 10$.

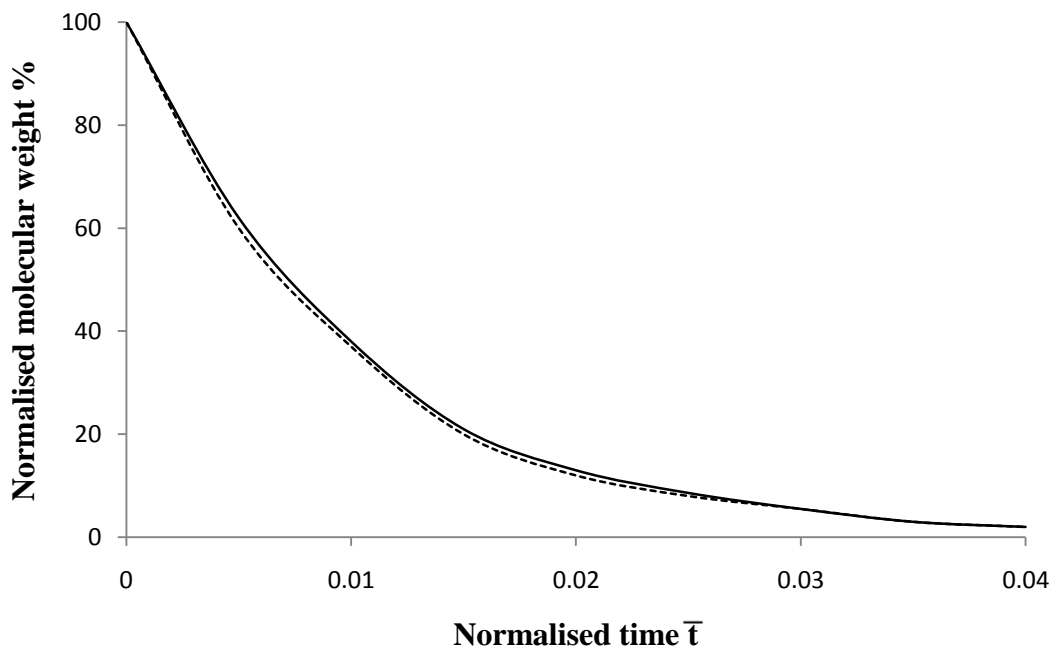


Figure 2.4.5 Cases 5 and 6, $\bar{k}_1 = 55$.

**CHAPTER 2 GOVERNING EQUATIONS FOR BIODEGRADATION AND
BIODEGRADATION MECHANISM MAPS**

All these cases are on either the fast or slow diffusion limit. Cases 1 and 2 share a low value of $\bar{k}_1 = 0.1$ as in figure 2.4.3. Because the degradation is dominated by the auto-catalysed hydrolysis, it can be observed from figure 2.4.3 that the diffusion rate has a major impact on the overall degradation rate. For cases 3 and 4 (figure 2.4.4) the non-catalysed hydrolysis is much faster than the auto-catalysed hydrolysis, i.e. $\bar{k}_1 = 10$. It can be seen from figure 2.4.4 that the impact of diffusion on the degradation rate is much less significant. Cases 5 and 6 have a high value of $\bar{k}_1 = 55$ (figure 2.4.5). It can be seen from figure 2.4.5 that diffusion has no effect at all on the degradation under this condition. It is interesting to observe that the fast diffusion limit (upper boundary) is independent of \bar{k}_1 . In fact, the numerical results did show a very weak dependence which was ignored when the map was constructed. To avoid confusion caused by too much information on the degradation map, a measure of the biodegradation rate is not presented. The biodegradation rate increases from the left to the right, and decreases from the bottom to the top. It is fastest toward the right bottom corner, and slowest toward the left upper corner. For a constant value of \bar{k}_1 , the difference between the degradation rates for different values of \bar{D}_0 is small if $\bar{k}_1 > 10$, as shown in figure 2.4.4, but only becomes completely negligible after $\bar{k}_1 > 50$, as shown in figure 2.4.5.

2.4.3 Biodegradation map for a solid cylinder

The biodegradation map changes if the shape of the device changes. To study the sensitivity of the degradation map to different geometry, the above analysis was repeated for an infinitively long and cylindrical pin. Owing to the axisymmetry of the problem, it can be solved as a one-dimensional problem. Similarly to the plate shape model, the spatial distribution of \bar{C}_e is obtained by solving the one-dimensional pin shape problem numerically then averaging over the entire geometry at these times. The spatially averaged \bar{C}_e will not change any further once the non-dimensional initial diffusion coefficient \bar{D}_0 reaches a value that is high or low enough. Similarly to the

**CHAPTER 2 GOVERNING EQUATIONS FOR BIODEGRADATION AND
BIODEGRADATION MECHANISM MAPS**

previous case, the higher diffusion limit and the lower diffusion limit are developing closer to each other as \bar{k}_1 increases, with a trend of convergence.

The biodegradation map for pin shape can be produced and it is similar to the biodegradation map for plate shapes, differing on its lower boundary and converging \bar{k}_1 point (figure 2.4.6).

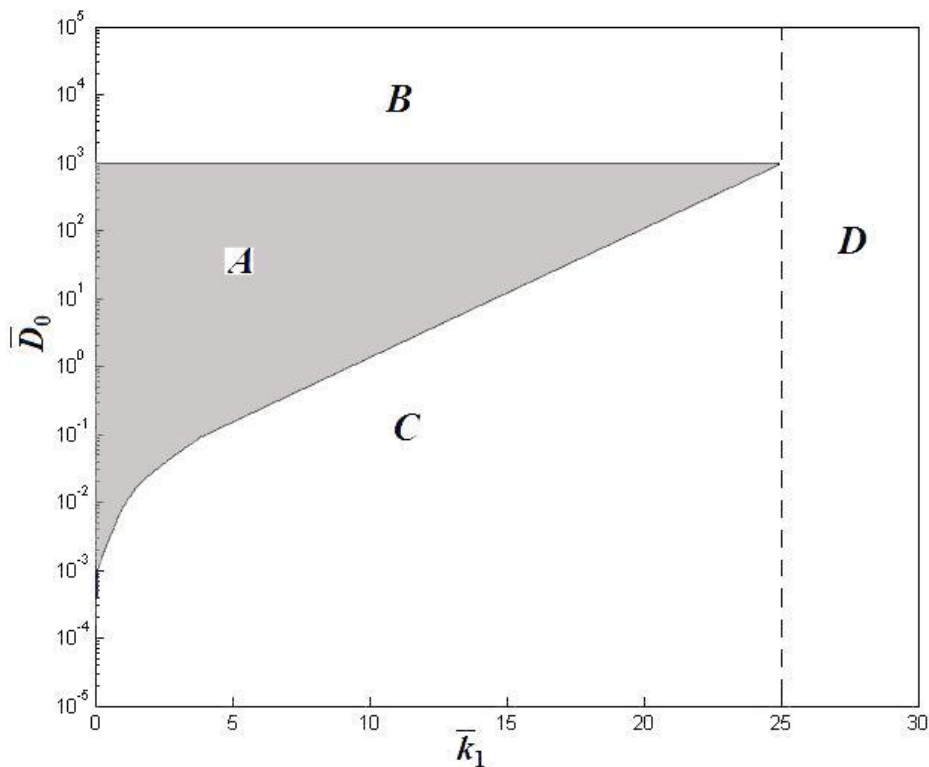


Figure 2.4.6 The biodegradation map for pin shapes.

The degradation map for pin shapes is shown in figure 2.4.6. The radius of the pin is used as the characteristic length in equations (2.3.10) and (2.3.11). Comparing the maps in figure 2.4.6 and figure 2.4.2, it can be seen that it is much easier for a pin to enter zone *D* than a plate, which means less help from the non-catalysed reaction is needed for a pin to have uniform degradation. This is simply because the pin has a larger contact area per unit volume of material with water than a plate does, which means a smaller \bar{C}_m inside the system would be observed compared with the plate shape

**CHAPTER 2 GOVERNING EQUATIONS FOR BIODEGRADATION AND
BIODEGRADATION MECHANISM MAPS**

material. So a relatively smaller \bar{k}_1 value is required to make the hydrolysis term dominant over the auto-catalysis. Again, the fast diffusion limit (the upper boundary) can be considered as independent of \bar{k}_1 .

2.4.4 Biodegradation map for plates using $n=2$

The biodegradation map for plates is re-calculated using $n=2$ which is shown in figure 2.4.7.

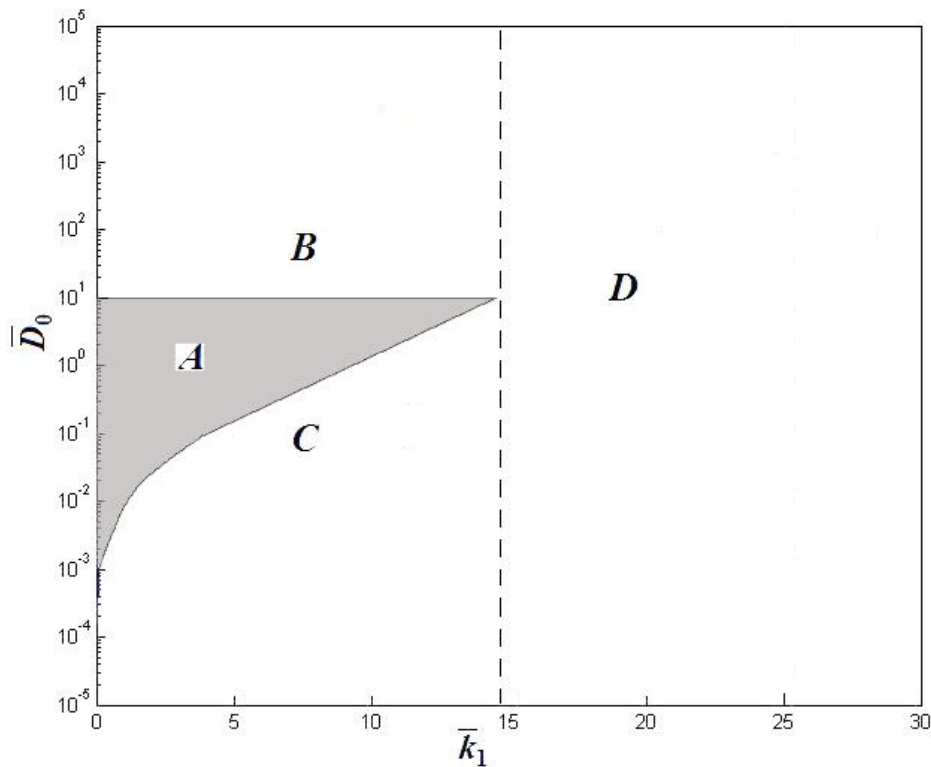


Figure 2.4.7 The biodegradation map for a plate shape; exponential parameter $n=2$.

The map in this case has a lower upper limit owing to a larger n value which makes the system more sensitive to the monomer concentration. In other words, any small loss in

**CHAPTER 2 GOVERNING EQUATIONS FOR BIODEGRADATION AND
BIODEGRADATION MECHANISM MAPS**

the monomer concentration would be amplified. As a result, it is easier for \bar{D}_0 to reach Zone B ($\bar{C}_m = 0$) so the upper bound of \bar{D}_0 is significantly lower compared with the biodegradation map for plates using $n=0.5$. Another difference in this case is that a smaller \bar{k}_1 is required for the device to enter Zone D ($\bar{C}_m = R = 0$). This is because \bar{C}_m , as a normalised variable, is always a value between zero and one; a higher order on \bar{C}_m in the reaction equation will make the auto-catalysis term smaller compared to the first case, with all other conditions remaining the same. Therefore a smaller \bar{k}_1 value is required to make the auto-catalysis term neglectable.

As seen in the three biodegradation maps, there are always a upper and lower limits of the diffusion coefficient above or below which the entire material will degrade uniformly and these two limits tend to converge when the hydrolysis-auto-catalysis ratio increases. The purpose of generating the biodegradation maps with four zones is to aid the design of the material. The different zones on the map represent the different degradation mechanisms of the biodegradable polymers and to satisfy specific requirements the materials have to be designed to fall into certain zones. The biodegradation maps will vary if the geometry or chemistry mechanism changes, in which case the biodegradation map has to be rebuilt.

2.5 The study of half degradation time

The maps in the previous section generate a clear picture of the degradation mechanisms. However, an important factor missing from the maps is the degradation rate, which is of course important because the design of a biodegradable device requires the degradation rate to be well understood. For a known geometry of the device, we can vary the values of \bar{k}_1 and \bar{D}_0 then calculate the ester bond concentration until its volume average reaches half of its initial value, i.e. we can calculate \bar{t}_{half}

corresponding to $\int_V \bar{C}_e dV = 0.5$ for different values of \bar{k}_1 and \bar{D}_0 . The half degradation time \bar{t}_{half} can then be used as an indicator for the degradation rate of a device.

2.5.1 Half degradation time for plates using $n=0.5$

Table 2.5.1 provide the values of \bar{t}_{half} calculated for plate with different combinations of \bar{k}_1 and \bar{D}_0 .

**CHAPTER 2 GOVERNING EQUATIONS FOR BIODEGRADATION AND
BIODEGRADATION MECHANISM MAPS**

**Table 2.5.1 The normalized half degradation time of various \bar{k}_1 \bar{D}_0 values for
plate shape using $n=0.5$**

$\bar{k}_1 \backslash \bar{D}_0$	0.001	0.01	0.1	1	10	50
10^{-6}	1.72	1.65	1.3	0.47	0.06	0.014
10^{-5}	1.72	1.65	1.3	0.47	0.06	0.014
10^{-4}	1.72	1.65	1.3	0.47	0.06	0.014
10^{-3}	1.74	1.67	1.31	0.47	0.06	0.014
0.01	1.79	1.73	1.34	0.48	0.06	0.014
0.1	2.07	2.02	1.55	0.49	0.06	0.014
1	25.7	15.25	3.94	0.58	0.06	0.014
10	157	41	5.78	0.67	0.07	0.014
100	396	60	6.6	0.71	0.07	0.014
1000	557	68	6.9	0.71	0.07	0.014
10^4	672	70	6.94	0.71	0.07	0.014
10^5	696	70	6.95	0.71	0.07	0.014

The highest value of \bar{t}_{half} occurs at the left bottom of table 2.5.1 where \bar{D}_0 is very large and \bar{k}_1 is very small. This is because very small hydrolysis autocatalysis ratio— \bar{k}_1 delays the initiation of degradation process significantly. The extreme case is when \bar{k}_1 equals to zero for which the degradation process would never start. On the other hand, very large value of \bar{D}_0 eliminates all the catalyst in the system therefore leads to a low degradation rate. The peak value of \bar{t}_{half} reduces if either \bar{k}_1 increases or \bar{D}_0 decreases. As \bar{k}_1 increases, the hydrolysis generates monomers while the diffusivity of

**CHAPTER 2 GOVERNING EQUATIONS FOR BIODEGRADATION AND
BIODEGRADATION MECHANISM MAPS**

the system remains the same. As \bar{D}_0 decreases, more monomers accumulate inside the system to act as catalysts while the hydrolysis-auto-catalysis ratio is fixed. On the right hand side of this table, the half degradation time reaches its minimum value. This value reduces even further as \bar{k}_1 increases while \bar{D}_0 has little impact on it. The reason for this is that the high \bar{k}_1 can see the plate to enter zone D in figure 2.4.2. In this case, according to equation (2.4.1), the decrease of the polymer concentration \bar{C}_e is exponential to the product of time and \bar{k}_1 , and \bar{t}_{half} can be calculated as

$$\bar{t}_{half} = -\ln 0.5 / \bar{k}_1 \quad (2.5.1)$$

2.5.2 Half degradation times for cylindrical pins

To test the effect of device shape on the degradation rate, the calculations of \bar{t}_{half} are repeated for cylindrical pins. The results are listed in table 2.5.2.

**CHAPTER 2 GOVERNING EQUATIONS FOR BIODEGRADATION AND
BIODEGRADATION MECHANISM MAPS**

**Table 2.5.2 The normalized half degradation time of various \bar{k}_1 \bar{D}_0 values for pin
shape using $n=0.5$**

$\bar{D}_0 \backslash \bar{k}_1$	0.001	0.01	0.1	1	10	25
10^{-6}	1.72	1.65	1.32	0.47	0.066	0.028
10^{-5}	1.72	1.65	1.32	0.47	0.066	0.028
10^{-4}	1.73	1.66	1.32	0.47	0.066	0.028
0.001	1.76	1.7	1.33	0.47	0.066	0.028
0.01	1.9	1.83	1.42	0.48	0.066	0.028
0.1	6.2	5.1	2.4	0.53	0.067	0.028
1	62	25.4	4.98	0.62	0.067	0.028
10	250	50.5	6.4	0.69	0.069	0.028
100	505	64.5	7.04	0.71	0.071	0.028
1000	646	70.2	7.16	0.71	0.071	0.028
10^4	680	71.6	7.22	0.71	0.071	0.028
10^5	710	71.6	7.22	0.71	0.071	0.028

Comparing table 2.5.2 with table 2.5.1, it can be observed that the half degradation times, similar to those results for plate shape, have the highest value when \bar{k}_1 is small and \bar{D}_0 is large. No difference between the half degradation times for these two geometries is found when either \bar{k}_1 or \bar{D}_0 is large. The reason for is because the shape difference is represented by the diffusion term in equation (2.3.12) and (2.3.13); large \bar{D}_0 or \bar{k}_1 eliminates the impact of the device shape. When \bar{k}_1 and \bar{D}_0 are both

**CHAPTER 2 GOVERNING EQUATIONS FOR BIODEGRADATION AND
BIODEGRADATION MECHANISM MAPS**

relatively small, the half degradation times for the pin shape are smaller than those for the plates. This is because the pin geometry has a large boundary per unit area compared to the plate; correspondingly it is always easier for the monomers in pin shape system to diffuse out. Therefore the time for pins to degrade half of its initial polymer concentration is always longer than those for plates.

2.5.3 Half degradation times of plates using $n=2$

Table 2.5.3 presents the half degradation time for plates calculated using $n=2$.

**CHAPTER 2 GOVERNING EQUATIONS FOR BIODEGRADATION AND
BIODEGRADATION MECHANISM MAPS**

**Table 2.5.3 The normalized half degradation time of various \bar{k}_1 \bar{D}_0 values for
plate using $n=2$**

$\bar{k}_1 \backslash \bar{D}_0$	0.001	0.01	0.1	1	10	15
10^{-7}	47.8	14.8	4	0.63	0.068	0.046
10^{-6}	50.4	14.8	4	0.63	0.068	0.046
10^{-5}	50.5	15.8	4	0.64	0.068	0.046
10^{-4}	50.8	15.8	4.1	0.64	0.068	0.046
0.001	52.4	16.3	4.2	0.64	0.069	0.046
0.01	71	18.9	4.6	0.65	0.069	0.046
0.1	705	70	6.7	0.66	0.069	0.046
1	705	71	7	0.69	0.069	0.046
10	705	71	7.1	0.7	0.007	0.046
100	705	71	7.1	0.7	0.007	0.046
1000	705	71	7.1	0.7	0.071	0.046
10^4	705	71	7.1	0.7	0.071	0.046

Similarly to the previous two cases, the half degradation times in this case have the highest value when \bar{k}_1 is small and \bar{D}_0 is large. Again, very little difference between the half degradation tables is found when either \bar{k}_1 is large or \bar{D}_0 is large. In this case, the half degradation times can be calculated as equation (2.5.1) without any influence from the shape or the exponent n . Apart from those half degradation times that can be calculated directly, other half degradation times for $n=2$ are longer than those for $n=0.5$. This is because monomer concentration in the calculation is a normalised value that

**CHAPTER 2 GOVERNING EQUATIONS FOR BIODEGRADATION AND
BIODEGRADATION MECHANISM MAPS**

varies from 0 to 1, the large exponent reduces the absolute value of this term therefore delays the degradation for the entire system for $n=2$.

The half degradation time is a good indicator that is helpful in device design. As shown in Tables 2.5.1 to 2.5.3, the degradation time are affected significantly by \bar{k}_1 , \bar{D}_0 and the exponential parameter n . The degradation time becomes independent of \bar{D}_0 and n when (a) the diffusion is fast or (b) the hydrolysis auto-catalysis ratio is small. Under these circumstances, \bar{t}_{half} can be calculated as equation (2.5.1)

2.6 Concluding remarks

The biodegradation of biodegradable polymers is affected by a wide range of factors including chemical composition, molecular structure, morphology and processing conditions of the polymers. Correlating the degradation rate with all these factors in a quantitative way seems to be a formidable task. This chapter shows, however, that it is possible to develop a phenomenological framework based on the existing understanding of the biodegradation mechanisms. The phenomenological model can capture the key characteristics of the existing observations of the biodegradation. It is therefore a useful tool to guide the design of biodegradable devices. Discussion of the results of the calculation led to the degradation maps which can be used to guide the design of experiments to determine the material parameters required by the computer model. Half degradation time is a useful indicator for the degradation rate of the bioresorbable device that can be calculated numerically using the phenomenological model in general situations and using an analytical expression if the diffusion of the monomers in either extremely large or small.

Chapter 3 Effective Diffusion Coefficient of Monomers in a Degrading Polymer

3.1 Introduction

The effective diffusion coefficient for monomer diffusion in a degrading polymer is one of the controlling parameters in the mathematical model for biodegradation presented in the previous chapter. A biodegradable polymer becomes porous as a consequence of monomers diffusing out of the system. The porous structure will allow the monomer to escape at an even faster rate (Figure 3.1.1). The effective diffusion coefficient is therefore a strong function of the porosity (Siepmann *et al.*, 2002; Göpferich and Langer, 1995).

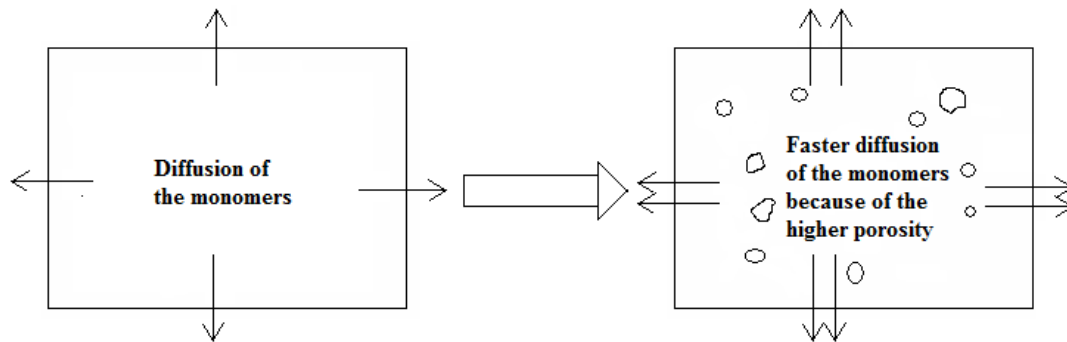


Figure 3.1.1 The effective diffusion coefficient is a function of the porosity.

Because the degradation process takes place randomly within the material and further degradation produces heterogeneous structures at both macro and micro levels in the system, the effective diffusion coefficient is not straight forward to obtain. In order to calculate monomer diffusion in a degrading polymer, two approaches can be used. The first one is to generate a large finite element model using many elements which are so finely meshed to directly calculate monomer diffusion considering the actual micro structures throughout the material. The second one, which is taken in this thesis, is to

avoid the formidable computing task by firstly obtaining an effective diffusion coefficient for a representative unit of the material (figure 3.1.2) and then use it as the diffusion coefficient for the entire domain in the diffusion-reaction model.

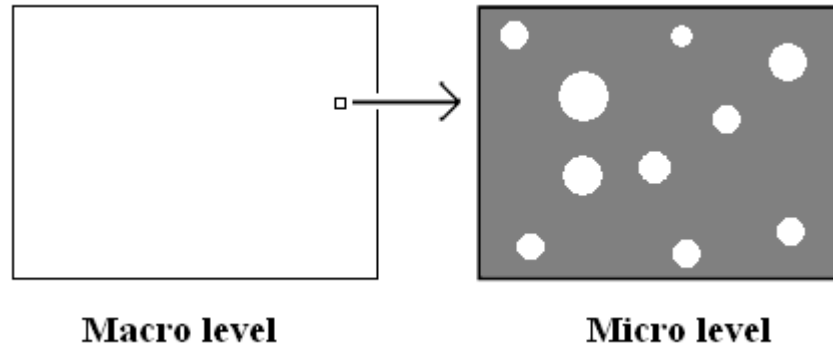


Figure 3.1.2 Scheme of multi-scale modelling.

In the calculation, a representative element of the material, typically a three-dimensional cube or a two-dimensional square is considered. The dark grey colour represents the polymer matrix while white circles denote the pores. This chapter presents numerical studies on the relationship between the effective diffusion coefficient and the structure of the pores as well as the porosity. Our particular attention is paid to the circumstances under which porosity cannot be used as the only controlling factor for the monomer diffusion.

3.2 A review of the literature

One of the areas that has a major interest in the effective diffusion coefficient of the biodegradable polymers is controlled drug release because (a) the tablet coating or matrix are often made of biodegradable polymers and (b) the effective diffusion coefficient affects the amount of the drug released over time. Faisant *et al.* (2002) suggests that the effective diffusion coefficient depends on the weight average molecular weight M_w in the following manner:

$$D(M_w) = D_0 + \frac{k}{M_w} \quad (3.2.1)$$

where D_0 is the initial diffusion coefficient of the drug in undegraded polymer, k is a constant, and

$$M_w(t) = 78.4 \exp(-k_{\text{deg},r} t) \quad (3.2.2)$$

where $k_{\text{deg},r}$ is the pseudo first order degradation rate of the polymer. Similarly, Charlier *et al.* (2000), considered the polymer degradation and drug diffusion. Under the assumption that the polymer chain cleavage follows a first order kinetics that the effective diffusion coefficient is proportional to the inverse of the polymer molecular weight, they obtain that:

$$D = D_0 \exp(kt) \quad (3.2.3)$$

where D_0 is the initial diffusion coefficient of the drug prior to polymer degradation; and k is the degradation rate. Joshi and Himmelstein (1991) established a comprehensive reaction-diffusion-transport model and suggested that the diffusion coefficient is an exponential function of the polymer concentration:

$$D_i = D_i^0 \exp\left(\frac{\mu(C_D^0 - C_D)}{C_D^0}\right) \quad (3.2.4)$$

in which D_i and D_i^0 are the diffusion coefficients of either water, acid or drug at any time and $t=0$ respectively, C_D^0 and C_D are the concentrations of polymer material at $t=0$ and any other time respectively, and μ is a constant. In order to calculate drug release from PLGA based micro-particles, Raman *et al.* (2005) applied Fick's second law for spherical geometry:

$$\frac{\partial C}{\partial t} = \frac{1}{r^2} \frac{\partial}{\partial r} \left(r^2 D(M_w) \frac{\partial C}{\partial r} \right) \quad (3.2.5)$$

where C is the concentration of the drug, t is time, r the radial coordinate and $D(M_w)$ is the drug diffusivity which is taken as a function of the weight average molecular weight (measured from experiment) given by:

$$\ln D = -0.347(\ln M_w)^3 + 10.394(\ln M_w)^2 - 104.95(\ln M_w) + 316.95. \quad (3.2.6)$$

Siepmann *et al.* (2002) and Göpfreich and Langer (1995) suggested that the effective diffusion coefficient can be considered as linearly proportional to the porosity as discussed in Chapter 2

3.3 Methods of calculating the effective diffusion coefficient for a representative unit

3.3.1 Direct calculation using a finite element model

Considering one unit volume of a biodegradable material, as shown in figure 3.3.1, the diffusion coefficient of the material at any time during the degradation can be calculated by applying two fixed concentrations at both horizontal boundaries respectively while the two vertical boundaries are kept under insulation condition. A horizontal flux will be generated in the material as a consequence of the concentration difference.

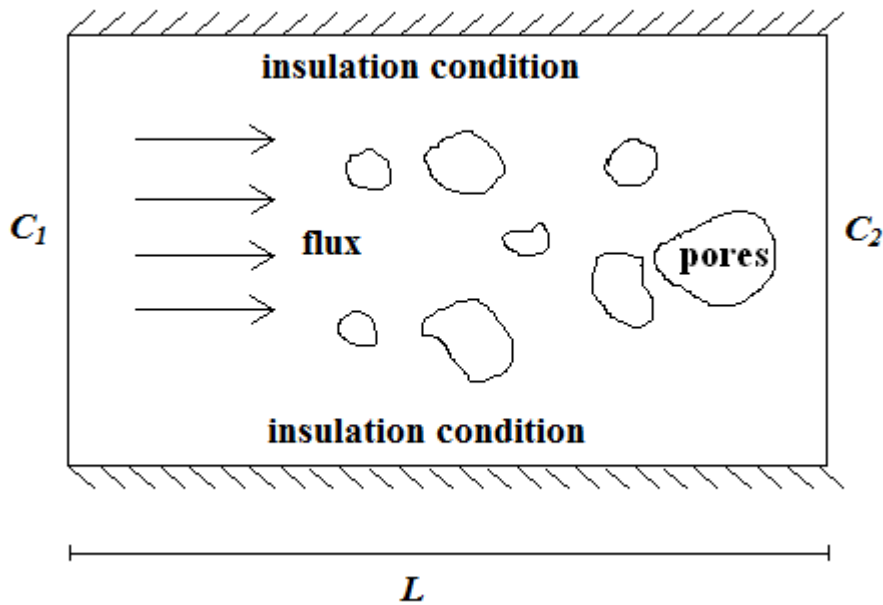


Figure 3.3.1 A scheme of the calculation of the effective diffusion coefficient.

Fick's first law suggests that

$$J = -D \frac{\partial C}{\partial x} \quad (3.3.1)$$

where J is the diffusion flux, x is the horizontal coordinate, C is the concentration and D is the diffusion coefficient.

We refer to the diffusion coefficient of the material for the polymer matrix (undegraded polymer) as D_0 , and assume that the diffusion rate inside the liquid-filled pore is much larger than D_0 . In our calculation it is assumed that $D_{pore} = 100D_0$ throughout the rest of this chapter unless stated otherwise. The finite element method is used to calculate the effective diffusion coefficient using the following steps:

1. Define the pore geometry within the system including pore shapes and sizes.
2. Apply appropriate boundary conditions: insulation condition on the top and bottom boundaries and concentration conditions on the left and right boundaries.

3. Calculate the concentration field until a steady state is reached.
4. Integrate the flux J on either the left or right boundary.
5. Calculate the effective diffusion coefficient according to:

$$D_{eff} = \frac{\int J dy}{(C_2 - C_1)/L} \quad (3.3.2)$$

3.3.2 Using the homogenization technique

Alternatively, to calculate the effective property of a material, a so called homogenization technique can be used (Nguyen *et al.*, 2005; Hassani and Hinton, 1998^a; Hassani and Hinton, 1998^b). The technique has been used to evaluate the effective material properties of composite materials such as effective Young's Modulus, effective diffusion coefficient, effective heat conductivity and so on. The main idea of the method is to replace the original material with an equivalent material that consists of a large number of identical representative units (as shown in figure 3.3.2). The coordinates of the macroscopic and microscopic material are referred to as $x_i (i = 1,2,3)$ and $y_i (i = 1,2,3)$, respectively.

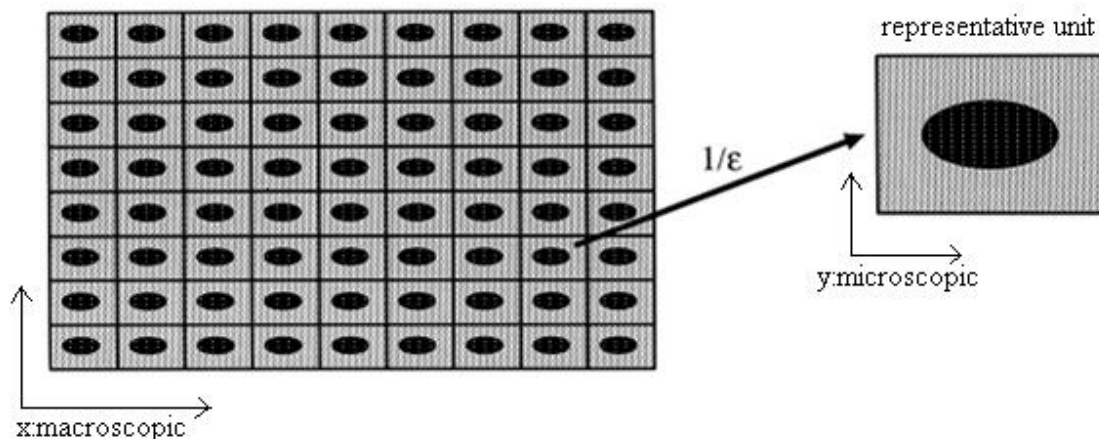


Figure 3.3.2 The idea of homogenization technique.

ϵ shown in the figure is always a small value that represents the ratio between the unit cell and the macroscopic dimension of the material, i.e.

$$\varepsilon = \frac{x}{y}$$

For diffusion problems which follow Fick's Second Law, we have, using tensor notation,

$$\frac{\partial}{\partial x_i} (D_{ij} \frac{\partial C}{\partial x_j}) = \frac{\partial C}{\partial t} \quad (3.3.3)$$

Its equivalent weak form is:

$$\int_V \frac{\partial \delta C}{\partial x_i} D_{ij} \frac{\partial C}{\partial x_j} dV = \int_V \delta C \frac{\partial C}{\partial t} dV \quad (3.3.4)$$

Using the following asymptotic expansion for the concentration field C :

$$C(x, y, t) = C_0(x, y, t) + \varepsilon C_1(x, y, t) + \varepsilon^2 C_2(x, y, t) + \dots \quad (3.3.5)$$

together with the fact that:

$$\frac{\partial}{\partial x} \phi(x, y = \frac{x}{\varepsilon}) = \frac{\partial \phi}{\partial x} + \frac{1}{\varepsilon} \frac{\partial \phi}{\partial y} \quad (3.3.6)$$

and by comparing the same order of the ratio ε , it can be shown that the following expression is valid (Nguyen *et al.*, 2005; Hassani and Hinton, 1998^a; Hassani and Hinton, 1998^b):

$$\int_V \delta_{ij} D_{ij} \frac{\partial \delta C}{\partial x_i} (\delta_{kj} - \frac{\partial \chi_k(x, y)}{\partial y_j}) \frac{\partial C_0}{\partial x_k} dV = \int_V \delta C \frac{\partial C_0}{\partial t} dV \quad (3.3.7)$$

in which δ_{ij} is the Kronecker delta. Therefore the effective diffusion coefficient can be defined as

$$D_{jk}^{eff} = \frac{1}{|V|} \int_V \delta_{ij} D_{ij} \left(\delta_{kj} - \frac{\partial \chi_k(x, y)}{\partial y_j} \right) dV \quad (3.3.8)$$

in which the vectorial field $\chi_i (i=1,2,3)$ is the solution of the following equation associated with a periodic boundary condition (Nguyen *et al.*, 2005; Hassani and Hinton, 1998^a; Hassani and Hinton, 1998^b):

$$\int_V D_{ij} \frac{\partial \delta C}{\partial y_i} \frac{\partial \chi_k(x, y)}{\partial y_j} dV = \int_V D_{ij} \frac{\partial \delta C}{\partial y_i} dV. \quad (3.3.9)$$

A numerical case is presented to show the results obtained using the direct calculation and the homogenization technique respectively. We consider a piece of material that has an isotropic diffusion coefficient $D_{11}=D_{22}=D_0$, and a non-symmetric pore which has the diffusion coefficient of $100D_0$ as shown in figure 3.3.3. The strange non-symmetric pore shape is used here to highlight the difference between the direct calculation and the homogenization technique. Firstly the concentration field obtained by the direct FE calculation is shown in figure 3.3.3.

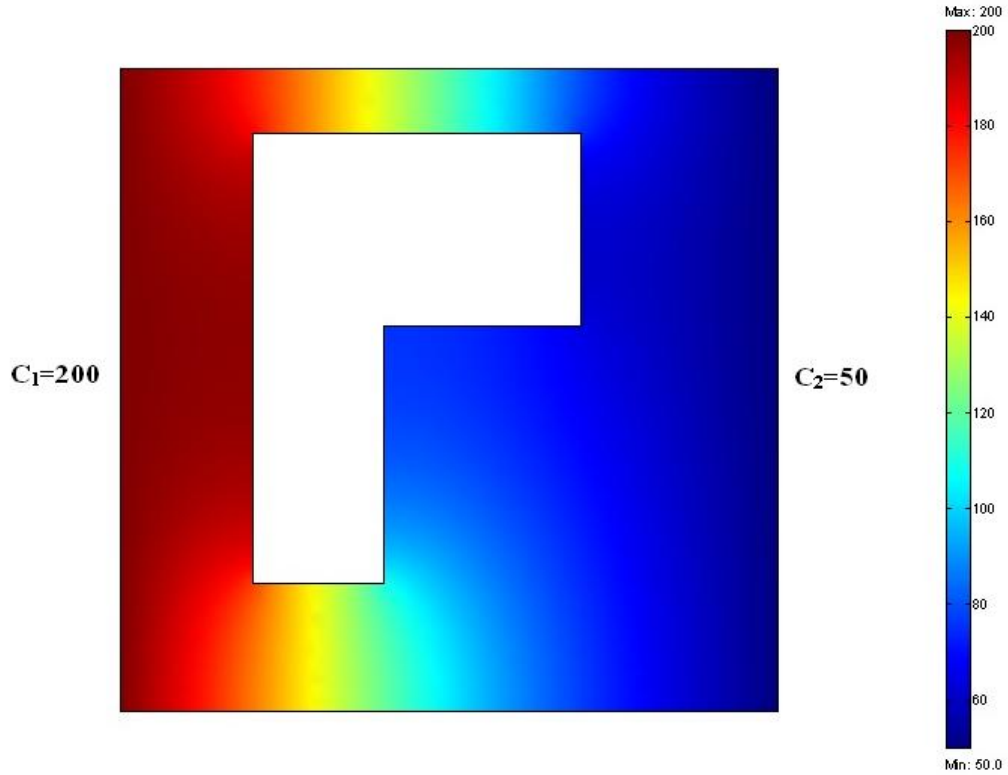


Figure 3.3.3 Concentration field using FE method.

Two concentrations of $C_1=200$ and $C_2=50$ are applied on the left and right boundaries. The figure shows the concentration field at the steady state, in which the red colour indicates higher value of C while the blue colour indicates lower value. The concentration difference generates a flux field from the left to the right. Integrating the flux field over the left boundary we obtain a total horizontal flux which is defined as:

$$-\int_{\partial\Omega} D \frac{\partial C}{\partial x} d\partial\Omega = J_{total}. \quad (3.3.10)$$

In general we have

$$J_{total} = -(D_{11}^{eff} \frac{\partial C}{\partial x} + D_{12}^{eff} \frac{\partial C}{\partial y}). \quad (3.3.11)$$

Therefore the horizontal flux also depends on the gradient of the concentration in the vertical direction. From the finite element results, it is found that the ratio between $\frac{\partial C}{\partial y}$ and $\frac{\partial C}{\partial x}$ is about 1:200, therefore the second item in the equation (3.3.11) is dropped and the effective diffusion coefficient in the horizontal direction, D_{11}^{eff} , is obtained as $0.449697D_0$.

Alternatively using the homogenization technique we have

$$D_{11}^{eff} = D_0 \int_{\Omega} \left(1 + \frac{\partial \chi_1}{\partial x}\right) d\Omega \quad (3.3.12)$$

in which the field χ_1 is obtained by solving equation (3.3.9) on the same geometry with periodic boundary conditions for the two sets of opposite boundaries. The field is shown in figure 3.3.4. The horizontal effective diffusion coefficient for this case is calculated as $0.462045D_0$ using equation (3.3.12).

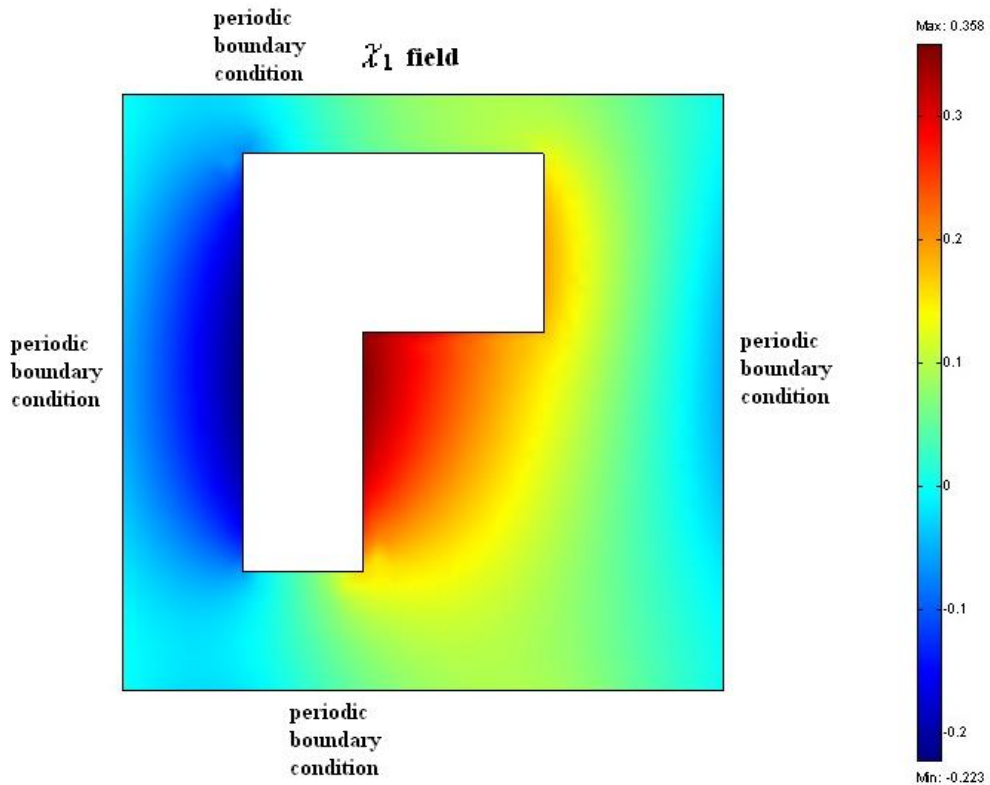


Figure 3.3.4 The field of χ_1 obtained by solving equation (3.3.9).

The homogenization technique can always provide the correct effective property of the material while the accuracy of the direct calculation depends on whether the imposed boundary conditions are correct or not. For example, the top and the bottom boundaries of the representative unit should not be treated as insulating boundaries in general. However, as demonstrated in this numerical case study, the difference between the two results is small. The direct method is much more convenient to use especially when dealing with three dimensional problems. In this work, the direct method will be adopted.

3.4 Case studies of the effective diffusion coefficient

The study of the effective diffusion coefficient of a representative unit can be generally categorized into two scenarios: (a) the pores are mostly isolated from each other; and (b) the pores are mostly connected and some of them form tunnels connecting the inner part of the material to the outside environment. For the first case, the effective diffusion coefficient depends on the porosity and the distribution of the pores while for the second case once a tunnel is formed the diffusion of the monomers will be considerably faster and the effective diffusion coefficient can be controlled by a combination of the tunnelling effect and the pore size.

3.4.1 Effective diffusion coefficient in polymers containing randomly distributed pores

Recently, a pure random case study is undertaken by Jiang and Pan (2008) using a 3-dimensional cubic representative unit as shown in figure 3.4.1. The representative unit is modelled using cubic finite elements as shown in the figure. The white cubic elements represents the polymer matrix with the diffusion coefficient of D_0 while the black elements are randomly generated “pores” which are assigned a diffusion

coefficient of $1000D_0$. Effective diffusion coefficient is calculated using the finite element model for a range of values of total porosity

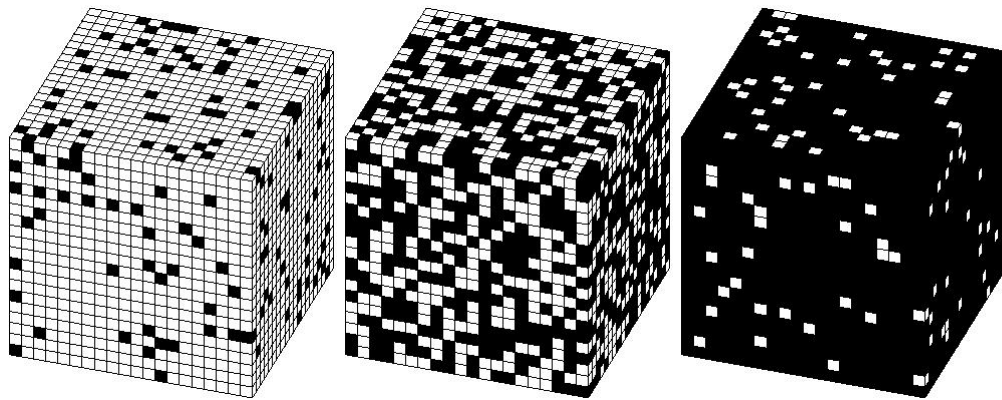


Figure 3.4.1 Finite element model of randomly generated pores by Jiang and Pan (2008).

Figure 3.4.2 shows the relative effective diffusion coefficient (normalized by D_0) of the above case as function of the porosity.

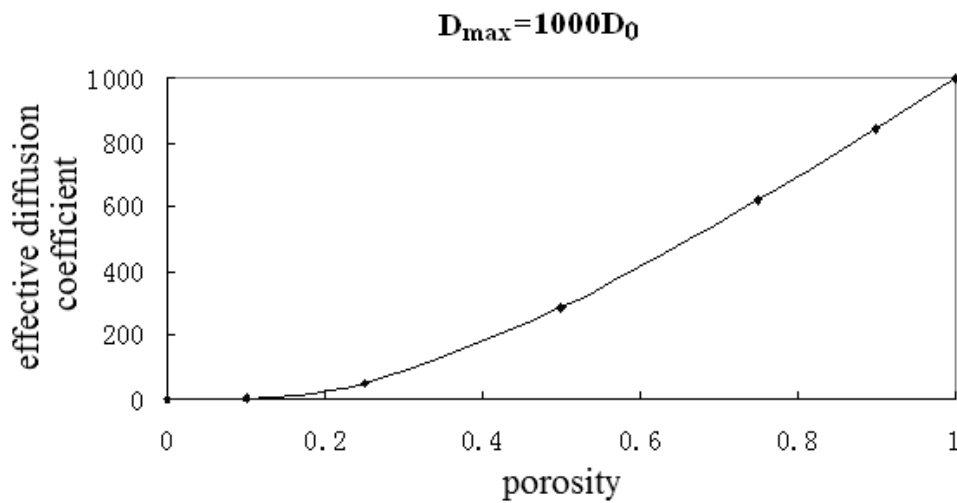


Figure 3.4.2 Effective diffusion coefficient versus the porosity for randomly generated pores.

The result demonstrates that the effective diffusion coefficient increases slowly with porosity when porosity is small and increase sharply after a critical porosity is reached. The sharp increase is due to the tunnelling effect as mentioned early. The location of the

“turning point” can be understood through a concept of percolation threshold in statistics which is demonstrated using the array of cells as shown in figure 3.4.3. The array is so large that any boundary effect is negligible once a certain fraction of the array is occupied. Any two cells inside the large array sharing a common side, e.g. cell A and cell B, will be named as nearest neighbor and any two cells which have only one point in contact, e.g. cell A and cell C, will be named as the next nearest neighbor. The percolation theory states that there is a critical value of the fraction of the grey cells, above which the occupied (grey) cells can percolate the array by the nearest neighbors therefore the grey cells are connected through their nearest neighbors (Stauffer and Aharony, 1994).

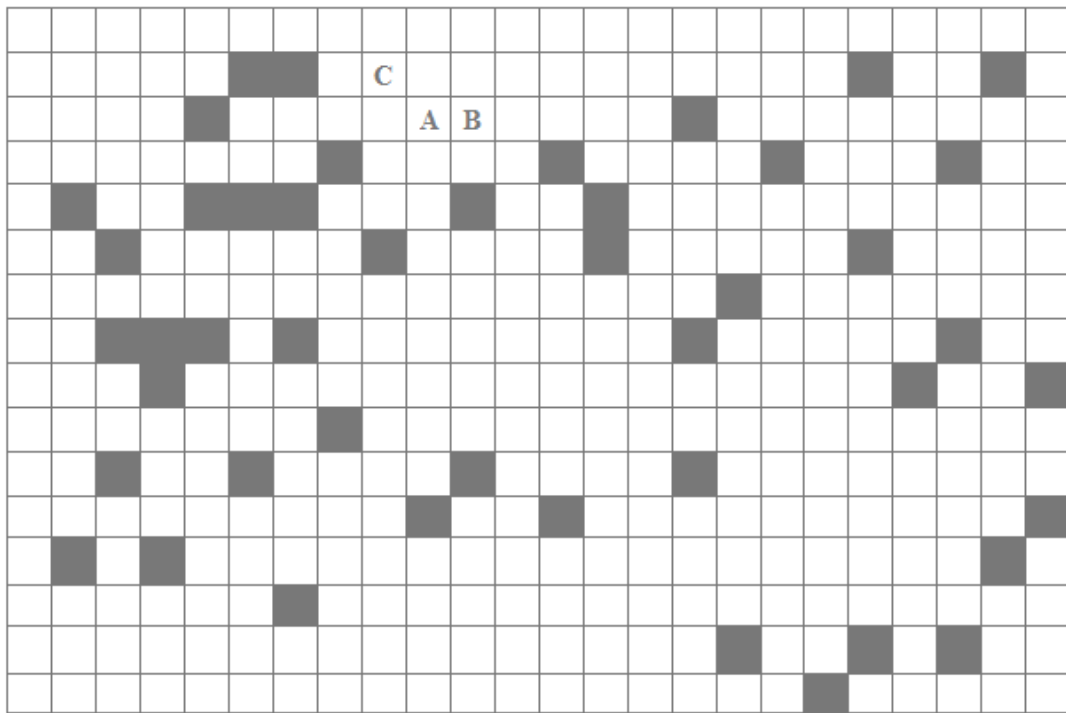


Figure 3.4.3 Demonstration of the percolation theory.

The threshold or, in another word, the critical fraction varies with the shape of the cells. In random simulation by Jiang and Pan (2008), the cell shape is selected as simple cubic for which the percolation theory predicts that the threshold value is 31.16% (Stauffer and Aharony, 1994). In other word, once this critical volume fraction of porosity is reached by degradation, the effective diffusion coefficient increases shapely. It can be

observed from Figure 3.4.2 that the percolation theory is consistent with the numerical prediction of Jiang and Pan (2008). Jiang and Pan (2008) fitted their numerical results to the following analytical expression:

$$D = D_0 \left[1 + (1.3V_{pore}^2 - 0.3V_{pore}^3) \left(\frac{D_{pore}}{D_0} - 1 \right) \right] \quad (3.4.1)$$

This equation is used in chapter two in the phenomenological model for biodegradation. It is however important to further study the conditions under which the expression is valid, which is the purpose of the following sections in this chapter.

3.4.2 Effective diffusion coefficient of polymers containing highly localized pores

A number of degradation experiments of the biodegradable polymers revealed that the pores generated during the degradation can be highly localized as shown in figure 3.4.4 (Cai *et al.*, 2003).

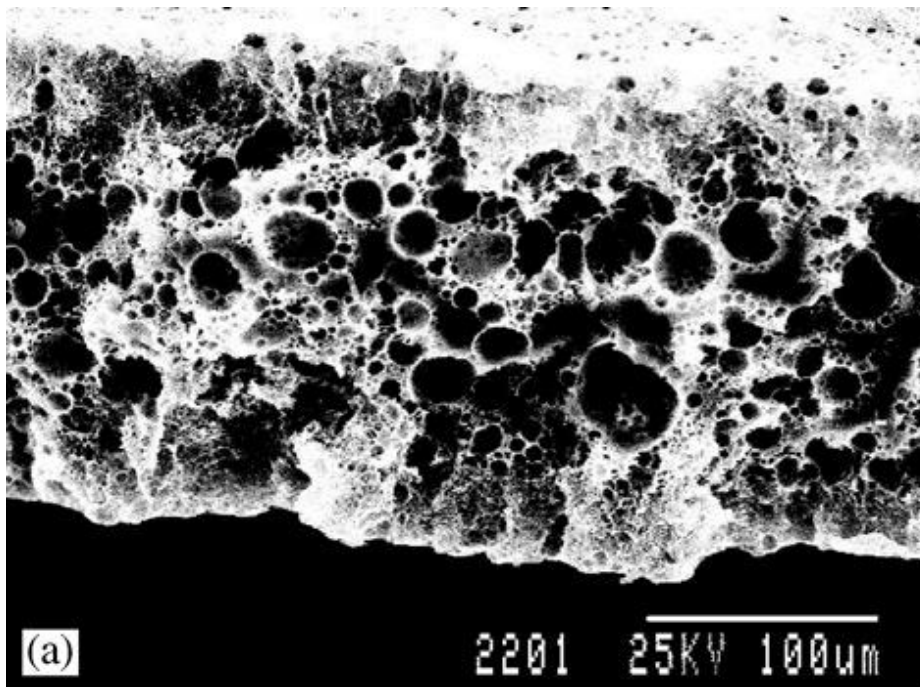


Figure 3.4.4 The highly localized pore structure (Cai *et al.*, 2003).

The image shows the cross section of a 0.2mm thick PLGA film after 2 weeks of degradation obtained using scanning electron microscope (SEM). The localized pore structure may be due to the autocatalytic effect in the hydrolysis reaction caused by the accumulated monomers. In that case, the porosity of the geometry increases owing to the self-expanding pore size rather than the formation of new pores. In this section, we focus on the spherical or circular pore structures to study the effective diffusion coefficient with respect to the total porosity, which is caused by the self expansion of the pore.

First we consider the effective diffusion coefficient for homogenous pore distribution; we start with a simple case of one spherical pore located at the centre of a three dimensional cubic representative unit of the material as shown by figure 3.4.5.

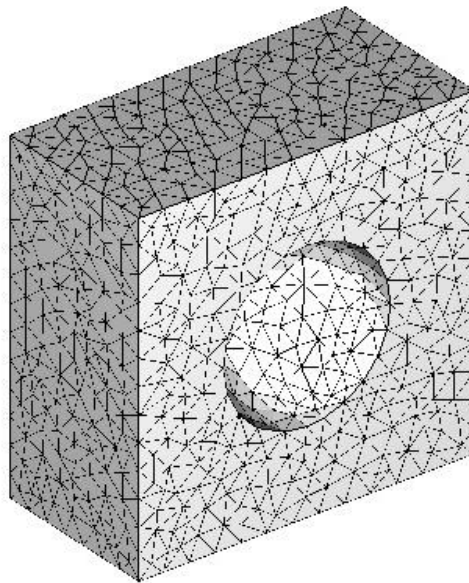


Figure 3.4.5 Cross section image of 3D representative unit with a central spherical pore.

The effective diffusion coefficient for this simple case is plotted in figure 3.4.6 with respect to porosity.

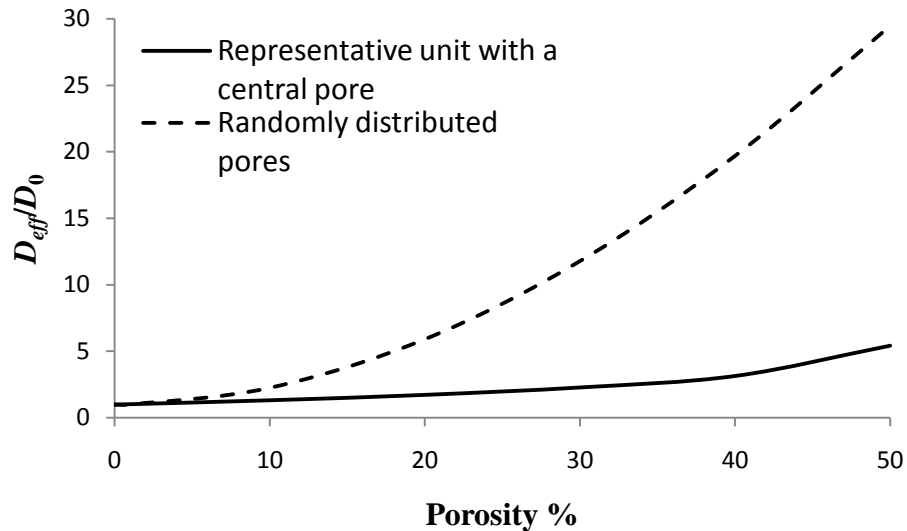


Figure 3.4.6 Effective diffusion coefficient versus porosity for a cubic representative unit of the polymer containing one spherical pore.

It can be observed that the diffusion coefficient and the porosity follows a roughly linear relationship at relative low porosity (<40%). The linear relationship is a very welcome simplification for the early stages of degradation. The empirical equation (3.4.1) for D obtained by Jiang and Pan (2008) is also included in figure 3.4.6 for comparison. It can be concluded that the effective diffusion coefficient for this simple model increases significantly slower than the random pore distribution case. Perhaps this is because Jiang and Pan (2008) take cubic as the shape of the pores which is easier to build connected structures, while the central pore geometry never percolated through the system.

The increase in the porosity may be accompanied by the localization of the pore structure, with the location of these pore structures randomly distributed. In other word, the formation of the pores may occur at any position at the early stage of degradation; once these pores are generated, the porosity increases by the self-expansion of these pores. Therefore, a very fine and uniform pore structure may not be obtained unless certain processing methodology is used (Nam and Park, 1999). To relate the effective diffusion coefficient to the self-expansion of randomly located pores, we used the following steps as illustrated in figure 3.4.7:

1. Divide the representative unit into a number of sub-domains, each containing a pore.
2. Allow each pore to make a random movement within their sub-domain.
3. Once the locations of the pores are “randomly” decided, calculate the effective diffusion coefficient for the entire domain.
4. Fix the locations of all the pores and increase their sizes. Update the FEM model and calculate the effective diffusion coefficient.
5. Repeat step 4 to obtain a series data for the effective diffusion coefficient with respect to porosity.

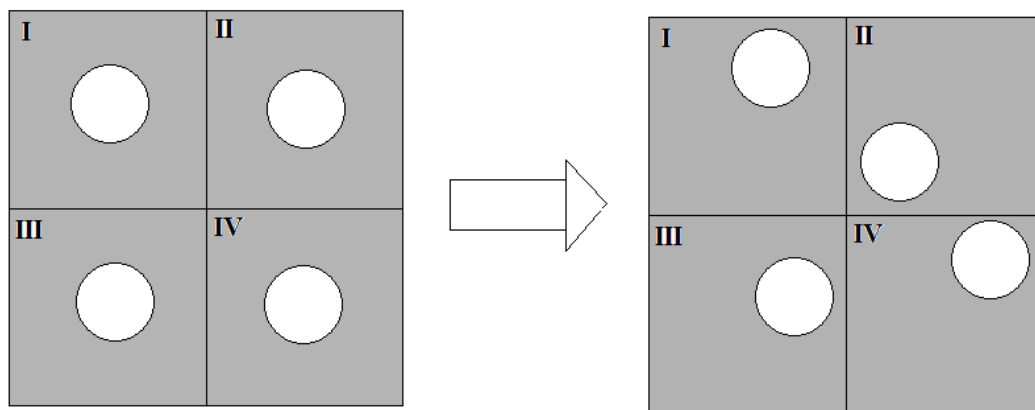


Figure 3.4.7 The scheme of the “sub-domain” of the system.

Actual calculations are executed on a 3D cubic unit with 8 spherical pores located in 8 sub-domains. Step 2 to 5 is repeated 10 times and 10 groups of the effective diffusion coefficients versus porosities are listed in table 3.4.1. The mean value of these ten groups of results is plotted (black solid line) in figure 3.4.8 showing the relative effective diffusion coefficient versus porosity. The numerical results shown in figure 3.4.8 that obtained using equation (3.4.1) are also plotted (dashed line) for a comparison.

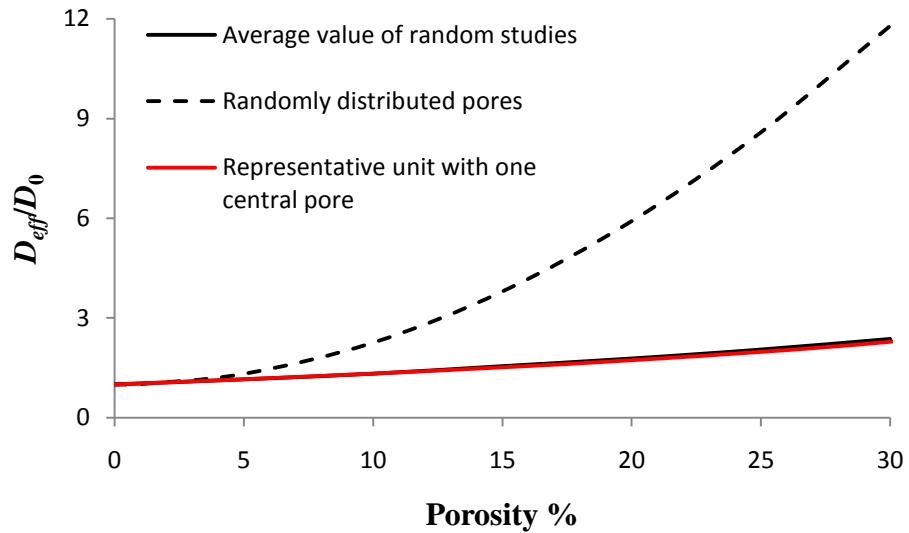


Figure 3.4.8 The average value of relative effective diffusion coefficient from 10 random cases compare to the effective diffusion coefficient from one central spherical pore.

Figure 3.4.8 shows that the simple model of a single expanding pore (red line) is in fact very good in comparison to the much more sophisticated model of randomly located self expanding pores. These results are however rather different from that obtained by Jiang and Pan (2008) in which pores are much more randomly generated.

Table 3.4.1 The 10 group of random distributed spherical pore structure and their effective diffusion coefficient's plot against the porosity.

porosity groups	1%	5%	10%	20%	30%
Group 1	1.0293	1.153	1.3237	1.743	2.392
Group 2	1.0294	1.1533	1.325	1.745	2.419
Group 3	1.0295	1.153	1.322	1.733	2.336
Group 4	1.0295	1.153	1.321	1.7247	2.2936
Group 5	1.0295	1.1533	1.323	1.736	2.36
Group 6	1.0297	1.154	1.325	1.752	2.45
Group 7	1.0294	1.153	1.3245	1.7444	2.403
Group 8	1.0294	1.153	1.321	1.729	2.338
Group 9	1.0294	1.153	1.328	1.737	2.304
Group 10	1.0294	1.153	1.323	1.742	2.384
Average	1.0294	1.1532	1.3236	1.7386	2.368

It can be observed in table 3.4.1 that the ten different groups of results corresponding to different pore locations are very similar to each other. From the numerical results, it can be conclude that for such porous structure, the effective diffusion coefficient can be related to the porosity in a linear relationship:

$$D_{eff} = D_0 + D_0 \cdot k \cdot V_{pore} \quad (3.4.2)$$

in which $k=4.5$ and V_{pore} represents the porosity, subject to the following conditions:

1. The pores are relatively uniformly distributed within the system.
2. The size of these pores is relatively close to each other.
3. The total porosity in the system is less than 40%.

3.4.3 The tunnelling effect

During the degradation process of a biodegradable polymer, sometimes cracks can be observed on the cross section of the material (figure 2.3.3) which implies that tunnels can be built during the degradation process. These cracks connect the cores inside the polymer to the surrounding environment and significantly enhance the diffusivity of the material. Figure 2.3.3 shows a PLLA implant inside the muscle of a rat after 80 weeks. The effective diffusion coefficient for this type of structure has to consider the short circuit effect of the tunnels. It is obvious that porosity is not the only factor that controls the diffusion of monomers in the polymer.

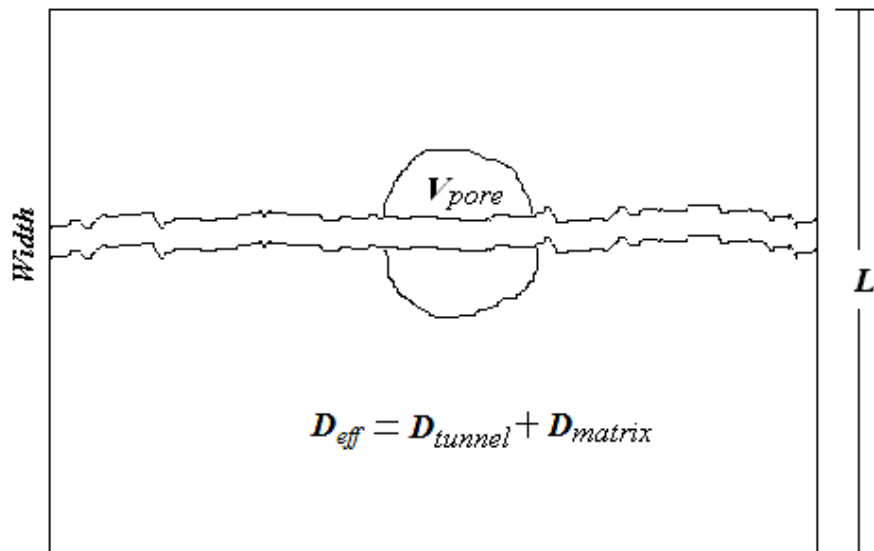


Figure 3.4.9 The effective diffusion coefficient of a tunnel structure can be recognized as the combination of the two structures.

We propose the following expression for the effective diffusion coefficient to consider the tunnelling effect:

$$D_{eff} = D_{tunnel} + k' \cdot V_{pore} \cdot D_0 \tag{3.4.3}$$

in which D_{eff} is the effective diffusion coefficient, k' is constant depends on the tunnel width, V_{pore} is the volume fraction of the pore, D_{tunnel} is the effective diffusion coefficient of the material containing the tunnel only which can be calculated as:

$$D_{tunnel} = \frac{Width}{L} \times D_{max} + \left(1 - \frac{Width}{L}\right) \times D_0 \quad (3.4.4)$$

where, D_0 is the diffusion coefficient for polymer matrix, D_{max} represents the diffusion coefficient in the liquid medium and $Width/L$ is the ratio of tunnel width over the length of the material boundary. On 3D level, this ratio could also be cross section area of the tunnel over the surface area of the representative unit.

Equation (3.4.3) assumes that the effective diffusion coefficient of a tunnelled polymer is a simple superposition of the effective diffusion coefficient of the polymer without tunnels and that of the polymer containing tunnels alone. In order to test this idea, numerical case studies are undertaken using a cubic representative unit containing a spherical pore located at the centre which is connected to the unit boundaries by a cylindrical tunnel as shown in figure 3.4.10.

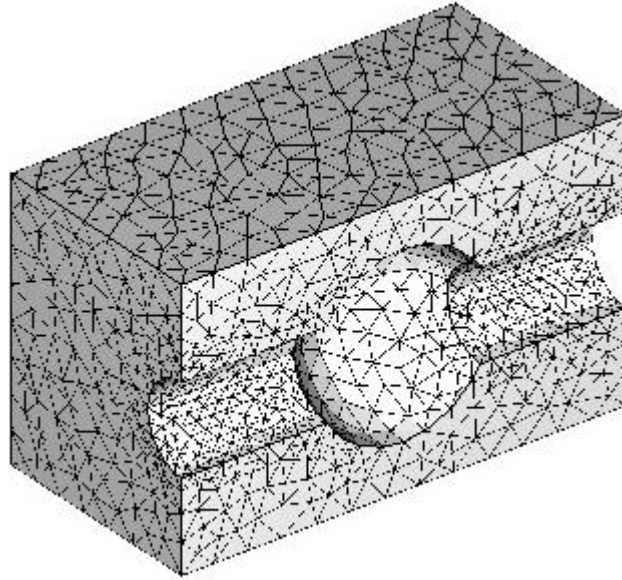


Figure 3.4.10 Cross section image of 3D representative unit with a tunnel and central spherical pore.

The calculations of the effective diffusion coefficient are repeated using various tunnel widths. The results are plotted in figure 3.4.11 showing the relative effective diffusion coefficient versus the V_{pore} for different radius of the tunnel.

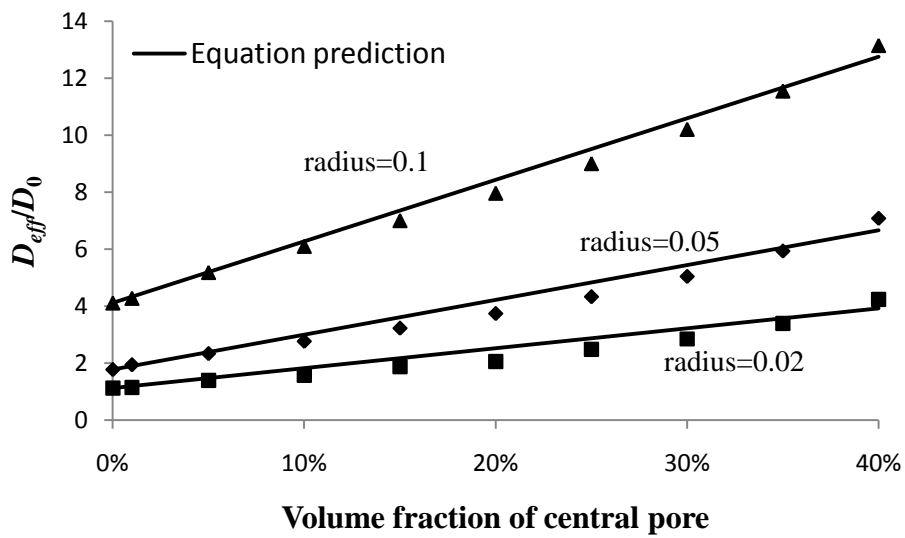


Figure 3.4.11 The relative effective diffusion coefficient for the tunnel with centre spherical pore structure on 3D level.

The results presented are for the tunnel radius of 0.02 (squares), 0.05 (diamonds) and 0.1 (triangles), respectively. The comparison between the full numerical results (discrete symbols) and that predicted by equation (3.4.3) (lines) show that the simple superposition provides a very good estimation subject to the condition that the total porosity of the central pore is less than 40%. In fact, the concept of superposition can be extended to randomly distributed pores with tunnels by using the empirical equation developed by Jiang and Pan (2008) for the polymer matrix, i.e. we could have

$$D_{eff} = D_{tunnel} + D_0 \left[1 + \left(\frac{D_{max}}{D_0} - 1 \right) (1.3 \cdot V_{pore}^2 - 0.3 \cdot V_{pore}^3) \right] \quad (3.4.5)$$

3.4.4 Encapsulation case

To demonstrate that porosity is not always the controlling factor for monomer diffusion, we consider a very rare structure of pore containing a suspending particle inside as shown in figure 3.4.12. The inner and outer space are treated as continuum material and the grey ring between them indicates the liquid filled pore.

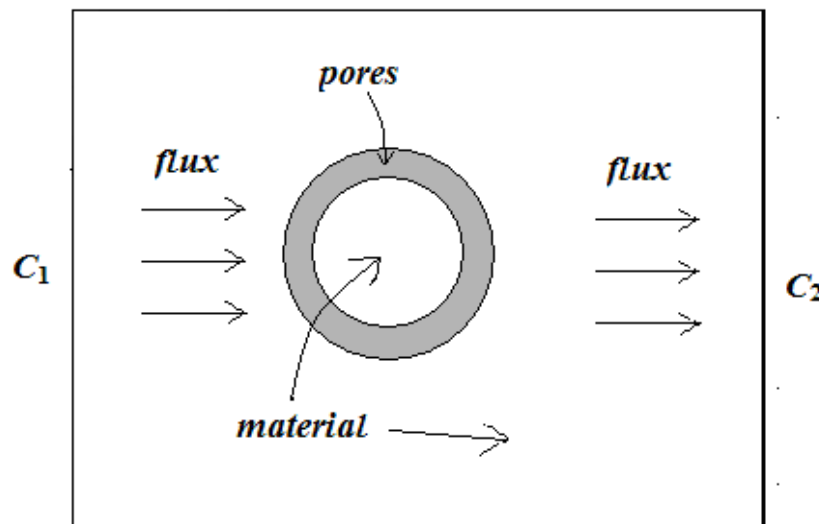


Figure 3.4.12 The explanation of encapsulation structure.

Figure 3.4.13 and 3.4.15 show the effective diffusion coefficient for three different microstructures: (a) a pore containing a suspending particle, (b) same size as (a) but

without the suspending particle and (c) pore of the same volume fraction as (a) but without the suspending particle hence much smaller in size. If porosity controls the effective diffusion coefficient, then cases (a) and (c) would give the same result. The numerical results clearly show that case (a) and (b) give almost identical result, i.e. it is the outer radius of the pore, not the porosity that controls the diffusion coefficient.

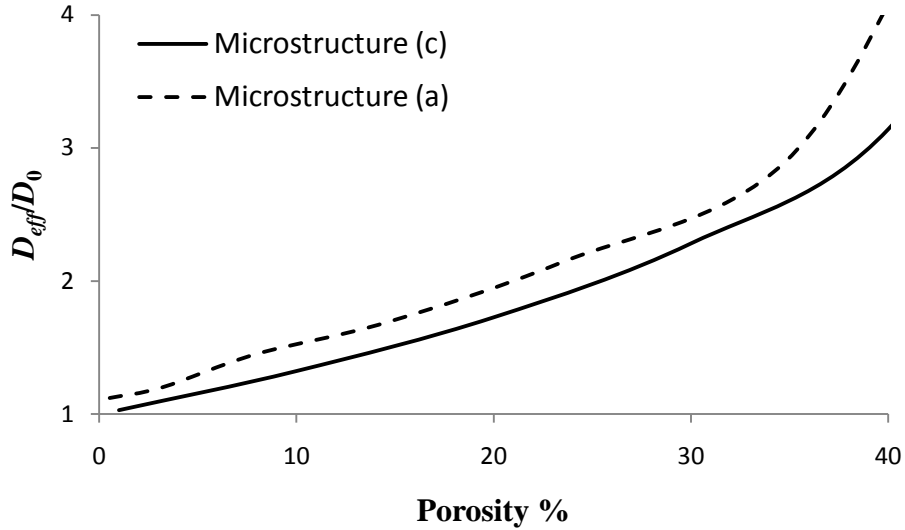


Figure 3.4.13 Effective diffusion coefficient for polymer of microstructures (a) and (c).

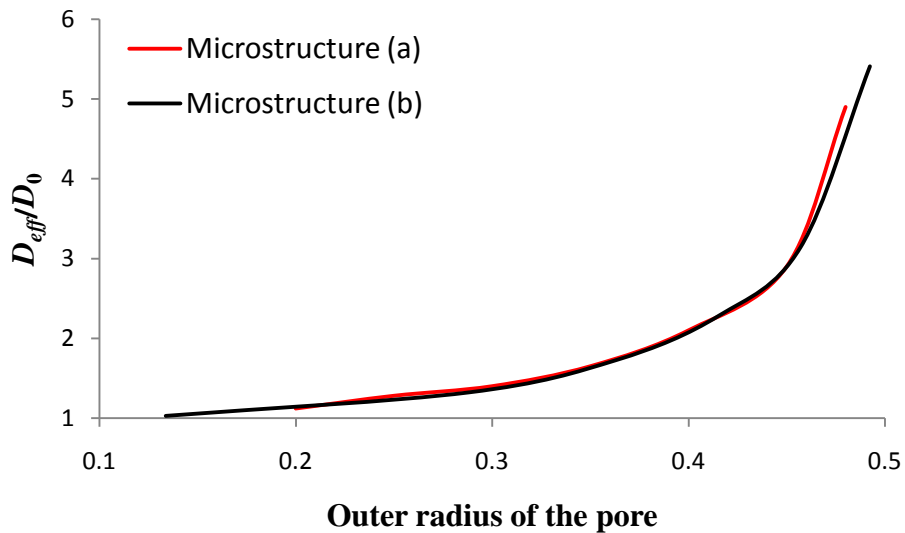


Figure 3.4.14 Effective diffusion coefficient for polymer of microstructures (a) and (b).

3.5 Conclusion

The numerical studies in this chapter demonstrated that porosity is not always the controlling factor for monomer diffusion in a degrading polymer. A practical case of the exception is that a polymer containing tunnels as a consequence of the cracking of the material. An un-practical but nevertheless instructive case of the exception is that some materials are suspended in the pores. The study further shows that it is possible to take the tunnelling effect into account by using a simple theory of superposition.

Chapter 4

An Entropy Spring Model for Change in Young's Modulus of Amorphous Biodegradable Polymers during Biodegradation

4.1 Introduction

A critical issue in the use of biodegradable bone fixation devices is to understand the load transfer from a device to the protected bone as the bone heals and the device degrades. The polymer-chain scissions in a biodegradable polymer owing to hydrolysis reaction ultimately lead to the reduction in the Young's modulus. A simple rule of mechanics tells us that the device shares less load if its stiffness is reduced. If the Young's modulus reduces too fast, then the healing bone would be put in danger. On the other hand, if the Young's modulus reduces too slowly, the bone would be weakened by the well-known stress-shielding effect. Therefore there is an optimised degradation rate which ensures both the complete healing and the healthy growth of a broken bone. The current generation of biodegradable devices has not fully exploited this optimised potential owing to the lack of a predictive tool for the stress transfer. To be on the safe side, the polymers are often over-designed, with very high molecular weight and degree of crystallinity. The degradation time of these devices is very long, sometimes over four years (Barber, 2000). Extensive experimental studies have been carried out on the degradation behaviour of biodegradable polymers. For example, Tsuji and his co-workers (Tsuji, 2000; Tsuji, 2002; Tsuji and Muramatsu, 2001; Tsuji and Ikarashi, 2004; Tsuji and Ikada, 2000) published a series of experimental data on the degradation of polylactic acids (PLA) and their co-polymers. These are long-term data, some over a period of 36 months, showing average molecular weight, degree of crystallinity, weight loss, Young's modulus, ultimate strength and elongation to failure as functions of the

CHAPTER 4 AN ENTROPY SPRING MODEL FOR CHANGE IN YOUNG'S MODULUS OF AMORPHOUS BIODEGRADABLE POLYMERS DURING BIODEGRADATION

degradation time. One observation of the data is that the Young's modulus reduction significantly lags behind the reduction in the average molecular weight for most of the biodegradable polymers. In fact the Young's modulus often increases, instead of decreasing, at the early stage of the degradation. A reasonable understanding has also been obtained on the 'degradation pathways'. It has been concluded that the water molecules diffuse into the amorphous region of the polymers relatively quickly and attack the backbones of the amorphous polymer chains. There is however some confusion about whether the chain cleavage occurs randomly along the polymer chains, referred to as random scission, or dominantly at the end of the polymer chains like unzipping, referred to as end scission (van Nostrum *et al.*, 2004; Shih, 1995^a; Shih, 1995^b; Belbella *et al.*, 1996; de Jong *et al.*, 2001). As degradation proceeds further, the water molecules enter the narrow amorphous gaps between the crystalline lamellae causing chain scissions there (Zong *et al.*, 1999). In the final stage of the degradation, water attacks the crystalline phase which takes a much longer time to degrade. One complication is that the degree of crystallinity can increase significantly during the degradation process (Zong *et al.*, 1999; Tsuji and Ikada, 2000). This has been explained as the chain cleavage providing the amorphous polymer chains with extra mobility and allowing small crystals to form first in the large amorphous region and later between the gaps of the lamellae (Zong *et al.*, 1999). The cleavage-induced crystallisation may partially explain the increase in Young's modulus in the early stage of the degradation.

Chapter 2 presented a phenomenological model for polymer degradation which can predict the average molecular weight as a function of location and time in a device of any sophisticated shape. Such a model, when connected with a model for predicting the change in elastic properties, would be a powerful tool to assist device manufacturers and orthopaedic surgeons to optimise the device design and applications. Unfortunately, existing theories for property degradation of polymers cannot capture the observed behaviour of biodegradable polymers. The modern constitutive laws for elastomers have taken the effect of chain scissions into account (Wineman, 2005; Shaw *et al.*, 2005), which was built on the experimental and theoretical work of Tobosky (1960). These

CHAPTER 4 AN ENTROPY SPRING MODEL FOR CHANGE IN YOUNG'S MODULUS OF AMORPHOUS BIODEGRADABLE POLYMERS DURING BIODEGRADATION

constitutive laws were, however, targeted at rubbers undergoing oxidation. The fundamental trend in these materials is that the Young's modulus reduces exponentially with time, which is well captured by Tobosky's theory (1960). Consequently the same theory cannot be applied to biodegradable polymers which show an incubational behaviour (Tsuji, 2002).

The purpose of this chapter is to present a model relating Young's modulus to the average molecular weight for biodegradable polymers. The model is based on the entropy spring theory for amorphous polymers, which predicts that the Young's modulus depends linearly on the number of polymer chains inside the system (Ward and Hadley, 1993). A central issue in using the entropy theory is how to count the number of molecular chains as chain scissions occur. Two concepts, a molecular weight threshold and a so-called 'no-rise rule', are proposed. The model is then used to explain the experimental data for poly(L-lactic acid) (PLLA) and poly(D-lactic acid) (PDLA) by Tsuji (2002). A demonstration case is provided to show how to connect the biodegradation model developed in Chapter 2 with the model for Young's modulus change for a three-dimensional device. The focus of this chapter is on amorphous polymers because (a) some biodegradable polymers remain amorphous throughout the biodegradation process and (b) the amorphous region is the weak link in the degradation of semi-crystalline biodegradable polymers; the composite theory can be used to predict the Young's modulus of a semi-crystalline polymer from its degree of crystallinity and Young's modulus of the amorphous region.

4.2 Entropy theory for Young's modulus of polymers

This section presents a brief outline of the entropy theory for the Young's modulus of amorphous polymers (Ward and Hadley, 1993). Consider that a force applied on a piece of material, f , is related to its stretched length, l , through its internal energy, U , and entropy, S , such that

**CHAPTER 4 AN ENTROPY SPRING MODEL FOR CHANGE IN YOUNG'S MODULUS OF
AMORPHOUS BIODEGRADABLE POLYMERS DURING BIODEGRADATION**

$$f = \left(\frac{\partial U}{\partial l} \right)_T - T \left(\frac{\partial S}{\partial l} \right)_T \quad (4.2.1)$$

in which T represents the temperature. For most engineering materials, the entropy term can be ignored. For amorphous polymers, the entropy spring model assumes that the internal energy term can be ignored and it is the entropy increase of the polymer chains from a disordered state to a more ordered state during deformation that provides the elasticity of the material. The entropy spring theory reflects the fact that very little force is carried by the polymer backbone during deformation; hence the total internal energy change is small relative to the entropy change. During the polymerisation process, the repeating units connect to each other to form long polymer chains following the random walk mechanism. The polymer chains have their end-to-end distances distributed in the form of a Gaussian error function. The entropy of a single chain can be calculated as (Ward and Hadley, 1993)

$$s = c - kb^2 r^2 = c - kb^2 (x^2 + y^2 + z^2) \quad (4.2.2)$$

in which b is the length of the polymer ester bond, c is an arbitrary constant, k is the Boltzmann constant, r is the end to end distance of a polymer chain, x, y, z are the spatial coordinates of the chain end.

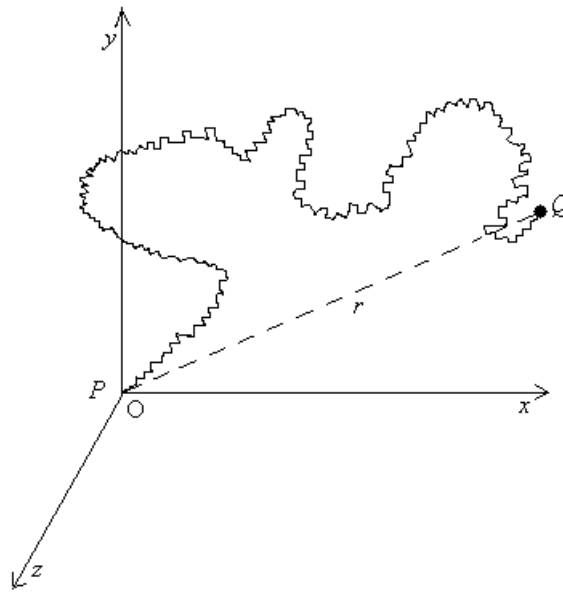


Figure 4.2.1 A single polymer chain.

The entropy changes if the polymer chain deforms, i.e. if the chain end moves from Q to Q' , as in figure 4.2.2.

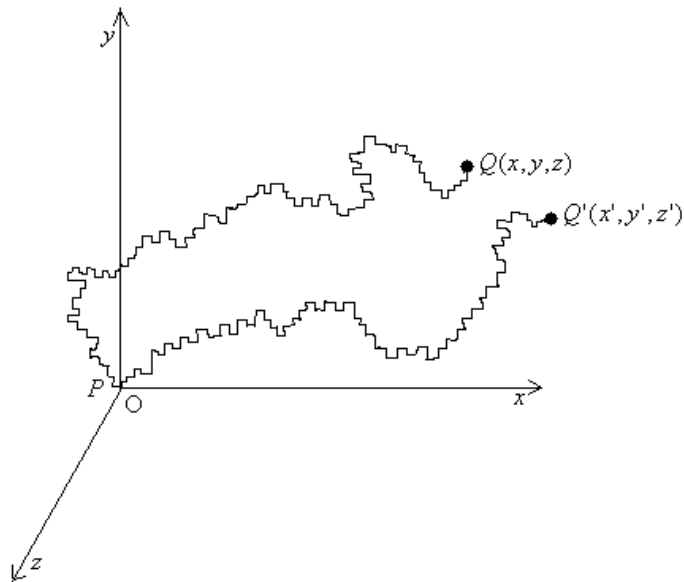


Figure 4.2.2 Change in entropy of a single chain as the polymer deforms.

If the deformation of this chain follows

**CHAPTER 4 AN ENTROPY SPRING MODEL FOR CHANGE IN YOUNG'S MODULUS OF
AMORPHOUS BIODEGRADABLE POLYMERS DURING BIODEGRADATION**

$$x' = \lambda_1 x; \quad y' = \lambda_2 y; \quad z' = \lambda_3 z \quad (4.2.3)$$

the entropy of the chain after the deformation becomes:

$$s' = c - kb^2(\lambda_1^2 x^2 + \lambda_2^2 y^2 + \lambda_3^2 z^2) \quad (4.2.4)$$

The difference of the entropy in this case is:

$$\Delta s = -kb^2[(\lambda_1^2 - 1)x^2 + (\lambda_2^2 - 1)y^2 + (\lambda_3^2 - 1)z^2] \quad (4.2.5)$$

For N chains per unit volume in the system, because there is no preferred direction for the chain vectors in the isotropic state, there is no preference for the x, y, z directions with the mean square chain length, so that:

$$\sum_1^N x^2 = \sum_1^N y^2 = \sum_1^N z^2 = \frac{1}{3} \sum_1^N r^2 = \frac{1}{3} N \overline{r^2} = \frac{1}{3} N \left(\frac{3}{2b^2} \right) \quad (4.2.6)$$

Note that $\overline{r^2} = \sum_1^N r^2 / N = \left(\frac{3}{2b^2} \right)$ owing to the Gaussian distribution of polymer chain length. The total entropy change for all the N chains in a unit volume can be derived as:

$$\Delta S = \sum_1^N \Delta s = -\frac{1}{2} Nk[(\lambda_1^2 + \lambda_2^2 + \lambda_3^2) - 3] \quad (4.2.7)$$

The Helmholtz function (free energy) is defined by:

$$A = U - TS \quad (4.2.8)$$

**CHAPTER 4 AN ENTROPY SPRING MODEL FOR CHANGE IN YOUNG'S MODULUS OF
AMORPHOUS BIODEGRADABLE POLYMERS DURING BIODEGRADATION**

in which, U is the internal energy, T is the absolute temperature, S is the entropy. Assuming there is no change in the internal energy on deformation, under isothermal condition:

$$\Delta A = -T \Delta S = \frac{1}{2} NkT[(\lambda_1^2 + \lambda_2^2 + \lambda_3^2) - 3] \quad (4.2.9)$$

The change in strain energy comes from the change in Helmholtz free energy and if the strain-energy function U is zero initially, then we have

$$U = \Delta A = \frac{1}{2} NkT[(\lambda_1^2 + \lambda_2^2 + \lambda_3^2) - 3] \quad (4.2.10)$$

Consider the simple elongation λ in x direction; the incompressibility relationship indicates $\lambda_1 \lambda_2 \lambda_3 = 1$, and by symmetry we have $\lambda_2 = \lambda_3 = \lambda^{-1/2}$

Equation (4.2.9) becomes

$$U = \Delta A = \frac{1}{2} NkT(\lambda^2 + \frac{2}{\lambda} - 3) \quad (4.2.11)$$

Then we have

$$f = \frac{\partial U}{\partial \lambda} = NkT(\lambda - \frac{1}{\lambda^2}) \quad (4.2.12)$$

For small strain, let $\lambda = 1 + e_{xx}$, and equation (4.2.11) is approximated as:

$$f = \sigma_{xx} = 3NkTe_{xx} = Ee_{xx} \quad (4.2.13)$$

Thus we have

$$E = 3NkT, \quad (4.2.14)$$

that is, the Young's modulus under isothermal condition is proportional to the number of polymer chains of a unit volume of polymers times the absolute temperature.

4.3 The degradation theory of rubber oxidation due to Tobolsky (1960)

Tobolsky (1960) studied the stress decay of rubbers during the oxidation process. Their study starts from the stress-relaxation experiment on rubbers of several kinds. The measurement of Young's modulus in his work is given by equation (4.3.1)

$$\frac{E}{E_0} = \frac{f(t)}{f(0)} = \frac{n(t)}{n(0)} \quad (4.3.1)$$

in which E is the Young's modulus, $f(t)$ is the stress that is measured from the experiment at time t , $n(t)$ is the number of network chains that are still supporting the stress at time t . According to this equation, the Young's modulus of rubber is proportional to the number of polymer chain and the rule for counting $n(t)$ is the number of network chains that have never been cut up to time t .

If scissions occur randomly within the system (which means the polymer chains can be cut more than once), the Young's modulus can be calculated as:

$$\frac{E}{E_0} = \frac{f(t)}{f(0)} = \exp\left(-\frac{q'_0 t}{n(0)}\right) \quad (4.3.2)$$

in which q'_0 is the rate of scission (equal to the total number of scissions over time). If the chain scission occurs only at the cross-link sites and each chain can only be cut once, the Young's modulus is also an exponential function of time.

**CHAPTER 4 AN ENTROPY SPRING MODEL FOR CHANGE IN YOUNG’S MODULUS OF
AMORPHOUS BIODEGRADABLE POLYMERS DURING BIODEGRADATION**

$$\frac{E}{E_0} = \frac{f(t)}{f(0)} = \exp(-k't) \quad (4.3.3)$$

in which k' is a constant.

Both equation (4.3.2) and equation (4.3.3) suggest an exponential relationship between Young’s modulus and time. This relation is supported by the stress-relaxation experiment from rubber as shown in figure 4.3.1.

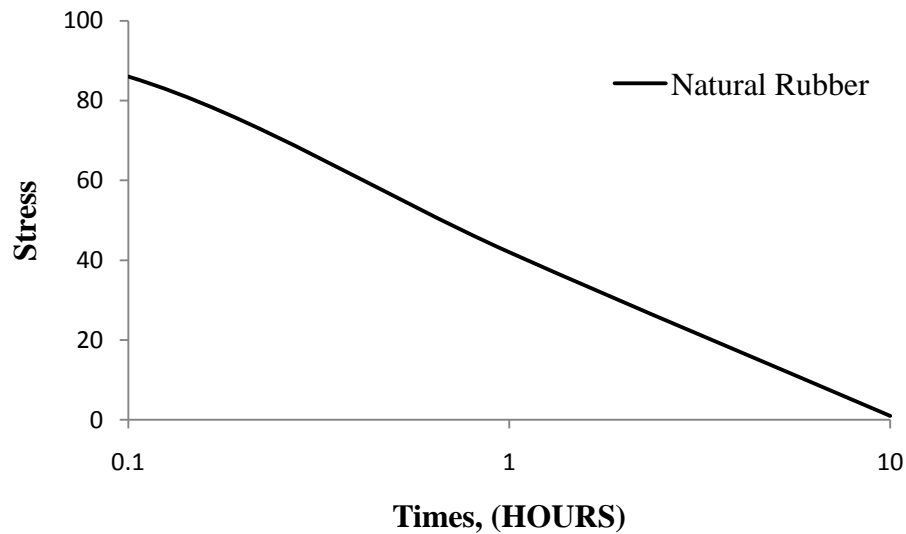


Figure 4.3.1 The change of Young’s modulus for rubber in stress-relaxation experiment with respect to time (Tobolsky, 1960).

Figure 4.3.1 shows the stress-relaxation for natural rubber in the stress-relaxation experiment, Young’s modulus is proportional to the measured stress as strain was kept constant. The exponential decay of stress suggests that the Young’s modulus decays in the accordance with equation (4.3.2).

4.4 The experimental data by Tsuji (2002)

A long-term degradation experiment was reported by Hideto Tsuji in 2002. The degradation samples are four species from the PLA family: PLLA, PDLA, PDLLA and

CHAPTER 4 AN ENTROPY SPRING MODEL FOR CHANGE IN YOUNG'S MODULUS OF AMORPHOUS BIODEGRADABLE POLYMERS DURING BIODEGRADATION

PLLA/PDLA (1:1). The polymers are made into films with the dimension of $3\text{mm} \times 30\text{mm} \times 50\text{--}100\ \mu\text{m}$ and $18\text{mm} \times 30\text{mm} \times 25\ \mu\text{m}$ in order to eliminate any acceleration from the accumulated oligomers (reach zone *B* in our biodegradation map in Chapter 2) and kept in 10mL of phosphate-buffered solution ($\text{pH } 7.4 \pm 0.1$) at 37°C for up to 60 months. The initial number average molecular weights are: PLLA: $5.4 \times 10^5\ \text{g} \cdot \text{mol}^{-1}$, PDLA: $4.4 \times 10^5\ \text{g} \cdot \text{mol}^{-1}$, PDLLA: $3.7 \times 10^5\ \text{g} \cdot \text{mol}^{-1}$, and PLLA/PDLA (1:1): $4.4 \times 10^5\ \text{g} \cdot \text{mol}^{-1}$. All four groups of samples are amorphous throughout the experiment; we choose the data of PDLA and PLLA for the case study in the rest of this chapter. The GPC (Gel Permeation Chromatography) curves for PLLA and PDLA polymer samples are shown in figures 4.4.1 and 4.4.2 respectively, for the degradation times of 0, 8, 16, 24 months from the right to left.

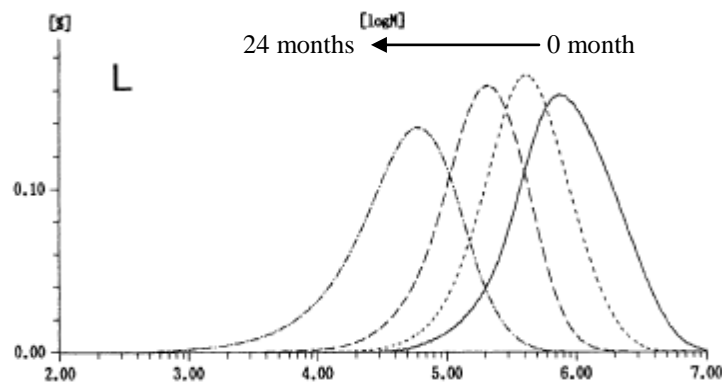


Figure 4.4.1 GPC curves for PLLA at four different times (Tsuji, 2002).

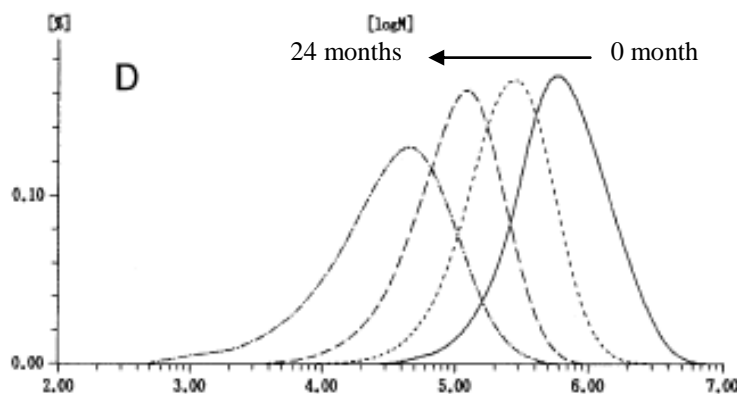


Figure 4.4.2 GPC curves for PDLA at four different times (Tsuji, 2002).

CHAPTER 4 AN ENTROPY SPRING MODEL FOR CHANGE IN YOUNG'S MODULUS OF AMORPHOUS BIODEGRADABLE POLYMERS DURING BIODEGRADATION

The number average molecular weights reduction with respect to times (0 4 8 12 16 20 24 months) for PLLA (triangles) and PDLA (squares) are shown in figure 4.4.3.

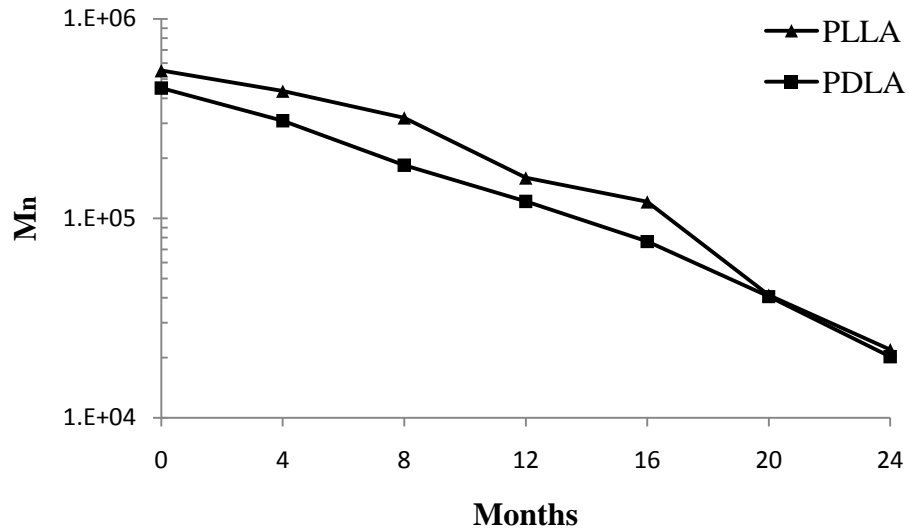


Figure 4.4.3 The number average molecular weight loss versus time (Tsuji, 2002) for PLLA (triangles) and PDLA (squares).

The number average molecular weight shown in figure 4.4.3 roughly follows an exponential relation with the degradation time. This trend can be well captured by our previous model in Chapter 2. The change in Young's modulus at 0 4 8 12 16 20 24 months for PLLA (triangles) and PDLA (squares) samples are plotted in figure 4.4.4.

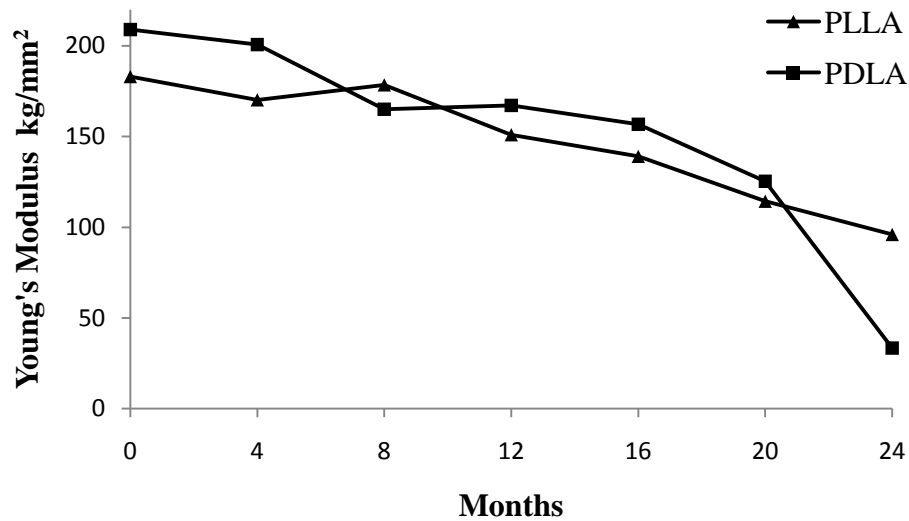


Figure 4.4.4 Young's Modulus versus time averaged from four samples (Tsuji, 2002) for PLLA (triangles) and PDLA (squares).

The reduction in Young's modulus in figure 4.4.4 is measured by tensile tester at 25⁰C at a relative humidity of 50%, without any influence of crystallisation phenomenon from the polymers. Because PLLA and PDLA are both amorphous material the reinforcement of their strength should be excluded, and therefore this set of experimental data was chosen to be compared with the theoretical work as these polymers remain amorphous throughout the experiment.

4.5 An entropy based model for change in Young's modulus

4.5.1 Description of the model

Comparing figure 4.4.4 with figure 4.3.1, it is obvious that the Young's modulus reduction for rubber and PLA behave very differently from each other. Therefore the theory from Tobolsky (1960) cannot be applied to biodegradable polymers. This is because in rubbers it is the cross-link density that provides the resistance to deformation, while in amorphous polymers, it is the entropy change that provides the resistance to deformation. The PLA polymers lost their Young's modulus slowly at first and then

**CHAPTER 4 AN ENTROPY SPRING MODEL FOR CHANGE IN YOUNG'S MODULUS OF
AMORPHOUS BIODEGRADABLE POLYMERS DURING BIODEGRADATION**

very quickly at the late stage. If the N is taken as the total number of polymer chains per unit volume, equation (4.2.14) seems to predict an ever-increasing Young's modulus for a degrading polymer as the chain cleavage always increases the total number of polymer chains. However the entropy theory was developed for fresh polymers and a fundamental assumption leading to equation (4.2.14) is that the end-to-end distance of a single polymer chain is much smaller than the extended chain length. Under this assumption, the end-to-end distance follows the Gaussian distribution. This assumption is no longer valid if random chain cleavage occurs. It is complicated to calculate the entropy taking into account of the random scission. Instead an intuitive argument is suggested here to modify the entropy spring theory. As schematically illustrated in figure 4.5.1 (a) & (b), an isolated chain scission of a very long chain should not affect the entropy change during the deformation of the polymer because the long polymer chain is constrained by its surrounding chains. It is then reasonable to assume that N does not increase after a chain cleavage. This is referred to as the 'no-rise rule' in the following discussion. Furthermore, a very short chain does not contribute to the entropy change during deformation. It has long been recognised that polymers with a very small degree of polymerisation have little strength and stiffness (Kaufman and Falcetta, 1976). Therefore chains shorter than a critical degree of polymerisation should not be counted when equation (4.2.14) is used. Consequently, a polymer chain should be removed from the entropy calculation if enough cleavages have occurred such that its molecular weight is smaller than the threshold. This is schematically shown in figure 4.5.1 (a) & (c). From a known initial distribution of polymer molecular weight, the random and end scissions can be simulated numerically on a computer using the classical Monte Carlo scheme. By means of the "no-rise" rule and the molecular weight threshold, the value of N , hence the Young's modulus, and the average molecular weight can be calculated. A relationship between the Young's modulus and the average molecular weight is then determined.

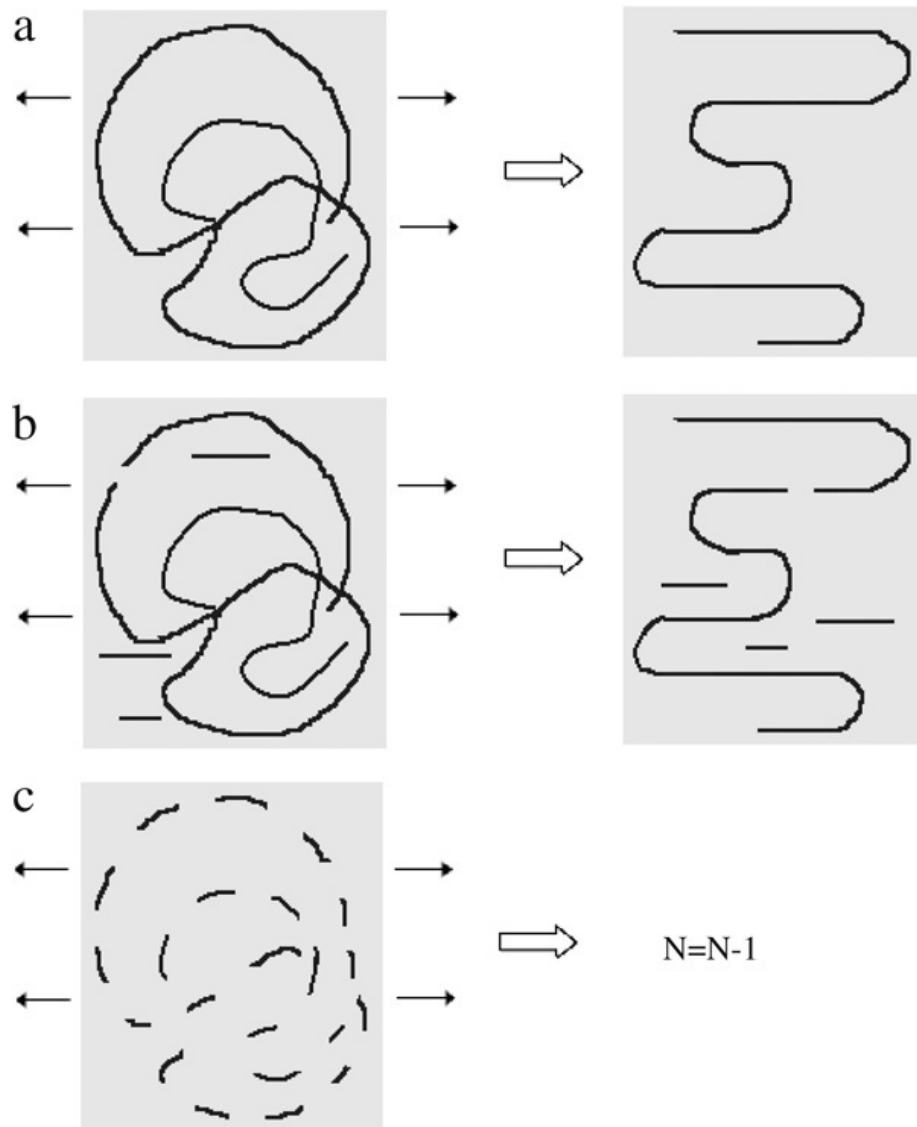


Figure 4.5.1 Illustration of entropy theory for elasticity.

A computer code is developed to implement a Monte Carlo scheme for polymer chains scissions and to calculate the Young's modulus – number average molecular weight relation. Figure 4.5.2 shows the flowchart of the Monte Carlo scheme.

CHAPTER 4 AN ENTROPY SPRING MODEL FOR CHANGE IN YOUNG'S MODULUS OF
AMORPHOUS BIODEGRADABLE POLYMERS DURING BIODEGRADATION

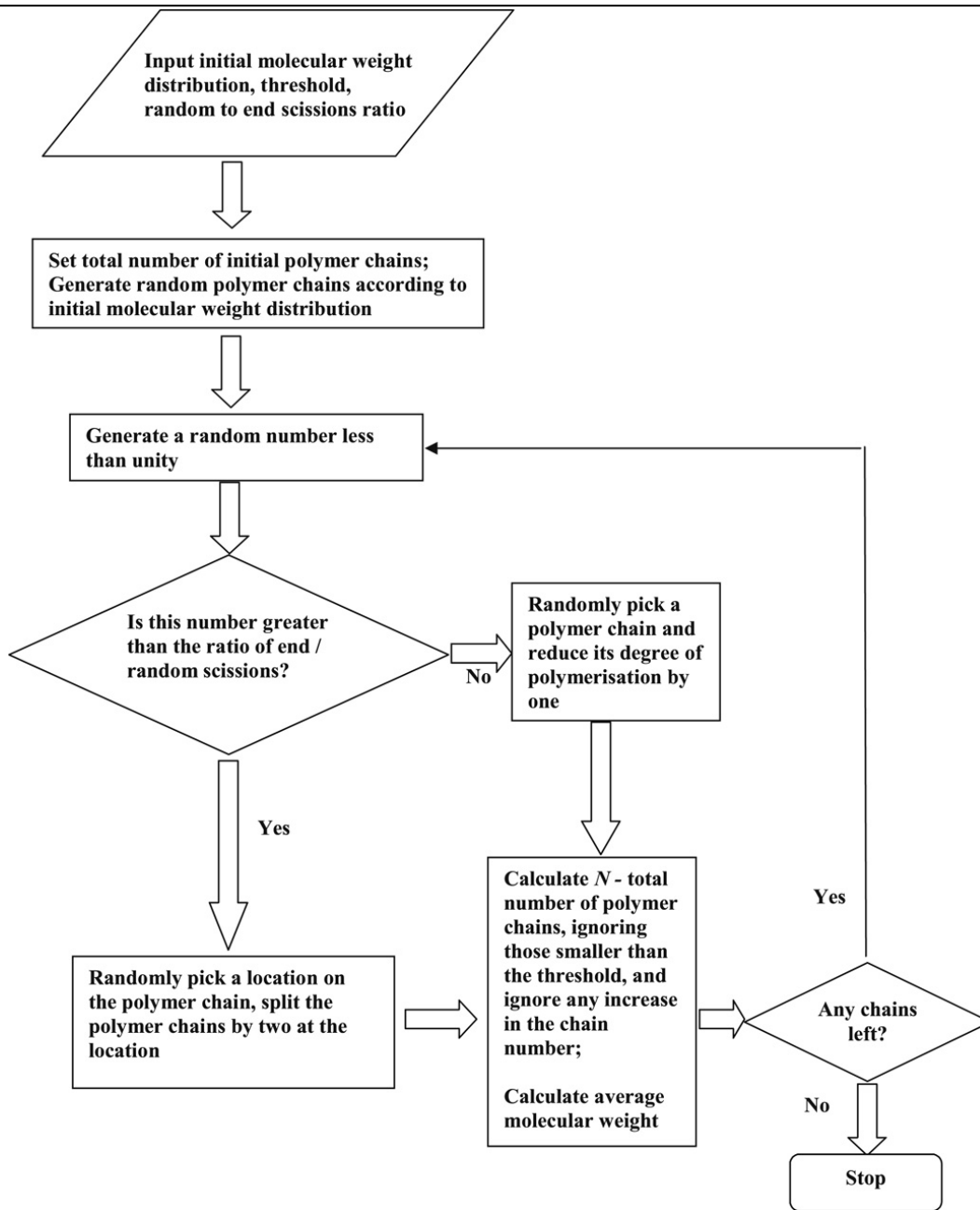


Figure 4.5.2 Flowchart showing the Monte Carlo scheme to simulate polymer chain scissions and to calculate the corresponding Young's modulus and average molecular weight.

The Monte Carlo simulation starts from a numerically generated matrix representing the polymer chains with their degrees of polymerisation following a known initial molecular weight distribution. The information is contained in the two columns of the matrix generated from GPC curves figures 4.4.1 and 4.4.2. As shown in figure 4.5.3, the

**CHAPTER 4 AN ENTROPY SPRING MODEL FOR CHANGE IN YOUNG'S MODULUS OF
AMORPHOUS BIODEGRADABLE POLYMERS DURING BIODEGRADATION**

first column is a number that identifies a single polymer chain. The second column contains the corresponding degree of polymerisation of the polymer chain.

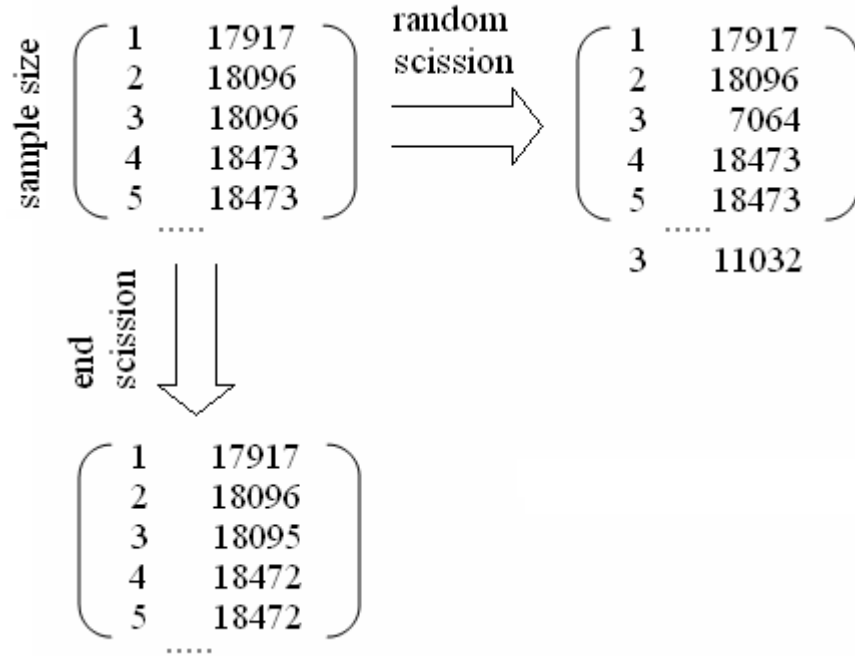


Figure 4.5.3 Data structure for computer simulation of polymer chain scission.

The sample size (the initial number of polymer chains) in the simulation has to be chosen arbitrarily, the effect of which will be further discussed in the following section. At each time step, either a random or end scission is prosecuted. The probability of end scission is taken as

$$P_{end} = \frac{P_{end}}{P_{random} + P_{end}} = \frac{K_{end}N_{end}}{K_{end}N_{end} + K_{random}(N_{total} - N_{end})} \quad (4.5.1)$$

in which P_{end} and P_{random} represent the probability for end and random scission respectively ($P_{end} + P_{random} = 1$), N_{end} is the number of polymer chain ends inside the system at the current time step and N_{total} is the total number of repeating units in the system at the current time step. $\frac{K_{end}}{K_{random}}$ is an input parameter representing the relative rates of the two scission mechanisms. During the simulation, a random number between

CHAPTER 4 AN ENTROPY SPRING MODEL FOR CHANGE IN YOUNG'S MODULUS OF AMORPHOUS BIODEGRADABLE POLYMERS DURING BIODEGRADATION

zero and one is generated. If the random value is less than P_{end} then end scissions occurs. The computer programme will randomly pick a polymer chain, i.e. a row of the matrix, and reduce its degree of polymerisation, i.e. the value of the second-column, by one unless the 'chain length' number is one, in which case the entire row will be removed. If the random value is larger than or equal to P_{end} , then random scission occurs. The computer code will pick a random row and position on the row and generate two new polymer chains accordingly. After each time step, the average molecular weight and the value of N are calculated according to the rules discussed above. According to these rules, the value of N never increases and is reduced by one if the degree of polymerisation of all the polymer chains sharing same identity become smaller than a threshold which will be referred to as M_{th} .

4.5.2. Comparison with the experimental data by Tsuji (2002)

The experimental data on poly(L-lactide) and poly(D-lactide) produced by Tsuji (2002) are used here for comparison with the entropy spring model. In figure 4.4.4, the Young's modulus of the PDLA samples at $t=0$ and $t=24$ are 2.09 and 0.33 *GPa* respectively. With a series of trial and error simulations, it was found that $M_{th} = 1.15 \times 10^5$ g/mol leads to a good fitting for between equation (4.2.14) and the experimental data. With this value of the threshold and the initial sample size of 3000 chains, the normalised Young's modulus versus the number average molecular weight is obtained for PDLA as shown in figure 4.5.4 (solid line) which also shows the experimental data (discrete dots) by Tsuji (2002).

CHAPTER 4 AN ENTROPY SPRING MODEL FOR CHANGE IN YOUNG'S MODULUS OF
AMORPHOUS BIODEGRADABLE POLYMERS DURING BIODEGRADATION

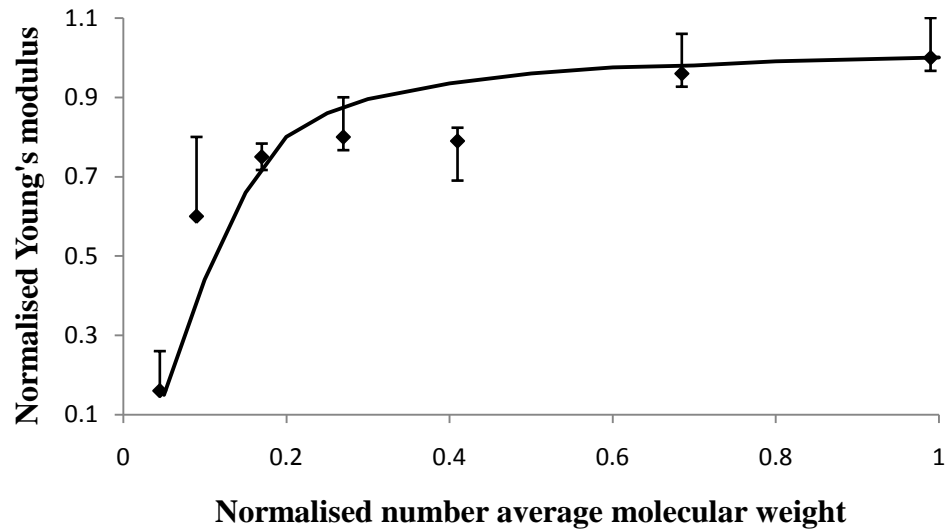


Figure 4.5.4 Normalised Young's modulus versus normalised average molecular weight for PDLA. Solid line – model prediction using $M_{th} = 1.15 \times 10^5$ g/mol initial sample size of 3000 polymer chains and the random to end scission ratio of 1:1; discrete dots – experimental data obtained from figures 4.4.3 and 4.4.4

In the numerical simulation, the ratio of $\frac{P_{end}}{P_{random}}$ was initially set at 1:1 (by choosing $\frac{K_{end}}{K_{random}} = 3500$). This simulation is repeated to fit the PLLA data obtained by Tsuji (2002). It was found that $M_{th} = 1.3 \times 10^5$ g/mol leads to a good fit. Figure 4.5.5 compares the predicted (solid line) and experimental (discrete dots) relation between the Young's modulus and average molecular weight. As in the previous simulation, 3000 initial polymer chains were used and $\frac{P_{end}}{P_{random}}$ was initially set at 1:1.

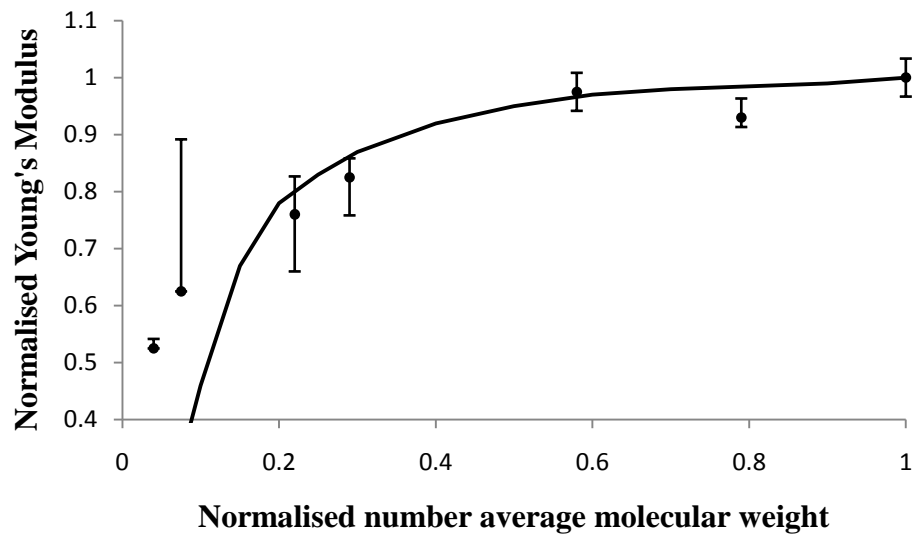


Figure 4.5.5 Normalised Young's modulus versus normalised average molecular weight for the PLLA used by Tsuji (2002). Solid line – model prediction using $M_{th} = 1.3 \times 10^5$ g/mol, initial sample size of 3000 polymer chains and the random to end scission ratio of 1:1; discrete dots – experimental data obtained by Tsuji (2002).

In the two fitting curves (figures 4.5.4 and 4.5.5), the simulation results rely on the two values of parameter M_{th} . These two thresholds determined for PDLA and PLLA correspond to degrees of polymerisation of about 1600 and 1800, respectively. Kaufman and Falcetta (1976) stated that it is the molecular weight that decides the mechanical strength for polymer materials. According to their theory, when the degree of polymerisation of polymers is low there will be no such strength; when the degree of polymerisation is beyond a critical value the mechanical strength will show a step rise until the polymerisation reaches a large value above which the mechanical property remains stable, as figure 4.5.6 demonstrates.

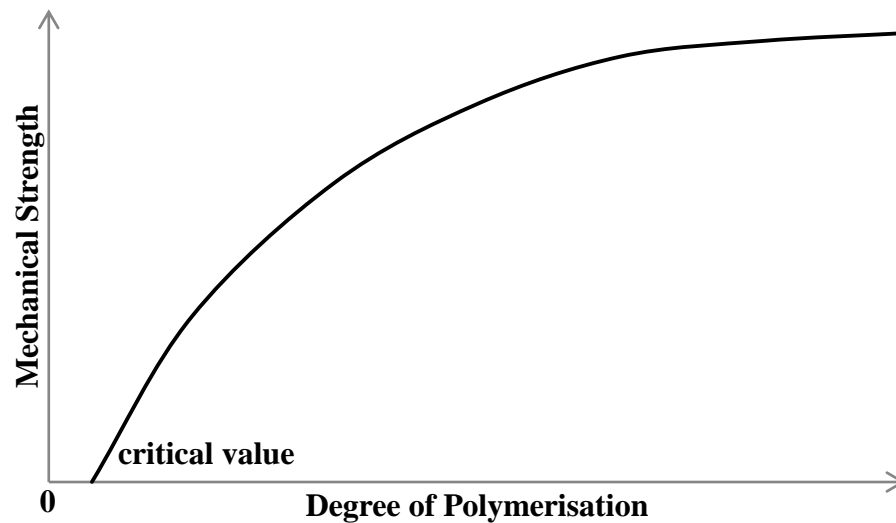


Figure 4.5.6 Relation between mechanical property and degree of polymerisation according to Kaufman and Falcetta (1976).

Almost all polymers follow this trend of the relationship and the usual threshold of degree of polymerisation above which the mechanical property remains stable is between 600 and 900. The critical values of M_{th} therefore well above these known threshold values for polymers to have stable mechanical strength.

4.5.3 Effect of the simulation parameters on the predicted Young's modulus

It can be observed from figures 4.5.4 and 4.5.5 that the simple model proposed in this chapter can capture the trend of the Young modulus reduction very well. In this section, we will change the inputs to the model to test the importance of the parameters. The first input to the model to be changed is the initial polymer chain number, i.e. the sample size. To show that the initial sample size of 3000 polymer chains is large enough, the simulation was repeated using sample sizes of 10000 and 30000 respectively with all other inputs remaining the same. The results are shown below in figure 4.5.7.

CHAPTER 4 AN ENTROPY SPRING MODEL FOR CHANGE IN YOUNG'S MODULUS OF
AMORPHOUS BIODEGRADABLE POLYMERS DURING BIODEGRADATION

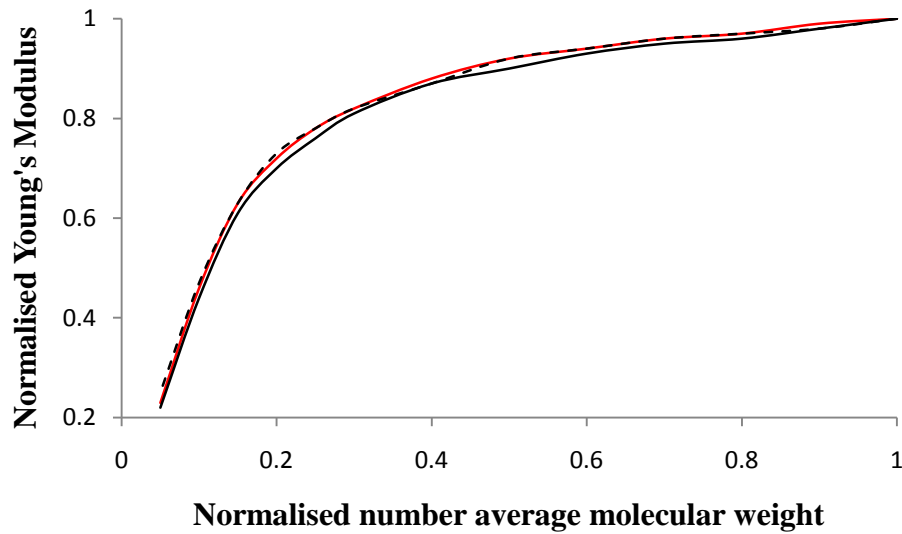


Figure 4.5.7 The normalised Young's Modulus versus normalised number average molecular weight with sample size of 3000 (red), 10000 (dotted), 30000 (solid line) for PDLA.

All these curves in figure 4.5.7 are very close to each other, showing that the sample size of 3000 polymer chains is large enough. The second parameter to study is the ratio of $\frac{K_{end}}{K_{random}}$. The simulation was repeated using the $\frac{P_{end}}{P_{random}}=10:1, 1:1, \text{ and } 1:10$ (by choosing $\frac{P_{end}}{P_{random}}=35000, 3500, 350$) at initial stage respectively and the results are plotted in figure 4.5.8.

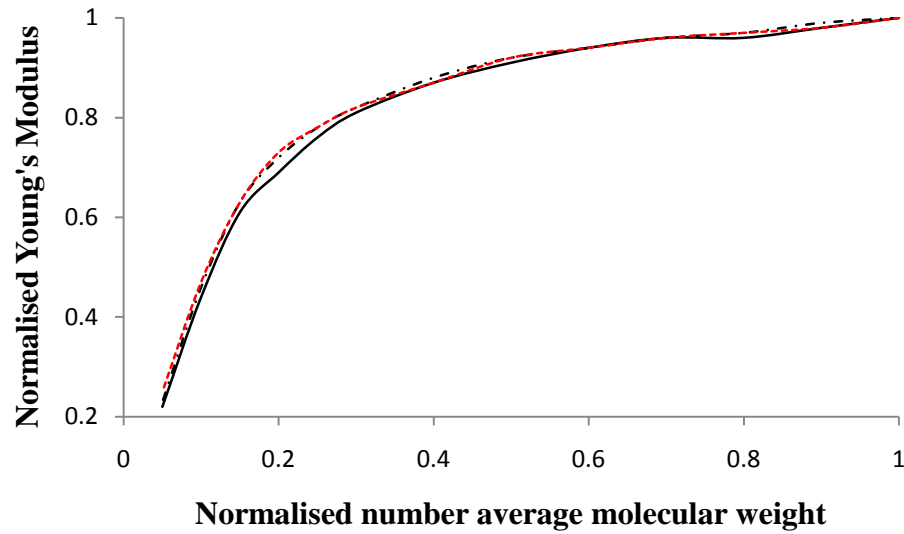


Figure 4.5.8 The normalised Young's modulus versus normalised number average molecular weight with end scission to random scission of 10:1 (red), 1:1 (dotted), 1:10 (solid line) for PDLA.

It can be observed from figure 4.5.8 that the result is insensitive to the random to end scission ratio. The initial degree of polymerisation for PDLA in Tsuji's (2002) experiment is approximately 6100. With 3000 initial polymer chains, the system contains about 1.8×10^7 repeating units which are subject to hydrolysis cleavage. Therefore, the reduction in the number average molecular weight is mostly caused by the increasing of the polymer chain number (random scission) rather than the decreasing of the polymer chain unit (end scission). The ratio of $\frac{P_{end}}{P_{random}}$ does not affect the change in the average molecular weight unless the probability for random scission is a tiny number, i.e. 1/10000.

The simulation results are however sensitive to the choice of M_{th} . To show this, we changed the threshold value while all other parameters remained the same. Figures 4.5.9 (a) and (b) show the simulation results using different threshold values.

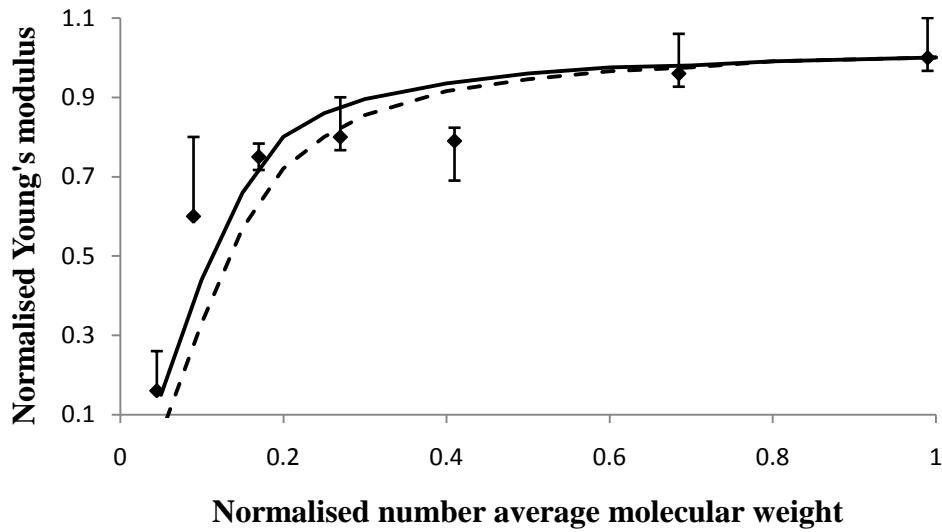


Figure 4.5.9 (a) Influence of M_{th} on the model result for PDLA; $M_{th} = 1.15 \times 10^5$ (solid line) and $M_{th} = 1.3 \times 10^5$ (dashed line).

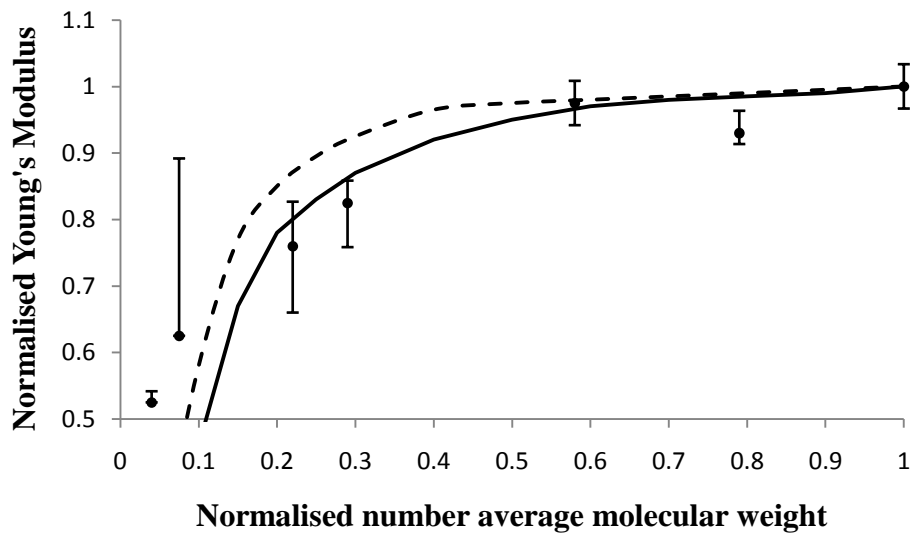


Figure 4.5.9 (b) Influence of M_{th} on the model result for PLLA; $M_{th} = 1.3 \times 10^5$ (solid line) and $M_{th} = 1.1 \times 10^5$ (dashed line).

Figure 4.5.9 (a) and (b) show the impact from changing M_{th} values. Comparing to figure 4.5.7 and figure 4.5.8, figure 4.5.9 (a) & (b) indicates the difference on two M_{th} values which are not very far from each other could still provide a clearly different prediction

**CHAPTER 4 AN ENTROPY SPRING MODEL FOR CHANGE IN YOUNG'S MODULUS OF
AMORPHOUS BIODEGRADABLE POLYMERS DURING BIODEGRADATION**

result. In other words, the model is much more sensitive to M_{th} value than the initial end to random scission ratio as well as the sample size.

4.5.4. A discussion on end scission versus random scission

Using equation (4.5.1) for the initial state of the polymer gives

$$\frac{P_{end}^0}{P_{end}^0 + P_{random}^0} = \frac{K_{end}N_{end}^0}{K_{random}(N_{total}^0 - N_{end}^0) + K_{end}N_{end}^0} \quad (4.5.2)$$

where the superscript 0 indicates the value of the variable at time zero. Here N_{total} represents the total number of ester bond (repeating units) and N_{end} represents the total number of polymer ends. Noting that $P_{end}^0 + P_{random}^0 = 1$ and using N_{ch} to represent the total number of polymer chains, we have:

$$P_{end}^0 = \frac{K_{end}(2N_{ch}^0)}{K_{random}(DP_0 \cdot N_{ch}^0 - 2N_{ch}^0) + K_{end}(2N_{ch}^0)} = \frac{2K_{end}}{K_{random}(DP_0 - 2) + 2K_{end}} \quad (4.5.3)$$

Similarly at any scission step, we have

$$P_{end} = \frac{2K_{end}}{K_{random}(DP - 2) + 2K_{end}} \quad (4.5.4)$$

Combining (4.5.3) with (4.5.4) we obtain

$$P_{end} = \frac{1}{\frac{(1 - P_{end}^0)}{P_{end}^0(DP_0 - 2)}(DP - 2) + 1} \quad (4.5.5)$$

**CHAPTER 4 AN ENTROPY SPRING MODEL FOR CHANGE IN YOUNG'S MODULUS OF
AMORPHOUS BIODEGRADABLE POLYMERS DURING BIODEGRADATION**

Because $DP \gg 2$, and $DP_0 \gg 2$; $\frac{DP}{DP_0} = \frac{M_n}{M_{n0}} = \bar{M}_n$, the above equation can be

rewritten as:

$$P_{end} \approx \frac{1}{\alpha \bar{M}_n + 1} \quad (4.5.6)$$

in which

$$\alpha = \frac{P_{rand}^0}{P_{end}^0} = \frac{K_{random} N_{total}^0}{K_{end} N_{end}^0}$$

For reasonable values of $\frac{K_{end}}{K_{random}}$, value of α is very large because the total number of

ester bonds is much larger than the total number of chain ends. Equation (4.5.5) indicates that the probability of end scission increase from a very small value to unity towards the end of the degradation as M_n reaches zero. Figures 4.5.10 (a) –(c) shows the actual probability of end scissions observed in our simulations for three different values: $K_{end}/K_{random}=35000, 3500, 350$; $P_{end}/P_{random}=10:1, 1:1, 1:10$.

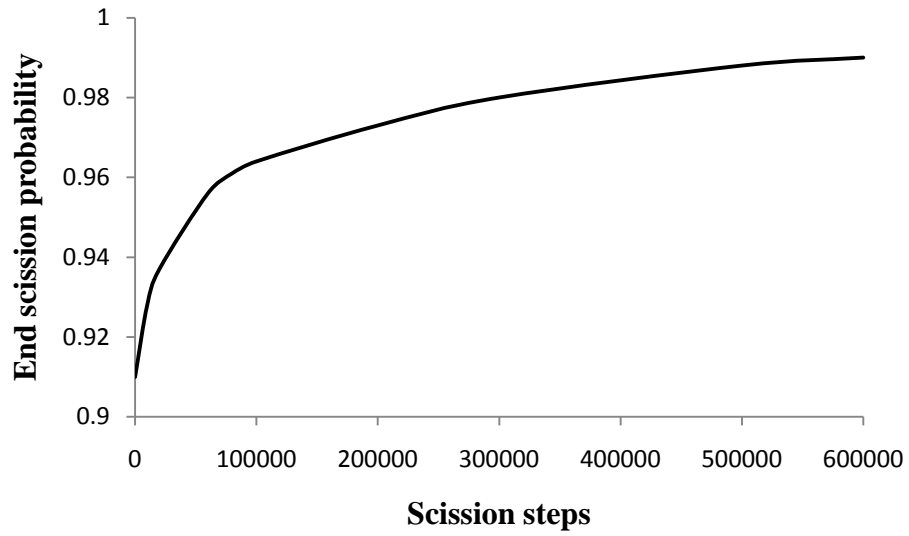


Figure 4.5.10 (a) End scission probability versus total number of chain scissions

with initial input $\frac{P_{end}}{P_{random}} = 10:1$ for PDLA.

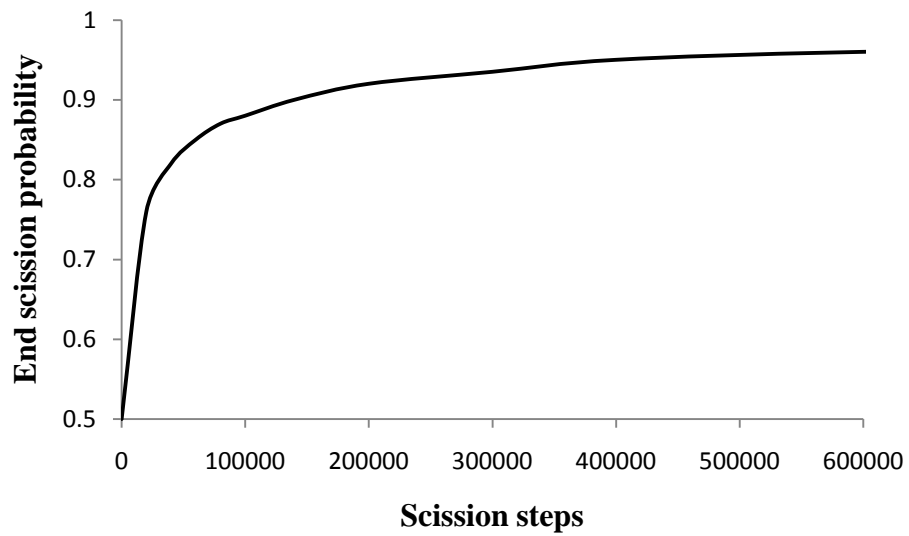


Figure 4.5.10 (b) End scission probability versus total number of chain scissions

with initial input $\frac{P_{end}}{P_{random}} = 1:1$ for PDLA.

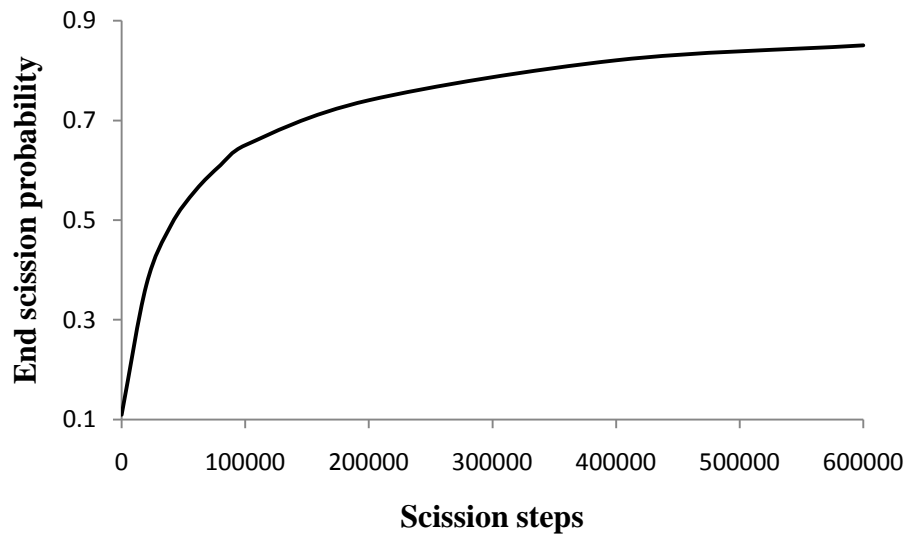


Fig 4.5.10 (c) End scission probability versus total number of chain scissions with

$$\text{initial input } \frac{P_{end}}{P_{random}} = 1:10 \text{ for PDLA.}$$

It is apparent from these figures that end scission dominates during the later stage of the hydrolysis degradation. This observation is also supported by experimental observations by Shih (1995^a). Note that the end scission has a much smaller effect on the reduction in the average molecular weight. This is simply because a random scission can cut a polymer chain by half while an end scission only reduces the degree of polymerisation by one. Therefore it is important not to confuse the fact that “end scission dominates the hydrolysis reaction”, meaning more end scissions occur than random scission, with the fact that “the average molecular weight and consequently the mechanical properties are more affected by random scission”.

4.6 Connecting biodegradation with property degradation

Next we demonstrate how to connect the entropy spring model and the biodegradation model to predict stiffness change of a biodegradable device. The spatial and temporal evolution of the average molecular weight can be calculated using finite element method for equations (2.3.12) and equation (2.3.13). The corresponding spatial and

temporal distribution of Young's modulus in a device can be obtained by using the relation between Young's modulus and average molecular weight given by, for example, figure 4.5.5. As a demonstration case, we consider a biodegradable rod made of PLLA as shown in figure 4.6.1: a small section of the rod is modelled with the finite element method. Despite the obvious axisymmetry of the problem, we still solve it as a general three-dimensional problem just to show that the method is generally valid.

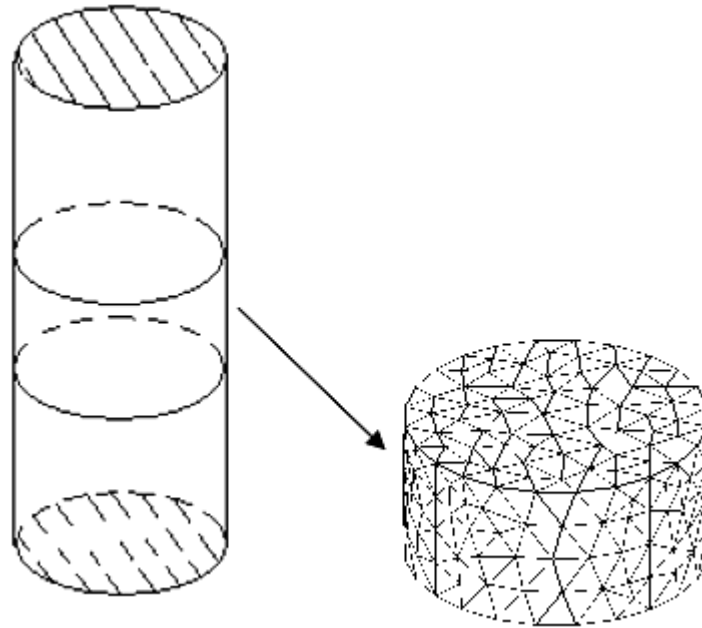


Figure 4.6.1 A biodegradable rod and its finite element model.

The boundary conditions are that there is no diffusive flux of C_m normal at the top and bottom cross-sections and that $C_m = 0$ at the outer surface of the rod. The following non-dimensional parameters were used in the analysis, as Chapter 3 suggests:

$$\bar{k}_1 = \frac{k_1}{k_2 C_{e0}^n} = 0.1 \quad \text{and} \quad \bar{D}_0 = \frac{D_0}{C_{e0}^n k_2 R^2} = 0.01. \quad \text{Here } D_0 \text{ is the diffusion coefficient of}$$

the monomers in the non-degraded polymer and R is the radius of the rod. The spatial distributions of the average molecular weight field at two different degradation times are presented in figure 4.6.2.

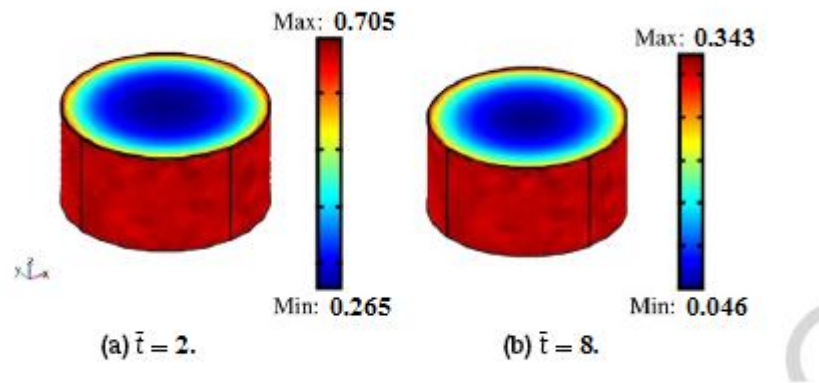


Figure 4.6.2 Distribution of normalised average molecular weight obtained by solving equations (2.3.12) and (2.3.13) using the finite element method at two normalised times of degradation.

The finite element results clearly show the heterogeneous nature of the biodegradation owing to the autocatalytic effect. The degradation is much faster at the core of the rod because of acid accumulation there. Each field in figure 4.6.2 corresponds to a distribution of Young's modulus calculated from the empirical fitting to the curve in figure 4.5.5:

$$\begin{aligned} \bar{E} = & -27.928\bar{C}_e^6 + 98.832\bar{C}_e^5 - 139.47\bar{C}_e^4 + 100.74\bar{C}_e^3 - 39.902\bar{C}_e^2 \\ & + 8.6334\bar{C}_e + 0.0195 \end{aligned} \quad (4.6.1)$$

The effective Young's modulus in the axial direction of the rod is then calculated as a function of the degradation time and presented in figure 4.6.3. This curve is the critical information from which the stress transfer from the rod to the broken bone that the rod protects can be calculated with the finite element method.

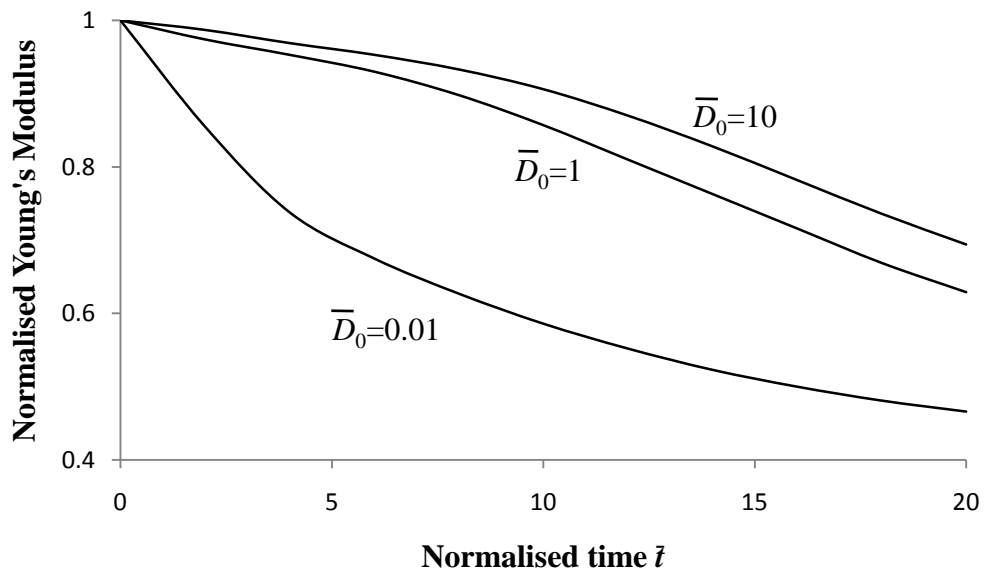


Figure 4.6.3 Effective Young's modulus of a biodegradable rod in its axial direction as a function of the normalised degradation time

An interesting observation in figure 4.6.3 is that the reduction in the effective Young's modulus of the rod does not show the incubation effect as much as the thin sample did. The acid accumulation at the core of the rod accelerates the initial degradation and leads to significant reduction in effective Young's modulus of the rod even in the early stage of the degradation.

4.7 Concluding remarks

In this chapter, a common thread in the set of long-term data for the degradation of PLAs reported by Tsuji (2002) is provided using the entropy spring theory. The central assumption is that relatively short polymer molecules do not affect the entropy change of an amorphous polymer during its deformation. By counting the number of polymer chains which are long enough to be mechanically active, the Young's modulus of the degrading polymer can be related to its average molecular weight in a Monte Carlo simulation of random and end scissions of the polymer chains. Four inputs of the model

**CHAPTER 4 AN ENTROPY SPRING MODEL FOR CHANGE IN YOUNG'S MODULUS OF
AMORPHOUS BIODEGRADABLE POLYMERS DURING BIODEGRADATION**

are (a) the rate ratio of end to random scissions, (b) initial molecular weight distribution of the polymer, (c) a threshold for the molecular weight, and (d) the sample size. Our study shows that the first and last parameters have little effect on the relationship between Young's modulus and the average molecular weight. The numerical results obtained from this simulation provides a connection between Young's modulus and average molecular weight that can be used in the biodegradation model to predict the spatial and temporal distribution of the Young's modulus in a device of any sophisticated shape. The case study in section 4.6 shows that even in the simple case of a cylindrical rod, the experimental data for the Young's modulus change obtained with very thin samples cannot be directly used to assess the stiffness of the rod. This is because the Young's modulus varies significantly in a device owing to the heterogeneous nature of the hydrolysis reaction. It is the stiffness of the rod, or the effective Young's modulus, that determines the stress transfer from the degrading device to the healing bone. The effective Young's modulus can only be determined after combination of this model with the degradation model in the previous chapter.

Chapter 5

Interaction between Device Degradation and Bone Healing in Orthopaedic Fixation – A Numerical Case Study

5.1 Introduction

Chapters 2, 3, and 4 have provided a complete set of models to capture the main features of biodegradable polymer degradation and Young's modulus decay. In this chapter, we focus on the practical application in orthopaedic device. As regarding to the biodegradable polymers, one of their important applications is fixation devices for fractured bones. As stated before, in order to ensure the complete healing of the broken bone, the mechanical property loss of the supporting devices needs to be controlled. Up to now, all our discussions have been about the biodegradable polymers themselves without consideration of the fractured bone. For bone regeneration, it is well known that the bone density is adaptive to the loading environment at a certain stage of the healing process. This brings extra complexity as the healing bone density is not only a function of time but also a function of mechanical loading. Models predicting the bone remodelling to loading environment are well developed, and can be sub-categorised into three types: bone remodelling is stimulated by strain (Turner *et al.*, 1997), stress (Sanz-Herrera *et al.*, 2009) or strain energy (Wienans *et al.*, 1992). The strain, stress or strain energy can all be calculated from structural mechanics analysis assuming that the elastic properties of the degrading device and the healing bone are known. Therefore the device degradation has a direct impact on bone healing – as the stiffness of the device gets smaller due to polymer degradation, more load is carried by the bone which stimulates further bone remodelling. If the device degrades too slowly, the bone would weaken itself due to lack of mechanical stimulation. The corresponding mathematical

problem is coupled between stress analysis, bone healing and polymer degradation. In this chapter we integrate stress analysis, a bone remodelling model and our polymer degradation model together. Our aim is to find out how the degradation rate of the material affects bone regeneration. The work presented in this chapter connects all parts of this thesis together and provides a complete case study for the biodegradation of orthopaedic fixation devices.

5.2 An integrated model for device degradation and bone remodelling

Stress shielding is the reduction in bone density attributed to removal of normal stress from the bone by an implant. According to Wolff's law, the bone in a healthy person or animal will remodel in response to the loads it is placed under. Therefore, if the loading on a bone decreases, the bone will become less dense and weaker because there is negative stimulus for continued remodelling. Ideally, the bone strength and the transfer of the mechanical load should follow the trend in the right-hand side of the curve below (figure 5.2.1).

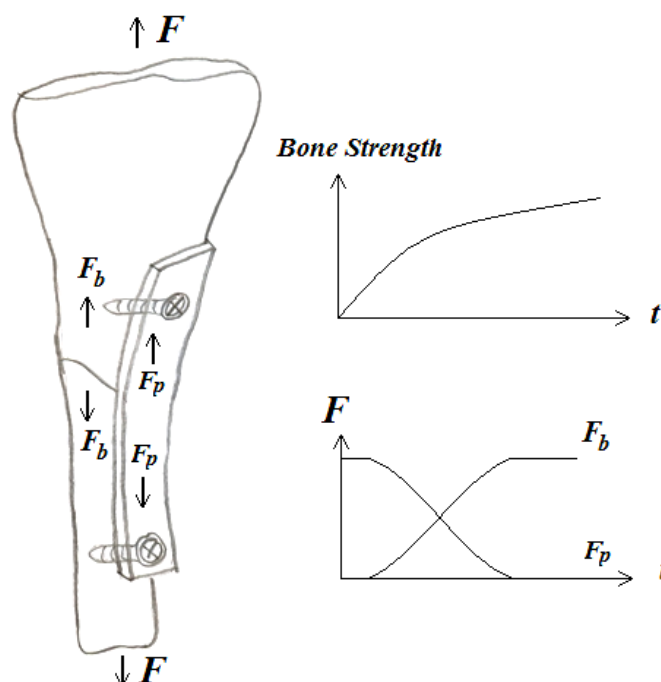


Figure 5.2.1 Scheme of the load transfer for biodegradable bone-supporting device applied to fractured bone during the healing process.

CHAPTER 5 INTERACTION BETWEEN DEVICE DEGRADATION AND BONE HEALING IN ORTHOPAEDIC FIXATION-A NUMERICAL STUDY

As the figure demonstrates, the load applied to the bone is allocated on the supporting plate at the beginning and slowly decreases thereafter as the device degrades. As a result, the bone gradually takes over the load from the plate and grows denser. This ideal situation requires the stiffness of the plate decreases to be achieved in a controlled and predictable manner.

The healing process of a broken bone can be divided into 3 distinctive stages (URL: http://en.wikipedia.org/wiki/Bone_healing; Doblar *et al.*, 2004):

I. Reactive stage

Not long after the bone fracture occurs, blood cells fill the gap of the fracture to stop the further bleeding and initiate the forming of granulation tissue.

II. Reparative stage

The granulation tissue is replaced by woven bone and cartilage in this step. The fracture gap is then filled by these woven bones and cartilage, restoring some of the original strength. Later, further ossification takes place to substitute both the cartilage and woven bone with trabecular bone which has most of the bone's original strength.

III. Remodelling stage

In the end, the entire fracture callus is remodelled in order to retrieve the original bone strength and shape.

The ideal load transfer from a degrading fixation device to a healing bone is schematically shown in figure 5.2.2.

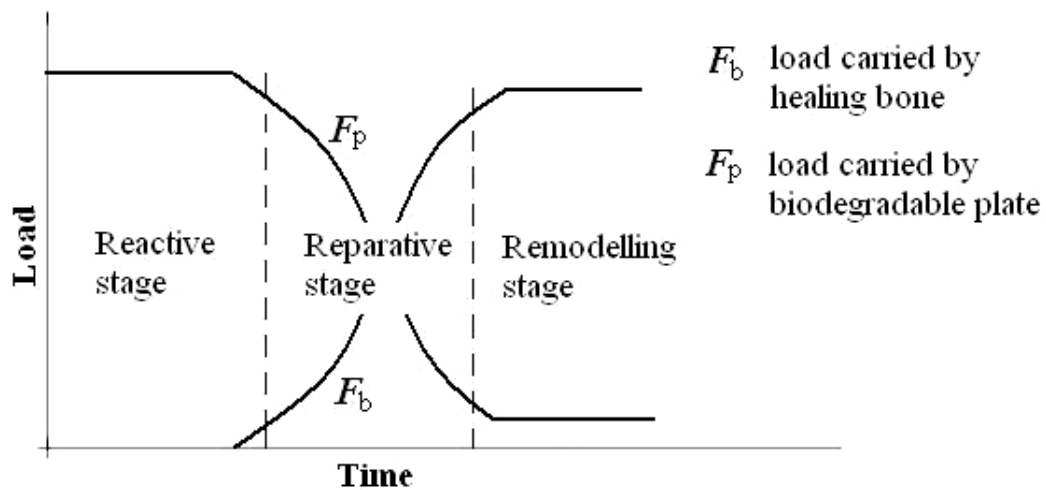


Figure 5.2.2 Schematic illustration of ideal load transfer from a fixation device to a healing bone corresponding to the bone healing stages

For stage I and the early part of stage II, the broken bone needs full protection as any Young's modulus decay in these stages would put the healing bone in danger. Therefore our study focuses on the later part of the reparative stage and the entire remodelling stage. The bone remodelling process is a lifelong process of generation and degeneration of bone cells. Mechanical stimulation plays a critical role in the process. A classical example is that of astronauts, who may lose part of their bone density in outer space whereas certain exercises help them to retrieve their bone strength. The fundamental considerations in the model for bone healing and device degradation are:

- A. The starting point of the model is when the fractured bone has already restored most of its strength and Young's modulus while the polymeric device, on the other hand, has only lost very little of its original stiffness.
- B. The supporting device loses its mechanical property because of the polymer degradation while the bone is remodelled to its original strength and shape.
- C. The degradation of the supporting devices affects the remodelling of bone as the bone density is adaptive to the loading condition.

A flow chart to demonstrate this interaction between different elements of the integrated model is shown in figure 5.2.3.

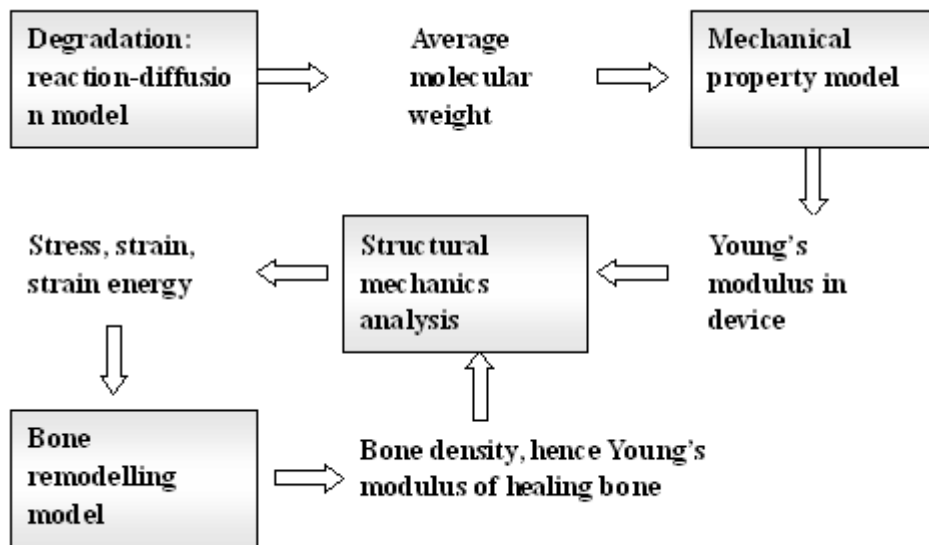


Figure 5.2.3 Integrated model for bone healing supported by a biodegradable fixation device

It is worth to point out again that the bone has regained most of its strength and Young's modulus at the beginning of this flow chart. At each time step, four steps are involved in the calculation, each feeding information to the others. The output of the analysis includes temporal and spatial evolution of the bone density and average molecular weight of the device. A finite element model is developed broadly based on the geometry of a bone fixation device as shown in figure 5.2.4.

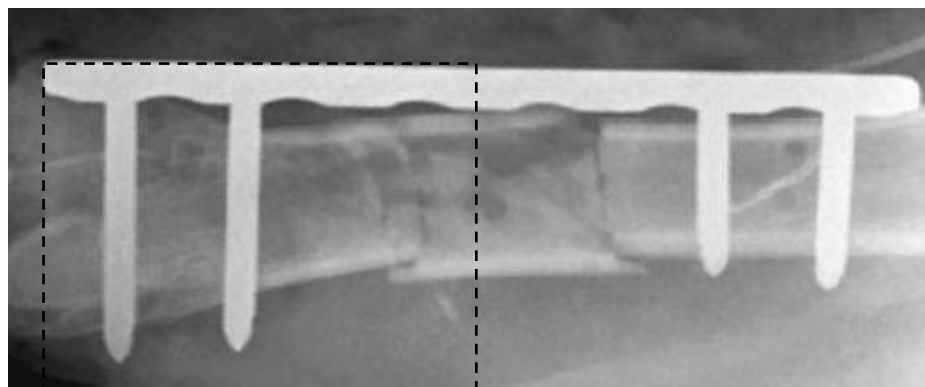


Figure 5.2.4 One-sided bone fixation (Reichert *et al.*, 2009).

**CHAPTER 5 INTERACTION BETWEEN DEVICE DEGRADATION AND BONE HEALING
IN ORTHOPAEDIC FIXATION-A NUMERICAL STUDY**

The part of the fixation-bone system outlined using the dash line in figure 5.2.4 is isolated out for analysis as shown in figure 5.2.5. For simplicity we consider a two dimensional model and assume plane stress condition in the stress analysis.

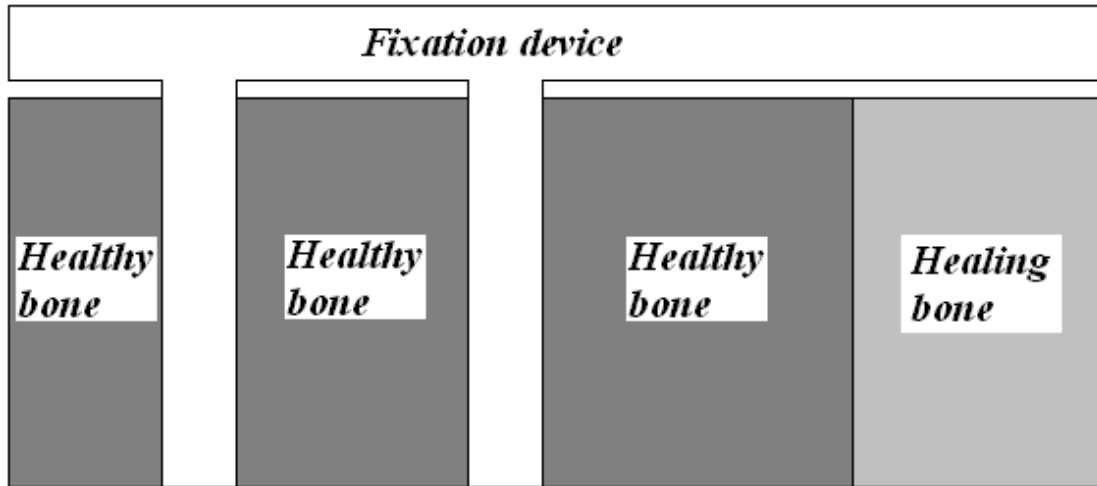


Figure 5.2.5 Geometry of the case study.

The model consists of three types of sub-domains: (1) the fixation device made of biodegradable polymer (white); (2) the healthy bone which has not fractured (deeper grey); (3) the healing bone with less density than normal bone (lighter grey). In the region of fractured bone, Young's modulus is considered as a power function of the bone density (Wienans *et al.*, 1992):

$$E = C_{density} \rho^3 \quad (5.2.1)$$

$C_{density}$ is the constant which is taken as $3790\text{MPa}(\text{gcm}^{-3})^{-3}$ following Wienans *et al.* (1992). Bone remodelling consists of two sub-processes: formation of the new bone and removal of the old bone. It is well known that bone can be self-adaptive to the loading environment and we take this factor into account by applying a rate equation following Turner *et al.* (1997)

$$\frac{dE}{dt} = A\varepsilon - B \quad (5.2.2)$$

in which E is the Young's modulus of the bone, A is the rate constant; B is the threshold constant value, ε represents the average strain that equals to the average absolute value of the three in plane principal strains:

$$\varepsilon = \frac{|\varepsilon_1| + |\varepsilon_2| + |\varepsilon_3|}{3} \quad (5.2.3)$$

Note that this remodelling equation only applies to the fractured bone; the remodelling process in the healthy bone is not considered in our model. For simplicity we neglect the fact that the bone is anisotropic and its Young's modulus can be different in different directions. In the special case shown in figure 5.2.4, the shear strain in the healing bone is small owing to the loading and boundary conditions. The two in plane principal strains can be taken as

$$\begin{aligned} \varepsilon_1 &\approx \varepsilon_x \approx \frac{\sigma_x}{E} \\ \varepsilon_2 &\approx \varepsilon_y \approx -\nu \frac{\sigma_x}{E} \\ \varepsilon_3 &\approx \varepsilon_z \approx -\nu \frac{\sigma_x}{E} \end{aligned}$$

in which ε_x , ε_y and σ_x , σ_y are the normal strains and direct stresses in the x and y directions; ν is the Poisson's ratio which is taken as 0.33 throughout the chapter. We therefore rewrite (5.2.2) as:

$$\frac{dE}{dt} = \frac{A}{2}(1 + 2\nu)\left(\frac{|\sigma_x|}{E}\right) - B \quad (5.2.4)$$

CHAPTER 5 INTERACTION BETWEEN DEVICE DEGRADATION AND BONE HEALING
IN ORTHOPAEDIC FIXATION-A NUMERICAL STUDY

Recently Sanz-Herrera *et al.* (2009) proposed a model to predict the bone remodelling behaviour inside biodegradable scaffolds. They proposed the following equations:

$$\frac{dC_{water}}{dt} = \alpha \Delta C_{water} \quad (5.2.5)$$

$$\frac{dMn}{dt} = -\beta C_{water} \quad (5.2.6)$$

and

$$E = E_0 \frac{Mn(t)}{Mn_0} \quad (5.2.7)$$

in which, C_{water} is the concentration of water in the polymer, Mn is the polymer molecular weight, E is Young's modulus of the biodegradable polymer, and α and β are constants. This is the state of the art of mathematical models for the interaction between polymer degradation and bone remodelling. It is obviously over simplistic and does not fit with the existing experimental evidence. For example, there is no experimental evidence for the polymer degradation rate to be dependent on the water concentration. In fact most experimental data show that water penetrates into the polymer much faster than the polymer degradation and that the degradation rate is independent of the water concentration. Furthermore the reduction in the Young's modulus always significantly lags behind the reduction in the average molecular weight as shown in Chapter 4. The linear relation of (5.2.7) cannot be correct. We therefore used the models developed in Chapters 2 and 4 to replace (5.2.6) and (5.2.7) and assume that the water penetration is much faster than all the other processes.

For the biodegradable polymer, the reaction-diffusion model developed in Chapter 2 is applied to calculate the molecular weight distribution:

IN ORTHOPAEDIC FIXATION-A NUMERICAL STUDY

$$\frac{dC_m}{dt} = k_1 C_e + k_2 C_e C_m^n + \frac{\partial}{\partial x} \left(D \frac{\partial C_m}{\partial x} \right) + \frac{\partial}{\partial y} \left(D \frac{\partial C_m}{\partial y} \right) \quad (5.2.8)$$

$$\frac{dC_e}{dt} = -(k_1 C_e + k_2 C_e C_m^n) \quad (5.2.9)$$

in which C_e, C_m are the concentration of ester bond and monomers, respectively; D is the diffusion coefficient; k_1 and k_2 are rate constants; x and y are the spatial coordinate; and t is the time. The stress distributed on the polymeric device could accelerate the degradation rate of the polymer but we ignored this factor here for simplicity. Followed the previous discussion in Chapter 2, the average molecular weight is calculated using:

$$\frac{Mn}{Mn_0} = \frac{C_e}{C_{e0}} \quad (5.2.10)$$

in which Mn is the polymer molecular weight, Mn_0 is the initial polymer molecular weight and C_{e0} is the initial ester bond concentration for polymers. It is convenient to use normalised equations in numerical studies. To normalise the equation, we define the following non-dimensionalised variables or constants:

$$\bar{C}_e = \frac{C_e}{C_{e0}} ; \quad \bar{C}_m = \frac{C_m}{C_{e0}} ; \quad \bar{x}_i = \frac{x_i}{l} ; \quad \bar{t} = \frac{t(1+2\nu)A\sigma_{\max}}{2E_{bone}^2} ; \quad \bar{A} = \frac{(1+2\nu)A\sigma_{\max}}{2E_{bone}^2 k_2 C_{e0}^n} ;$$

$$\bar{B} = \frac{2BE_{bone}}{(1+2\nu)A\sigma_{\max}} ; \quad \bar{\rho} = \frac{\rho}{\rho_{bone}} ; \quad \bar{\sigma} = \frac{\sigma}{\sigma_{\max}} ; \quad \bar{E} = \frac{E}{E_{bone}} ; \quad \bar{k}_1 = \frac{k_1}{C_{e0}^n k_2} ;$$

$$\bar{C}_{density} = \frac{\rho_{bone}^3}{E_{bone}} C_{density} ; \quad \bar{D}_0 = \frac{2D_0 E_{bone}^2}{(1+2\nu)A\sigma_{\max} l^2}$$

in which ρ_{bone} is the density of the healthy bone which is taken as 1.74g/cm^3 (Weinans *et al.*, 1992), l is a characteristic length scale taken as the diameter of the fixation pin.

CHAPTER 5 INTERACTION BETWEEN DEVICE DEGRADATION AND BONE HEALING
IN ORTHOPAEDIC FIXATION-A NUMERICAL STUDY

E_{bone} is the Young's modulus of healthy bone which is taken as 20GPa (Weinans *et al.*, 1992), σ_{max} is the stress that the fractured bone carries after the biodegradable device vanishes. We then have:

$$\frac{d\bar{C}_m}{d\bar{t}} = \frac{1}{A} (\bar{k}_1 \bar{C}_e + \bar{C}_e \bar{C}_m^n) + \frac{\partial}{\partial \bar{x}_i} (\bar{D} \frac{\partial \bar{C}_m}{\partial \bar{x}_i}) \quad (5.2.11)$$

$$-\frac{d\bar{C}_e}{d\bar{t}} = \frac{1}{A} (\bar{k}_1 \bar{C}_e + \bar{C}_e \bar{C}_m^n) \quad (5.2.12)$$

$$\bar{E} = \bar{C}_{density} \bar{p}^3 \quad (5.2.13)$$

$$\frac{d\bar{E}}{d\bar{t}} = \frac{|\bar{\sigma}_x|}{\bar{E}} - \bar{B} \quad (5.2.14)$$

$$\bar{Mn} = \bar{C}_e \quad (5.2.15)$$

The Young's modulus for the biodegradable polymer is calculated using equation (4.6.1). The effective diffusion coefficient D for monomers, we follow the expression presented in Chapter 3, i.e. D is related to porosity p through a numerical fitted relation:

$$D = D_0 + (1.3p^2 - 0.3p^3)(D_{max} - D_0) \quad (5.2.16)$$

in which D_0 is the diffusion coefficient of the monomers in the polymer before degradation starts, D_{max} is the diffusion coefficient of the monomers in the liquid filled pores which is taken as $D_{max} = 100D_0$, and p is the porosity which can be estimated as $1 - (\bar{C}_m + \bar{C}_e)$.

CHAPTER 5 INTERACTION BETWEEN DEVICE DEGRADATION AND BONE HEALING
IN ORTHOPAEDIC FIXATION-A NUMERICAL STUDY

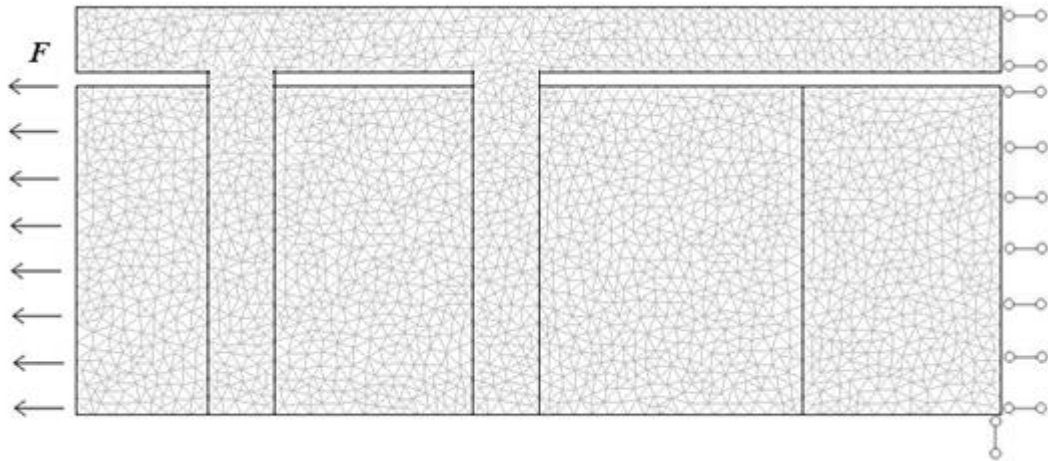


Figure 5.2.6 FE model of large bone defect with fixation showing boundary conditions.

Figure 5.2.6 show an example of the finite element models used in this study. A uniform normal stress is applied on the left boundary of the healthy bone, and perfect sink condition ($C_m = 0$) is assumed at the boundary of the fixation device. The right bottom corner is completely fixed to eliminate rigid motion. The applied load is carried at the right boundary by both the device and the bone. The total load carried by the device is referred to as F_p and the total load carried by the healing bone is referred to as F_b , both of which are calculated at each time step of the calculation. Due to mechanical equilibrium these two forces always add up to the applied load F , as schematically shown in figure 5.2.1. The initial conditions of the analysis are given in table 5.2.1.

**CHAPTER 5 INTERACTION BETWEEN DEVICE DEGRADATION AND BONE HEALING
IN ORTHOPAEDIC FIXATION-A NUMERICAL STUDY**

Table 5.2.1 The initial conditions for the case study

Region \ Model	Structural Mechanics	Reaction-Diffusion Model
Normal bone domain	$\bar{\rho} = 1; \bar{E} = 1;$ $\rho = 1.74g / cm^3;$ $E = 20GPa$	N/A
Healing bone domain	$\bar{\rho} = 0.95; \bar{E} = 0.85;$ $\rho = 1.65g / cm^3;$ $E = 17GPa$	N/A
Degradable polymer domain	$\bar{E} = 2;$ $E = 40GPa$	$\bar{C}_e = 1; \bar{C}_m = 0$

As shown in table 5.2.1, the initial value of Young's modulus for the unmanned biodegradable polymer is taken as 40GPa which can be reached only in reinforced biodegradable polymers rather than in normal PLA/PGAs. The initial Young's modulus of the fractured bone is taken as 17GPa, corresponding to the initial bone density of 1.65g/cm³ according to equation (5.2.1). This relatively large initial value for the Young's modulus of the healing bone is because the fractured bone has restored most of its Young's modulus in the reactive and partially reparative stages. Parameters shown in table 5.2.2 are fixed for all the cases in order to provide systematic reference point for the numerical study.

Table 5.2.2 Material parameters used in the analysis

\bar{k}_1	0.5
\bar{D}_0	0.01
\bar{B}	-1.74
$\bar{C}_{density}$	1

**CHAPTER 5 INTERACTION BETWEEN DEVICE DEGRADATION AND BONE HEALING
IN ORTHOPAEDIC FIXATION-A NUMERICAL STUDY**

The boundary conditions in figure 5.2.6, the initial conditions in table 5.2.1 and the parameters in table 5.2.2 are all applied to solve the non-dimensionalised equations of 5.2.11 to 5.2.15 using the finite element method. The output of the analysis includes the spatial and time evolution of the normalised bone density, which is calculated from the Young's modulus using equation (5.2.13), as well as the time evolutions of F_b and F_p . The finite element analysis was carried out using a commercial finite element package Comsol®.

5.3 Numerical results

The main purpose of this case study is to demonstrate how the degradation of the fixation device affects the healing process of the bone. In order to present the results relatively, we measure the normalised half degradation time for the degradable polymer to reach $\bar{C}_e = 0.5$ in each case to provide a reference to the bone remodelling rate. It

is useful to note that the definition of $\bar{A} = \frac{(1+2\nu)A\sigma_{\max}}{2E_{bone}^2 k_2 C_{e0}^n}$ indicates that this parameter

represents the relative rate between polymer degradation and bone remodelling. In other words, in the numerical analysis we manipulate the rate of bone remodelling relative to that of the degradation by adjusting this parameter \bar{A} . We study three different scenarios:

- A) the remodelling time is much longer than the half degradation time;
- B) infinit half degradation time;
- C) remodelling time is comparable to the half degradation time.

We consider two different defects in a healing bone. Firstly we consider a large cavity under healing i.e. the preclinical large segmental defects (Reichert *et al.*, 2009). Secondly we consider a normal fractured bone which has a crack like healing zone i.e. fatigue damage in the compact bone (Taylor and Lee, 1998). Note that the ratio of healing bone area size does not represent the real size ratio between segmental defects

**CHAPTER 5 INTERACTION BETWEEN DEVICE DEGRADATION AND BONE HEALING
IN ORTHOPAEDIC FIXATION-A NUMERICAL STUDY**

and fatigue damage; we only use a much smaller healing bone area to represent the size difference here instead of using exactly the actual size ratio. The numerical studies start with one-sided fixation and the analysis is then repeated for symmetric fixation in order to study the possible different behaviour in the two types of supports.

5.3.1 Large healing cavity

Scenario A – Fast device degradation

Scenario A means the polymer device loses most of its stiffness at the beginning of the bone remodelling. The growth of healing bone density (averaged over the entire remodelling bone sub-domain) and the load transfer from the supporting device to the bone are presented in figures 5.3.1 and 5.3.2. The polymer molecular weight averaged over the device domain is also plotted in the figures to provide a reference.

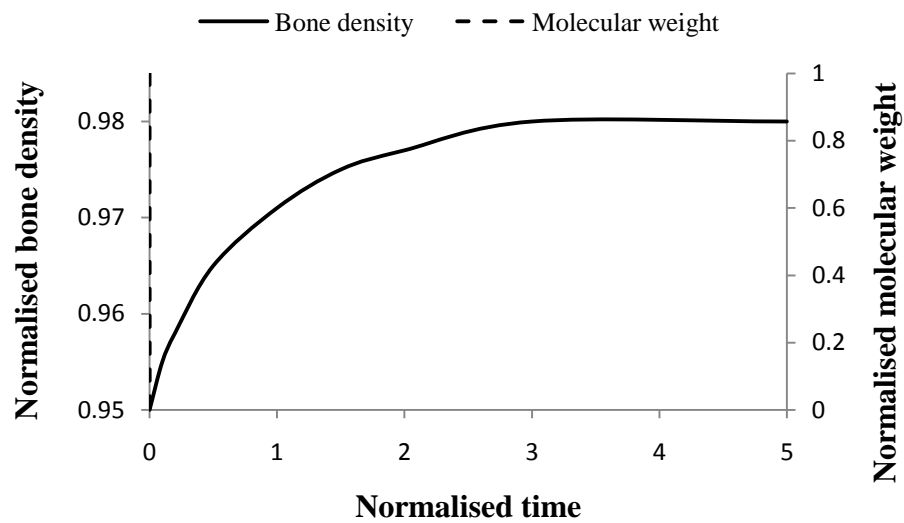


Figure 5.3.1 Bone density and polymer molecular weight averaged over the bone and polymer domains respectively as functions of time for large bone defect fixation with $\bar{A} = 5 \times 10^{-4}$ (scenario A).

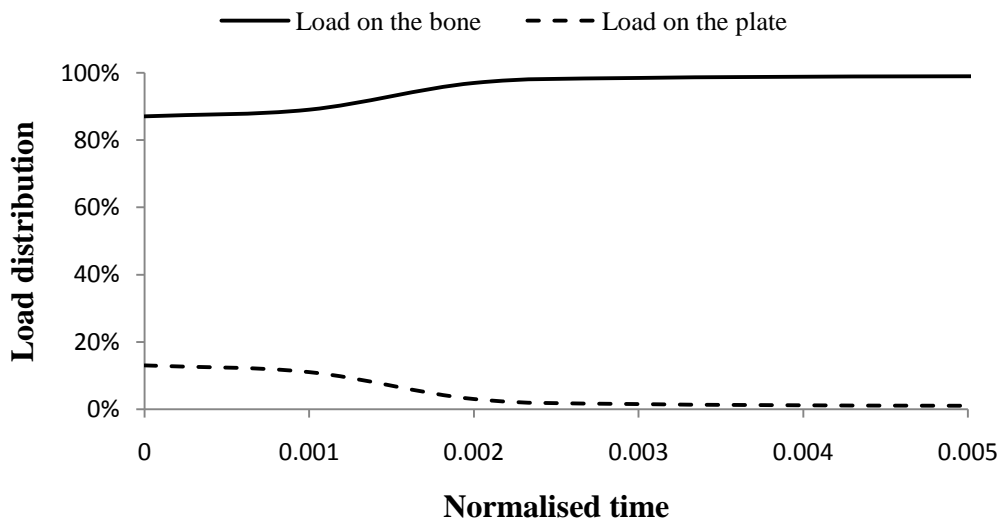


Figure 5.3.2 Load transfer from the supporting device to the healing bone for large bone defect fixation with $\bar{A} = 5 \times 10^{-4}$ (scenario A).

The density growth follows a smooth curve and reaches 98% of the normal healthy bone. The Young's modulus of the fixation device does not reach zero even in the very late stage of calculation. Hence the bone does not carry the full load that would make it

**CHAPTER 5 INTERACTION BETWEEN DEVICE DEGRADATION AND BONE HEALING
IN ORTHOPAEDIC FIXATION-A NUMERICAL STUDY**

to reach the full healthy density. While the bone is regaining its original density, the load allocated on the healing bone increases owing to the molecular weight and stiffness loss for the fixation devices. The actual molecular weight distributions in the fixation device at various times are shown in figure 5.3.3.

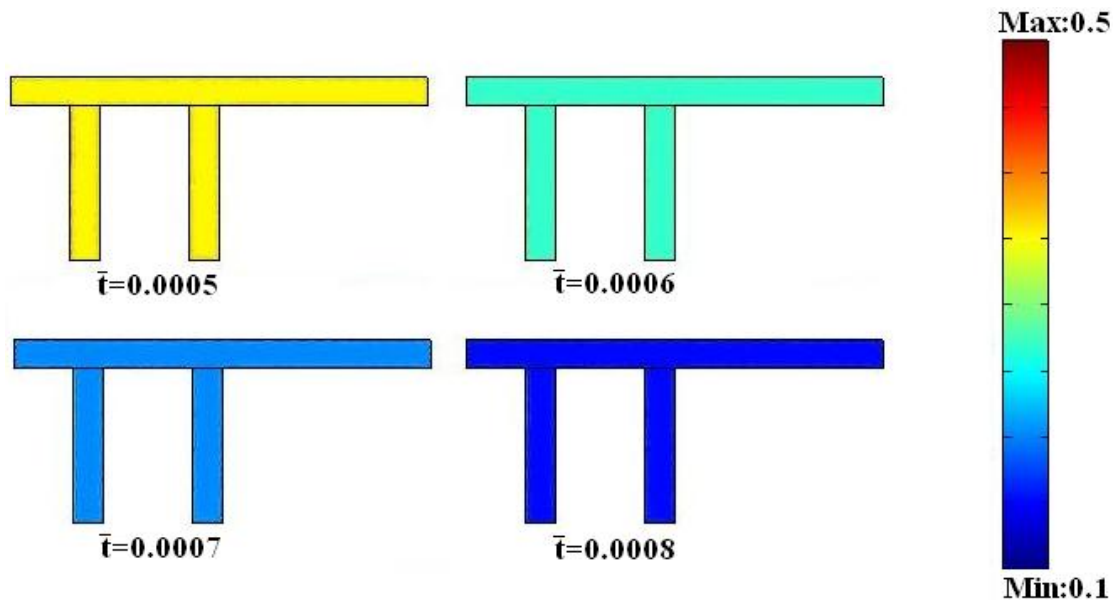


Figure 5.3.3 The spatial distribution of the average molecular weight in the fixation device at $\bar{t} = 5 \times 10^{-4}$, $\bar{t} = 6 \times 10^{-4}$, $\bar{t} = 7 \times 10^{-4}$, $\bar{t} = 8 \times 10^{-4}$, respectively.

The colour represents the normalised average molecular weight.

Figure 5.3.3 shows the spatial distribution of the average molecular weight at 4 different normalised times. The colour represents the average molecular weight normalised by its initial value. It can be observed that the degradation is heterogeneous with the inside of the device degrading faster than the surface regions. The very small normalised time indicates that the degradation of the polymer is considerably faster than the bone remodelling shown in figure 5.3.1.

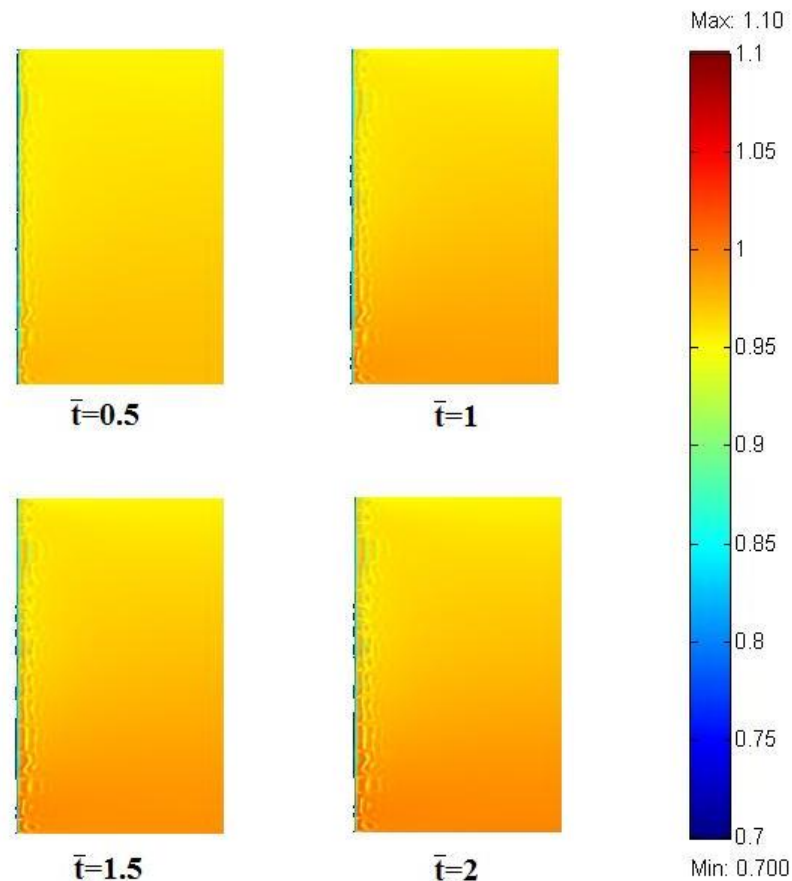


Figure 5.3.4 The spatial distribution of bone density at $\bar{t}=0.5$, $\bar{t}=1$, $\bar{t}=1.5$, $\bar{t}=2$, respectively. The colour represents the bone density normalised by 20GPa.

Figure 5.3.4 shows the spatial distribution of the bone density at 4 different normalised times. In consistency with figure 5.3.1, the average bone density in these 4 time steps are monotonically increasing. It can be observed from the figure that distribution of the bone density is more or less uniform in the healing region throughout the remodelling process.

Scenario B – Zero device degradation

Now let us consider a situation where the polymeric device degrades at a very slow rate, which is the current practice in most of the orthopaedic fixations using bioresorbable polymers. Some biodegradable device remains intact after 5 years of implantation.

CHAPTER 5 INTERACTION BETWEEN DEVICE DEGRADATION AND BONE HEALING
IN ORTHOPAEDIC FIXATION-A NUMERICAL STUDY

The extreme is that the fixation device never loses its Young's modulus. Assuming no degradation in the device, the change of bone density and the load transfer from the device to the bone are shown in figures 5.3.5 and 5.3.6.

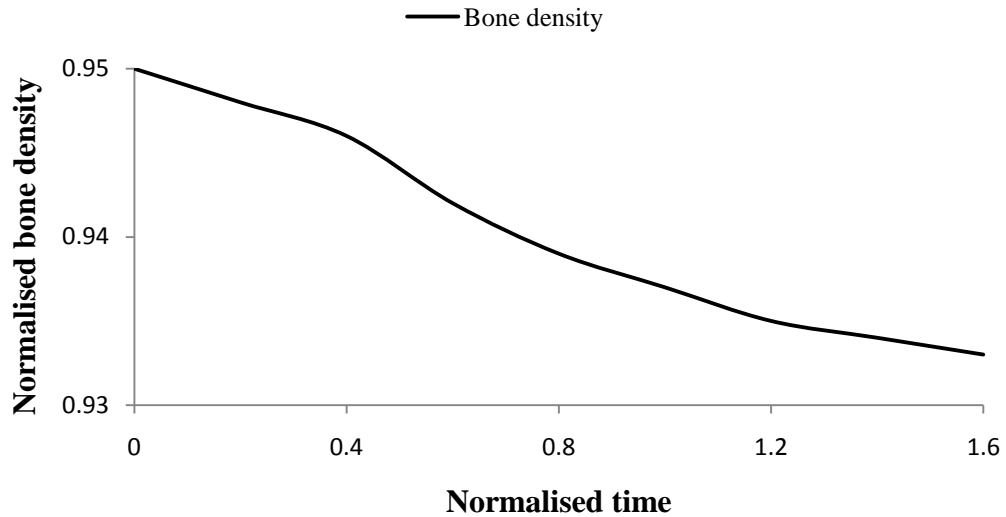


Figure 5.3.5 Bone density averaged over the bone domain as a function of time for large bone defect fixation with $\bar{A} \rightarrow \infty$ (scenario B).

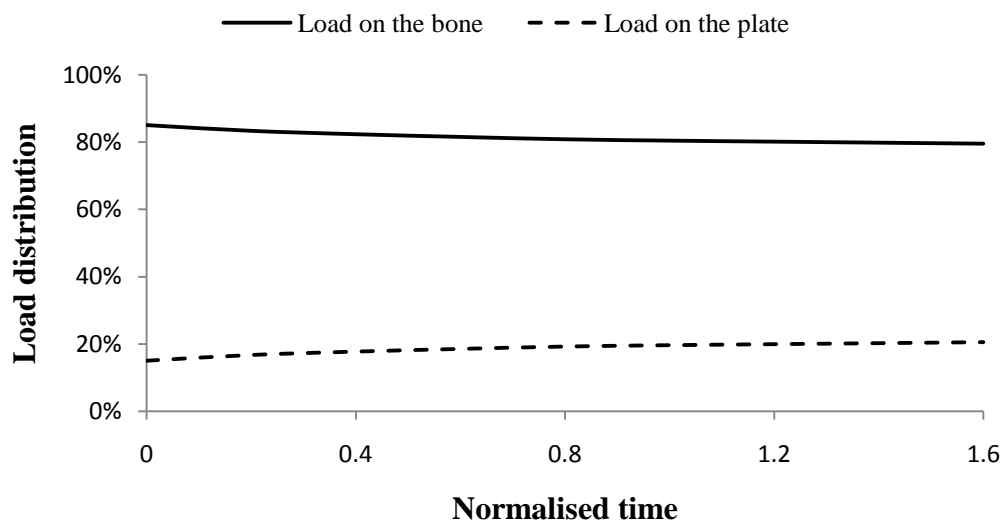


Figure 5.3.6 Load transfer from the fixation device to the healing bone for large bone defect with $\bar{A} \rightarrow \infty$ (scenario B)

**CHAPTER 5 INTERACTION BETWEEN DEVICE DEGRADATION AND BONE HEALING
IN ORTHOPAEDIC FIXATION-A NUMERICAL STUDY**

Bone density continues to decrease as shown in figure 5.3.5 because the strong fixation device shields the remodelled bone from sufficient stress to cause positive growth of the bone. A small transfer of load from the bone to the device occurs as shown in figure 5.3.6 as the bone degrades and its Young's modulus reduces. The transfer is nevertheless stabilised over a longer term. Setting $\bar{A} \rightarrow \infty$ means that equations (5.2.11) & (5.2.12) are ignored during the calculation and we only solve equations (5.2.13) to (5.2.15) and the stress analysis simultaneously.

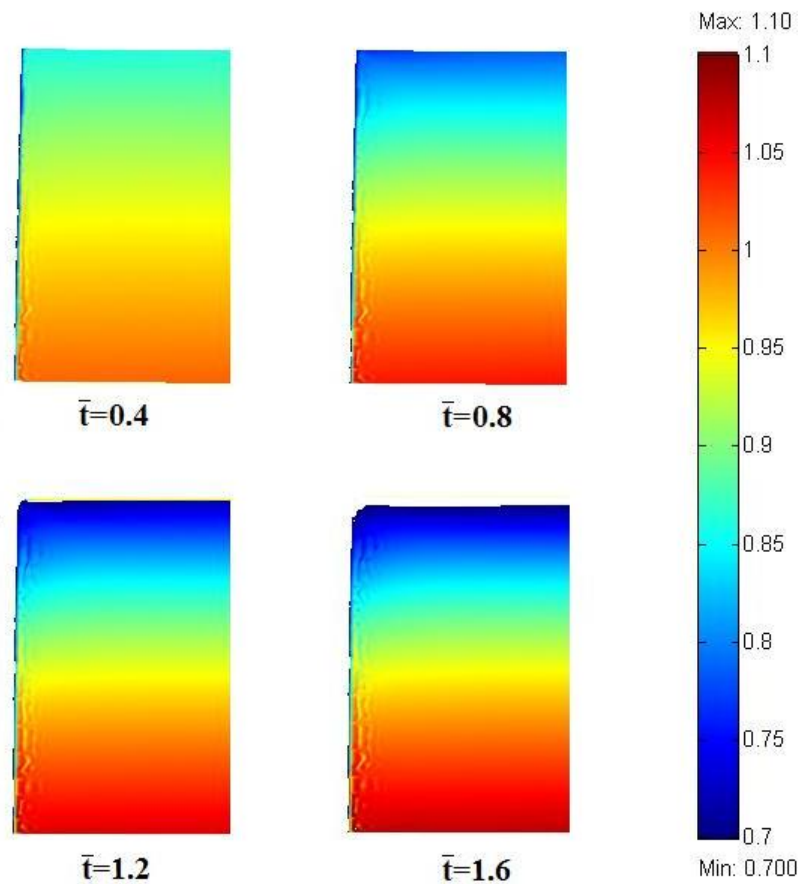


Figure 5.3.7 The spatial distribution of bone density at $\bar{t} = 0.4$, $\bar{t} = 0.8$, $\bar{t} = 1.2$, $\bar{t} = 1.6$, respectively. The colour represents the bone density normalised by 20GPa.

Figure 5.3.7 shows the spatial distribution of the bone density at 4 different normalised times. It can be observed from the figure that during the remodelling process, the top part of the healing bone is degenerated owing to the lack of stress stimulation while the bottom part of the remodelling bone reaches the full healthy bone density. At later time,

**CHAPTER 5 INTERACTION BETWEEN DEVICE DEGRADATION AND BONE HEALING
IN ORTHOPAEDIC FIXATION-A NUMERICAL STUDY**

we can observe that the healing bone changes its shape as the top region of the remodelling bone keeps losing its density. Therefore the vertical height of the remodelling bone is reduced. In other words, using a non-degradable fixation plate with high Young's modulus, the near side of the remodelling bone would be degenerated by stress shielding and the remodelling bone would change its shape. The stress shielding can be understood by examining the strain distribution from the top to the bottom of the remodelling bone which is given in figure 5.3.8.

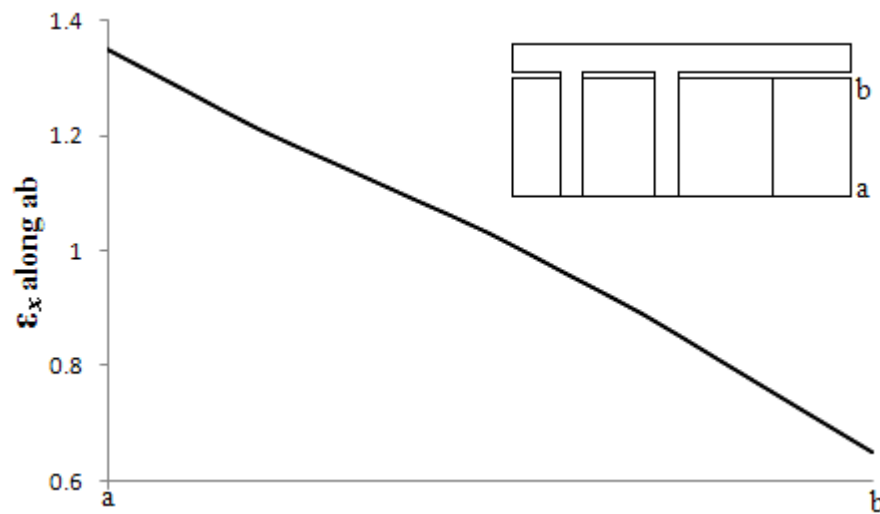


Figure 5.3.8 Distribution of direct strain in the horizontal direction along the side a-b of the healing bone

The vertical axis in figure 5.3.8 represents the normalised direct strain in the horizontal direction along the side $a-b$ of the healing bone. The horizontal axis is the position on that boundary from a to b as indicated in the figure. The figure corresponds to the first image in figure 5.3.7 at $\bar{t}=0.4$. Note that the strain in this figure is a value normalised by $\frac{\sigma_{\max}}{E_{bone}}$ because both the stress and Young's modulus have been normalised in the previous discussion. We can observe that it is this heterogeneous strain distribution that reduces the bone density at top end of the remodelling bone in the later time steps.

Scenario C –Moderate degradation

Now let's consider the scenario between the previous two situations. In this case, the bone remodelling rate is comparable to the degradation rate of the polymer device. The change in bone density and the load transfer are shown in figures 5.3.9 and 5.3.10. The change in the polymer molecular weight averaged over the entire device is also shown in the figures to provide a reference.

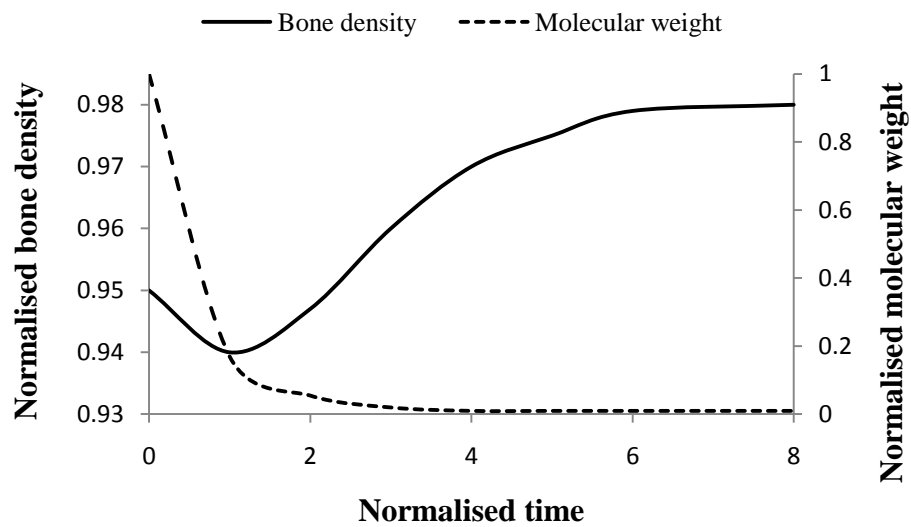


Figure 5.3.9 Bone density and polymer molecular weight averaged over the bone and polymer domains respectively as functions of time for large bone defect with $\bar{A} = 0.5$ (scenario C).

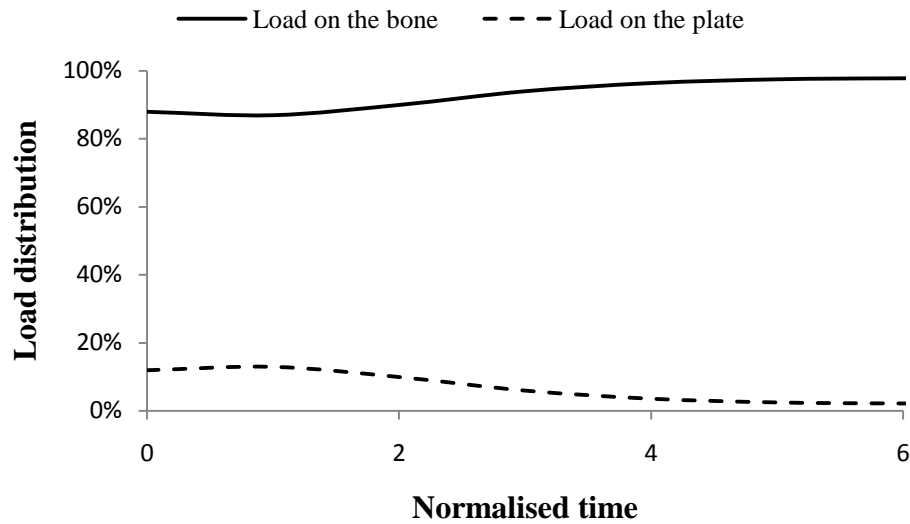


Figure 5.3.10 Load transfer from the supporting device to the healing bone for large bone defect with $\bar{A} = 0.5$ (scenario C)

The density of the bone reduces at first because the strong supporting device shields the bone and later increases because the weakening fixation transfers the load back to the remodelled bone. It is noteworthy that, according to the two curves in figure 5.3.9, the positive bone remodelling process started when the polymer lost most of its Young's modulus. After that, the remodelling bone retrieved its original density and Young's modulus rapidly. The molecular weight distribution in the degrading device during the degradation is presented in figure 5.3.11.

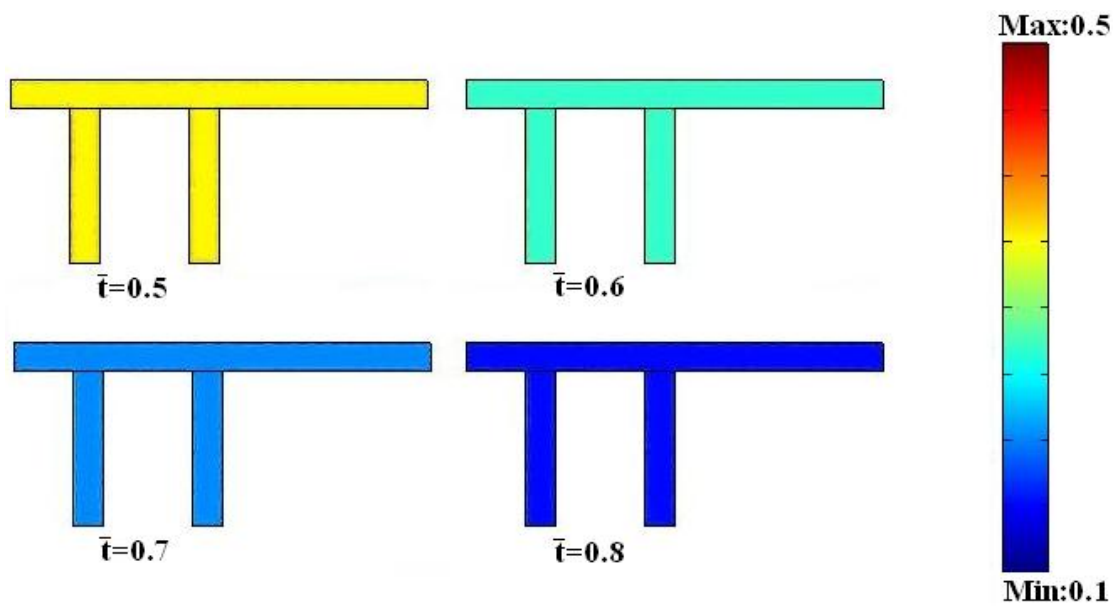


Figure 5.3.11 The spatial distribution of the average molecular weight at $\bar{t} = 0.5$, $\bar{t} = 0.6$, $\bar{t} = 0.7$, $\bar{t} = 0.8$, respectively. The colour represents the distribution of polymer concentration.

The molecular weight distribution at four different times in figure 5.3.11 shows identical degradation situation as those in the figure 5.3.3 with only difference in the degradation time. According to equations (5.2.11) & (5.2.12), the degradation behaviour of the biodegradable material is determined by the values of \bar{k}_1 , \bar{D}_0 and \bar{A} . We have fixed the values of \bar{k}_1 and \bar{D}_0 are fixed, and varied the value of \bar{A} in our studies. However changing \bar{A} only scales the normalised time in equations (5.2.11) & (5.2.12) and does not change the molecular weight distribution in the device.

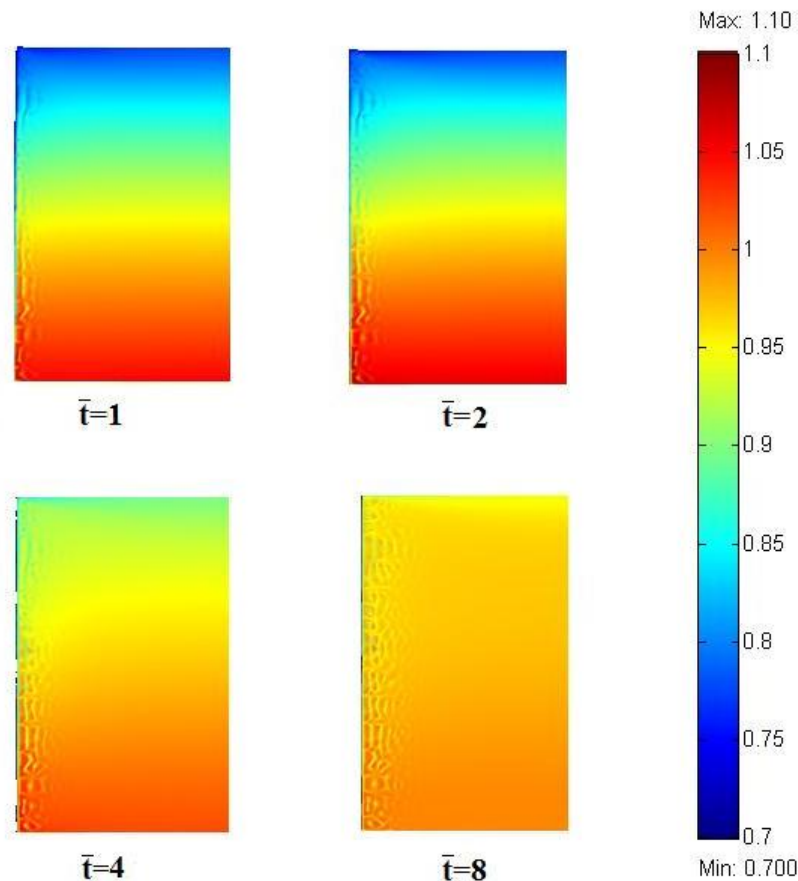


Figure 5.3.12 The spatial distribution of bone density at $\bar{t}=1$, $\bar{t}=2$, $\bar{t}=4$, $\bar{t}=8$, respectively. The colour represents the bone density normalised by 20GPa.

Figure 5.3.12 shows the distribution of bone density in the remodelling bone. At early time steps, similar to scenario B, the top part of the remodelling bone lost its density while the bottom part remains unchanged. As the fixation device degrades and load is transferred to the remodelling bone, the entire remodelling bone domain shows uniform distribution like scenario A. We can consider the bone density evolution in scenario C as a combination of the previous two scenarios.

We can conclude from the above three cases that bone remodelling can lead to either degeneration owing to the stress shielding or strengthening owing to the device degradation. Which of the two trends occurs is controlled by the parameter \bar{A} , which describes the relative rate ratio between the bone growth and the device degradation.

**CHAPTER 5 INTERACTION BETWEEN DEVICE DEGRADATION AND BONE HEALING
IN ORTHOPAEDIC FIXATION-A NUMERICAL STUDY**

In scenarios A and C, the parameter \bar{A} is chosen to be small enough to ensure that the bone remodels up to almost its full density, while in case B the parameter \bar{A} is set so large that most of the load is transferred from the fixation plate back to the remodelling bone. A critical value of the parameter \bar{A} therefore exists below which the bone density growth can overcome the negative effect from stress shielding and regenerate up to full density. Our numerical study shows that the critical value is around $\bar{A} = 2$. Figures 5.3.13 and 5.3.14 show the density change and load transfer for $\bar{A} = 2$.

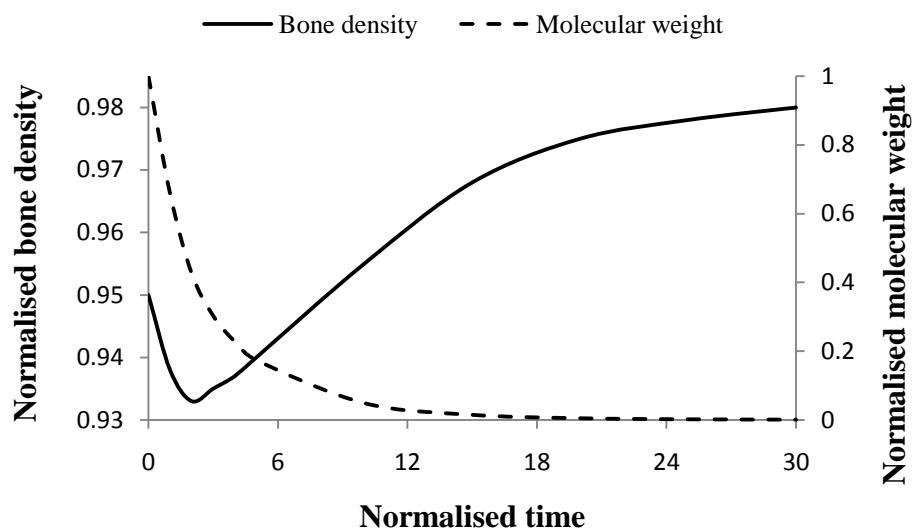


Figure 5.3.13 Bone density and polymer molecular weight averaged over the bone and polymer domains respectively as functions of time for large bone defect for $\bar{A} = 2$.

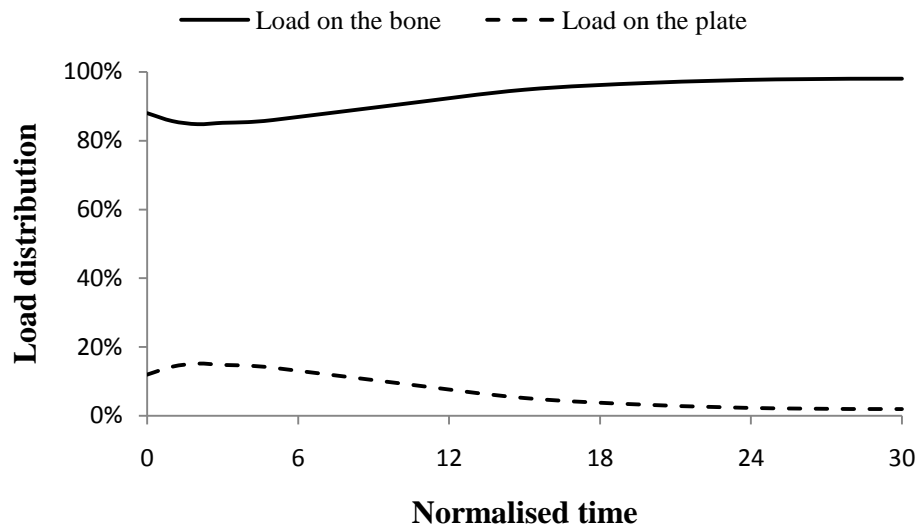


Figure 5.3.14 Load transfer from the supporting device to the healing bone for large bone defect fixation with critical value $\bar{A} = 2$.

A mechanism similar to scenario C can be observed from the above two figures. The difference between these two cases is that the bone density decreases for a longer time in figure 5.3.13 comparing to that in figure 5.3.9 of scenario C, and that after the load has been transferred to the remodelling bone, the bone requires longer time to retrieve its full density. The load applied on the remodelling bone in figure 5.3.14 also takes a longer time to reach its maximum value. The reason for these two differences is because the polymer degradation time, which is decided by \bar{A} , is longer than that in scenario C.

5.3.2 Crack like healing zone

Next we consider a case of a fractured bone with a crack like defect as shown in figure 5.3.15.

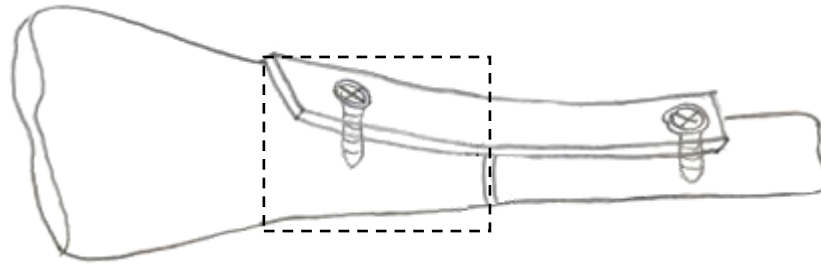


Figure 5.3.15 A schematic illustration of bone fracture and fixation

We use a model that is identical to that shown in figure 5.2.6 except for the size of bone defect. We can therefore compare the numerical results between two cases and highlight the possible effect of the defect size on the bone remodelling process. The FE mesh for this case is presented in figure 5.3.16.

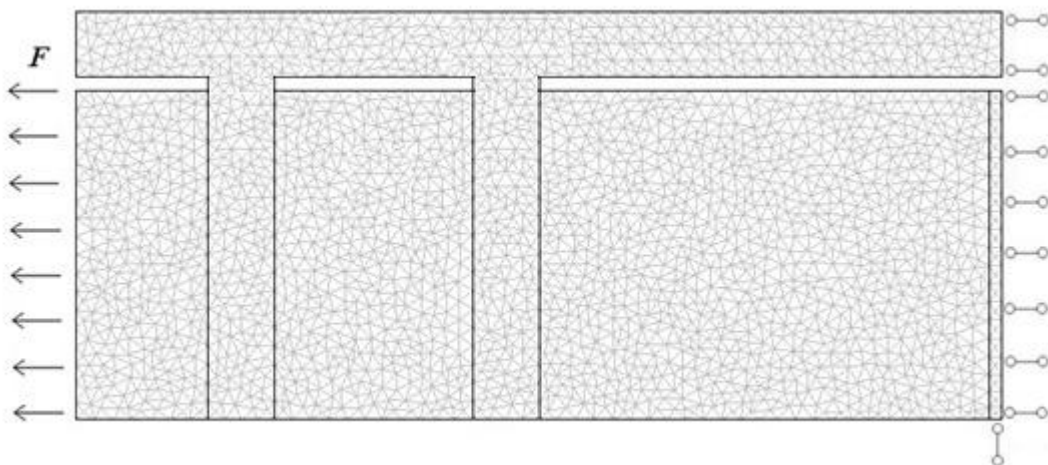


Figure 5.3.16 FE mesh and boundary conditions for a bone with crack like defect and fixation

The analysis for the three scenarios of the previous case is repeated here.

Scenario A – Fast device degradation

The numerical results of changes in the bone density and molecular weight are presented in figure 5.3.17 and the load transfer curves are shown in figure 5.3.18.

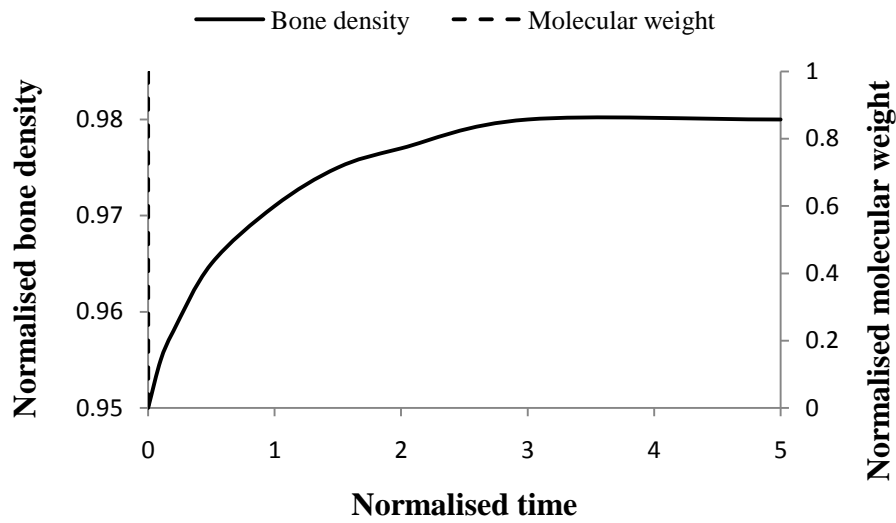


Figure 5.3.17 Bone density and polymer molecular weight averaged over the bone and polymer domains respectively as functions of time for crack like defect with $\bar{A} = 5 \times 10^{-4}$ (scenario A).

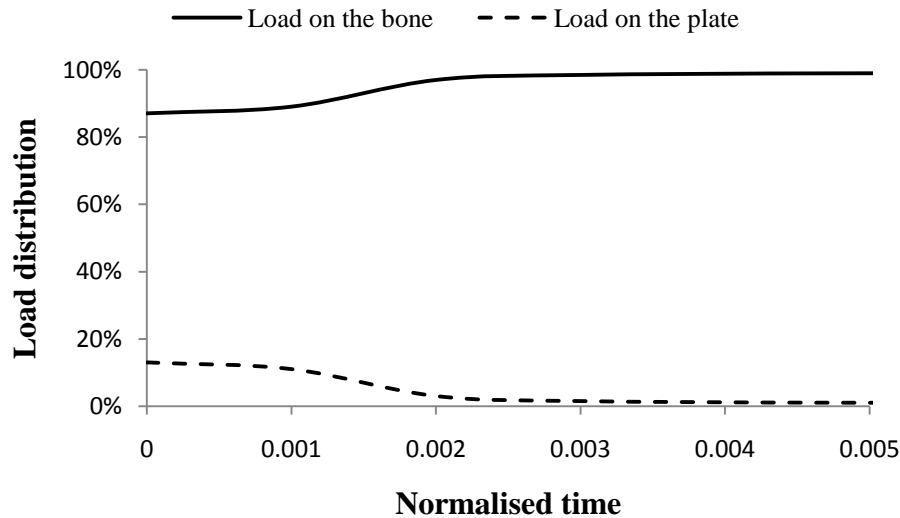


Figure 5.3.18 Load transfer from the supporting device to the healing bone for crack like bone defect using $\bar{A} = 5 \times 10^{-4}$ (scenario A).

For scenario A, figure 5.3.17 shows that the bone density increases to almost its full healthy density; while figure 5.3.18 shows that the load on the boundary of healing bone follows the same trend with bone density remodelling. Note that the above two figures

**CHAPTER 5 INTERACTION BETWEEN DEVICE DEGRADATION AND BONE HEALING
IN ORTHOPAEDIC FIXATION-A NUMERICAL STUDY**

are very similar to figures 5.3.1 and 5.3.2. This suggests that the bone remodelling is not affected by the size of the defect. We further study if this is the case for scenarios B and C.

Scenario B – Zero device degradation

The change in the bone density for the remodelling bone and the load transfer curves are shown in figures 5.3.19 and 5.3.20, respectively.

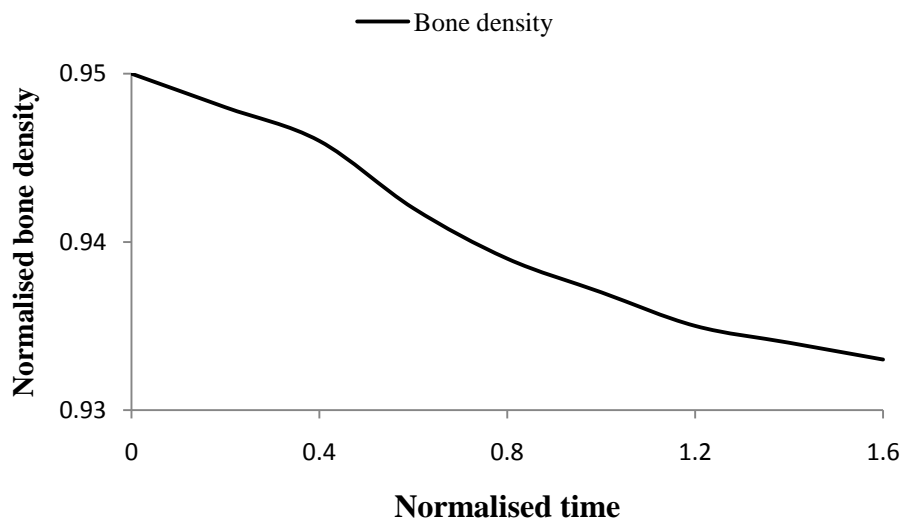


Figure 5.3.19 Bone density averaged over the bone domain as function of time for crack like small bone defect with $\bar{A} \rightarrow \infty$ (scenario B).

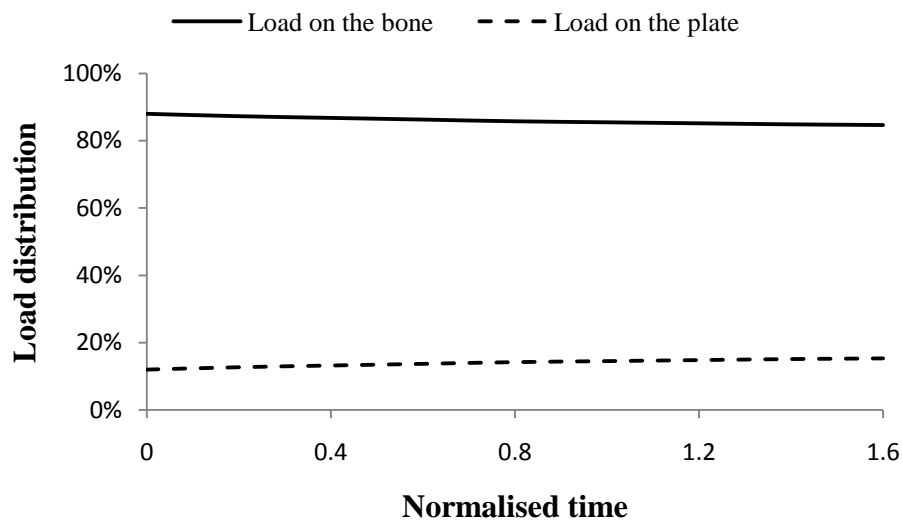


Figure 5.3.20 Load transfer from the supporting device to the healing bone with a crack like defect for $\bar{A} \rightarrow \infty$ (scenario B).

The density growth curves for scenario B (figure 5.3.19) is rather expected since we assume the device degrades similarly to that in the large defect case. The monotonic degeneration of the remodelling bone is caused by a negative feedback mechanism: if the Young's modulus of the remodelling bone becomes smaller, less load will be allocated on the remodelling bone domain; if less load is applied, the bone will degenerate more. Again the behaviour here is very similar to that shown in the case of large defect zone.

Scenario C –Moderate degradation

The change in the average bone density within remodelling bone domain and the load transfer from the supporting device to the remodelling bone are shown in figures 5.3.21 and 5.3.22, respectively. The change of molecular weight of the device is also plotted in figure 5.3.21 for reference.

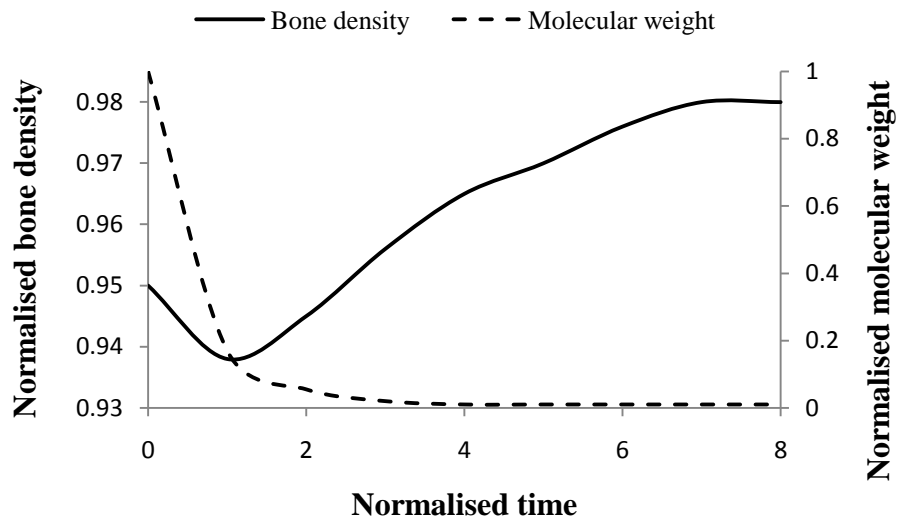


Figure 5.3.21 Bone density and polymer molecular weight averaged over the bone and polymer domains respectively as functions of time for small crack like bone defect with $\bar{A} = 0.5$ (scenario C).

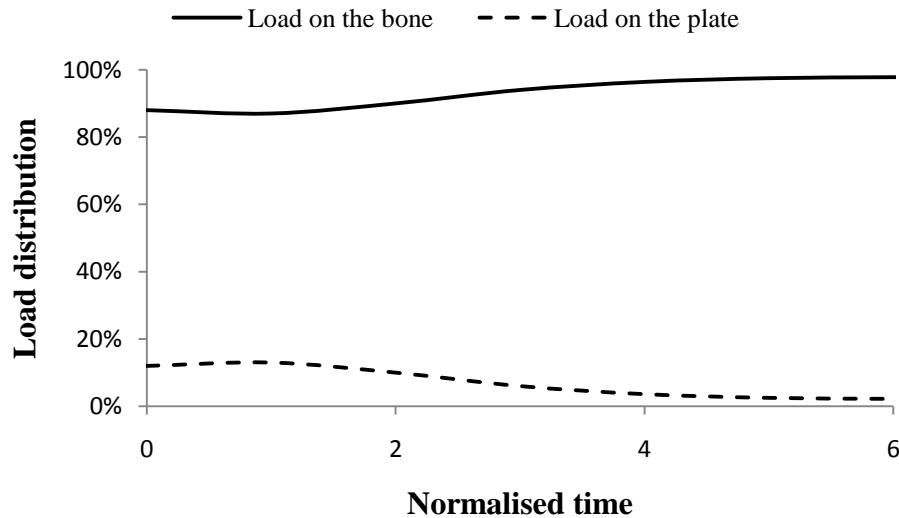


Figure 5.3.22 Load transfer from the supporting device to the healing bone with a crack like defect for $\bar{A} = 0.5$ (scenario C).

It can be observed from these figures that the change in the bone density (figure 5.3.21) and the load transfer (figure 5.3.22) behave very similar to scenario C for the case of a

large defect. Therefore it can be concluded that the size of the defect has little effect on the bone remodelling behaviour.

5.3.3 Symmetric fixation

Our final case study is a discussion on the effect of the mechanical boundary condition on the bone remodelling. We consider a different boundary condition as shown in figure 5.3.23. This boundary condition represents a symmetric fixation which is rarely practiced in orthopaedic surgery because it requires opening far more tissues around the broken bone than the one-sided fixation. However the study in this section will demonstrate that the symmetric fixation is beneficial to the bone healing. Therefore if circumstance allows, in a severe injury for example, symmetric fixation should be preferred.

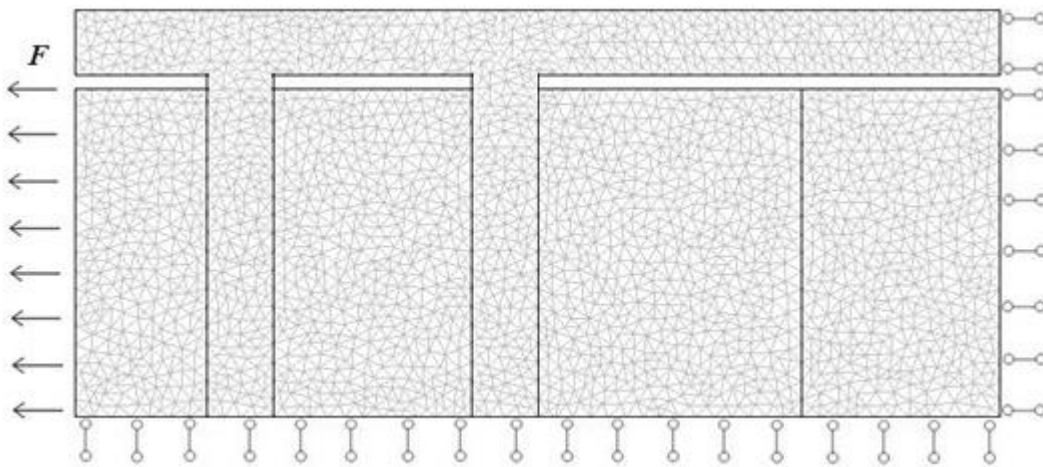


Figure 5.3.23 FE mesh of symmetric fixation with boundary condition

We consider two sided fixation as in figure 5.3.23. Everything in this case remains the same as those in the one-side fixation except that the bottom boundary is not allowed to move freely in the vertical direction. The entire bottom boundary therefore represents a symmetry line. The boundary condition for the monomer diffusion in the fixation pins at the bottom boundary should be set as zero flux across the boundary. However in order to highlight the effect of the displacement boundary condition on the model

**CHAPTER 5 INTERACTION BETWEEN DEVICE DEGRADATION AND BONE HEALING
IN ORTHOPAEDIC FIXATION-A NUMERICAL STUDY**

outcome, the same perfect sink condition is used as that in the one-sided fixation. Figure 5.3.24 and 5.3.25 compares the deformation and the spatial distribution of the average principal strain in the system. It can be observed from the two figures that a significant bending deformation occurs in the non-symmetric case, leading to a non-uniform distribution of the average principal strain in the bone. Because the average strain acts as the mechanical stimulus for the bone remodelling, this non-uniform distribution causes differential bone healing which does not exist in the symmetric fixation as shown the following results.

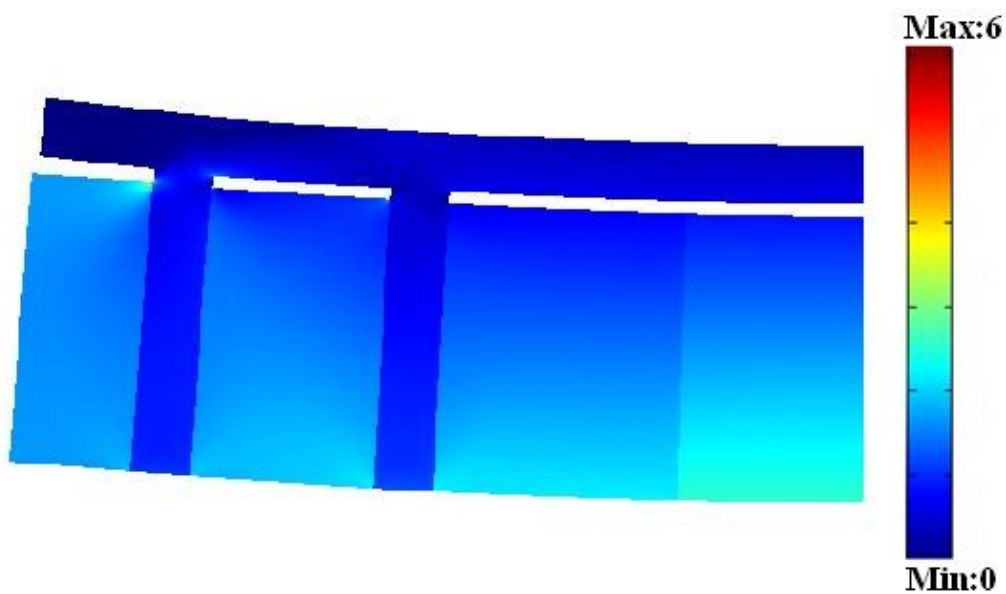


Figure 5.3.24 The deformation of one-side bone fixation, colour represents average strain.

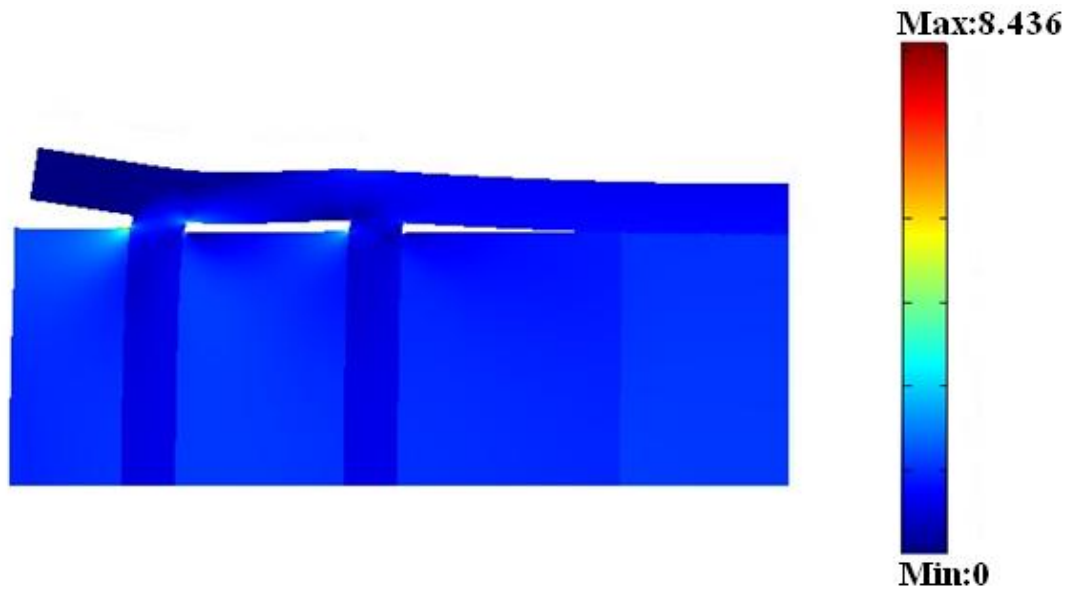


Figure 5.3.25 The deformation of symmetric bone fixation, colour represents average strain.

Figure 5.3.24 and 5.3.25 are both the average strain distribution to the entire bone fixation system; colour in the figures represents the average strain which is defined in equation (5.2.3). The deformation shapes from these two figures are quite different from each other and so is the average strain distribution within the healing bone domain. Instead of a heterogeneous average strain distribution in healing bone area in figure 5.3.24, figure 5.3.25 shows a uniform strain field in the healing bone domain. This would change the remodelling behaviour of the bone significantly, the discussion is presented in this section.

Scenario A – Fast device degradation

The bone density growth together with the molecular weight loss is shown in figure 5.3.26 while the load transfer curves are shown in figure 5.3.27.

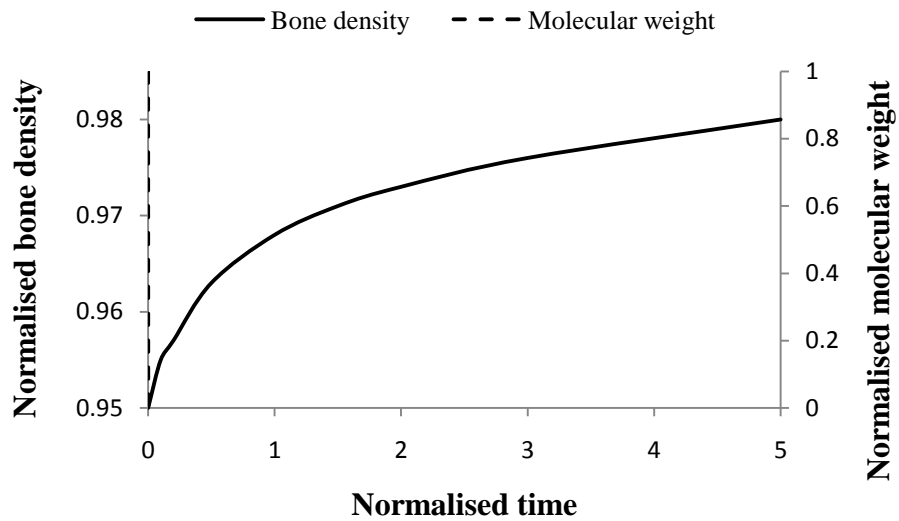


Figure 5.3.26 Bone density and polymer molecular weight averaged over the bone and polymer domains respectively as functions of time for symmetric fixation with $\bar{A} = 5 \times 10^{-4}$ (scenario A).

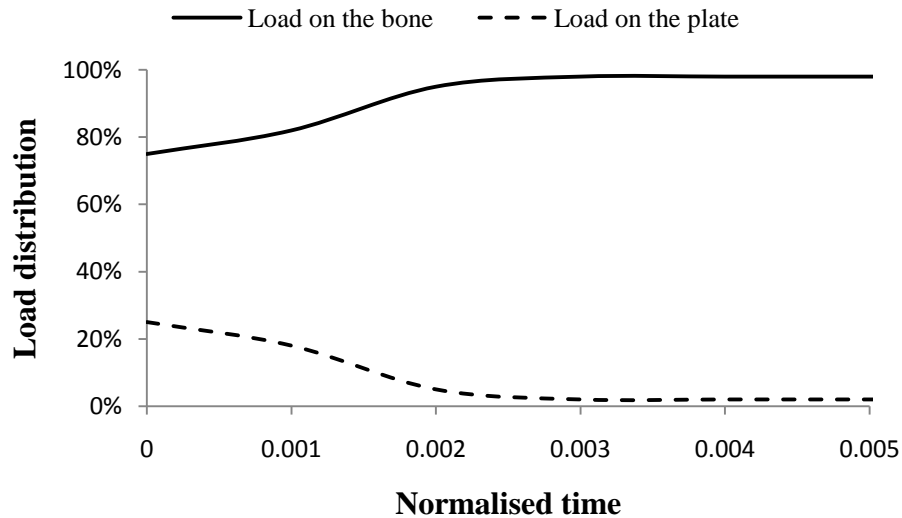


Figure 5.3.27 Load transfer from the supporting device to the healing bone with symmetric fixation for $\bar{A} = 5 \times 10^{-4}$ (scenario A).

Figure 5.3.26 shows that bone density increases to the same saturated value as in figure 5.3.1; while figure 5.3.27 shows that the load on the boundary of healing bone domain follows the same trend as that of the bone density remodelling. The bone density takes

longer time to grow to this saturated value because the symmetric fixation appears stiffer than the un-symmetric one. The load transfer curves, on the other hand, follow the trend very much like that in figure 5.3.2 but with different initial values of the two loads. The bone density distributions at different times are presented in figure 5.3.28.

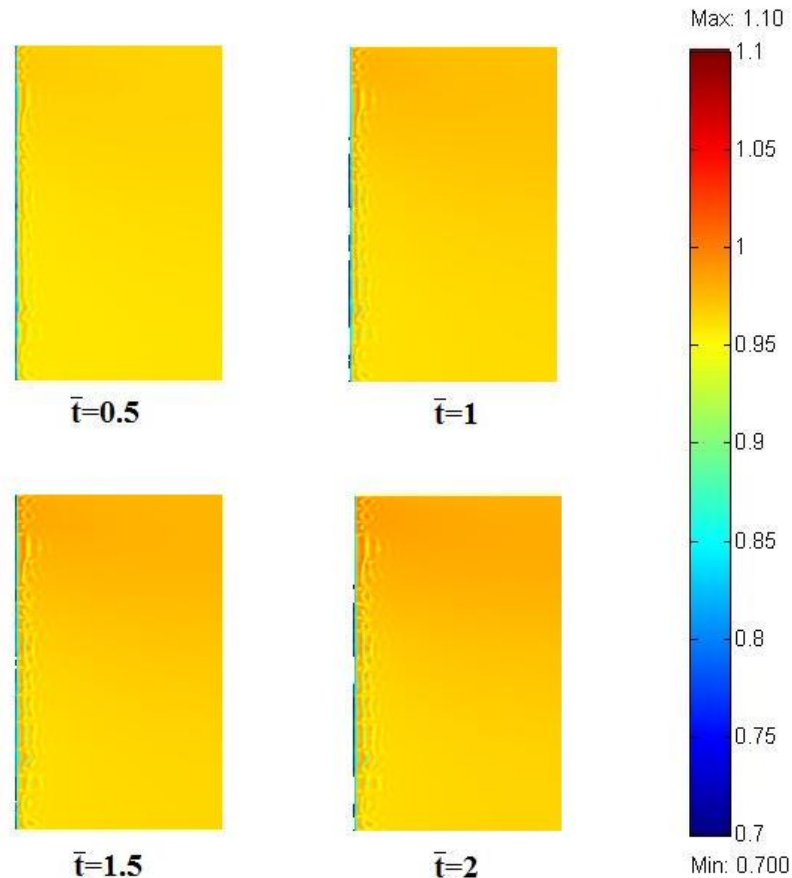


Figure 5.3.28 The spatial distribution of bone density at $\bar{t} = 0.5$, $\bar{t} = 1$, $\bar{t} = 1.5$, $\bar{t} = 2$, respectively. The colour represents the distribution of bone density normalised by 20GPa.

The four bone density distributions are all uniform distribution and almost identical to those in figure 5.3.4.

Scenario B – Zero device degradation

CHAPTER 5 INTERACTION BETWEEN DEVICE DEGRADATION AND BONE HEALING
IN ORTHOPAEDIC FIXATION-A NUMERICAL STUDY

The numerical results for the bone density growth and the load transfer curves are shown in figures 5.3.29 and 5.3.30.

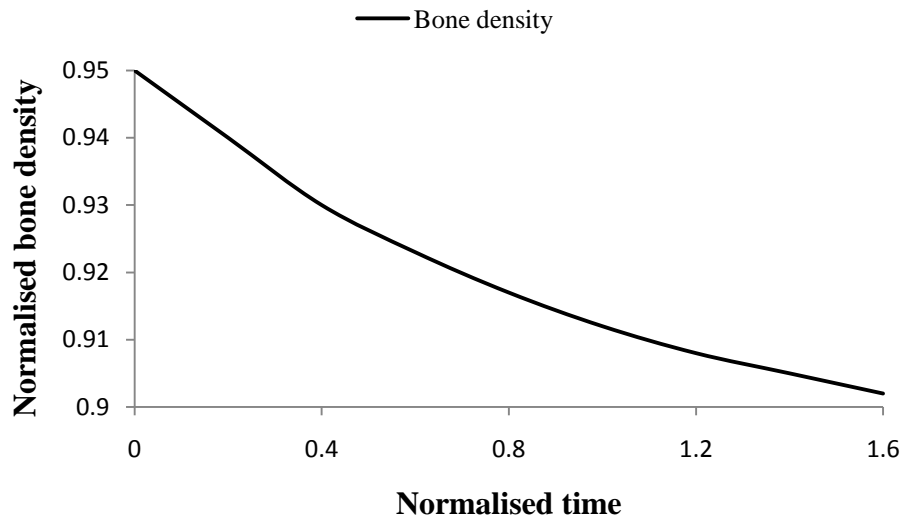


Figure 5.3.29 Bone density averaged over the bone domain as function of time for symmetric fixation with $\bar{A} \rightarrow \infty$ (scenario B).

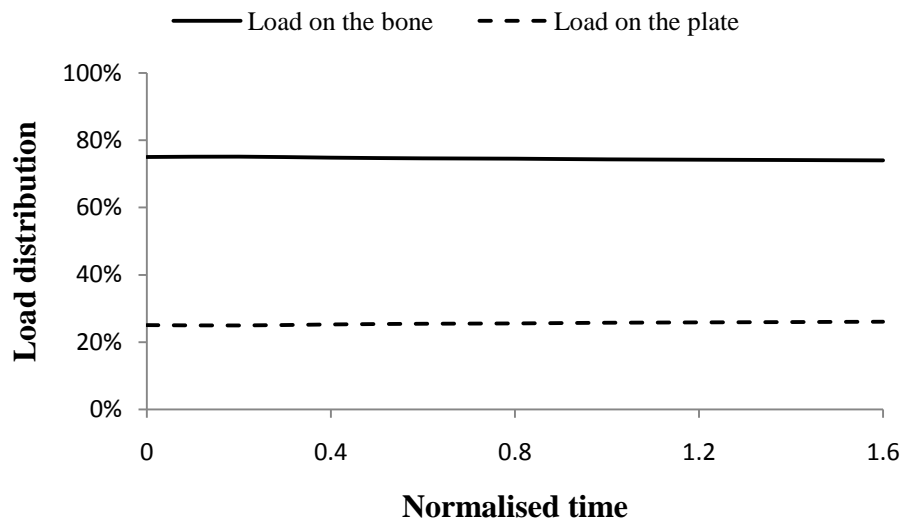


Figure 5.3.30 Load transfer from the supporting device to the healing bone with symmetric fixation for $\bar{A} \rightarrow \infty$ (scenario B).

The bone density loss in figure 5.3.29 is faster than that for the one-side fixation case (figure 5.3.6) because the two-side fixation shields more stress. Figure 5.3.30 shows that

very few load is transferred between remodelling bone and fixation device as the fixation device in this case never degrades. The bone density distribution shown in figure 5.3.31 in this scenario is however very interesting in comparison to the non-symmetric case shown in figure 5.3.7.

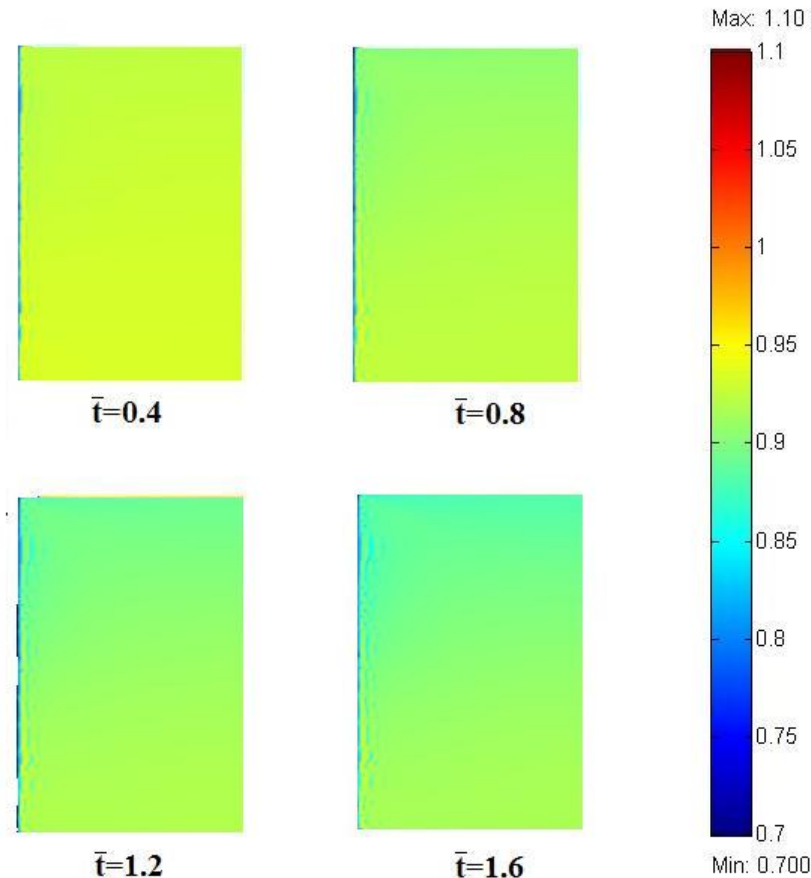


Figure 5.3.31 The spatial distribution of bone density at $\bar{t} = 0.4$, $\bar{t} = 0.8$, $\bar{t} = 1.2$, $\bar{t} = 1.6$, respectively. The colour represents the distribution of bone density normalised by 20GPa.

The density distribution remains much more uniform throughout the healing process although the healing rate is slightly slower. The cause for this difference in uniformity is due to the difference in the distribution of the average strains shown in Figures 5.3.32 and figure 5.3.8.

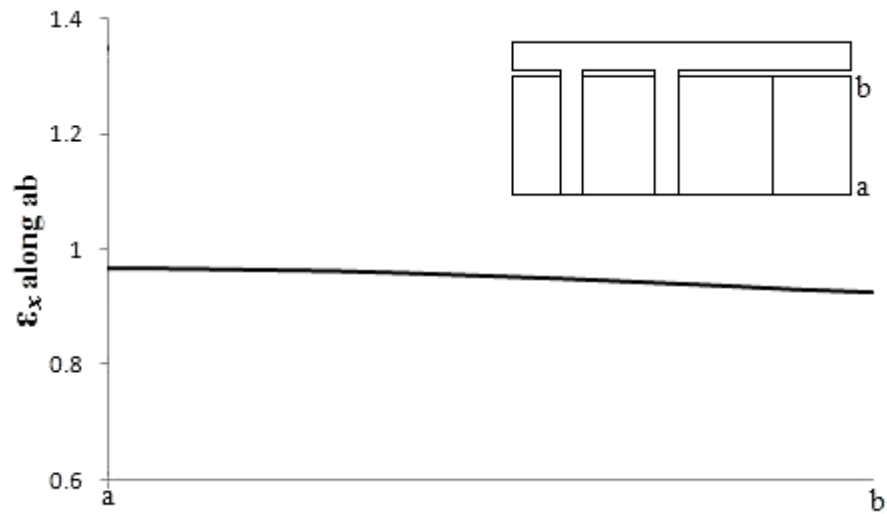


Figure 5.3.32 The normal strain distribution on the right boundary of the bone remodelling domain.

To show this point more clearly, figure 5.3.32 shows the distribution of the direct strain in the horizontal direction along the left boundary, a-b, of the healing bone. This strain distribution is taken at time of $\bar{t} = 0.4$. Notice that the strain in this figure is not the actual deformed strain for the system, but a value that has been normalised by $\frac{\sigma_{\max}}{E_{bone}}$.

The difference between the maximum and minimum strain values here is 10 times smaller than that shown in figure 5.3.8. The uniform normal strain distribution in figure 5.3.31 explained the uniform bone density distributions.

Scenario C –Moderate degradation

The change of average bone density and molecular weight are shown in figure 5.3.33 while the load transfer curves are in figure 5.3.34.

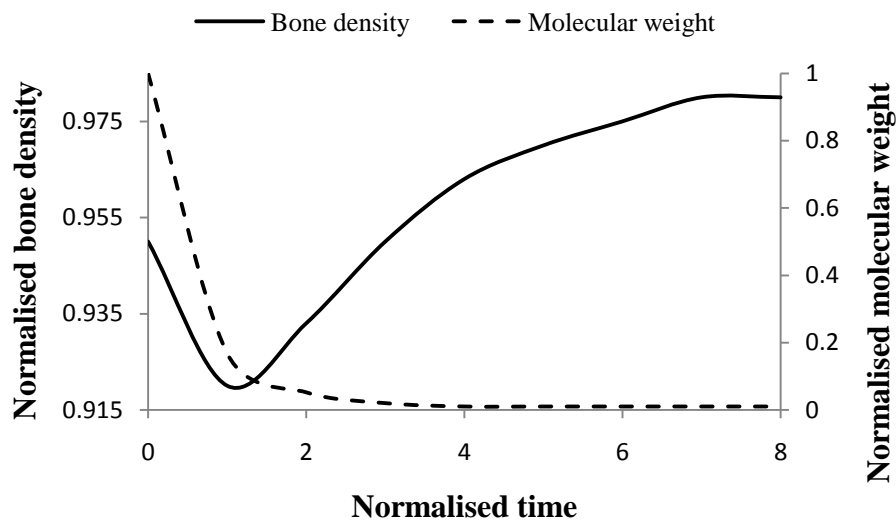


Figure 5.3.33 Bone density and polymer molecular weight averaged over the bone and polymer domains respectively as functions of time for symmetric fixation with $\bar{A} = 0.5$ (scenario C).

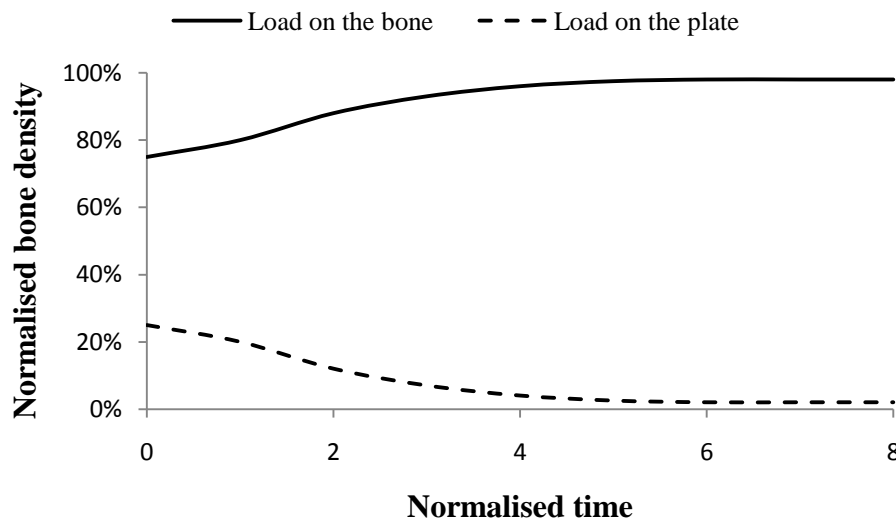


Figure 5.3.34 Load transfer from the supporting device to the healing bone with symmetric fixation for $\bar{A} = 0.5$ (scenario C).

The bone density in figure 5.3.33 follows the same trend as that in figure 5.3.9 except that the density decreases faster at first until degradation of the device transfers the load to the remodelling bone. The load transfer in figure 5.3.34 also follows the same trend

CHAPTER 5 INTERACTION BETWEEN DEVICE DEGRADATION AND BONE HEALING
IN ORTHOPAEDIC FIXATION-A NUMERICAL STUDY

as that in figure 5.3.10 except that the initial load sharing is different. The bone density distributions at different times are shown in figure 5.3.35.

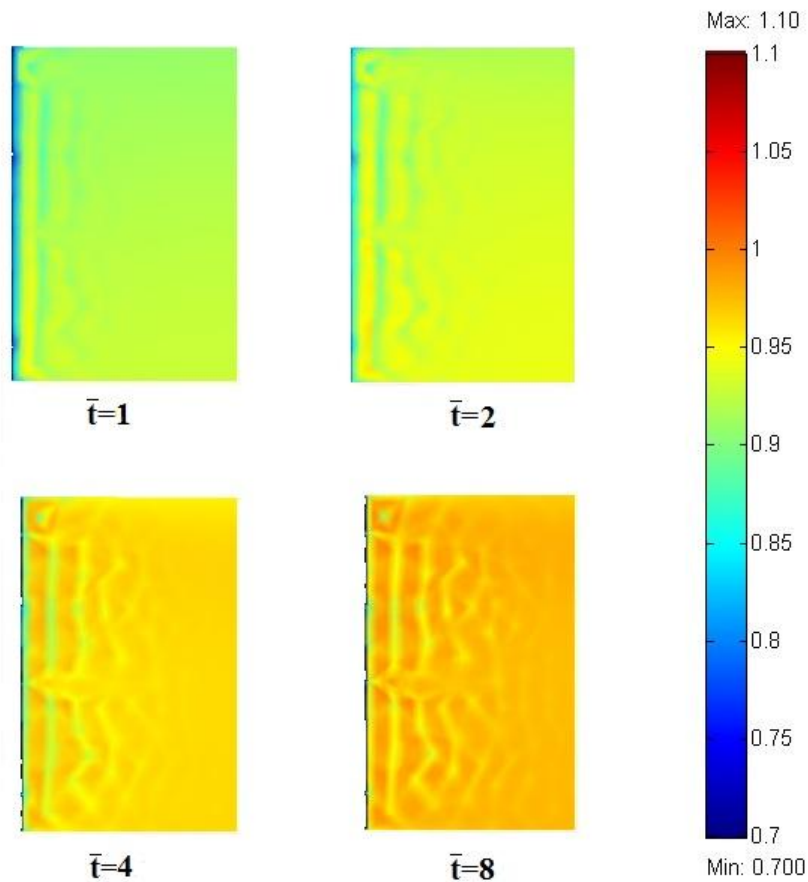


Figure 5.3.35 The spatial distribution of bone density at $\bar{t} = 1, \bar{t} = 2, \bar{t} = 4, \bar{t} = 8$, respectively. The colour represents the distribution of bone density normalised by 20GPa.

Again a uniform distribution for the bone density is observed for the same reason as explained in scenario B.

Generally speaking, figures 5.3.26, 5.3.29, 5.3.33 show that the bone density increases under this circumstance which is not much different from the scenarios A B and C in one-sided fixation (figures 5.3.1, 5.3.5, 5.3.9). This is because the load transfer shown in figures 5.3.27, 5.3.30, 5.3.34 are very similar to those in the one-side fixation as shown in figures 5.3.2, 5.3.6, 5.3.10. The initial load sharing between the device and the

**CHAPTER 5 INTERACTION BETWEEN DEVICE DEGRADATION AND BONE HEALING
IN ORTHOPAEDIC FIXATION-A NUMERICAL STUDY**

bone is however slightly different because the device is the symmetric fixation appears stiffer than the one-sided fixation. The two-side fixation device therefore shields more stress from the bone than the one-side fixation does. It is interesting to note that in figures 5.3.27 and 5.3.34, the normalised times for the bone to reach its full load sharing in each scenario equals to the normalised times in figure 5.3.2 and 5.3.10. This observation indicates that it is the degradation of the fixation device, rather than the change of the bone density, that controls the load transfer from the device to the bone.

5.4 Concluding remarks

This chapter demonstrates that the combined application of all our previous models can provide a methodology for the multi-disciplinary study of bone remodelling with simultaneous polymer degradation. With the help of proper software, variables such as polymer concentration, molecular weight distribution, Young's modulus change, bone density and stresses can be obtained simultaneously within an integrated model. This model consists of three different types of sub-domains: normal healthy bone, healing or remodelled bone, biodegradable polymer fixation device. Models with corresponding initial and boundary conditions for the different processes are applied to the different sub-domains and boundaries. The results in this chapter suggest that the degradation can prevent the stress shielding and aid the growth of bone density, regardless of the bone defect size that applies. Therefore, the biodegradable polymer fixation device has its advantages, not only in the elimination of the need for surgical removal but also in avoiding the stress shielding aspect. Three conclusions from this series of case study curves are: (a) the bone healing behaviour is controlled by a non-dimensional grouping, \bar{A} , of the various parameters in the equations govern the degradation, bone growth and stress analysis; (b) the time for the bone to reach to its healthy density is controlled by the degradation rate of the polymer; and (c) symmetric fixation, when applicable, can ensure a more uniform healing of the bone.

Chapter 6

Some Further Studies of the Degradation Model

6.1 Introduction

A complete model for the degradation of biodegradable polymeric devices has been presented in the previous chapters of this thesis. The study so far is driven by developing a simplest possible model which is not overwhelmed by too many “material parameters” so that they can be used in practical device design. The purpose of this chapter is to present a further study of the biodegradation model addressing slightly more complex issues which only future experimental studies can help to resolve fully. In this chapter, we present a more complex phenomenological model for biodegradation taking into account of the actual mechanism of random and end scissions in contrast to the Monte Carlo model presented in Chapter 4.

6.2 A phenomenological model considering end and random scissions

The literature shows some confusion in our current understanding in the hydrolysis mechanism during biodegradation. Some well know literature claims that for the degradation in acid environment, chain end scission is faster than random scission for biodegradable polymers (Shih, 1995^b); while others claimed just the opposite mechanism (Belbella *et al.*, 1996). The evidence for the above opinions is from degradation tests in PLA solutions rather than in solid state. It is therefore useful to develop a mathematical model that considers the two mechanisms simultaneously and explicitly. The relative importance of the two mechanisms can then be varied in the computer simulated degradation. Comparing the computer simulation with experimental studies, yet to be carried out, would then provide an in depth understanding in the hydrolysis mechanism.

The phenomenological model presented in Chapter 2 does not separate the two different scissions. We now distinguish the end scissions from random scissions through a series of definitions:

- R_s : Number of scission steps, including both random scission and end scission, that have ever occurred within the system
- R_m : Number of monomer units that have been produced within the system by either random scission or end scission
- C_{middle} : concentration of all the polymer (not monomers) ester bonds excluding all those at the end positions of the polymer chains
- C_{end} : concentration of the polymer chain (exclude monomers) ends. Note that this number is always twice the value of the total chain number within the system.
- C_m : monomers concentration; the monomers are defined here as being small group of repeating units whose number of the repeating units is no more than a critical value N_{mono} . This is usually the definition of oligmers, but we use this term interchangeably with monomers. N_{mono} is a threshold value for the definition of monomers which is normally around 7 to 9 repeating units (Saha and Tsuji, 2006). In this chapter we take $N_{mono}=5$.

Now we split both R_s and R_m into contributions from random scission and end scission respectively.

$$R_s = R_s^{random} + R_s^{end} \quad (6.2.1)$$

$$R_m = R_m^{random} + R_m^{end} \quad (6.2.2)$$

in which, R_s^{end} is the number of end scission that ever occurred within the system; R_s^{random} is the number of random scission that ever occurred within the system; R_m^{end} is the number of monomers that ever produced by end scission mechanism; R_m^{random} is the

number of monomers that ever produced by random scission mechanism. We define two types of end scission situations:

- E1: Normal chain scission takes place on a relatively long polymer chain.

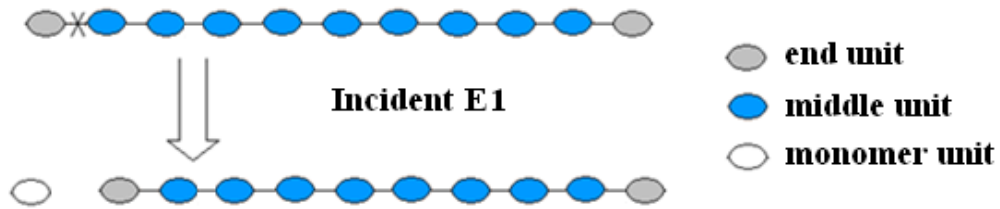


Figure 6.2.1 The scheme for incident E1.

- E2: Chain scission occurs when small polymer chain length equals to $N_{mono}+1$.

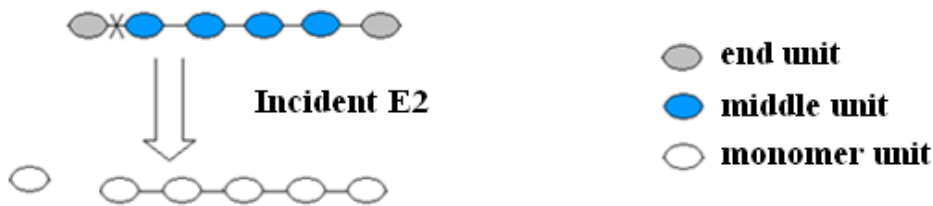


Figure 6.2.2 The scheme for incident E2.

The monomer production rate equation for incident E1 is:

$$\frac{dR_m^{end}}{dt} = \frac{dR_s^{end}}{dt} \tag{6.2.3}$$

This is because for every step of E1, one and only one monomer unit will be produced.

The monomer production rate equation for incident E2 is:

$$\frac{dR_m^{end}}{dt} = (1 + N_{mono}) \frac{dR_s^{end}}{dt} \tag{6.2.4}$$

For every step of E2, the entire polymer with the length of $N_{mono} + 1$ will become monomers. We define r_{E2} as the ratio between number of incident E1 and incident E2. In other word, for every R_s times of E1 incident occurred, $R_s \cdot r_{E2}$ times of E2 happened at the same time. Therefore equation (6.2.3) and (6.2.4) can be combined together as:

$$\frac{dR_m^{end}}{dt} = r_{E2}(1 + N_{mono})\frac{dR_s^{end}}{dt} + \frac{dR_s^{end}}{dt} \quad (6.2.5)$$

We define three types of random scission situations:

- R1. Normal chain scission takes place at any random ester bond position, exclude those on any polymer chain ends.

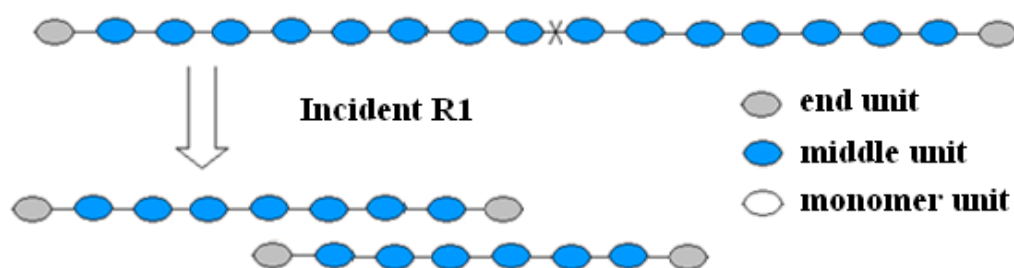


Figure 6.2.3 The scheme for incident R1.

- R2. Chain scission that produces a shorter polymer chain and one small monomer group (chain length no more than N_{mono})

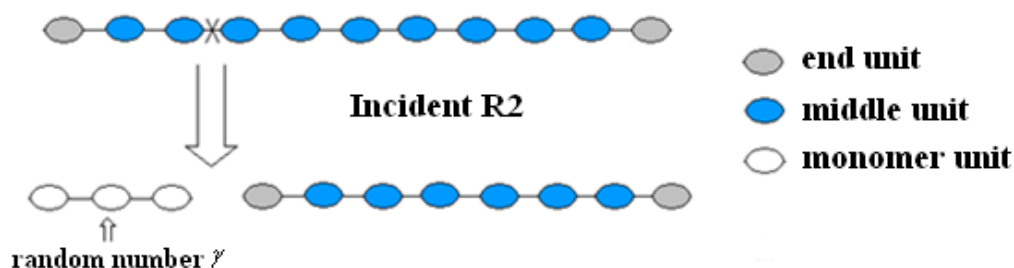


Figure 6.2.4 The scheme for incident R2.

- R3. Chain scission occurs that produce two small monomer group (both chain length is no more than N_{mono})

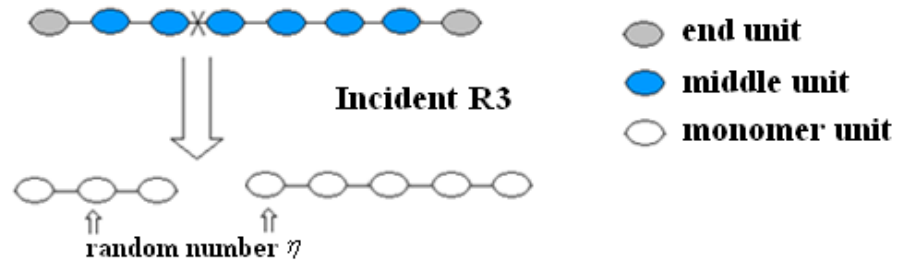


Figure 6.2.5 The scheme for incident R3.

The monomer production rate equation for incident R1 is:

$$\frac{dR_m^{random}}{dt} = 0 \cdot \frac{dR_s^{random}}{dt} \quad (6.2.6)$$

Incident R1 produces no monomers. The monomer production rate equation for incident R2 is:

$$\frac{dR_m^{random}}{dt} = \gamma \cdot \frac{dR_s^{random}}{dt} \quad (6.2.7)$$

in which γ is a random integer number between $[2, N_{mono}]$, which is the number of monomer units for a single step of incident R2 could possibly produce. The monomer production rate equation for incident R3 is:

$$\frac{dR_m^{random}}{dt} = \eta \cdot \frac{dR_s^{random}}{dt} \quad (6.2.8)$$

where η is a random integer number between $[N_{mono} + 1, 2N_{mono}]$, which is the number of monomer units that incident R3 could produce.

For every R_s steps of R1 incidents, $R_s \cdot r_{R2}$ times of R2 and $R_s \cdot r_{R3}$ times of R3 occur at the same time. Therefore equations (6.2.6), (6.2.7) and (6.2.8) can be combined together as:

$$\frac{dR_m^{random}}{dt} = \eta \cdot \frac{dR_s^{random}}{dt} \cdot r_{R3} + \gamma \cdot \frac{dR_s^{random}}{dt} \cdot r_{R2} \quad (6.2.9)$$

The combination of equations (6.2.5) and (6.2.9) provides a complete equation for monomers produced by both types of chain scissions:

$$\frac{dR_m}{dt} = (\eta \cdot r_{R3} + \gamma \cdot r_{R2}) \cdot \frac{dR_s^{random}}{dt} + [r_{E2}(1 + N_{mono}) + 1] \frac{dR_s^{end}}{dt} \quad (6.2.10)$$

We define the scission rate equations as:

$$\frac{dR_s^{end}}{dt} = k_1 C_{end} + k_2 C_{end} C_m^n \quad (6.2.11)$$

$$\frac{dR_s^{random}}{dt} = k_3 C_{middle} + k_4 C_{middle} C_m^n \quad (6.2.12)$$

in which k_1, k_2, k_3, k_4 are all rate constants here. Equation (6.2.11) indicates that end scission rate is decided by the concentration of end ester bond units while equation (6.2.12) suggests the random scission rate is decided by the concentration of non-end ester bond units. Both equations consider the hydrolysis together with auto-catalysis mechanism as the original phenomenological model suggests. Using equation (6.2.11) and (6.2.12) in equation (6.2.10), and taking into account of the monomer diffusion, we obtain that:

$$\frac{dC_m}{dt} = (\eta \cdot r_{R3} + \gamma \cdot r_{R2}) \cdot (k_3 C_{middle} + k_4 C_{middle} C_m^n) + [r_{E2}(1 + N_{mono}) + 1] \cdot (k_1 C_{end} + k_2 C_{end} C_m^n) + \frac{\partial}{\partial x_i} D \frac{\partial C_m}{\partial x_i} \quad (6.2.13)$$

in which D is the diffusion coefficient and x_i is the spatial coordinate. Repeating the above analysis for the changing rate of middle units and end units under each of the 5 incidents, the results are listed in table 6.2.1.

Table 6.2.1 The changing rates for C_m , C_{middle} and C_{end} caused by incidents E1, E2, R1, R2, R3.

Variables \ Incidents	C_m	C_{middle}	C_{end}
E1	1	-1	0
E2	$(1 + N_{mono})$	$-(N_{mono} - 1)$	-2
R1	0	-2	2
R2	γ	$-\gamma$	0
R3	η	$-(\eta - 2)$	-2

With the information from table 6.2.1, we could obtain the equations for the changing rate of middle units and end units:

$$\frac{dC_{middle}}{dt} = (-2 - (\eta - 2) \cdot r_{R3} - \gamma \cdot r_{R2}) \cdot (k_3 C_{middle} + k_4 C_{middle} C_m^n) + [-(N_{mono} - 1) \cdot r_{E2} - 1] \cdot (k_1 C_{end} + k_2 C_{end} C_m^n) \quad (6.2.14)$$

$$\frac{dC_{end}}{dt} = (2 - 2 \cdot r_{R3}) \cdot (k_3 C_{middle} + k_4 C_{middle} C_m^n) + (-2 \cdot r_{E2}) \cdot (k_1 C_{end} + k_2 C_{end} C_m^n) \quad (6.2.15)$$

The ratio parameters r_{E2} , r_{R2} , r_{R3} should all be very small, because incident E2 and R3 happen only when the polymer chain length is very short i.e. contains less than $2N_{mono}$ repeating units while incident R2 relies on the random scission taking place at a

position very close to a polymer chain end, normally less than N_{mono} ester bonds away. Compared with the usual 2000 to 7000 degrees of polymerisation for polymer chains, the probability of these situations can be considered trivial unless the degradation reaches the late stage when most of the chains are short; in which case these three ratios would be much larger values. Therefore r_{E2} , r_{R2} , r_{R3} are neglectable numbers at the early stage of the scission but becomes much larger towards the end of the degradation. Setting r_{E2} , r_{R2} , r_{R3} as zero, the model can be simplified as:

$$\frac{dC_m}{dt} = (k_1 C_{end} + k_2 C_{end} C_m^n) + \frac{\partial}{\partial x_i} D \frac{\partial C_m}{\partial x_i} \quad (6.2.16)$$

$$\frac{dC_{middle}}{dt} = -2(k_3 C_{middle} + k_4 C_{middle} C_m^n) - 1(k_1 C_{end} + k_2 C_{end} C_m^n) \quad (6.2.17)$$

$$\frac{dC_{end}}{dt} = 2(k_3 C_{middle} + k_4 C_{middle} C_m^n) \quad (6.2.18)$$

Similar to our phenomenological model, we normalise this model using the following definitions:

$$C_{e0} = C_{middle0} + C_{end0}; \quad \bar{C}_{end} = \frac{C_{end}}{C_{e0}}; \quad \bar{C}_m = \frac{C_m}{C_{e0}}; \quad \bar{C}_{middle} = \frac{C_{middle}}{C_{e0}}; \quad \bar{x}_i = \frac{x_i}{l}$$

$$\bar{k}_1 = \frac{k_1}{k_2 C_{e0}^n}; \quad \bar{k}_3 = \frac{k_3}{k_2 C_{e0}^n}; \quad \bar{k}_4 = \frac{k_4}{k_2}; \quad \bar{D}_0 = \frac{D_0}{k_2 C_{e0}^n l^2}; \quad \bar{t} = (k_2 C_{e0}^n) t$$

in which C_{e0} is the ester bond concentration at the beginning of the biodegradation, l is a characteristic length of the device, D_0 is the initial diffusion coefficient. The equations (6.2.16)-(6.2.18) can be normalised as:

$$\frac{d\bar{C}_m}{d\bar{t}} = (\bar{k}_1 \bar{C}_{end} + \bar{C}_{end} \bar{C}_m^n) + \frac{\partial}{\partial \bar{x}} (\bar{D} \frac{\partial \bar{C}_m}{\partial \bar{x}}) \quad (6.2.19)$$

$$-\frac{d\bar{C}_{middle}}{d\bar{t}} = 2(\bar{k}_3 \bar{C}_{middle} + \bar{k}_4 \bar{C}_{middle} \bar{C}_m^n) + (\bar{k}_1 \bar{C}_{end} + \bar{C}_{end} \bar{C}_m^n) \quad (6.2.20)$$

$$\frac{d\bar{C}_{end}}{d\bar{t}} = 2(\bar{k}_3\bar{C}_{middle} + \bar{k}_4\bar{C}_{middle}\bar{C}_m^n) \quad (6.2.21)$$

Follow the previous chapters we take the effective diffusion coefficient as a function of porosity:

$$\bar{D} = \bar{D}_0 \left\{ 1 + (1.3p^2 - 0.3p^3) \left(\frac{D_{max}}{D_0} - 1 \right) \right\} \quad (6.2.22)$$

in which D_0 is the initial diffusion coefficient of the material at initial state, D_{max} is the diffusion coefficient in the aqueous media, p is the porosity that we can write as $p = 1 - (C_{middle} + C_{end} + C_m) / C_{e0} = 1 - \bar{C}_{middle} - \bar{C}_{end} - \bar{C}_m$ in this model.

If $\bar{k}_3, \bar{k}_4 \ll \bar{k}_1, 1$ in equation (6.3.19)-(6.2.21), this model is purely end scission controlled; if $\bar{k}_3, \bar{k}_4 \gg \bar{k}_1, 1$, this model is purely random scission controlled. The pure end scission controlled case can be written as:

$$\frac{d\bar{C}_m}{d\bar{t}} = (\bar{k}_1\bar{C}_{end} + \bar{C}_{end}\bar{C}_m^n) + \frac{\partial}{\partial \bar{x}} (\bar{D} \frac{\partial \bar{C}_m}{\partial \bar{x}}) \quad (6.2.23)$$

$$-\frac{d\bar{C}_{middle}}{d\bar{t}} = (\bar{k}_1\bar{C}_{end} + \bar{C}_{end}\bar{C}_m^n) \quad (6.2.24)$$

$$\frac{d\bar{C}_{end}}{d\bar{t}} = 0 \quad (6.2.25)$$

No new chains will be generated as equation (6.3.25) suggests. The pure random scission controlled case, on the other hand, can be written as:

$$\frac{d\bar{C}_m}{d\bar{t}} = 0 + \frac{\partial}{\partial \bar{x}} (\bar{D} \frac{\partial \bar{C}_m}{\partial \bar{x}}) \quad (6.2.26)$$

$$-\frac{d\bar{C}_{middle}}{d\bar{t}} = 2(\bar{k}_3\bar{C}_{middle} + \bar{k}_4\bar{C}_{middle}\bar{C}_m^n) \quad (6.2.27)$$

$$\frac{d\bar{C}_{end}}{d\bar{t}} = 2(\bar{k}_3\bar{C}_{middle} + \bar{k}_4\bar{C}_{middle}\bar{C}_m^n) \quad (6.2.28)$$

All the degradation behaviour in this case is converting the non-end repeating units into end repeating units. Note that the total chains number within the system always equal to $\bar{C}_{end}/2$, so the total chains number increasing rate is equal to the polymer chain scission rate. No monomers are generated and diffused during the process thus no weight loss for the system until the late degradation stage when r_{E2} , r_{R2} , r_{R3} became larger.

The impact of combined end scission and random scission on the number average molecular weight and weight loss can be generally categorised in terms of whether the random scission mechanism can be ignored:

1. Pure or almost pure end scission controlled ($\bar{k}_3, \bar{k}_4 \ll \bar{k}_1, 1$). In this case model equations are simplified in equations (6.2.23)-(6.2.25). Monomers are generated entirely from the middle units on the chain. The lost of monomers on polymer chain ends controls both the molecular weight loss and weight loss.
2. Random scission cannot be neglected. In this case the number of random scission decides the molecular weight loss. Because random scission affects polymer molecular weight by changing total chain number while end scission can only reduce one repeating unit on the polymer chains. Considering the fact that the degree of polymerisation for polymer chains is large at the early stages, random scission will certainly play a much more important role than end scission. As a consequence, the molecular weight calculations are different for the above two scenarios. For both situations:

$$M_n = \frac{(C_{middle} + C_{end}) \times M_{unit}}{\frac{C_{end}}{2}} \quad (6.2.29)$$

$$M_{n0} = \frac{(C_{e0}) \times M_{unit}}{\frac{C_{end0}}{2}} \quad (6.2.30)$$

In which M_{unit} is the molecular weight for a single repeating unit. The normalised molecular weight is:

$$\bar{M}_n = \frac{(\bar{C}_{middle} + \bar{C}_{end})\bar{C}_{end0}}{\bar{C}_{end}} \quad (6.2.31)$$

Because the first situation is a pure end scission controlled, the number of chains within the system does not change ($\bar{C}_{end} = \bar{C}_{end0}$). Equation (6.2.31) becomes:

$$\bar{M}_n = \frac{(\bar{C}_{middle} + \bar{C}_{end})\bar{C}_{end0}}{\bar{C}_{end}} = \bar{C}_{middle} + \bar{C}_{end} = \bar{C}_{middle} + \bar{C}_{end0} \quad (6.2.32)$$

Equation (6.2.32) indicates that the average molecular weight is almost equal to the normalised middle unit concentration which decreases as equation (6.2.24) suggests. Therefore, in order to capture the molecular weight loss from the experimental data describing amorphous PLA material (Grizzi *et al.*, 1995; Tsuji 2002; Saha and Tsuji, 2006), the degradation should be calculated to the late stage in order to simulate small average molecular weight values. In that case, all the parameters including r_{E2} , r_{R2} , r_{R3} are not neglectable and this complete model becomes too complicated to handle.

For the second situation, we apply this developed model to simulate the molecular weight loss of same polymer but two different thicknesses (Grizzi *et al.*, 1995). According to the experimental data, the initial number average molecular weights for the two samples are 20,000g/mol for 2mm thick plate and 34,000g/mol for 0.3mm thick film (Grizzi *et al.*, 1995). Therefore the initial degree of polymerisation can be obtained as 277 for 2mm plate and 472 for 0.3mm film. Among these numbers of ester bonds, the initial end units and initial middle units are:

$$\bar{C}_{end0} = \frac{2}{277}, \bar{C}_{middle0} = \frac{275}{277}; \bar{C}_{end0} = \frac{2}{472}, \bar{C}_{middle0} = \frac{470}{472}$$

The calculation of average molecular weight for this case can be obtained from equation (6.2.31)

$$\bar{M}_n = \frac{2}{277} \left(1 + \frac{\bar{C}_{middle}}{\bar{C}_{end}}\right); \bar{M}_n = \frac{2}{472} \left(1 + \frac{\bar{C}_{middle}}{\bar{C}_{end}}\right) \quad (6.2.33)$$

We can use the model to show that the polymer lost most of its average molecular weight while the weight loss of the sample remains very small. One group of the fitting data can be used to produce the change in average molecular weight versus time (Grizzi *et al.*, 1995).

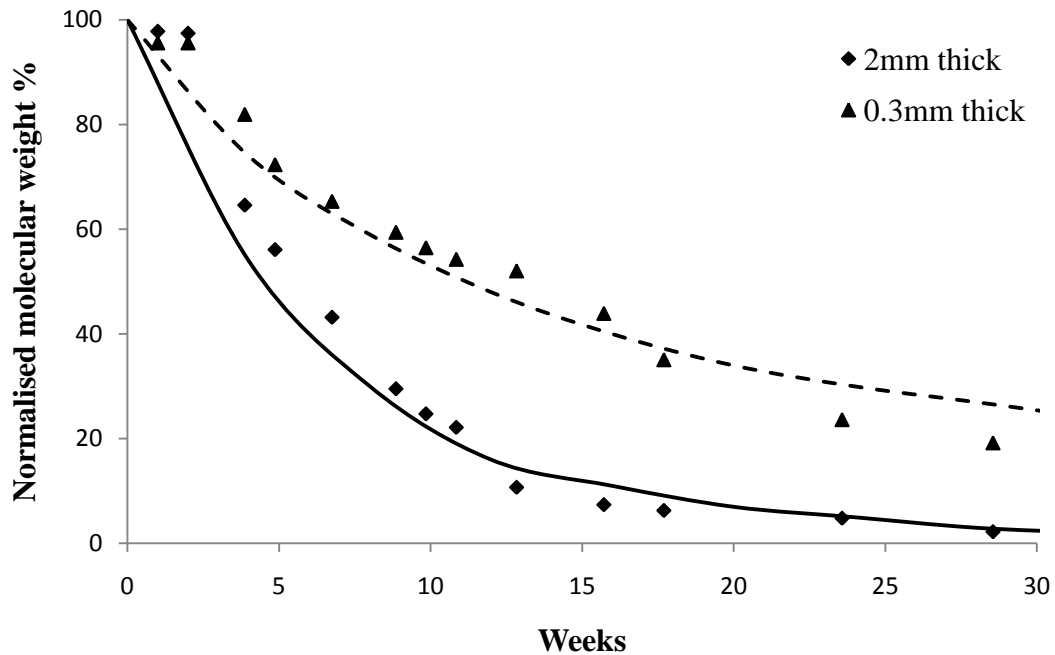


Figure 6.2.6 A numerical fitting to the experimental data of two thicknesses in the amended phenomenological model (Grizzi *et al.*, 1995).

The two experimental curves presented in discrete symbols in figure 6.2.6 are the degradation behaviour of the same material with different thicknesses of 2mm (dashed line) and 0.3mm (solid line) respectively (Grizzi *et al.*, 1995). The fitting data are produced using $n=0.5$, with the following parameters: $\bar{k}_1 = 2.5 \times 10^{-5}$, $\bar{k}_3 = 2.5 \times 10^{-4}$,

$\bar{k}_4 = 10$, $\bar{t} = 25$, $\bar{D}_0 = 2000$ and 40 . The weight loss calculated using the above fitting data are both almost zero (less than 1%) until the end of the degradation. By separating the end scission and random scission, this model can well fit the reported phenomenon that PLA polymer lost its molecular weight while the weight loss remains very little during the degradation for amorphous PLA polymers (Saha and Tsuji, 2006; Tsuji, 2002).

6.3 Concluding remarks

This chapter provides some further discussion on the phenomenological model by separating the end scission and random scission. A new model making a clear distinction between the random and end scission mechanism is proposed with full consideration of all the possible incidents that may occur during hydrolytic reactions. This complete model contains one extra variable and seven more parameters, although it can be simplified at extreme conditions. It is possible to use the model to explain the often observed phenomenon that polymer loses most of its molecular weight before any significant weight loss occurs.

Chapter 7 Concluding remarks and future work

Biodegradable polymers, especially the homo and co-polymers of poly lactic acid (PLA) have been used widely in orthopaedic surgery as bone fixation devices. The design of such devices is complicated requiring not only the prediction of the polymer degradation and Young's modulus decay but also the stress shielding effect of the bone. In this thesis, the finite element method is used to:

- a) predict the polymer degradation using a phenomenological model,
- b) determinate the effective diffusion coefficient and,
- c) predict the bone remodelling process and its interaction with the polymer degradation.

These models are integrated in a complete case study.

Chapter 2 presents a phenomenological model to simulate the degradation rate and molecular weight distribution for biodegradable polymers. This model can very well capture the heterogeneous pattern of the device degradation. A degradation map was established to guide the design of simple devices. Finally, half degradation times was calculated to relate the degradation rate for a biodegradable device to its geometry and both hydrolyze and diffusion rates.

Chapter 3 combined the multi-scale modelling idea with the finite element method to establish a case study on an important factor in the degradation model – the effective diffusion coefficient. We discussed several possible micro structures and calculated the effective diffusion coefficient. One conclusion from those case studies is that the diffusion coefficient can be presented as a linear function of porosity if the total porosity is low. We also recognised that the effective diffusion coefficient can be affected by many factors and can only be related to porosity for tunnelling effect can be ignored.

Chapter 4 focused on using the entropy theory to explain how molecular weight affects the Young's modulus decay of the degrading polymers. A statistical model was set up to simulate the chain scission process. This model has captured the major trend of Young's modulus reduction during degradation: slight loss before molecular weight reaches a critical value and rapid loss towards the end of degradation.

Chapter 5 demonstrates that this series of models can be integrated to provide a complete methodology for modelling the bone healing process with the presence of a biodegradable bone fixation device. The coupled model contains several analyses at the same time: polymer degradation, monomer diffusion, Young's modulus decay, structural mechanics analysis and bone remodelling process. All these models depend on the calculation results from other models and generate certain results for other models as inputs. The series of case studies demonstrated that:

- (a) a biodegradable fixation device has the advantage of not only eliminating the necessity for surgical removal but also helping the healing bone to be remodelled to its full density;
- (b) on the assumption that bone remodelling follows the stimulus of the stress distribution, the bending moment, can be an important factor in bone healing simulation.

Chapter 6 provides some further discussion on the phenomenological model. A new model separating random and end scission mechanism is proposed with full consideration of all the possible situations during hydrolytic chain cleavage. This complete model can be used to explain the common experimental observation that polymer loses most of its molecular weight before any significant weight loss occurs.

The degradation of polymeric bioresorbable device is a very complicated process. The behaviour of the healing bone under the "protection" of a resorbable device is even more sophisticated. Many issues remain unresolved including:

1. The bone remodelling models lack experimental validation.

2. The hydrolysis mechanisms of the polymers are still not well understood.
3. Many factors, from processing conditions, storing condition, sterilization procedure, to the details of the polymer chemistry, affect the degradation rate. These effects are however poorly understood.

The work presented in this thesis attempts to overcome these difficulties by developing a simple but phenomenological model. A complete experimental validation of the approach adopted in this thesis is the next logical but step outside the scope of this thesis due to the limitation of the project duration.

References

- Athanasidou, K.A., Niederauer, G.G., 1996. Sterilization, toxicity, biocompatibility and clinical applications of polylactic acid/polyglycolic acid copolymers. *Biomaterials* 17, 93-102.
- Barber, F.A., Elrod, B.F., McGuire, D.A., Paulos, L.E., 2000. Bioscrew fixation of patellar tendon autografts. *Biomaterials* 21, 2623-2629.
- Belbello, A., Vauthier, C., Fessi, H., Devissaguet, J., Puisieux, F., 1996. In vitro degradation of nanospheres from poly(D,L-lactide) of different molecular weights and polydispersities. *International Journal of Pharmaceutics* 129, 95-102.
- Cai, Q., Shi, G., Bei, J., Wang, S., 2003. Enzymatic degradation behavior and mechanism of Poly(lactide-co-glycolide) foams by trypsin. *Biomaterials* 24, 629-638.
- Cameron, R.E., Kamvari-Moghaddam, A., 2008. Chapter 3 in *Degradation rate of bioresorbable materials Prediction and evaluation*. Edited by Buchanan, F. Woodhead Publishing and Manery Publishing on behalf of The Institute of Materials, Minerals & Mining.
- Charlier, A., Leclerc, B., Couarraze, G., 2000. Release of mifepristone from biodegradable matrices: experimental and theoretical evaluations. *International Journal of Pharmaceutics* 200, 115-120.
- Chu, P.K., Liu, X., 2008. *Biomaterials fabrication and processing handbook*. Taylor & Francis Group, pp. 457-465.
- de Jong, S.J., Arias, E.R., Rijkers, D.T.S., van Nostrum, C.F., Kettenes-van den Bosch, J.J., Hennink, W.E., 2001. New insights into the hydrolytic degradation of poly (lactic acid): participation of the alcohol terminus. *Polymer* 42, 2795-2802.
- Doblaré M., García, M.J., Gómez, M.J., 2004. Modelling bone tissue fracture and healing: a review. *Engineering Fracture Mechanics* 71, 1809-1840.
- Entrialgo-Castaño, M., Lendlein, A., Hofmann, D., 2006. Molecular modelling investigations of dry and two water-swollen states of biodegradable polymers. *Advanced Engineering Materials* 8 No.5, 434-439.
- Faisant, N., Siepmann, J., Benoit, J.P., 2002. PLGA-based microparticles: elucidation of mechanisms and a new, simple mathematical model quantifying drug release. *European Journal of Pharmaceutical Sciences* 15, 355-366.
- Farrar, D., 2008. Chapter 9 in *Degradation rate of bioresorbable materials Prediction and evaluation*. Edited by Buchanan, F. Woodhead Publishing and Manery Publishing on behalf of The Institute of Materials, Minerals & Mining.

REFERENCE

- Gopferich, A., Langer, R., 1995. Modelling monomer release from bioerodible polymers. *Journal of Controlled Release* 33, 55-69.
- Grizzi, I., Garreau, H., Li, S., Vert, M., 1995. Hydrolytic degradation of devices based on poly [DL-lactic acid] size dependence. *Biomaterials* 16, 305-311.
- Gupta, B., Revagade, N., Hilborn, J., 2007. Poly (lactic acid) fiber: An overview. *Progress in Polymer Science* 32, 455-482.
- Gutwald, R., Schon, R., Gellrich, N.C., Schramm, A.A., Schmelzeisen, R., Pistner, H., 2002. Bioresorbable implants in maxillo-facial osteosynthesis: Experimental and clinical experience. *Injury, International Journal of the Care of Injured* 33, 4-16.
- Han, X., Pan, J., 2009. A model for simultaneous crystallisation and biodegradation of biodegradable polymers. *Biomaterials* 30, 423-430.
- Hassani, B., Hinton, E., 1998^a. A review of homogenization and topology optimization I-homogenization theory for media with periodic structure. *Computers and Structures* 69, 707-717.
- Hassani, B., Hinton, E., 1998^b. A review of homogenization and topology optimization II-analytical and numerical solution of homogenization equations. *Computers and Structures* 69, 719-738.
- Hurrell, S., Cameron, R., 2001^a. Polyglycolide: degradation and drug release. Part I: Changes in morphology during degradation. *Journal of Materials Science: Materials in Medicine* 12, 811-816.
- Hurrell, S., Cameron, R., 2001^b. Polyglycolide: degradation and drug release. Part II: Drug release. *Journal of Materials Science: Materials in Medicine* 12, 817-820.
- Hurrell, S., Cameron, R., 2002. The effect of initial polymer morphology on the degradation and drug release from polyglycolide. *Biomaterials* 23, 2401-2409.
- Hurrell, S., Milroy, G.E., Cameron, R.E., 2003. The distribution of water in degrading polyglycolide. Part I: Sample size and drug release. *Journal of Materials Science: Materials in Medicine* 14, 457-464.
- Hurrell, S., Cameron, R., 2003. The effect of buffer concentration, pH and buffer ions on the degradation and drug release from polyglycolide. *Polymer International* 52, 358-366.
- Jiang, W., Pan, J., 2008. Effective diffusion coefficient of biodegradation polymers and its role in degradation. University of Leicester Research Report.
- Joshi, A., Himmelstein, K.J., 1991. Dynamics of controlled release from bioerodible matrices. *Journal of Controlled Release* 15, 95-104.
- Kaufman, H.S., Falchetta, J.J., 1976. Introduction to polymer science and technology. Wiley Interscience, pp. 11-12.
- Li, S., Garreau, H., Vert, M., 1990^a. Structure-property relationships in the case of the degradation of massive aliphatic poly-(α -hydroxy acids) in aqueous media. Part 1:

REFERENCE

- Poly (DL-lactic acid). *Journal of Materials Science: Materials in Medicine* 1, 123-130.
- Li, S., Garreau, H., Vert, M., 1990^b. Structure-property relationships in the case of the degradation of massive poly(α -hydroxyacids) in aqueous media. Part 2: Degradation of lactid-glycolide copolymers: PLA37.5GA25 and PLA75GA25. *Journal of Materials Science: Materials in Medicine* 1, 131-139.
- Li, S., Garreau, H., Vert, M., 1990^c. Structure-property relationships in the case of the degradation of massive poly(α -hydroxyacids) in aqueous media. Part 3: Influence of the morphology of poly (L-lactic acid). *Journal of Materials Science: Materials in Medicine* 1, 198-206.
- Milroy, G.E., Cameron, R.E., 2003. The distribution of water in degrading polyglycolide. Part II: Magnetic resonance imaging and drug release. *Journal of Materials Science: Materials in Medicine* 14, 465-473.
- Mohammadi, Y., Jabbari, E., 2006. Monte Carlo Simulation of Degradation of Porous Poly(lactide) Scaffolds, 1. Effect of Porosity on pH. *Macromolecular Theory and Simulations* 15, 643-653.
- Moses, M.A., Brem, H., Langer, R., 2003. Advancing the field of drug delivery: Taking aim at cancer. *Cancer Cell* 4, 337-341.
- Nam, Y.S., Park, T.G., 1999. Biodegradable polymeric microcellular foams by modified thermally induced phase separation method. *Biomaterials* 20, 1783-1790.
- Nguyen, V.H., Nedjar, B., Colina, H., Torrenti, J.M., 2005. A separation of scales homogenization analysis for the modelling of calcium leaching in concrete. *Computer Methods in Applied Mechanics and Engineering* 195, 7196-7210.
- Park, T.G., 1995. Degradation of poly(lactic-co-glycolic acid) microspheres: effect of copolymer composition. *Biomaterials* 16, 1123-1130.
- Raman, C., Berkland, C., Kim, K.K., Pack, D.W., 2005. Modelling small-molecule release from PLG micro-spheres: effects of polymer degradation and nonuniform drug distribution. *Journal of Controlled Release* 103, 149-158.
- Ratner, B.D., Hoffman, A.S., Schoen, F.J., Lemons, J.E., 2003. *Biomaterial science*, second ed. Elsevier Academic Press, pp. 123-124.
- Reichert, J.C., Saifzadeh, S., Wullschleger, M.E., Epari, D.R., Schütz, M.A., Duda, G.N., Schell, H., van Griensven, M., Redl, H., Hutmacher, D.W., 2009. The challenge of establishing preclinical models for segmental bone defect research. *Biomaterials* 30, 2149-2163.
- Renouf-Glause, A.C., Rose, J., Farrar, D., Cameron, R.E., 2005. A degradation study of PLLA containing lauric acid. *Biomaterials* 26, 2415-2422.

REFERENCE

- Rokkanen, P.U., Böstman, O., Hirvensalo, E., Mäkelä E.A., Partio, E.K., Pääkkönen H., Vainionpää S., Vihtonen, K., Törmälä P., 2000. Bioabsorbable fixation in orthopaedic surgery and traumatology. *Biomaterials* 21, 2607-2613.
- Saha, S.K., Tsuji, H., 2006. Effects of molecular weight and small amounts of D-lactide units on hydrolytic degradation of poly(L-lactic acid)s. *Polymer Degradation and Stability* 91, 1665-1673.
- Sanz-Herrera, J.A., García-Aznar, J.M., Doblaré M., 2009. On scaffold designing for bone regeneration: A computational multiscale approach. *Acta Biomaterialia* 5, 219-229.
- Sengers, B.G., Taylor, M., Please, C.P., Oreffo, R.O.C., 2007. Computational modelling of cell spreading and tissue regeneration in porous scaffolds. *Biomaterials* 28, 1926-1940.
- Shaw, J.A., Jones, A.S., Wineman, A.S., 2005. Chemorheological response of elastomers at elevated temperatures: Experiments and simulations. *Journal of the Mechanics and Physics of Solids* 53, 2758-2793.
- Shih, C., 1995^a. Chain-end scission in acid catalyzed hydrolysis of poly(D,L-lactide) in solution. *Controlled Release* 34, 9-15.
- Shih, C., 1995^b. A graphical method for the determination of the mode of hydrolysis of biodegradation polymers. *Pharmaceutical Research* 12, 2036-2040.
- Siepmann, J., Faisant, N., Benoit, J.P., 2002. A new mathematical model quantifying drug release from bio-erodible micro-particles using Monte Carlo simulations. *Pharmaceutics Research* 19, 1885-1893.
- Siparsky, G.L., Voorhees, K.J., Miao, F., 1998. Hydrolysis of polylactic acid (PLA) and polycaprolactone (PCL) in aqueous acetonitrile solutions: autocatalysis. *Journal of Environmental Polymer Degradation* 6, 31-41.
- Staggs, J.E.J., 2002. Modelling random scission of linear polymers. *Polymer Degradation and Stability* 76, 37-44.
- Staggs, J.E.J., 2004. Modelling end-chain scission and recombination of linear polymers. *Polymer Degradation and Stability* 85, 759-767.
- Stauffer, D., Aharony, A., 1994. Introduction to percolation theory, revised second edition. Taylor & Francis, pp. 1-17.
- Taylor, D., Lee, T.C., 1998. Measuring the shape and size of microcracks in bone. *Journal of Biomechanics* 31, 1177-1180.
- Tobolsky, A.V., 1960. Properties and structures of polymers, Wiley, New York, NY, pp. 223-235.
- Tsuji, H., Ikada, Y., 2000. Properties and morphology of poly (L-lactide) 4: effects of structural parameters on long-term hydrolysis of poly (L-lactide) in phosphatebuffered solution. *Polymer Degradation and Stability* 67, 179-189.

REFERENCE

- Tsuji, H., 2000. In vitro hydrolysis of blends from enantiomeric poly(lactide)s Part 1: well-stereo-complexed blend and non-blended films. *Polymer* 41, 3621-3630.
- Tsuji, H., Muramatsu, H., 2001. Blends of aliphatic polyesters V: non-enzymatic and enzymatic hydrolysis of blends from hydrophobic poly (L-lactide) and hydrophilic poly (vinyl alcohol). *Polymer Degradation and Stability* 71, 403-413.
- Tsuji, H., 2002. Autocatalytic hydrolysis of amorphous-made polylactides: effects of L-lactide content, tacticity, and enantiomeric polymer blending. *Polymer* 43, 1789-1796.
- Tsuji, H., Ikarashi, K., 2004. In vitro hydrolysis of poly (L-lactide) crystalline residues as extended-chain crystallites III: effects of pH and enzyme. *Polymer Degradation and Stability* 85, 647-656.
- Turner, C.H., Anne, V., Pidaparti, R.M.V., 1997. A uniform strain criterion for trabecular bone adaptation: Do continuum-level strain gradients drive adaptation? *Journal of Biomechanics* 30, 555-563.
- van Nostrum, C.F., Veldhuis, T.F.J., Bos, G.W., Hennink, W.E., 2004. Hydrolytic degradation of oligo(lactic acid): a kinetic and mechanistic study. *Polymer* 45, 6779-6787.
- Wang, Y., Pan, J., Han, X., Sinka, C., Ding, L., 2008. A phenomenal model for degradation of biodegradable polymers. *Biomaterials* 29, 3393-3401.
- Wang, Y., Han, X., Pan, J., Sinka, C., 2009. An entropy spring model for the Young's modulus change of biodegradable polymers during biodegradation. *Journal of the Mechanical Behaviour of Biomedical Materials*, accepted, available online.
- Ward, I.M., Hadley, D.W., 1993. *Mechanical properties of solid polymers*. Wiley, pp. 31-40.
- Weinans, H., Huiskes, R., Grootenboer, H.J., 1992. The behaviour of adaptive bone-remodelling simulation models. *Journal of Biomechanics* 25, 1425-1441.
- Wineman, A., 2005. Some comments on the mechanical response of elastomers undergoing scission and healing at elevated temperatures. *Mathematics and Mechanics of Solids* 10, 673.
- Wu, L., Ding, J., 2004. In vitro degradation of three-dimensional porous poly(D,L-lactide-co-glycolid) scaffolds for tissue engineering. *Biomaterials* 25, 5821-5830.
- Zong, X., Wang, Z., Hsiao, B.S., Chu, B., Zhou, J.J., Jamiolkowski, D.D., Muse, D., Dormier, E., 1999. Structure and morphology changes in absorbable poly(glycolide) and poly(glycolide-co-lactide) during in vitro degradation. *Macromolecule* 32, 8107-8114.